# UC Berkeley

**Title**

Nonlinear Behavior of Reinforced Concrete Cable Stayed Bridge Towers Under Cyclic Lateral Load

**Permalink**

**Author**

Ohuchi, Hajime

**Publication Date**

1988-10-01

# NONLINEAR BEHAVIOR OF REINFORCED CONCRETE CABLE STAYED BRIDGE TOWERS UNDER CYCLIC LATERAL LOAD

by
HAJIME OHUCHI
Visiting Scholar

Faculty Investigator. A. C. Scordelis

| 1. Report No. | 2. Government Accession No. | 3. Recipient's Catalog No. |
|---|---|---|

| 4. Title and Subtitle<br>Nonlinear Behavior of Reinforced Concrete<br>Cable Stayed Bridge Towers under Cyclic Lateral Load | 5. Report Date<br>Octorber 1988 |
|---|---|
| | 6. Performing Organization Code |

| 7. Author(s)<br>Hajime Ohuchi | 8. Performing Organization Report No.<br>UCB/SEMM-88/23 |
|---|---|

| 9. Performing Organization Name and Address<br>Department of Civil Engineering<br>University of California<br>Berkeley, California 94720 | 10. Work Unit No. |
|---|---|
| | 11. Contract of Grant No. |

| 12. Sponsoring Agency Name and Address<br>Ohbayashi Co.<br>2-3 Tsukasa-cho, Kanda,<br>Chiyoda-ku, Tokyo, Japan | 13. Type of Report and Period Covered |
|---|---|
| | 14. Sponsoring Agency Code |

15. Supplementary Notes
This study was made during the author's stay at Berkeley as a Visiting Scholar from Ohbayashi Co., Japan

16. Abstract
Inelastic behavior of a cable stayed bridge tower with slender columns is generally affected not only by material nonlinearity, but by geometric nonlinearity as well. This geometric nonlinear effect will be encouraged by gravity load level, creep deformation of concrete and lateral deformation increases.

A number of studies on hysteretic behavior of short columns have been conducted, meanwhile very few studies for a slender structure with more geometric nonlinear effects involved such as bridge towers under cyclic lateral load and creep deformation have been conducted.

For the contribution to the future seismic design of cable stayed bridges, a series of parametric analyses were carried out with various variables such as configuration of tower, reinforcement ratio, gravity load level, slenderness ratio, with and without creep of concrete and applied lateral load, i. e. monotoric or cyclic.

The present study particularly focuses on 1) Influence of creep deformation due to gravity load and cyclic lateral load on the ultimate strength and deformation characteristic, and 2) Applicability of current 'Moment Magnifier Method'.

The conclusions from this study are :
1) No significant effect of creep and cyclic load is indicated on the ultimate behavior in the region of $l/r \leq 100$ slenderness ratio and $\sigma o/f'c \leq 0.2$ gravity load.
2) Current moment magnifier method is on the conservative side eccept for the low slenderness region and less variation is shown in the above mentioned region of $l/r \leq 100$ and $\sigma o/f'c \leq 0.2$ by creep and cyclic load effect.
3) In order to acomplish the sufficient ductility design, both a low axial design load of $\sigma o/f'c$ of at most 0.1 and well confined concrete should be used.
4) In the present study, the max. displacement defined by ultimate load was used for estimation of ductility and absorbed energy. However, additional energy absorbtion can be expected even more in the softening range especially in the case of well confired concrete usage.
Further analytical study up for these regions is needed in future research.

| 17. Key Words<br>Cable Stayed Bridges, Reinforced Concrete,<br>Nonlinear analysis, Creep, Cyclic Lateral Load,<br>Hysteretic Characteristics | 18. Distribution Statement<br><br>Unilimited | | |
|---|---|---|---|
| 19. Security Classif. (of this report)<br>unclassified | 20. Securiby Classif. (of this page)<br>unclassified | 21. No.of Pages<br>173 | 22. Price |

Department of Civil Engineering

Division of Structural Engineering

Mechanics and Materials

# NONLINEAR BEHAVIOR OF REINFORCED CONCRETE CABLE STAYED BRIDGE TOWERS UNDER CYCLIC LATERAL LOAD

by

Hajime Ohuchi

Visiting Scholar

Faculty Investigator :

A. C. Scordelis

College of Engineering

University of California

Berkeley, California

October, 1988

# ACKNOWLEDGEMENTS

# Table of Contents

# List of Tables

## List of Figures

Page

Page

## 1. Introduction

### 1.1 General Remarks

In the family of bridge systems the cable supported bridges are distinguished by their ability to be used for large spans. A cable supported system permits the flexural stiffness of the girder to be less and the dead load reduction enables the span to be lengthened as a result.

It is indeed reported [1,2] that cantilevered bridges with long spans will need a box girder depth in excess of 30~40 feet at the support whereas a multiple-cable-stayed bridge of even longer spans may only require a depth of deck not exceeding about 8 feet. Based on this fact, cable-stayed-bridges are considered to be most economical for 600~1500 feet span bridges.

For a column structure like type of cable-stayed-bridge tower, reinforced concrete is effective from an economical point of view, since advantage can be taken of high concrete compressive strength . However, such towers may often have long columns and therefore some difficult design problems need to be resolved.

Under some high axial loads, the secondary moment in columns increases due to additional creep deformation in service load condition. In addition, combination with earthquake load may lead to further influence of this secondary moment. The present study is to investigate the influence of geometric nonlinearity on hysteretic characteristics and the applicability of current moment magnifier method to the frame type bridge tower like A-shaped tower, one of the representative shapes employed for cable-stayed-bridges. A series of parametric nonlinear analyses of such towers are conducted under a combination of gravity and seismic lateral load and the results interpreted from a design view point.

### 1.2 Current Design Problem

There have been many studies on the hysteretic characteristics of short columns under cyclic lateral loads. Very few, however are on that characteristics of a slender column such as the present tower. Geometric nonlinearity may have an affect even on ultimate load capacity and ductility. In addition the concrete creep effect due to high gravity load may not be neglected.

The Moment Magnifier Method has been available in the design of slender column, that is similar to the procedure used as part of the American Institute of Steel Construction Specifications[3].

The design moment Mc specified by ACI Code[4] is given by

$$M_c = \delta_b M_{2b} + \delta_s M_{2s} \qquad \text{------(1.1)}$$

where

$$\delta_b = \frac{C_m}{1 - P/\phi Pc} \geq 1.0 \qquad \text{---------- (1.2)}$$

$$\delta_s = \frac{C_m}{1 - \Sigma P/\phi \Sigma Pc} \geq 1.0 \qquad \text{---------- (1.3)}$$

$$Pc = \frac{n^2 EI}{(klu)^2} \qquad \text{---------- (1.4)}$$

$$EI = \frac{(EcIg/5) + EsIse}{1 + \beta_d} \qquad \text{---------- (1.5)}$$

$$C_m = 0.6 + 0.4 \frac{M_{1b}}{M_{2b}} \qquad \text{---------- (1.6)}$$

The above design equation was proposed by J.E. Breen alt[5],[6] based on experiments on columns and box type frames under monotonic axial loads with eccentricity. No axial load variation was considered in these experiments and in that sense, the above design equation can be applicable for a single column, whereas axial force variation exists in a frame type bridge tower. When this structure is subjected to a combination of cyclic lateral and imposed gravity load, the stress path on the M-N surface would be different from that under monotonic lateral load corresponding to the current design method. Therefore, it appears to be necessary to investigate validity of the current Moment Magnifier Method.

## 1.3 Objective and Scope of the Present Study

When seismic design is performed consistent with ultimate capacity, it is of significance to avoid brittle failure such as instability failure, i.e. buckling. The hysteretic characteristics of a slender frame under cyclic lateral load would be different mainly dependent on axial load, slenderness ratio of the column and configuration.

With the purposes to investigate the following :

1) applicability of current Moment Magnifier Method

2)   hysteretic characteristics including ultimate load and ductility

3)   final failure

a series of parametric analyses are conducted with axial load, configuration, slenderness ratio, reinforcement ratio, creep effect and lateral load (monotonic or cyclic) as parameters.

Chapter 2 presents a review of the analytical method used in the computer program, PCFRAME utilized in this study.

In chapter 3, several numerical test results are represented to verify the applicability of the program.

Chapter 4 describes the modeling of the structure studied, analytical parameters and external load assumptions.

In chapters 5, 6 and 7, analytical results for short time gravity + monotonic lateral load, long term gravity + monotonic lateral load and long term gravity + cyclic lateral load will be respectively discussed to evaluate concrete creep and cyclic load effects mainly on load resistance and moment behavior.

Finally, conclusions and recommended future research will be presented in chapter 8.

## 2. Review of Analytical Method

### 2.1 General Remarks

The analytical determination of the displacements, internal forces, stresses and deformations of reinforced concrete frames throughout their load history used in the present investigation is based on a comprehensive Ph.d. research study by Kang [7] at the University of California, Berkeley.

The purpose of Kang's Study was to develope an efficient numerical procedure and a general computer program (PCFRAME) for the material and geometric nonlinear analysis of planer reinforced and prestressed concrete frames including the time dependent effects due to load history, temperature history, creep, shrinkage and aging of concrete and relaxation of prestress. An accurate prediction of the response of these structures throughout their service history, as well as throughout elastic, inelastic and ultimate ranges was the primary objective.

A complete description of the analytical method and its theoretical bases, as well as a detailed description of the input-output capabilities of the computer program PCFRAME are given in Kang's Ph. d thesis [7]. In this chapter a review of the main features of the analysis as it applies only to the planar reinforced concrete frames investigated in the present study will be given for easy reference.

The analysis is based on the incremental form of the displacement formulation of the finite element method. Equilibrium equations for the total structure are set up and solved in a global coordinate system, which is fixed in space. The direct stiffness method is used to form the structure stiffness matrix. The structure is divided into straight, planar one dimensional beam elements with the usual three degrees of freedom at each end (Fig.2-1), and with the standard linear and cubic Hermitian shape functions describing the axial and transverse displacements between ends. Shearing deformations are not considered. The origin and direction of the local Cartesian coordinate system passing through the end of the element (Fig. 2-1a) follow the element, which is considered to be in a continuous quasi-static state. Nonlinear geometric effects are accounted for by a nonlinear term in the strain formulation and by continuously updating the nodal point geometry and the transformation matrix between local and global coordinates.

(a) Structure

(b) Element

(c) Actual and Idealized Cross Section
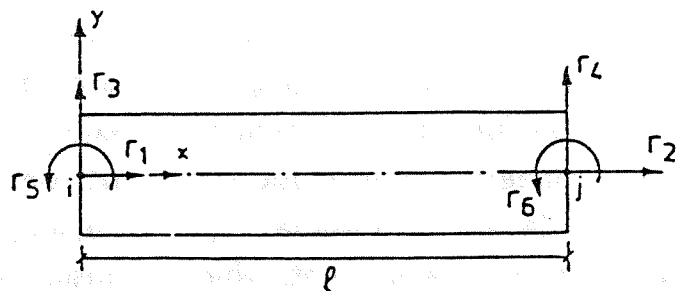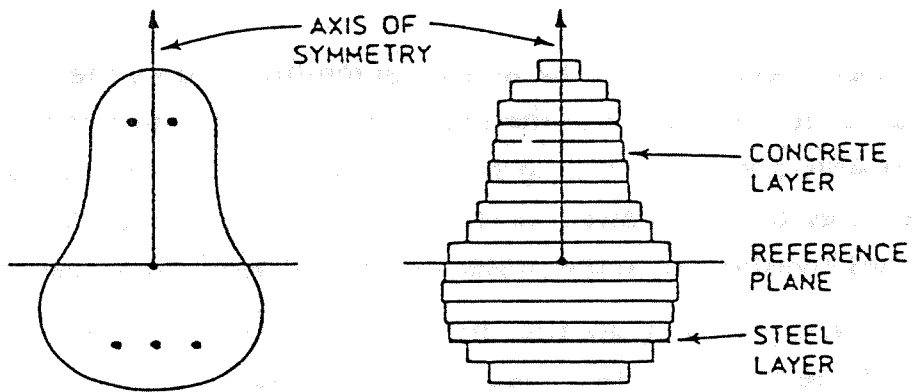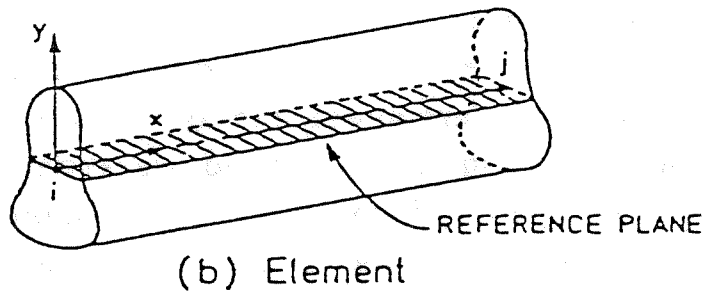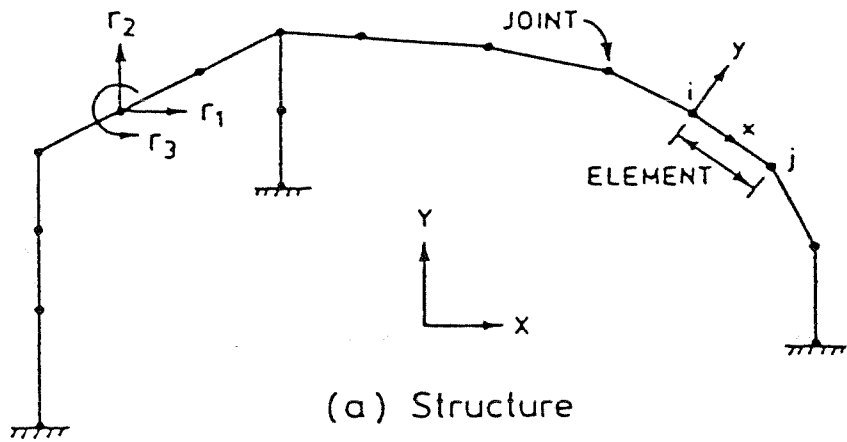
(d) Elevation of an Element and
Displacement Components

Fig. 2−1 GEOMETRY OF A PLANAR REINFORCED CONCRETE FRAME

Different cross sections, symmetric about the local y-axis (Fig. 2-1c), but otherwise of arbitrary shape, and different material properties may be assigned to each element. Cross sections are divided into a finite number of concrete and steel layers, each of which is assumed to be under uniaxial strain. Navier's plane section hypothesis is assumed to govern the distribution of total strains across sections. No bond slip is assumed to take place between rebars and concrete. Nonlinear material properties including cracking of concrete are considered.

Time dependent load history and time dependent effects of material properties are considered using a step forward integration approach by dividing the time domain into a finite number of intervals of constant or varing length. External loads and equivalent loads due to nonmechanical creep strain are applied in a specified number of load steps at each time step.

The nonlinear equilibrium equations are solved by an unbalanced load iteration method for each load step. Internal resisting loads are evaluated numerically by a 3-point Gaussian quadrature over the current length of the element combined with a mid-layer integration over the cross section. Stiffness matrices are evaluated using current material properties at the center of each element only. Incremental solutions for each load step are added to previous totals to arrive at the current updated solution. In this manner, the structural response can be traced through the elastic, cracked, inelastic and ultimate ranges.

In the following sections additional details are given for the modeling of the material properties for the concrete and reinforcing steel and also for the solution strategies used in the computer program PCFRAME [7] for the nonlinear analysis.

## 2.2 Modeling of Material Properties

### (1) Stress-Strain Relationship of Concrete

Concrete is used mostly in compression, so that its compressive stress-strain curve is of primary interest. A model which represents the stress-strain curve of wide variety of concrete in a mathematical formula was suggested by Hognestad, and is shown in Fig. 2-2a. For the present investigation, this model is utilized with minor modifications.

The ascending part of the curve is described by the equation,

$$\sigma = f_c'' \frac{\varepsilon^m}{\varepsilon_0} \left(2 - \frac{\varepsilon^m}{\varepsilon_0}\right) \qquad \text{---------- (2.1)}$$
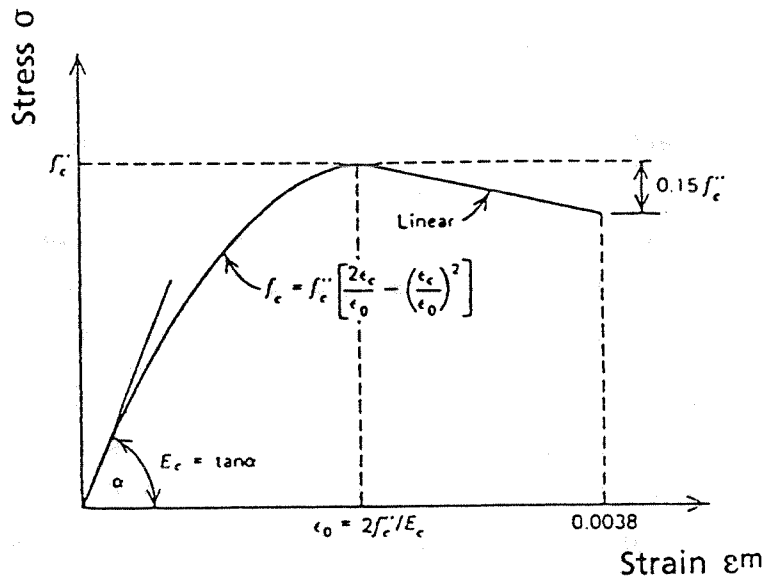
Fig. 2-2 (a) Idealized stress-strain curve for concrete in uniaxial compression.
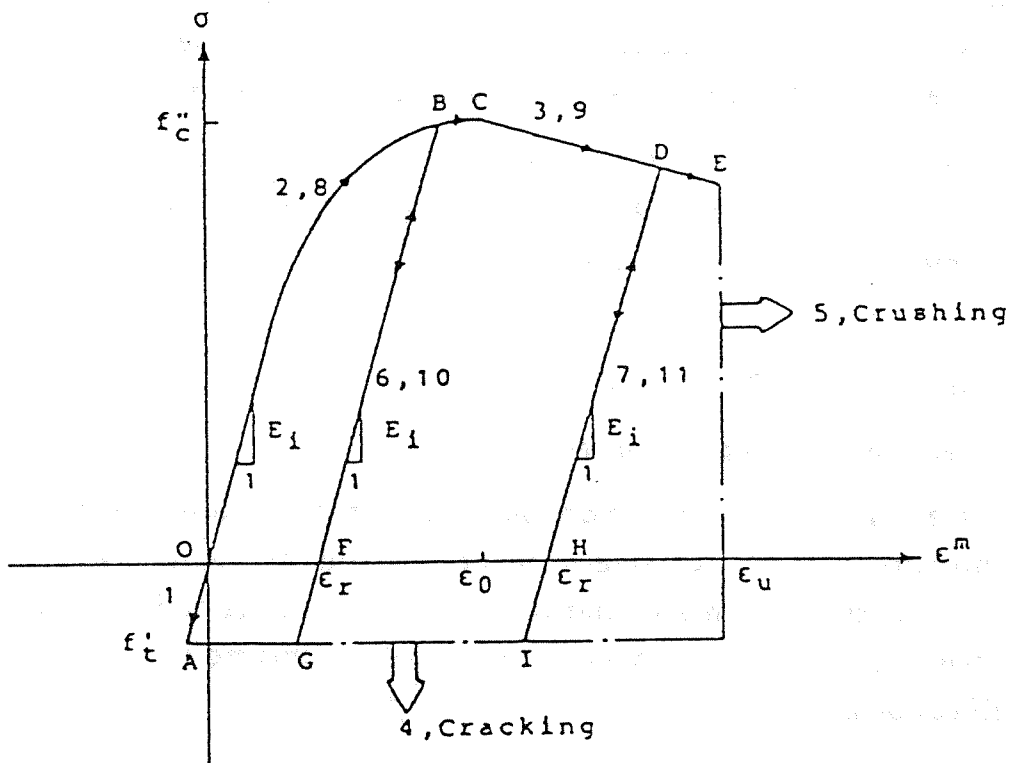


Fig. 2-2 (b) Stress-Strain Curve of Concrete Assumed in the Present Study (Numbers Represent the Material State of Concrete)

in which $\varepsilon^m$ is the mechanical strain and the strain $\varepsilon_0$ corresponding to the maximum compressive stress $f''_c$ is given by

$$\varepsilon_0 = \frac{2f'_c}{E_i} \qquad \text{---------- (2.2)}$$

Where $E_i$ is the initial tangent modulus. By differentiating eq. (2.1), the tangent modulus $E_t$ is obtained.

$$E_t = \frac{d\sigma}{d\varepsilon^m} = E_i(1 - \frac{\varepsilon^m}{\varepsilon_0}) \qquad \text{---------- (2.3)}$$

The descending part of the compressive stress-strain curve is a straight line. In this study, the tangent modulus of this part is assumed to be zero. But the decrease in stress with the increase with the mechanical strain is accounted for as unloading. The equation of this part can be written,

$$\sigma = -0.15f'_c \frac{\varepsilon^m - \varepsilon_0}{\varepsilon_u - \varepsilon_0} + f''_c ; \quad E_t = 0 \qquad \text{---------- (2.4)}$$

Maximum compressive strength $fc''$ is given by a fraction of the compressive strength $fc'$ as follows.

$$f''_c = \gamma_c f'_c \qquad \text{---------- (2.5)}$$

And $\gamma c = 1$ is assumed in the present study.

There are numerous empirical formulas for the evaluation of the initial tangent modulus $E_i$. ACI committee 209 recommends the following formula, [11]

$$E_i = 33 W^{1.5} f'_c \text{ psi} \qquad \text{---------- (2.6)}$$

where W is the unit weight of the concrete in pcf.

The maximum tensile stress in the stress-strain curve of concrete is assumed to have the value of the modulus of rupture, and will be denoted by ft'. ACI committee 209 also recommends the following value.

$$f'_c = \gamma_t \sqrt{W f'_c} \text{ psi} \qquad \text{---------- (2.7)}$$

where the parameter $\gamma_t$ has the value of 0.6 to 1.0 in general.

The slope of the tensile stress-strain curve is assumed to be constant and the same as the initial tangent modulus $E_i$. Then the tensile stress-strain relationship can be written as follows.

$$\sigma = E_i \, \epsilon^m \; ; \; E_t = E_i \qquad\qquad \text{---------- (2.8)}$$

Tension stiffening of concrete after cracking is neglected in this study.

Unloading and reloading due to cyclic lateral load history is accounted for by a simple load reversal model of the stress-strain curve. Even under a constant sustained load, unloading could take place in the reinforced concrete structure due to creep.

The load reversal model utilized in this study is shown in Fig. 2-2b.

The following assumptions are made in this model.

1) The slope of the load reversal path in the stress-strain curve is the same as the initial tangent modulus $E_i$.

2) Tensile failure or cracking of concrete occurs when the tensile stress reaches its maximum tensile stress $f'_t$.

3) Compressive failure of crushing of concrete when the compressive mechanical strain exceeds its maximum compressive strain $\epsilon_u$.

4) Once concrete is cracked, it cannot take any tensile stress again.

   But it can take compressive stress upon closing of the crack and reloading.

   Thus the crack is assumed to close in compression and reopen in tension without any resistance.

(2)   Creep deformation of Concrete

Creep strains are the time and stress dependent strains occurring beyond those defined by the mechanical stress-strain curve.

In this study, creep strain $\epsilon^c(t)$ is expressed with a superposition integral:

$$\epsilon^c(t) = \int_0^t c(t', t-t', T) \frac{\delta\sigma(t')}{\delta t'} dt' \qquad\qquad \text{---------- (2.9)}$$

in which the kernel function $c(t', t-t', T)$ is the specific creep function dependent on age and temperature variations.

The principle of superposition is assumed to be valid for the equation of creep strain (Fig. 2-3). Thus, total creep strain at any time t can be obtained as the sum of independent creep strains produced by stress changes at different ages with different durations of time up to t.

Concrete is assumed to be a thermorheologically simple material. such a material is defined as a material which obeys the time-shift principle for the temperature variation.

Stress and temperature changes are assumed to occur only at distinct time step $t_n$ : n = 1,2,.....,$n_t$ (Fig. 2-3a, b). And for the calculation of creep strain increment during some time interval, the stress and temperature are assumed to remain constant during the interval.

The following form of age and temperature dependent on specific creep function is used in this study:

$$c(t', t - t', T) = \sum_{i=1}^{m} a_i(t')[1 - e^{-\lambda i \phi(T)(t - t')}] \qquad \text{---------- (2.10)}$$

in which m, $a_i(t')$, $\lambda_i$, $\phi$ (T) are to be determined from experimental creep curves, or, if experimental data is lacking, from design curves recommended by ACI committee 209 [11].

The principle of superposition of creep strain is illustrated in Fig. 2-3 with given temperature and stress histories. The following definitions for incremental quantities of time steps, stresses and creep strains are used :

$$\Delta t_n = t_n - t_{n-1} \qquad \text{---------- (2.11)}$$

$$\Delta \sigma_n = \sigma_n - \sigma_{n-1} = \sigma(t_n) - \sigma(t_{n-1}) \qquad \text{---------- (2.12)}$$

$$\Delta \varepsilon_n^c = \varepsilon_n^c - \varepsilon_{n-1}^c = \varepsilon^c(t_n) - \varepsilon^c(t_{n-1}) \qquad \text{---------- (2.13)}$$

Total creep strain $\varepsilon_n^c$ at typical time step $t_n$ can be obtained by:

$$\varepsilon_n^c = \Delta \sigma_1 \cdot c(t_1, t_n - t_1, T) + \Delta \sigma_2 \cdot c(t_2, t_n - t_2, T)$$

$$+ ..... + \Delta \sigma_{n-1} \cdot c(t_{n-1}, t_n - t_{n-1}, T) \qquad \text{---------- (2.14)}$$

Total creep strain $\varepsilon_{n-1}^c$ at time step $t_{n-1}$ can be obtained by :

$$\varepsilon_{n-1}^c = \Delta \sigma_1 \cdot c(t_1, t_{n-1} - t_1, T) + \Delta \sigma_2 \cdot c(t_2, t_{n-1} - t_2, T)$$

$$+ ..... + \Delta \sigma_{n-2} \cdot c(t_{n-2}, t_{n-1} - t_{n-2}, T) \qquad \text{---------- (2.15)}$$
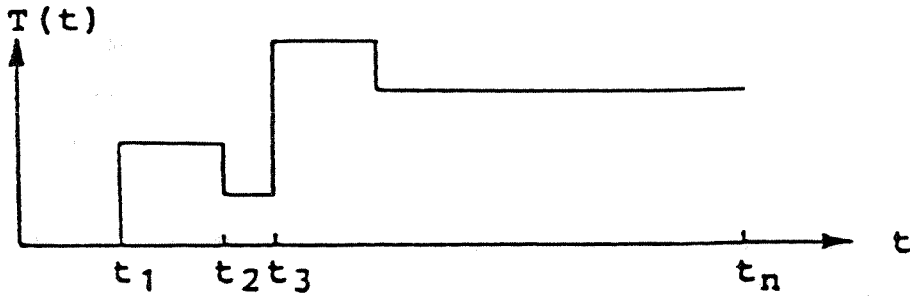
(a) Temperature History
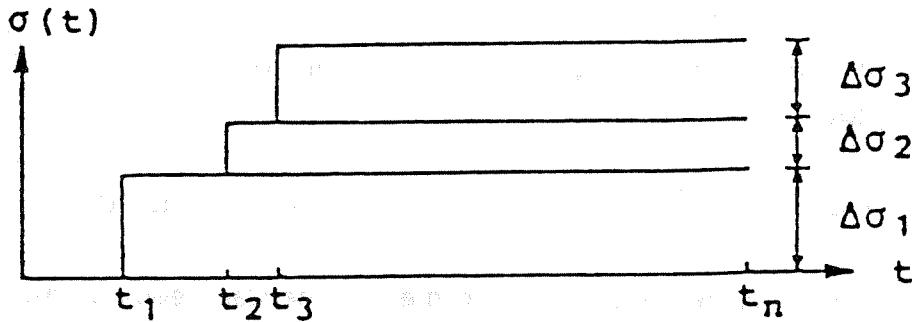
(b) Stress History
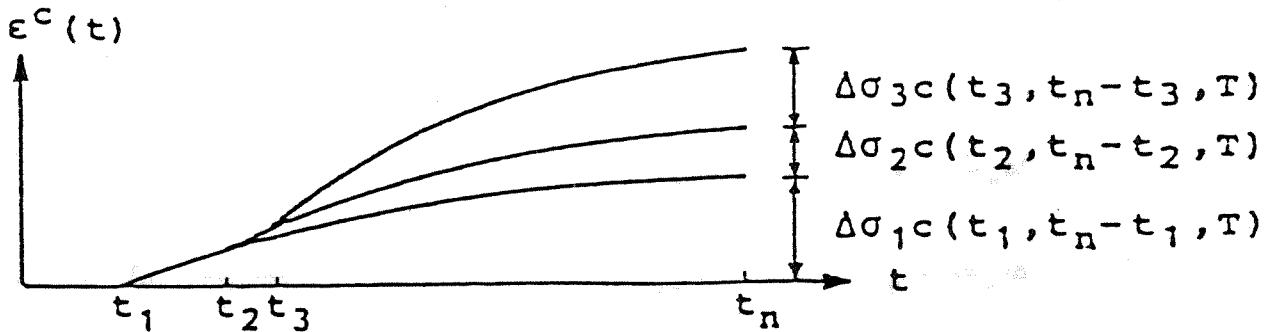
(c) Creep Strain History

Fig. 2-3   Superposition of Creep Strains

Substituting the value c (t', t-t' , T) from Eq. (2.10) into Eqs. (2.14) and (2.15), and those results into Eq. (2.13), after some extensive algebraic manipulations, the recursive relations necessary for calculating the increment of creep strain $\Delta\varepsilon^c_n$ at the time step $t_n$ are as follows:

$$\Delta\varepsilon^c_n = \sum_{i=1}^{m} A_{i,n}[1 - e^{-\lambda_i\phi(T_{n-1})\Delta t_n}] \qquad \text{---------- (2.16)}$$

$$A_{i,n} = A_{i,n-1}e^{-\lambda_i\phi(T_{n-2})\Delta t_{n-1}} + \Delta\sigma_{n-1}a_i(t_{n-1}) \qquad \text{---------- (2.17)}$$

$$A_{i,2} = \Delta\sigma_1 a_i(t_1) \qquad \text{---------- 2.18}$$

A very important advantage of the formulation indicated above is that the computational procedure for each new creep strain increment requires only the stress history of the last time step and not total stress history.

## (3) Reinforcing Steel

The properties of reinforcing steel, unlike concrete, generally are not dependent on environmental conditions or time.  Thus specification of its stress-strain relationship is sufficient to define its properties relevant in the analysis of reinforced concrete structures.  In this study a bilinear model which is symmetrical about origin, as shown in Fig. 2-4a, is used for monotonic loading.

The only modification added to the original PCFRAME computer program is a cyclic loading model for reinforcing steel as shown in Fig.2-4.  The bilinear cyclic model utilized in the original program is not sufficient to predict hysteretic behavior under a repeated lateral load such as earthquake load.

The unloading path for stresses of both signs follows the initial elastic slope.  After the first yield excursion the loading parts of the stress-strain curve may be represented by Ramberg-Osgood relationship[8].

$$\varepsilon_s - \varepsilon_{si} = \frac{f_s}{E_{se}}(1 + \mid \frac{f_s}{f_{ch}} \mid^{r-1}) \qquad \text{---------- (2.19)}$$

with the following empirical values determined by Kent and Park for intermediate grade steel

$$f_{ch} = f_y[\frac{0.744}{1n(1 + 1000\varepsilon_{ip})} - \frac{0.071}{1 - e^{1000\varepsilon_{ip}}} + 0.241] \qquad \text{---------- (2.20)}$$
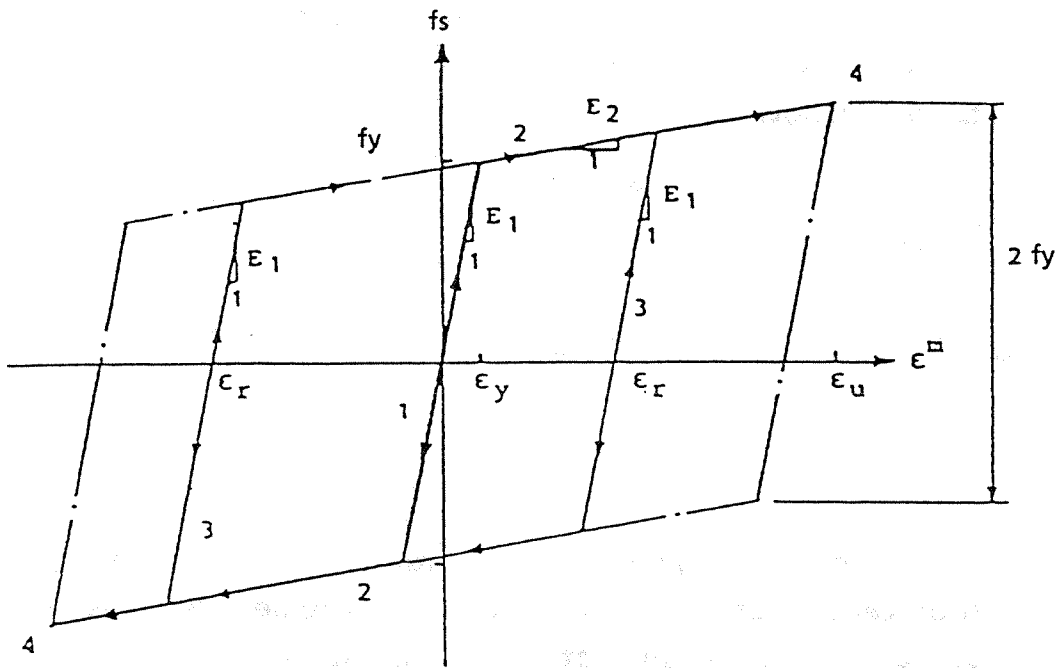
Fig. 2-4 (a)   Stress-Strain Curve of Reinforcing Steel Assumed in the Present Study (Numbers Represent the Material State of Reinforcing Steel)
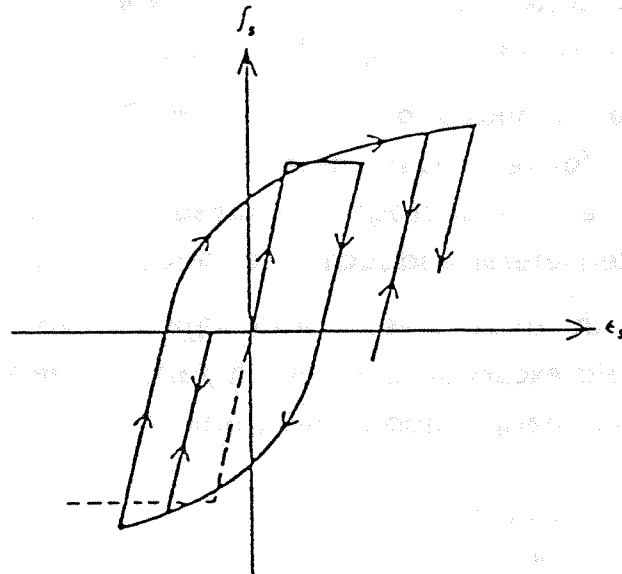


Fig. 2-4 (b)  Stress-strain curve for steel with cyclic loading illustrating the Bauschinger effect.

For odd-numbered loading runs (n = 1,3,5.....)

$$r = \frac{4.49}{\ln(1+n)} - \frac{6.03}{e^n - 1} + 0.297 \qquad \text{---------- (2.21)}$$

for even-numbered loading runs (n = 2,4,6.....)

$$r = \frac{2.20}{\ln(1+n)} - \frac{0.469}{e^n - 1} + 3.04 \qquad \text{---------- (2.22)}$$

where $\varepsilon_s$ is the steel strain, $\varepsilon_{si}$ is the steel strain at beginning of loading run, $f_s$ is the steel stress, $E_{se}$ is the modulus of elasticity of steel, $\varepsilon_{ip}$ is the plastic strain in steel produced in previous loading run, and n is the loading run number (first yield occurs at n = 0, n = 1 is the first postyield stress reversal, n = 2 is the second postyield stress reversal, etc.).

The stiffness of reinforcing steel in the nonlinear region is calculated differentiating Eq. (2.19) by the strain $\varepsilon_s$,

$$E_s = \frac{df_s}{d\varepsilon_s} - \frac{E_{se}}{1 + r \mid f_s / f_{ch} \mid^{r-1}} \qquad \text{---------- (2.23)}$$

## 2.3 Composite Layer System

A composite layer system consisting of concrete and reinforcing steel layers is constructed in order to account for varied material properties within a frame element, as shown in Fig. 2-1c. Each concrete or steel layer in a cross section is assumed to be in a state of uniaxial stress, and for each layer, the cross sectional area and distance from the reference plane are specified as geometric properties.

Since concrete and reinforcing steel are assumed to be perfectly bonded together, the displacement field of the reinforcing concrete frame element is continuous. Then any integral involving varying material properties over the volume of a frame element, such as the integral required to evaluate element stiffness matrix or internal force vector, can be performed layer by layer as follows.

$$\int_v \phi \psi \, dv = \sum_{i=1}^{n_c} \int_v \phi \psi_i \, dV + \sum_{i=1}^{n_s} \int_v \phi \psi_i \, dV \qquad \text{---------- (2.24)}$$

were, $\phi$ is a function of space, $\psi$ is a function of varying material properties such as tangent modulus, stress or various time dependent strains, $n_c$ is the number of concrete layers, and $n_s$ is the number of steel layers. Integration along the length of a frame element is performed by three point Gaussian quadrature.

## 2.4 Equilibrium Equations Including Geometric and Material Nonlinearities and Non-mechanical Strains

The displacement of any point along the frame axis can be expressed as follows, assuming a linear variation of $u_o(x)$ and cubic variation of $v(x)$.

$$u_o(x) = \underline{\phi}\, \underline{u} \qquad\qquad \text{---------- (2.25)}$$

$$\underline{\phi} = [1-p), p] \quad ; \quad p = x/L \qquad\qquad \text{---------- (2.26)}$$

$$v(x) = \underline{\psi} \begin{Bmatrix} \underline{v} \\ \underline{\theta} \end{Bmatrix} \qquad\qquad \text{---------- (2.27)}$$

$$\underline{\psi} = [(1-3p^2+2p^3), (3p^2-2p^3), L(p-2p^2+p^3), L(-p^2+p^3)]^3 \qquad \text{---------- (2.28)}$$

in which $\phi$ and $\psi$ are shape functions for $u_o(x)$ and $v(x)$ respectively, and these quantities are defined in local coordinates. Then, by the plane section assumption the x-displacement of any point in the element can be written as follows.

$$u(x,y) = u_o(x) - y \cdot dv(x)/dx = [\underline{\phi}, -y\underline{\psi}_{,x}]\, \underline{r} \qquad \text{---------- (2.29)}$$

$$v(x) = [\underline{0}, \underline{\psi}]\, \underline{r} \qquad\qquad \text{---------- (2.30)}$$

where

$$\underline{r} = \begin{Bmatrix} \underline{u} \\ \underline{v} \\ \underline{\theta} \end{Bmatrix} \qquad\qquad \text{---------- (2.31)}$$

Axial strain $\varepsilon(x, y)$ is defined by [9]

$$\varepsilon(x, y) = \frac{du(x,y)}{dx} + \frac{1}{2}\left(\frac{dv(x)}{dx}\right)^2 \qquad \text{---------- (2.32)}$$

in which the second term represents the nonlinear displacement effect.

Based on these equations, the tangential strain-displacement relationship at the state A (Fig.2-5b) is

$$d\varepsilon = \underline{B}\, d\underline{r} \qquad\qquad \text{---------- (2.33)}$$
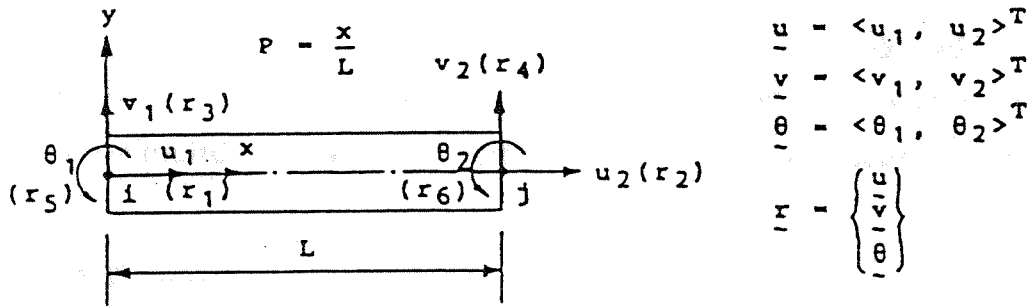
(a) Displacements of a Frame Element
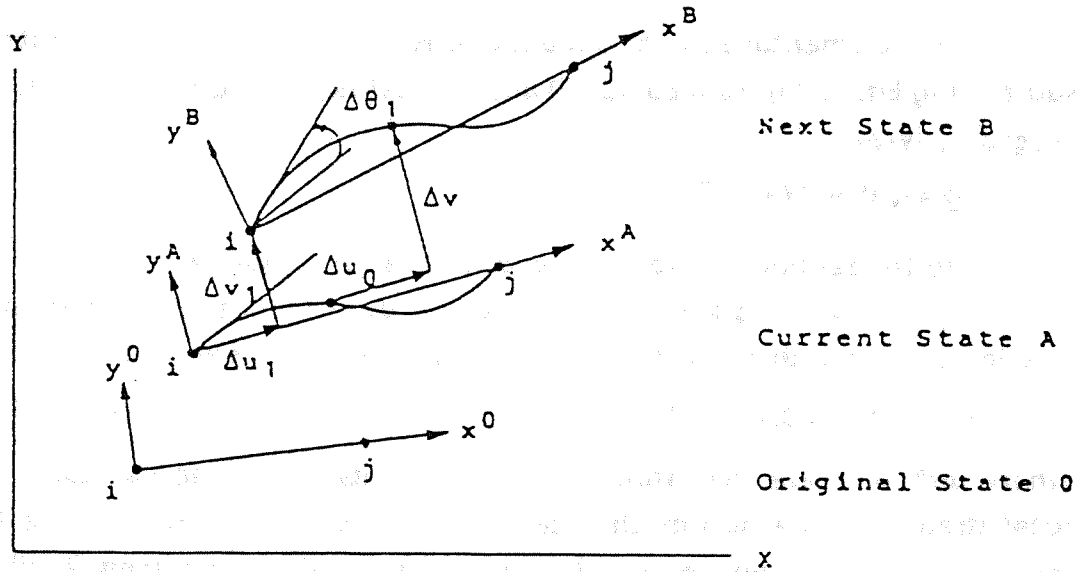


(b) Frame Element in Various States of Deformation

Fig. 2-5   Displacements and Deformations of a Frame Element

where

$$\underline{B} = [\underline{\phi}_{,x}, -y\underline{\psi}_{,xx}]$$
$$= [-1/L, 1/L, 6y(1-2p)/L^2, 6y(-1+2p)/L^2, 2y(2-3p)/L, 2y(1-3p)/L] \quad \text{------ (2.34)}$$

By considering virtual work equation, we obtain the total equilibrium equations at the state A.

$$\underline{R}^j = \int_v \underline{B}^T \sigma \, dV \qquad \text{--------- (2.35)}$$

The tangential strain-displacement at the next state B can be written

$$d\varepsilon = \underline{B} \, d\underline{r} + d\underline{r}^T \underline{c}^T \underline{c} \, \Delta\underline{r}$$
$$= d\underline{r}^T(\underline{B}^T + \underline{c}^T \underline{c} \Delta\underline{r}) \qquad \text{--------- (2.36)}$$

Similarly, we obtain the total equilibrium equations at the state B.

$$\underline{R}^j + \Delta\underline{R}^j = \int_v (\underline{B}^T + \underline{c}^T \underline{c} \, \Delta\underline{r})(\sigma + \Delta\sigma) \, dV \qquad \text{--------- (2.37)}$$

The incremental equilibrium equations at the state A are then obtained by subtracting Eq. (2.35) from Eq. (2.37) and neglecting the higher order term $\int_v \underline{c}^T \Delta\sigma \underline{c} \, dV \cdot \Delta r$

$$\Delta\underline{R}^j = \int_v \underline{B}^T \Delta\sigma \, dV + \int_v \underline{c}^T \sigma \underline{c} \, dV \cdot \Delta\underline{r} \qquad \text{--------- (2.38)}$$

The tangential equilibrium equations can be obtained from Eq. (2.38) by replacing $\Delta r$ by $dr$, $\Delta R^j$ by $dR^j$ and $\Delta\sigma$ by $d\sigma$. The tangential stress-strain relationship for both concrete and reinforcing steel can be written

$$d\sigma = E_t \, d\varepsilon^m = E_t(d\varepsilon - d\varepsilon^{nm}) \qquad \text{--------- (2.39)}$$

where $d\varepsilon^m$, $d\varepsilon^{nm}$ are the infinitesimal increments of the mechanical strain, the total strain and the non-mechanical strain respectively, and $E_t$ is the tangent modulus as defined before. By substituting Eq. (2.33) for $d\varepsilon$ into eq (2.39),

$$d\sigma = E_t \underline{B} \, d\underline{r} - E_t d\varepsilon^{nm} \qquad \text{--------- (2.40)}$$

Substitution of Eq. (2.40) into Eq. (2.38), after replacing the incremental operator $\Delta$ by the differential operator d, gives us the following tangential equilibrium equations at the current state A.

$$d\underline{R}^j = (\int_v \underline{B}^T E_t \underline{B} \, dV + \int_v \underline{c}^T \sigma \, \underline{c} \, dV) \cdot d\underline{r} - \int_v \underline{B}^T E_t \, d\varepsilon^{nm} dV \qquad \text{--------- (2.41)}$$

By defining the following terms

$$d\underset{\sim}{R}^{nm} = \int_v \underline{B}^T E_t \, d\varepsilon^{nm} \, dV \qquad \text{---------- (2.42)}$$

$$d\underset{\sim}{R} = d\underset{\sim}{R}^j + d\underset{\sim}{R}^{nm} \qquad \text{--------- (2.43)}$$

$$\underline{K}_e = \int_v \underline{B}^T E_t \underline{B} \, dV \qquad \text{-----------(2.44)}$$

$$\underline{K}_g = \int_v \underline{c}^T \sigma \underline{c} \, dV \qquad \text{-----------(2.45)}$$

$$\underline{K}_T = \underline{K}e + \underline{K}g \qquad \text{--------- (2.46)}$$

We can rewrite the Eq.(2.41)

$$d\underset{\sim}{R} = \underline{K}_t \, d\underset{\sim}{r} \qquad \text{--------- (2.47)}$$

## 2.5    Time Dependent Analysis Procedure

For the time dependent analysis, the time domain is divided into a discrete number of time intervals each of which need not have the same duration in time. The junctions of these time intervals are defined as time step $t_n$. Thus, a discrete number of time steps $t_n = 1, 2 \ldots\ldots, n_t$, exist, where $n_t$ is the total number of time steps considered in the analysis. Then a step forward integration is performed in which incremental solutions are successively added to the previous total to obtain the solution at the current time step, as follows.

At time step $t_{n-1}$, all the joint displacements $\underset{\sim}{r}$, total strains $\varepsilon$, total non-mechnical strains $\varepsilon^{nm}$, and stresses at every part of the structure are known. Evaluate the increments of non-mechanical strains $\Delta\varepsilon^{nm}_n$ due to creep ($\Delta\varepsilon^c_n$) and shrinkage ($\Delta\varepsilon^{sh}_n$) of concrete and temperature changes ($\Delta\varepsilon^T_n$) occurring during time steps $t_{n-1}$ and $t_n$. Then calculate the equivalent joint load increments $\Delta R_n^{nm}$ at time step $t_n$ which would produce the non-mechanical strain increments $\Delta\varepsilon^{nm}_n$ by treating them as initial strains. $\Delta\underset{\sim}{R}_n^{nm}$ for each element can be calculated by the equation:

$$\Delta\underset{\sim}{R}_n^{nm} = \int_v \underline{B}^T E_t \Delta\varepsilon^{nm}_n \, dV \qquad \text{----------(2.48)}$$

where B is the strain-displacement matrix, and $E_t$ is the tangent modulus.

At the time step $t_n$, load increment $\Delta\underset{\sim}{R}_n$ is obtained by adding external joint load increment $\Delta\underset{\sim}{R}^j_n$ and unbalanced load $\underset{\sim}{R}^u_{n-1}$ left over from time step $t_{n-1}$, to the equivalent joint increment $\Delta\underset{\sim}{R}_n^{nm}$ due to the non-mechanical strains:

$$\Delta\underset{\sim}{R}_n = \Delta\underset{\sim}{R}^j_n + \Delta\underset{\sim}{R}_n^{nm} + \underset{\sim}{R}^u_{n-1} \qquad \text{---------- (2.49)}$$

Then $\Delta \underset{\sim}{R} n$ is divided into load increments $\Delta \underset{\sim}{R}$, each of which need not be of equal magnitude. Then the incremental load analysis and the unbalanced load iteration are performed for each load step as follows.

(1) Form tangent stiffness for each element based on current geometry and material properties. Assemble structure tangent stiffness $\underset{\sim}{K}_t$ in global coordinates using current displacement transformation matrix for each element.

(2) Solve $\underset{\sim}{K}_t \Delta \underset{\sim}{r} = \Delta \underset{\sim}{R}$ for displacement increments $\Delta \underset{\sim}{r}$ and transform into local coordinates to obtain element end displacement increments.

(3) Compute strain increment $\Delta \varepsilon$ from element end displacement increments by using nonlinear incremental strain-displacement relationship, and add to previous total to obtain current total strain $\varepsilon$.

(4) Add displacements $\Delta \underset{\sim}{r}$ to previous total to get current total joint displacements $\underset{\sim}{r}$. Based on current total displacements $\underset{\sim}{r}$, update member geometry, i.e. update element length and displacement transformation matrix.

(5) Subtract current total nonmechnical strain $\varepsilon^{nm}$ due to creep, shrinkage and aging of concrete and temperature changes from current total strain $\varepsilon$ to obtain current total mechanical strain $\varepsilon^m$. Compute current stress $\sigma$ from nonlinear stress-strain $(\sigma\text{-}\varepsilon^m)$ law valid for the present time step $t_n$, taking load reversals into account.

(6) Compute element end forces by integrating current total stresses in concrete and reinforcing steel layers for each element in local coordinates, and transform into global coordinates using updated displacement transformation matrixes to assemble for the internal resisting loads $\underset{\sim}{R}^i$.

(7) Subtract internal resisting loads $\underset{\sim}{R}^i$ from current total external joint loads $\underset{\sim}{R}^j$ to obtain unbalanced loads $\underset{\sim}{R}^u$.

$$\underset{\sim}{R}^u = \underset{\sim}{R}^j - \underset{\sim}{R}^i \qquad \text{--------- (2.50)}$$

(8) Set $\Delta \underset{\sim}{R} = \underset{\sim}{R}^u$, and go back step (1). Steps (1) to (8) are continued until unbalanced loads $\underset{\sim}{R}^u$ are within allowable tolerances. At this point, the current unbalanced loads $\underset{\sim}{R}^u$ are added to the load increment $\Delta \underset{\sim}{R}$ for the next load step, and the iterative procedure (1) to (8) is performed again. At the end of the final load step, proceed to next time step $t_{n+1}$.

2.6    Solution Technique of Equilibrium Equation

There are various effective solution method for nonlinear problem. These method can be generally classified into three categories as follows.

1) Incremental Load Method

2) Iterative Method

3) Combined Method

The incremental load method generally gives a good approximation to the intermediate and final solutions while the iterative methods yields the final solution to the desired degree of accuracy. For concrete structures, the solution is generally path-dependent mainly due to the progressive cracking in tensile regions, so that it is desirable to use the incremental method. For this study the combined method is used to enhance the accuracy of the solution. An option is provided to use either tangent stiffness or constant stiffness during iterations.

In solving nonlinear equilibrium equations by iterative methods, the convergence at the end of an iteration can be measured by two criteria. The first criterion is the magnitude by which equilibrium is violated. This can be measured by the magnitude of the unbalanced loads. The second criterion is the accuracy of the total displacements. This can be measured by the magnitude of additional displacement increments.

For this study the displacement criterion is used as a primary convergence criterion. But to guard against the excessive violation of equilibrium, the unbalanced load criterion is also provided.

## 3. Preliminary Numerical Studies

The PCFRAME computer program[7] was developed mainly for monotonic loading analysis whether it is mechanical or time dependent load. Therefore, its applications[7,10] have been so far for monotonic loading. The present study is also due to cyclic loading and in that respect it is necessary to discuss its validity of prediction for such a loading case. In addition, the numerical accuracy due to load or time increments should be also investigated since the accuracy of numerical solution is generally governed by such increments.

### 3.1 Theoretical Studies

### (1) Timoshenko Beam

This computer program can deal with material and geometric nonlinearities. In this section, the accuracy of numerical prediction for a geometeric nonlinear problem will be discussed. An elastic beam with pinned supports at both ends under uniform load is the example for this purpose, which was earlier shown by Kang[7]. Focusing point is the comparison of numerical solutions between 5, 10 and 20 load increments up to $\delta/\ell = 0.1$ of displacement level, where $\delta$ is the central deflection and $\ell$ is the span length of the beam.

Fig.3-1 shows load-deflection curve, in which each case similarly provides slightly higher but good agreement with the exact solution. Also shown are axial stress and bending stress of central section in Fig.3-2. Excellent agreement is obtained for $\sigma_a$ and slightly higher values, but good agreement for $\sigma_b$ compared with the exact solution. Significant difference between various load increments is not observed. Based on this example, this computer program can provide good predictions even using coarse load increments in the finite deformation analysis of a pinned support beam with uniform load.
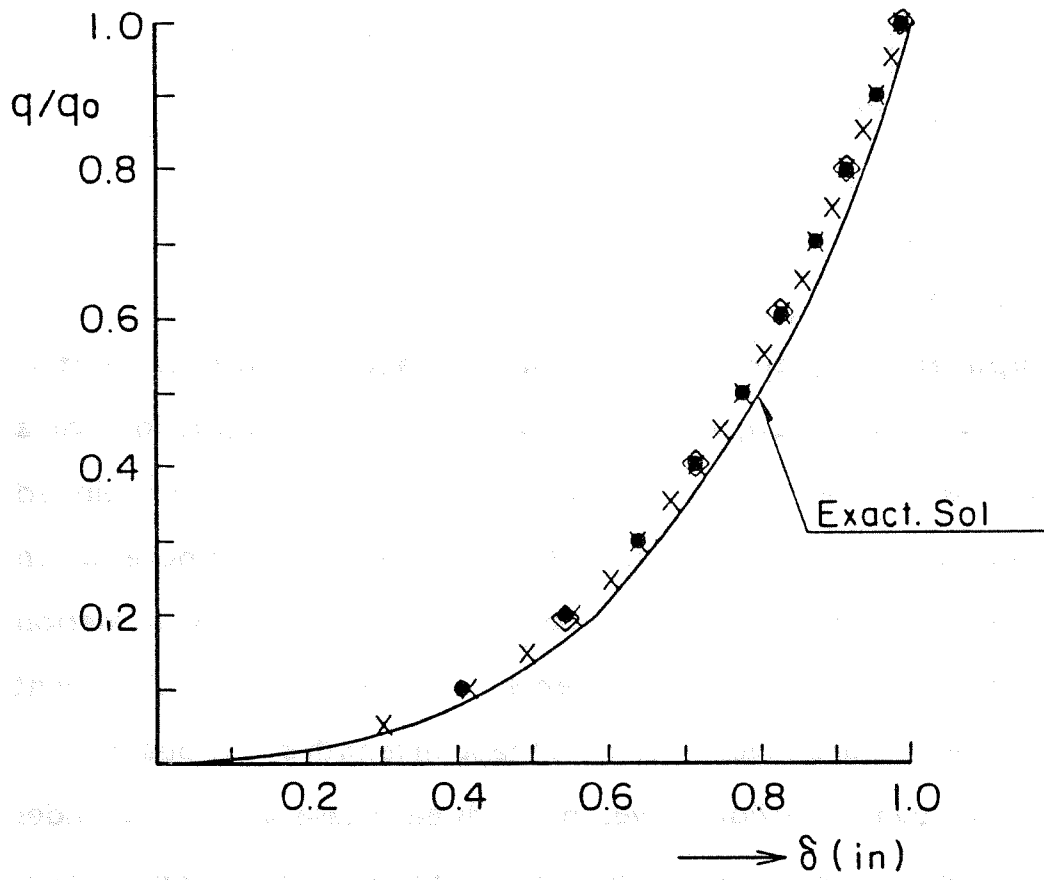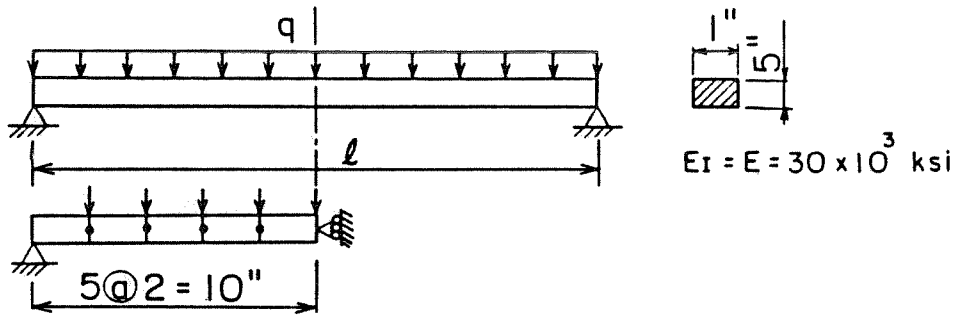
Fig.3-1   Timoshenko Beam Load - Deflection Relationship
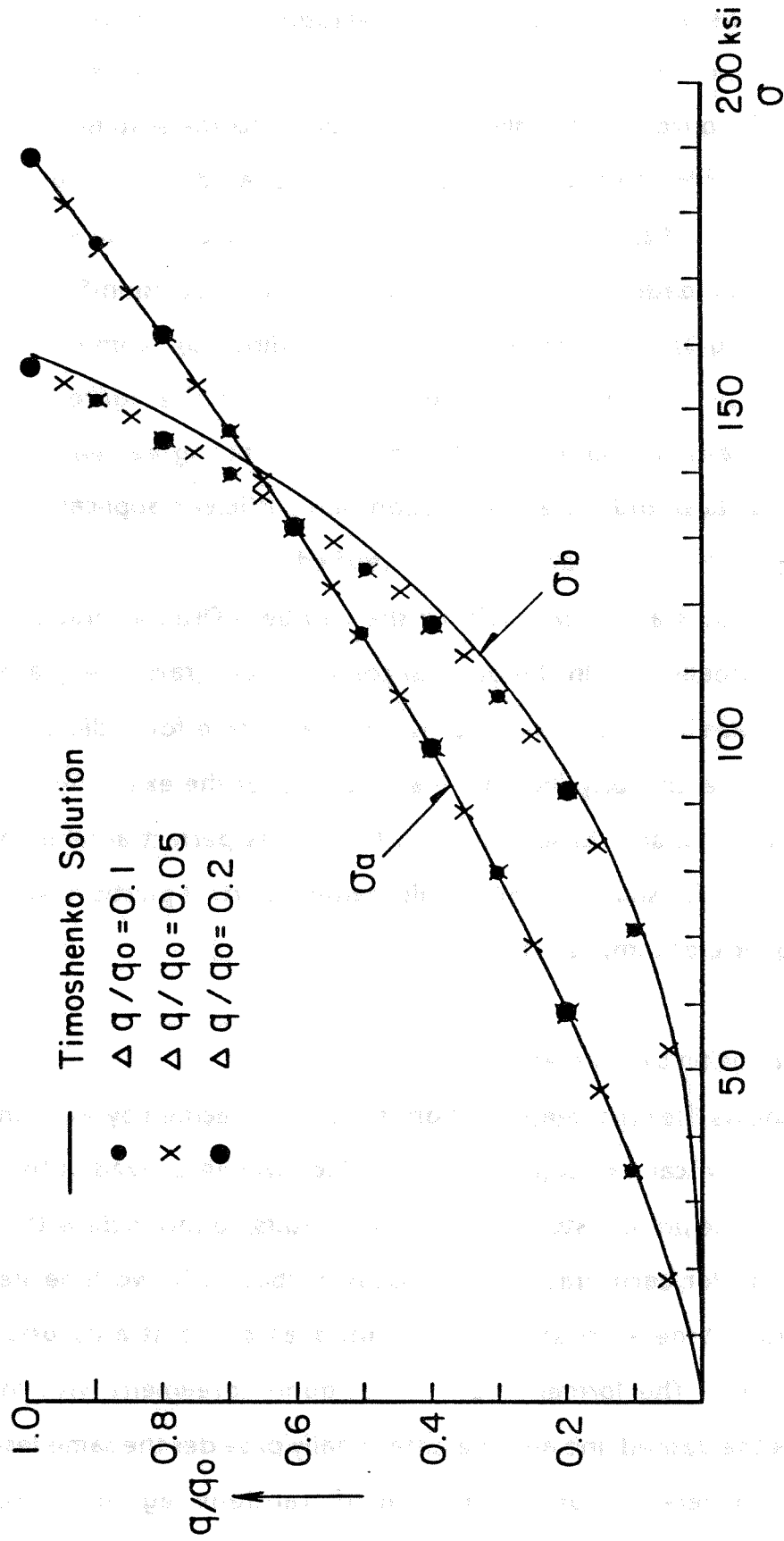
Fig.3-2  Timoshenko Beam Load-Midspan Stress Relationship

(2) Uniaxial Stress-Strain Relationship of Concrete and Steel under Cyclic Loading

Fig.3-3 shows a concrete stress-strain relationship under cyclic loading in which the solid line shows an exact solution and the round circle an analytical result. With the purpose of analysing behavior up to the softening branch, a cyclic load is applied to the two element model illustrated in the figure which consists of concrete and elastic spring elements. Loading procedures are 0→high compression(1) →unloading(2) →tensile loading(4) →compression(5)→maximum load(7) → softening(8) → unloading(9) →tensile loading(10)→compression(11)→ softening(12)→crushing(13). Also shown together in the figure are similar relationships of elastic spring and total model. Perfect agreement is achieved between an analytical and an exact solution and sufficient applicability of the computer program for cyclic load problem is verified.

Fig.3-4 provides a similar result for the Ramberg-Osgood model which is used for rebar modelling. In the original computer program[7], only a bi-linear model has been available for use which is not predictable for cyclic behavior of steel. In the figure, similarly shown are a solid line for the exact solution and a round circle for the analytical solution which provides perfect agreement. By setting a restriction of $|f_s| \leq |f_y|$ during cyclic loading, perfect plastic flow occurs in the 1st loading cycle of compression side.

(3) Creep Deformation of Concrete

Fig.3-5 shows the unit creep function (solid line) specified by ACI Committee 209[11] and the analytical model (dashed line) which will be utilized in the bridge tower analysis of the present study. Analytical results, round circle with ten time step, two fraction for each time step and cross symbol with two time step, nine fraction for each time step are also provided as creep strains under unit compressive load. The former case achieves good agreement with the input curve shown as the dashed line and the latter finally provides the same result with a considerable difference for the fraction of transient region. However,
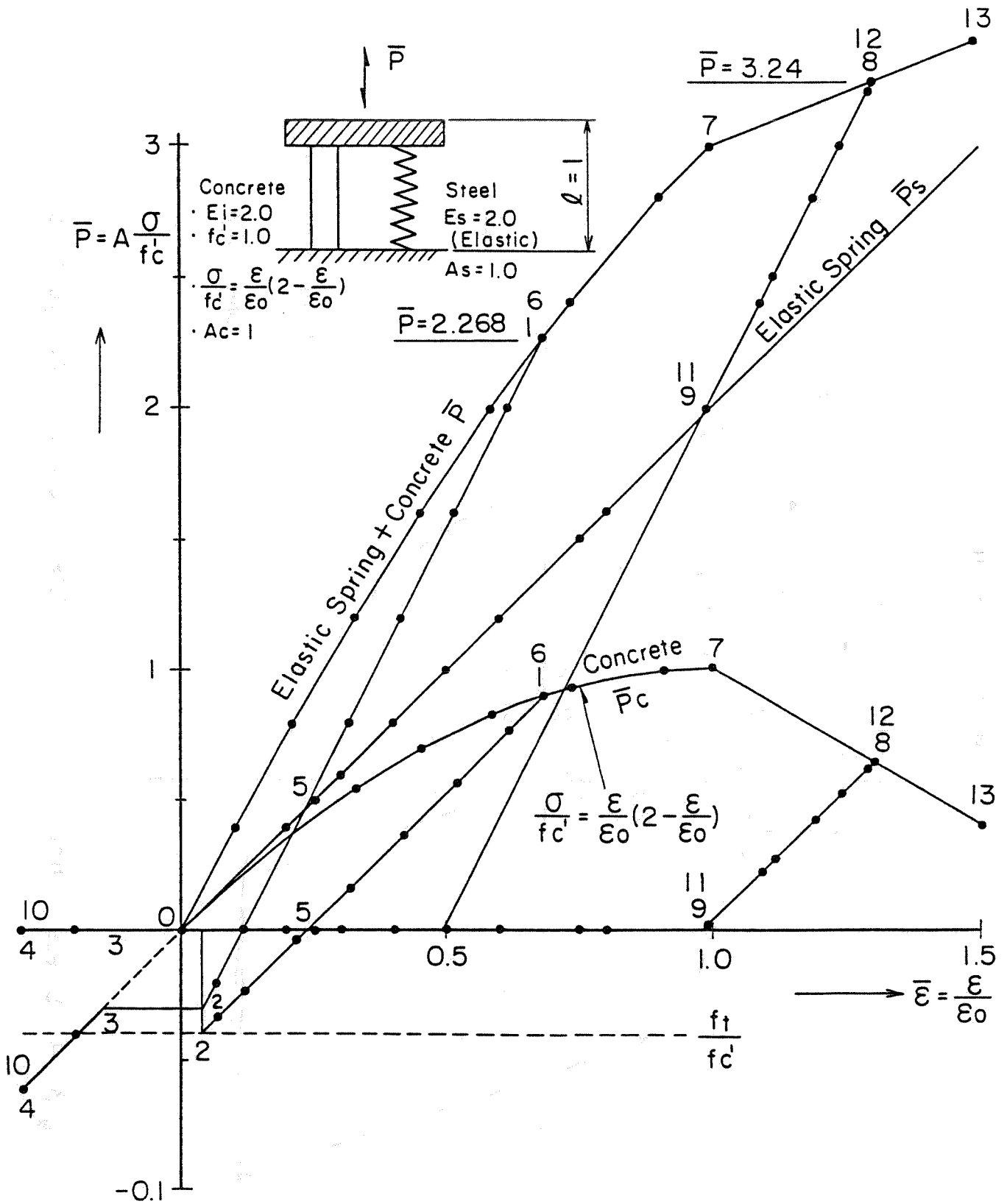
Fig.3-3   Stress-Strain Relationship of Concrete under
Uniaxial Cyclic Load
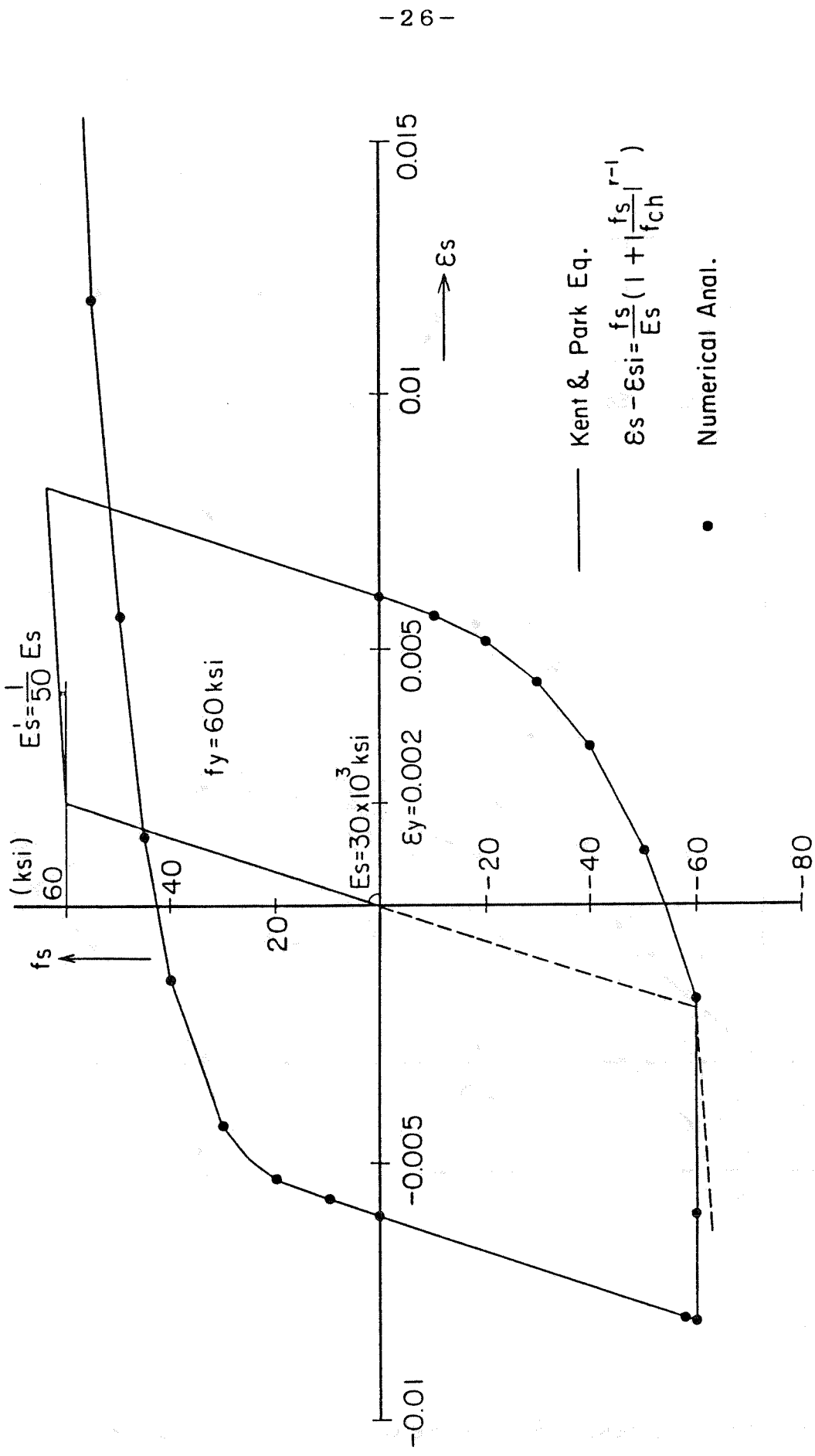
Fig. 3-4   Stress - Strain Relationship of Steel under Uniaxial Cyclic Load
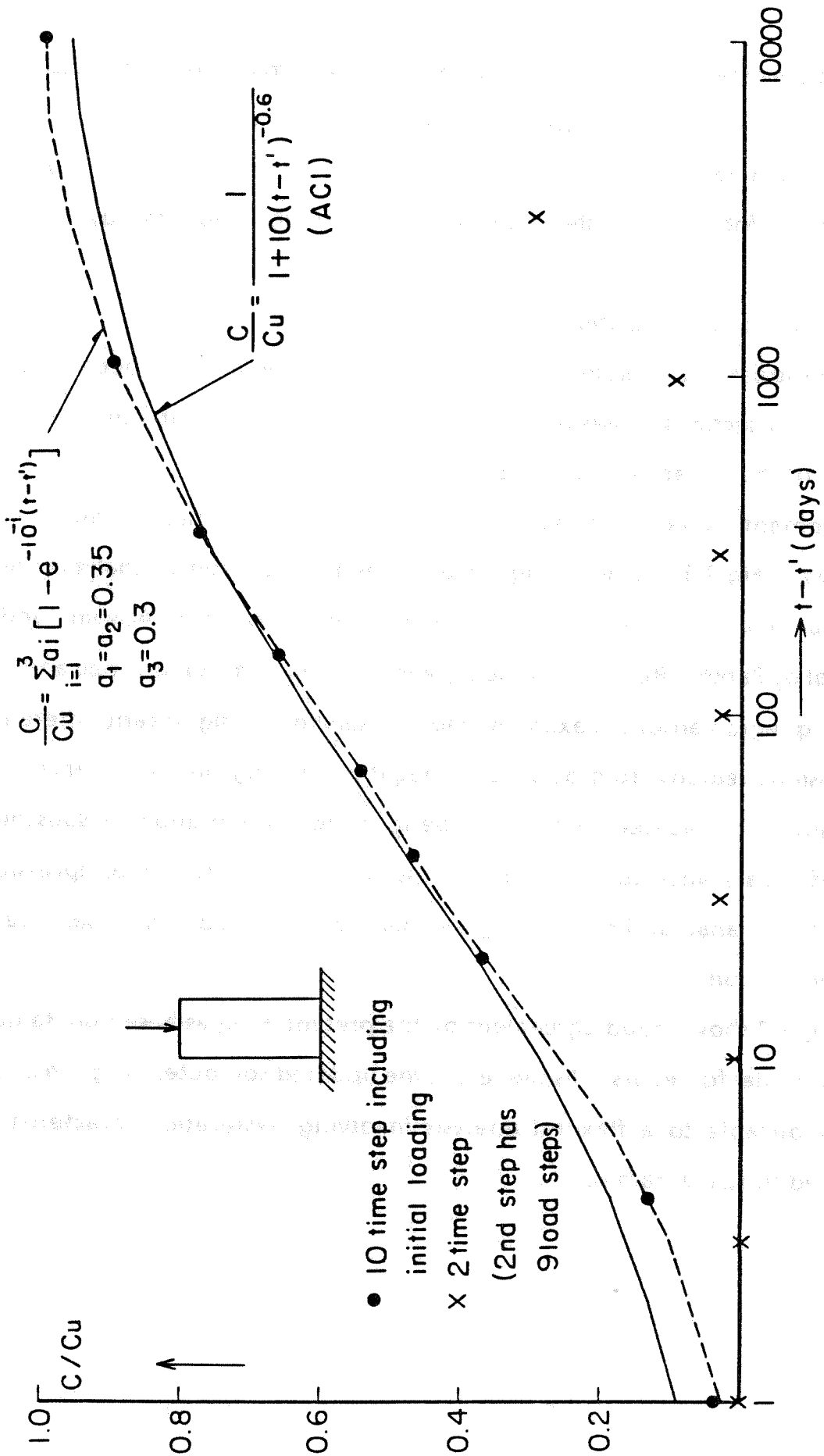
Fig. 3−5   Unit Creep Function of Concrete

sufficient time step discretization may be required to trace stress path dependent behavior since the present tower study has more complicated stress states under design load combinations. Based on these consideration, five time steps with two fractions for each time step will be employed in the present study.

## 3.2 Reinforced Concrete Member

The stress-strain relationships for individual materials have been studied in the previous sections, however more is needed to investigate the composite behavior of these materials together.

Moment-curvature relationships of a reinforced concrete member are presented in Fig.3-6 and 3-7. Fig.3-6 provides a comparison of analytical results using a bilinear rebar model with the experimental results by Aoyama and the analytical by Park[8]. Relatively good agreement around maximum load and in the unloading region around maximum load is observed, but significant difference in the transient regions from positive to negative loading and vice versa. This discrepancy is considered to be dependent on no consideration of Bauschinger effect of rebars since concrete fiber stress is not so serious in compression. Indeed, Park's analytical result using Ramberg-Osgood model for rebars presents good comparison.

Fig.3-7 shows good agreement by the present analysis based on Ramberg-Osgood model for rebars. As the result, the updated computer program is found to be applicable to a flexural analysis involving hysteretic characteristics of reinforced concrete frames.
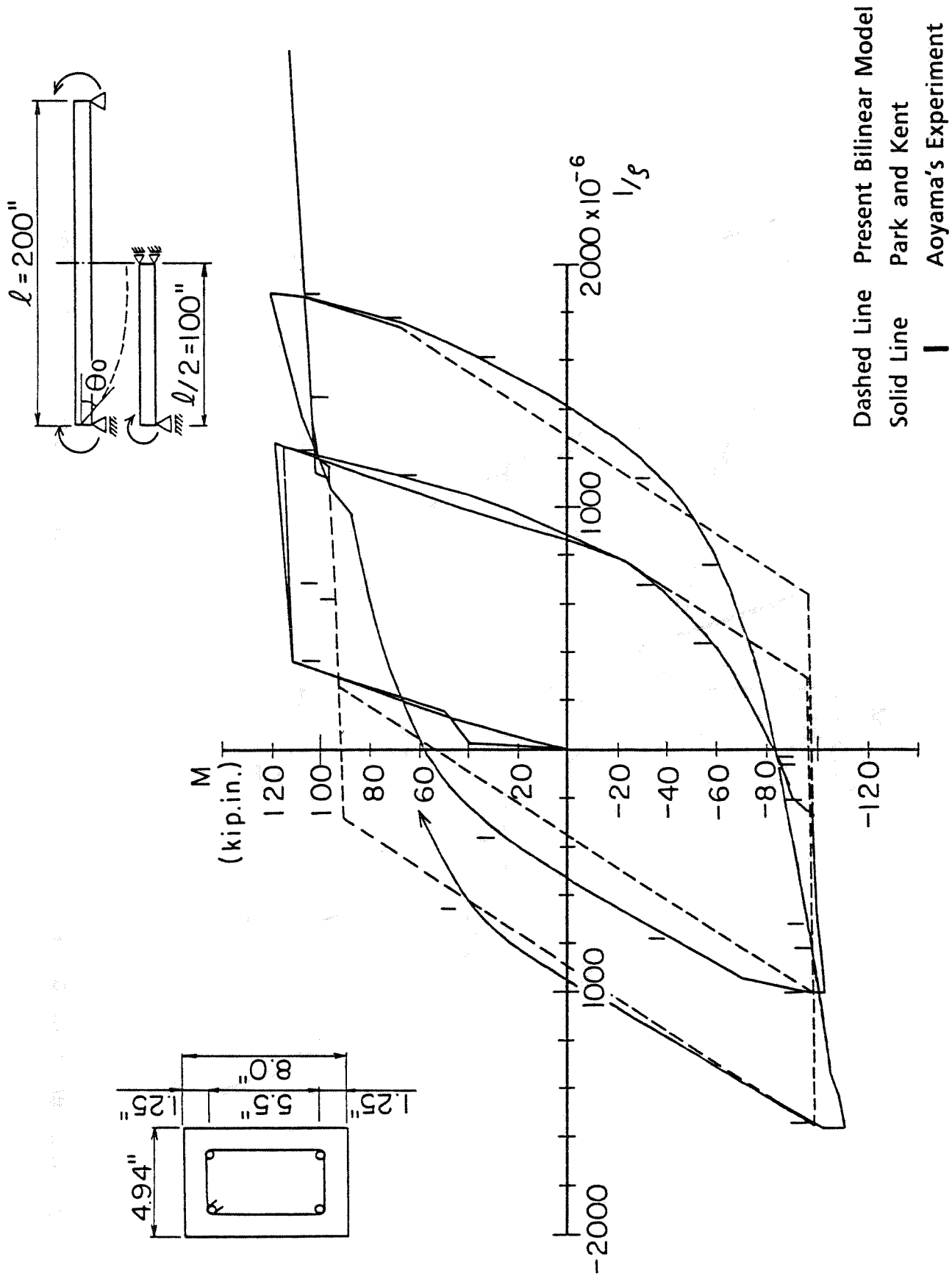
Fig.3-6 Moment-Curvature Curves of Beam 24(Bilinear Model for Rebars)
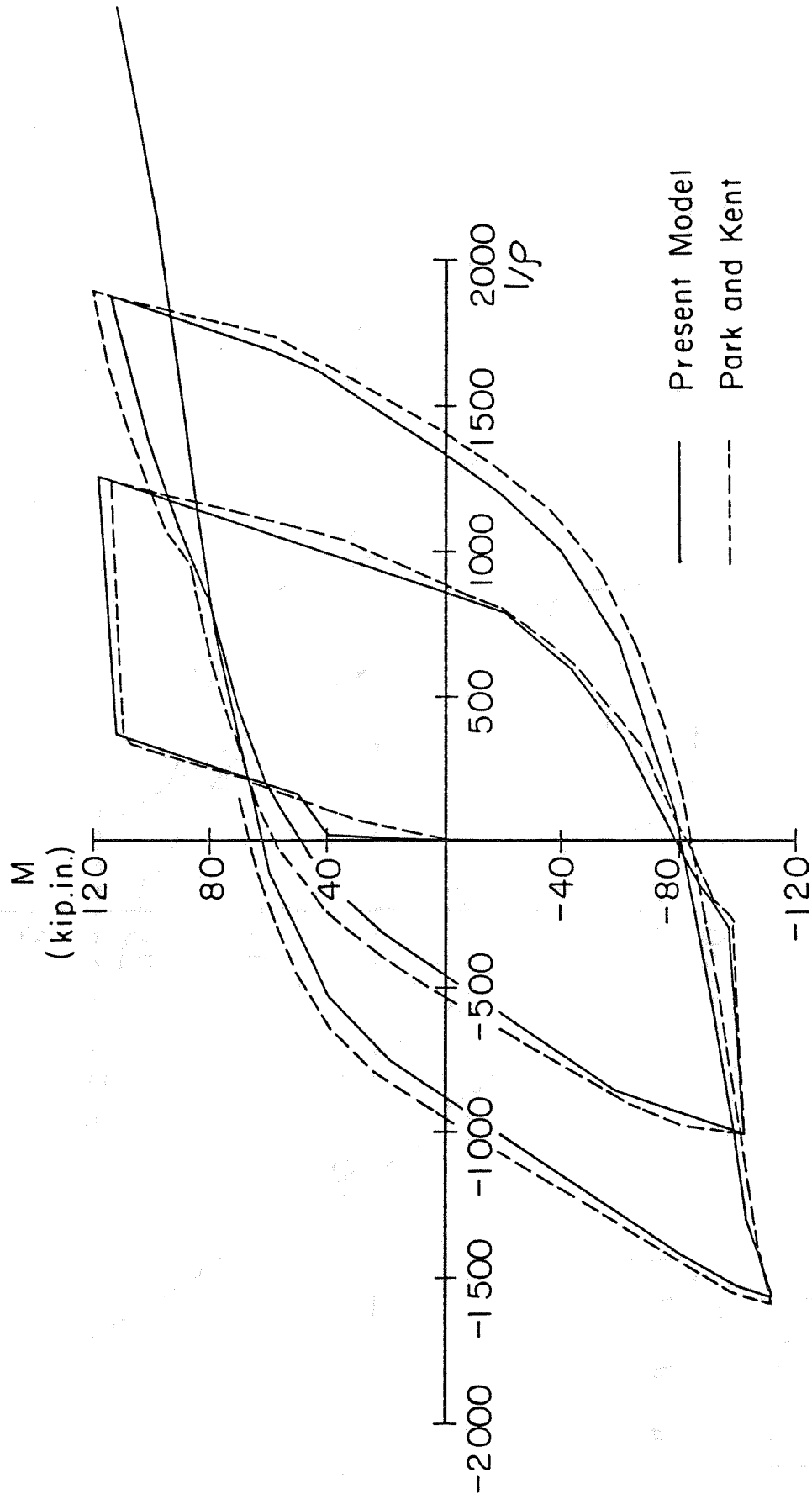
Fig. 3-7  Moment-curvature curves of beam 24 ( Ramberg-Osgood Model for Rebars)

## 4. Analytical Model

### 4.1 A-shaped Reinforced Concrete Bridge Towers

T. Y Lin[1] states that cable stayed concrete is more economical than cable stayed steel for less than 1200~2000ft span bridges and also that cable stayed bridges will take over from the cantilevered segmental bridges for span lengths exceeding some 500~700ft. He concluded that the cable stayed concrete bridge is most economical for 600~1500ft span brides. Leonhardt[2], on the other hand, has concluded that the cable stayed bridges are particulary suited for spans in excess 2000ft (600m) and may be constructed with the span of more than 5000ft(1500m). The longest span cable stayed bridge in the world is currently the new Annacis Bridge[12],[13] across the Frazer River, Canada which has a center span of 1526ft and a tower heigth of 502ft.

A free standing single column is mostly used as a cable stayed bridge tower. However, if considering lateral and torsional stiffness requirements, this single column type is less effective than the frame types shown in Fig.4-1. The East-Huntington[12],[14] and the Pasco-Kennwick Intercity Bridges[12],[15], which are both current representative concrete cable stayed bridges in the U.S., have a $\lambda$ shaped (Fig.4-1b) and a potral type tower (Fig.4-1c) respectively. And the new Annacis Bridge, the longest span cable stayed bridge as described before, has also a portal type tower (Fig.4-1d). A $\lambda$-shaped which has a relatively short vertical column on top, can be considered a kind of A-shaped type.

Of these types, an A-shaped reinforced concrete tower will be employed in the present study. In the Fig.4-2, the general shape of this tower and its finite element mesh utilized in the analyses are shown. A 400ft tower height is chosen, which would be used with a bridge span of 1300~1600ft. However, the results which will be discussed in the following chapter are all expressed in non-dimensional form and therefore can be applicable for other A-shaped reinforced concrete towers with different heights.
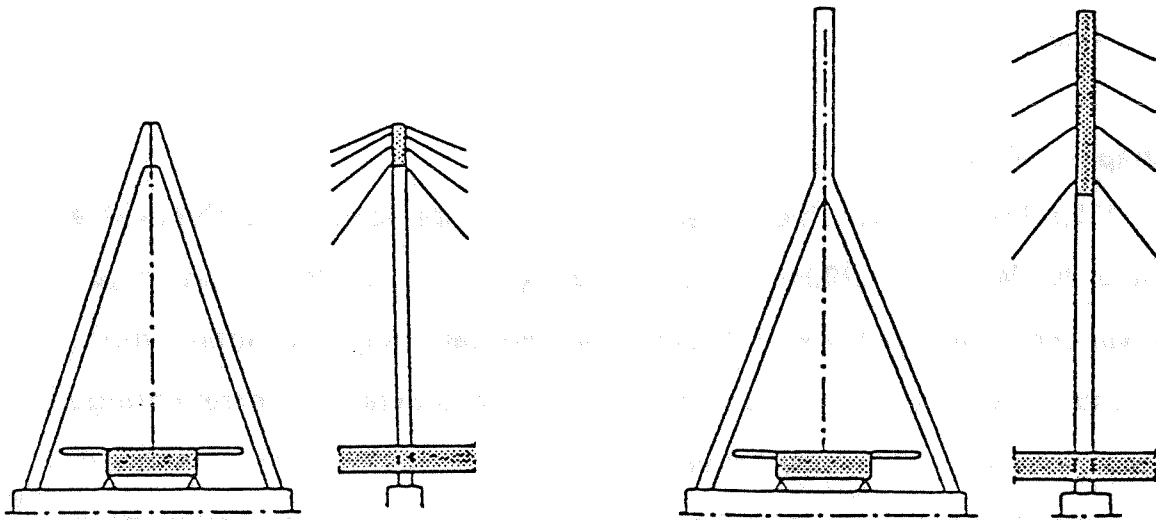
(a) A-shaped tower

(b) λ-shaped tower
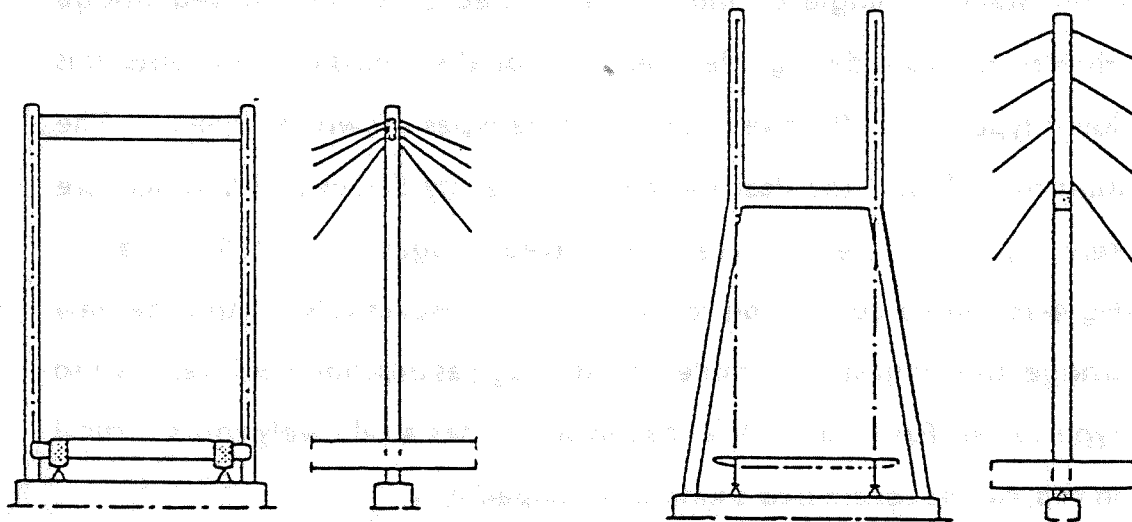
(c) Simple portal type tower

(d) Tower supporting two harp systems

Fig. 4-1 Frame Type Towers for Cable-Stayed Bridges

Front View

Section A-A

H = 400

$d_s = 0.4h$

$h/10$

$h$

$h/10$

$b = unit$

$0.05\ell$

$\ell$

$9 \times 0.1\ell$

$0.05\ell$

Y

X

$b = $ Unit Width

$10 \times h/10$

$0.4h$

$0.1h$

$A's = As$
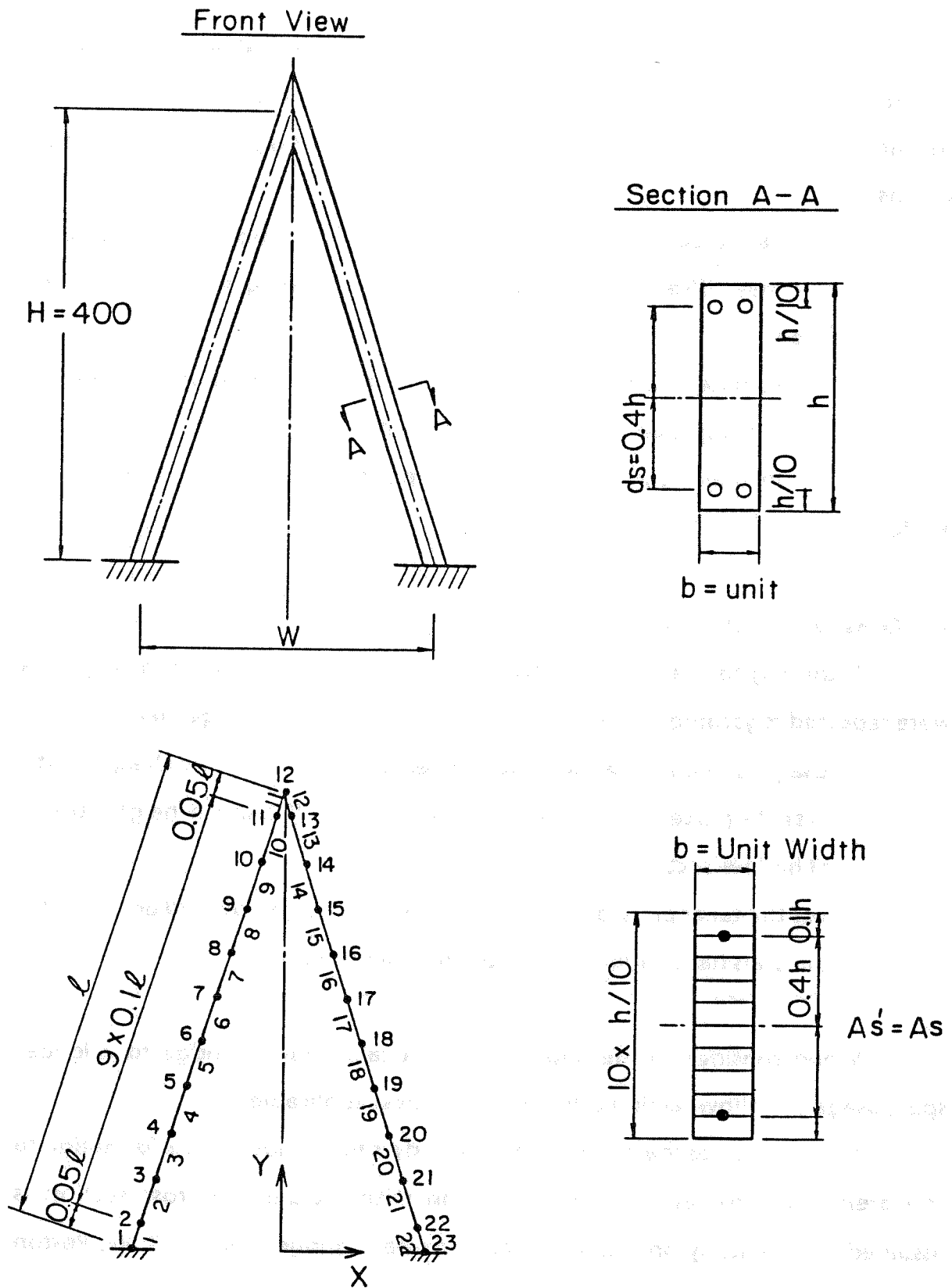
Fig. 4-2 Modelling of A Shape Tower into Finite
Elements and of Cross Sectio into Layers

Supporting condition at the tower base can be variable due to design condition. Generally speaking, however it can be recognized that it is advantageous to use fixed supports from the following design and construction aspects[16].

(1) The increased rigidity of the structure resulting from a fixed pylon base may offset the disadvantage of high bending moments in the pylon.

(2) A fixed base may be more practical from an erection point of view and be less costly than a heavy pinned bearing.

Based on these discussions, a fixed support is assumed in the present model.

## 4.2 Cross Section of a Column

According to the investigation by P. W. Poston alt.[17], the following facts were reported regarding a cross section for existing concrete bridge piers.

(1) Usage of hollow section piers increases dramatically with height and over 80 percent of the recent piers over 100ft (30.5m) in height are of hollow section.

(2) For the taller piers of over 100ft (30.5m) in height, over 70 percent of the piers have variable cross section dimensions

When considering the application of a cable stayed bridge to a longer span, usage of hollow section column may be most applicable.

However, since the objective of this study is to provide basic information to the preliminary design, a uniform column with rectangular cross section is assumed. The study on hollow section concrete bridge piers by R. W. Poston alt.[18], which indicates that a plane section assumption appears completely valid except for the case with a very thin wall, can be helpful. From their study, the result of the present study organized based on cross section characteristics such as

flexural stiffness EI and slenderness ratio l/r, would be applicable for columns with any type of cross section.

## 4.3 Analytical Parameters

There seems to be several factors which determine the structural behavior of present towers under the combination of seismic lateral and gravity loads :

(1) Configuration : W/H where W is the distance between bottom legs and H is the height of tower (Fig.4-2)

(2) Slenderness ratio : l/r (l/h), where l is the length of leg, h is the cross section height and r is the radius of gyration

(3) Reinforcement ratio : $p_g = (As + A's)/A_g$

(4) Gravity Load (Axial load) : $\sigma_0/f'c = N_0/A_g f'c$

(5) Concrete creep

(6) Cyclic lateral load

where (1) to (3) and (4) to (6) are factors corresponding to dimension and load type respectively.

In addition to these, eccentricity and dynamic loading effect are possible principal parameters which will be neglected in the present study. The reasons for this neglection are as follows. A gravity load is basically applied symmetrically and even if being considered, the eccentricity is generally quite small compared with the displacement due to lateral load. And as the main objective of cyclic lateral load analysis in this study is to focus on the hysteretic behavior under static load, the dynamic load effect is removed.

It should be noted that the shrinkage, thermal strain and aging dependent concrete properties are not considered for simplicity

## (1) Configuration Factor

This factor varies dependent on the design condition. It is considered that if W/H becomes larger, frame action contributes more against lateral load and

that the internal axial force and the flexural moment may be different among these factors. The structural resistance as an entire structure and the secondary moment could be different as a result.

Three cases of W/H = 0.2, 0.4 and 0.6, considered to be in the practical range, will be employed in the present study.

## (2) Slenderness Ratio

The slenderness ratio is one of the most important factors which affect the structural behavior of a slender column such as the present bridge tower. Geometric nonlinear effects appear more with increase of this factor. The practical range of this factor $l/r$ is considered to be from 40 to 80. Indeed, the practical examples of existing towers show 44~69 for Pasco Kennewick[15] ,74 for Hast Huntington[14] and 71 for James River bridges[12]. The use of a small column section, i, e. large slenderness ratio should be economical, but critical in a brittle failure such as buckling. It is of importance to investigate the limitation of a slendeness ratio in use for the future design of such a slender structure. On the basis of these discussions, six cases are chosen as parameters including a short column case without considering geometric nonlinearity and a very long column case up to over 200.

## (3) Reinforcement Ratio

In the current ACI code[4], area of longitudinal reinforcement for compression members are required to be not less than 0.01 nor more than 0.08 times gross area of cross section.

As a practical example, Pasco Kennewick bridge[15] has about a 1.5% reinforcement ratio ( $P_g = (A_s + A'_s) /A_g$ ). And the experimental test specimens by Iemura alt.[19], which have been conducted for the study of seismic safety of a cable stayed bridge tower, have 1.27 and 2.25% reinforcement ratios.

Reinforcement ratios of $P_g = 1.5$ and 3.0%, which are employed in the present study are considered to be in the practical range in reference to above values of cable stayed bridge towers in the moderate or high seismic zones.

## (4) Gravity Load (Axial Load)

It is recommended in the ACI code[4] that design axial load $\phi Pn$ of compression members shall not be taken greater than the following value.

For nonprestressed members with spiral reinforcement,

$$\phi\, p_n = 0.85[0.85f'_c\, (A_g\text{-}A_{st}) + f_yA_{st}] \qquad\cdots\cdots\cdots\cdots(4.1)$$

Now, assuming $\phi = 1.0$ and $f_y/f'_c = 10$ and dividing both side of Eq. (4.1) by $A_gf'_c$.

$$\frac{P_n}{A_gf'_c} = 0.85[0.85(1\text{-}p_{st}) + 10p_{st}] = 0.85[0.85 + 9.15p_{st}] \qquad\cdots\cdots\cdots\cdots(4.2)$$

where $A_g$ is a gross area of section and $p_{st}$ is total area of longitudinal reinforcement divided by $A_g$.

If considering reinforcement ratios, $p_g = 1.5$ and 3.0% provided in the previous section, the right side of Eq. (4.2) $P_n/A_gf'_c$ is given as 0.84 and 0.96. High axial load may cause a brittle failure of structure under seismic load and may lead to poor ductility design. On the other hand, the usage of high axial design load is cost effective .

Based on the above discussion, a relatively wide range of gravity loads $\sigma_0/f'_c = 0.1, 0.2, 0.4$ and 0.6 are employed as the present parameters. This would cover a sufficient range to provide effective information for ductility and cost effective design.

## (5) Concrete Creep

Concrete creep may bring significant influence on geometric nonlinear behavior of structures. Time dependent-deformation-increase enlarges the secondary moment. With an increase in axial load and in slenderness ratio, the above influence becomes large. In the present study, the creep deformation is assumed to take place under gravity load, but not under lateral load since the duration time of lateral load is far less than that of gravity load. In order to

evaluate the influence of creep deformation on the secondary moment behavior and the ultimate capacity, both cases with and without considering creep effect will be analyzed.

The following creep function is employed assuming no temperature dependence.

$$C(t', t-t',T) = \Sigma a_i(t') [1- e^{-10^{-i}(t-t')}] \qquad \cdots\cdots\cdots\cdots(4.3)$$

Coefficients $a_i(t')$ are given corresponding to the ACI Committee 209 recommendation[11],

$$a_i(t') = a_i(t_0') (t'/t_0')^{-0.118} ; \quad t_0' = 28 \text{days} \qquad \cdots\cdots\cdots\cdots(4.4)$$

In the present study, however constant coefficients are assumed as follows

$$a_1(t') = a_2(t') = 0.35C_u(t_0'), \quad a_3(t') = 0.3C_u(t_0')$$

$$( \because \sum_{i=1}^{3} a_i(t') = C_u(t_0')) \qquad \cdots\cdots\cdots\cdots(4.5)$$

Assuming the follows about the ultimate creep such as

$$C_u(t_0')E_i = 2.0 \qquad \cdots\cdots\cdots\cdots(4.6)$$

Substituting Eq.(4.6) into eq. (4.5),

$$a_1(t') = a_2(t') = 0.35\frac{2}{E_i} , \qquad a_3(t') = 0.3\frac{2}{E_i} \qquad \cdots\cdots\cdots\cdots(4.7)$$

## (6) Cyclic Lateral Load

It must be of great significance to predict a hysteretic behavior under cyclic lateral loads for a seismic design performance. A number of studies have been so far conducted by many researchers on this hysteretic behavior of short columns under seismic lateral loads. Meanwhile, there have been very few studies on this behavior of a slender column. In the case of a cable stayed bridge

tower with relatively large slenderness ratio, geometric nonlinerarity can be considered to affect its behavior.

As a simple example, the following discussion will be given about the single column behavior under a cyclic lateral load combined with a constant axial load. A moment displacement relationship between base moment and lateral displacement of top is illustrated as the dotted line in Fig.4-3a. Considering the linear relationship between secondary moment $M_B''$ and displacement $\delta$ due to a constant axial load, the primary moment by lateral load and displacement relationship, $M_B'$-$\delta$ is shown as the solid line. In Fig.4-3b and 4-3c, similar relationships for the tri-linear model under a constant axial load and a bi-linear model under a varying axial load are shown as well. It is obvious that the hysteretic characteristics of columns subjected to cyclic lateral loads may be different dependent on geometric nonlinearity.

The following is a discussion about absorbed energy using the bi-linear type of Fig.4-3a, where absorbed energy is defined as the area enclosed by load-displacement skelton curve. Fig.4-4 shows the relationship between the equivalent lateral load H and the top displacement $\delta$, where H is given as a total base moment $M_B$ divided by l.

The area surrounded by points A, B, C and D in the figure is given

$$A = \frac{\delta_B - \delta_A}{\cos\theta} \times 2H\cos\theta = 2H_y \cdot (\delta_B - \delta_A) \qquad \cdots\cdots\cdots\cdots(4.8)$$

where, $H_y$ is independent on axial force since it is defined as an equivalent lateral load due to zero displacement.

Based on the above description, it can be said that the shape of hysteretic curve is dependent on the axial load, but the absorbed energy is not.

In the present study, both monotonic and cyclic lateral load analyses are needed to be carried out in order to evaluate the cyclic load effect on hystertic behavior and ultimate capacity.

$M_B = H\ell + P\delta$

$= M_B' + M_B''$

$\therefore M_B' = M_B - M_B''$
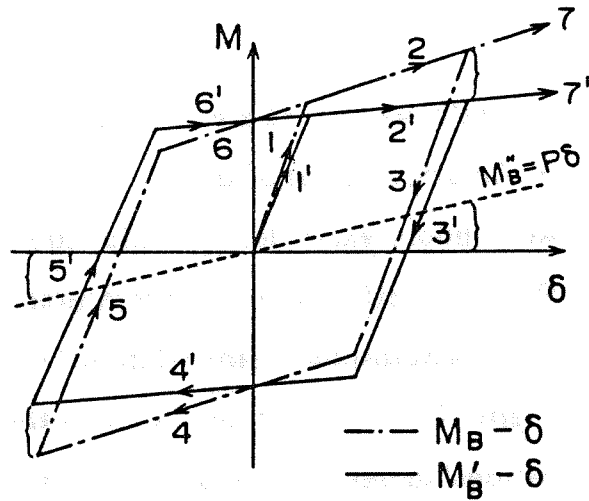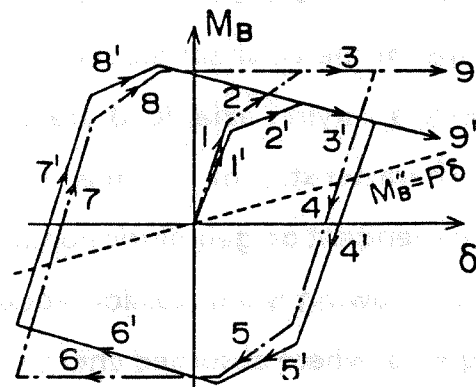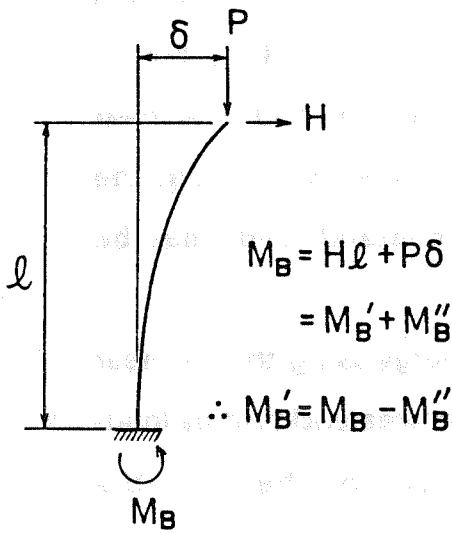
(a) Bi-linear Type

(b) Tri-linear Type
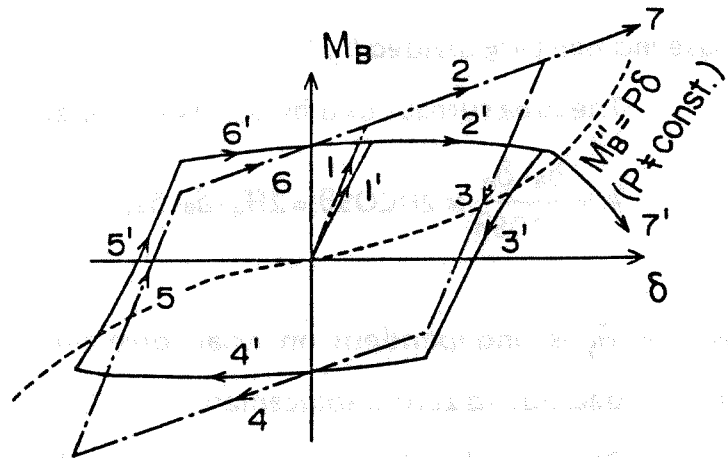
(c) Bi-linear Type with Varying Axial Load

Fig. 4-3  Moment-Displacement Relationship of Single  Column under Combination of Lateral and Axial Loads
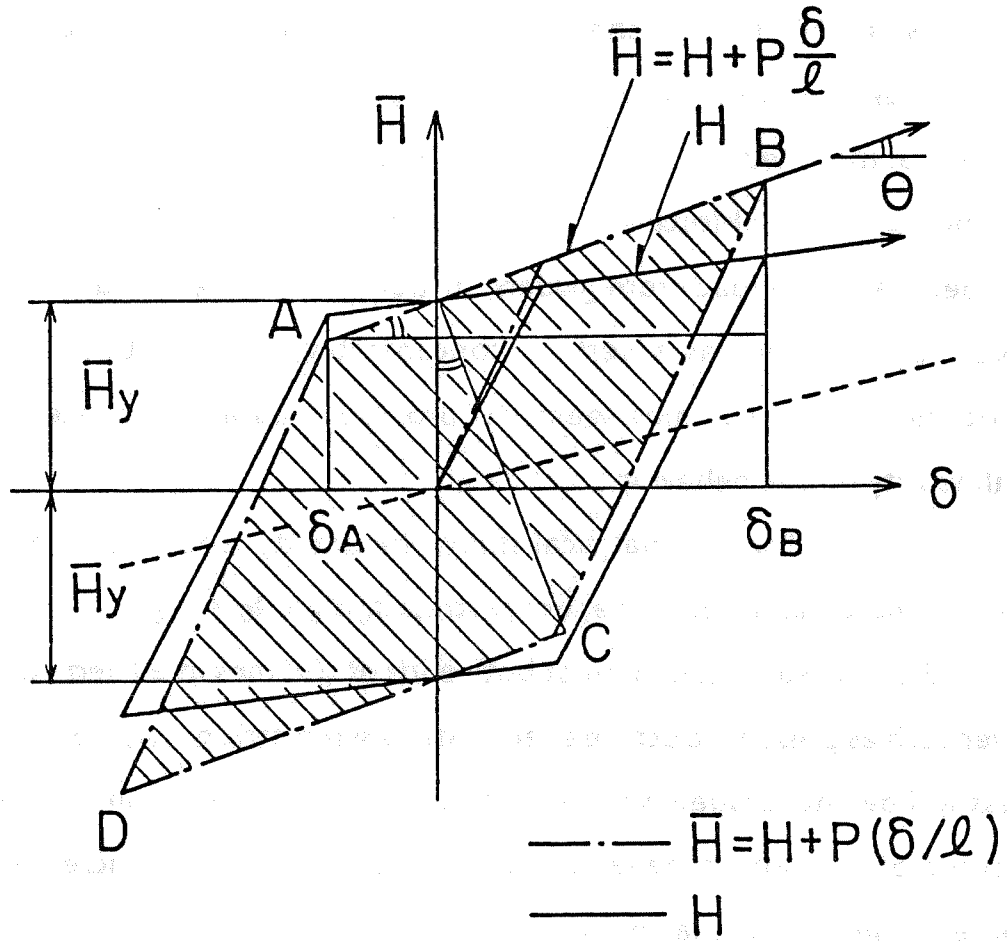
Fig. 4-4   Eguivalent Horizontal Load
$\overline{H} - \delta$ Relationship

## 4.4 Applied Gravity Load

A bridge tower has as a major function to support live and dead load from girders through supporting cables. Support distribution is different due to cable stayed system (Fig.4-5). In the fan system, cables are supported at the tower top and as a result uniform axial force acts along columns. On the other hand, in the harp or modified fan system, cable supports are distributed along the columns and the column axial force varies as a result. In the present study, it is assumed that dead and live load from girders including tower dead load itself act on the tower top together as a vertical concentrated load. Uniform axial force distribution along columns seems to provide greater influence of geometric nonlinearity on the behavior.

In the following analytical study, the gravity load effect described above will be handled as a constant average stress $\sigma_0/f'_c = N_0/A_g f'_c$.

Flexural stress can occur at both ends of columns in a fixed base frame type tower such as present structure even under a symmetric gravity load. This flexural stress will be encouraged when deformation increases with time. So-called creep buckling of a column is the failure which is caused by further increase of secondary moment due to this time dependent deformation. This type of failure may occur when slenderness ratio or axial load becomes large.

In the present study, two types of load combination as shown in Fig.4-6 will be considered to evaluate time dependent effect of a gravity load.

- Type (a) : Time dependent gravity load + Lateral load

    Gravity load itself does not vary but does internal force due to concrete creep. This case corresponds to realistic load combination of seismic lateral load and stational gravity load.

- Type (b) : Constant gravity load + Lateral load

    This case is the neglection of time dependent effect of gravity load and is necessary to evaluate its effect.
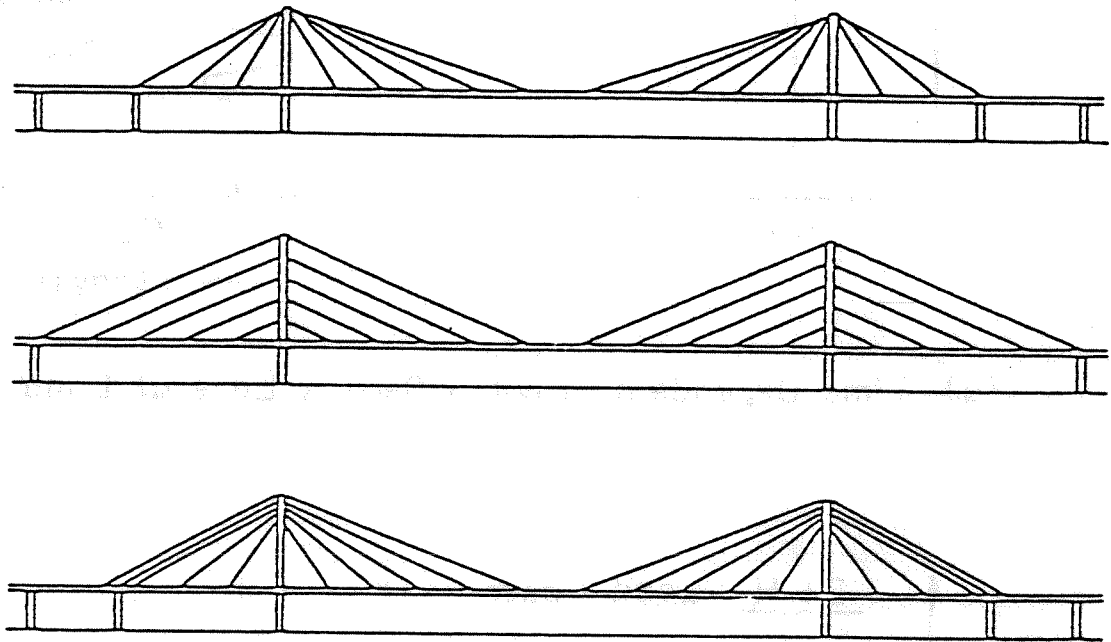
F i g. 4-5 Cable stayed bridge systems; top, pure fan system;
centre, harp system; bottom, modified fan system
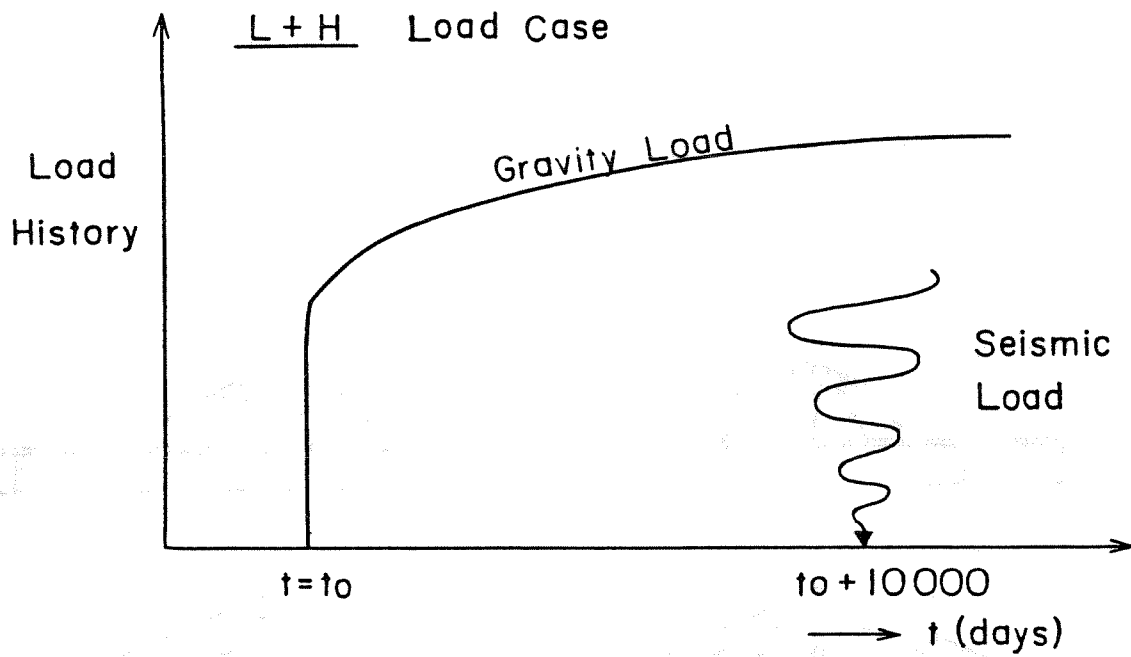
(a) Time Dependent Gravity + Seismic Lateral Load
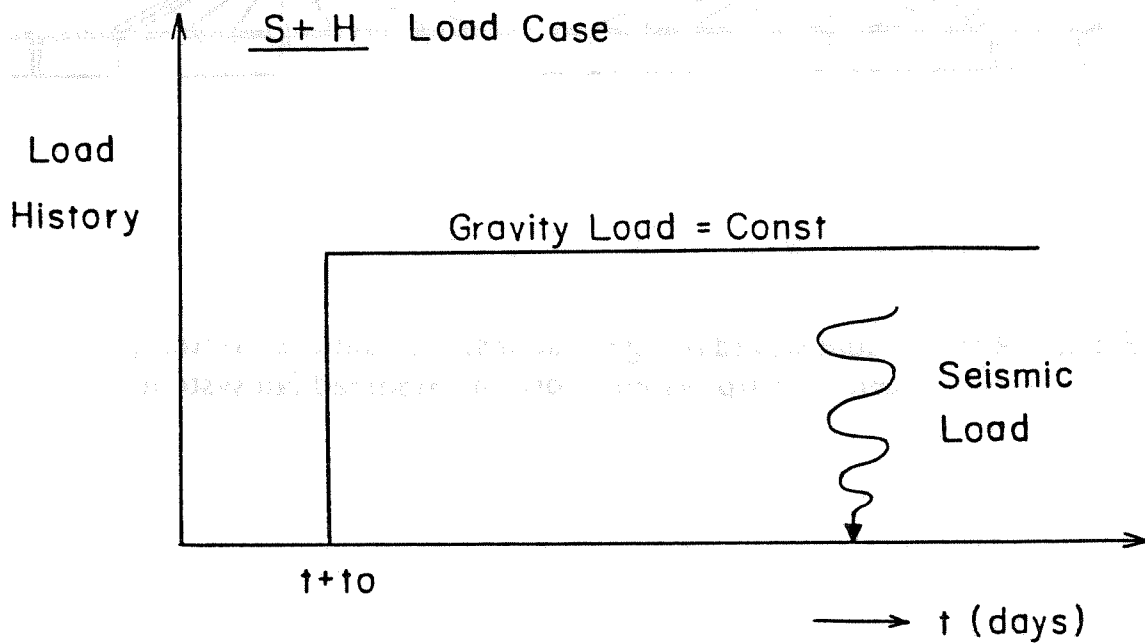


(b) Constant Gravity + Seismic Lateral Load

Fig 4-6 Load Combination Models

## 4.5 Applied Lateral Load

The structural behavior of a tower under seismic lateral loads perpendicular to longitudinal axis is focused neglecting interaction with supporting cables.

It is difficult to define this lateral load distribution since it varies due to tower shapes and flexural stiffnesses. Indeed, for instance it may be different in the nonlinear range.

In the present study, this lateral load distribution is respectively determined based on an elastic modal analysis for a tower with each configuration and slenderness ratio. Some results are shown in Fig.4-7. Smaller slenderness ratio cases ($l/r = 35$) show like triangular-shape distribution for smaller W/H as the result of dominant overturning moment behavior, and like bulging shape for larger W/H due to more local flexural deformation being involved. In the very slender case with $1/r = 208$, this local flexural deformation appears more and a paraboloidal distribution is obtained as the result.

By assuming that this elastic lateral load distribution is constant even in the nonlinear range, an incremental load will be proportionally applied .

The present study concerns the hysteretic behavior under static cyclic lateral load, not that under dynamic lateral load.

Two cases, i.e. monotonic and cyclic load analyses are to be carried out. The former case is not only for investigating the essential behavior of the present tower under combination of gravity and lateral load but for estimating the cyclic load effect.

## 4.6 Material Constants

Material constants utilized in the analysis are as follows

(1) Concrete

$$f_c'' = f_c' = 6000\text{psi}$$
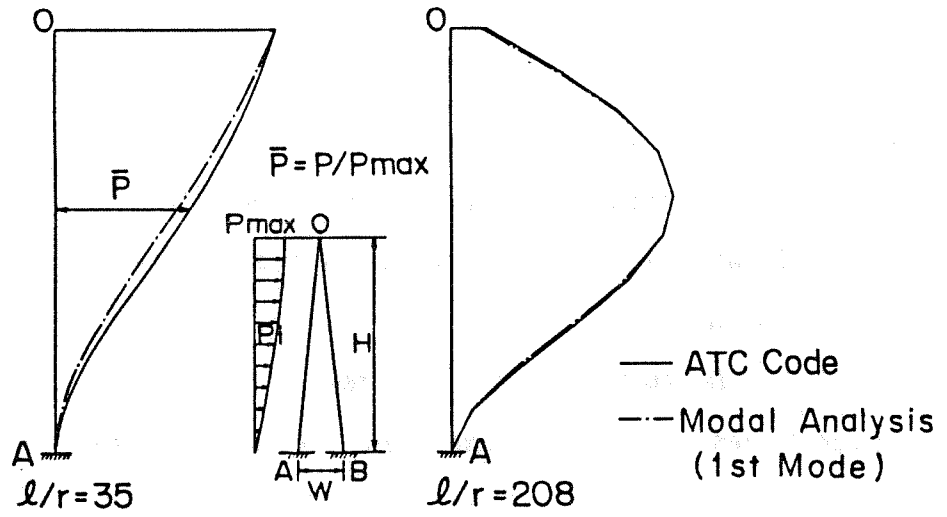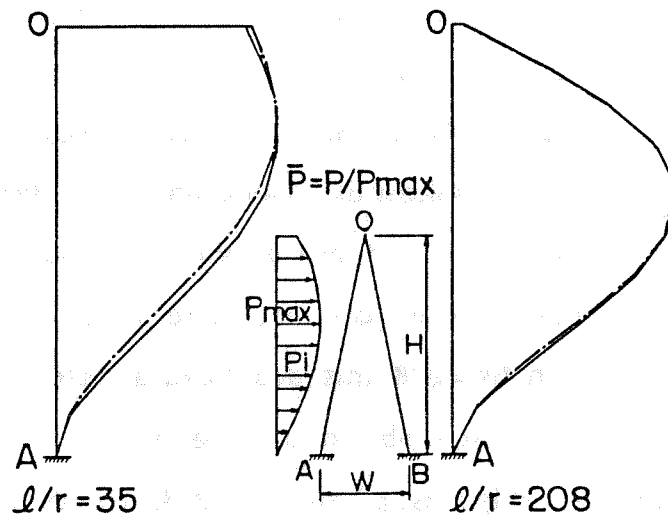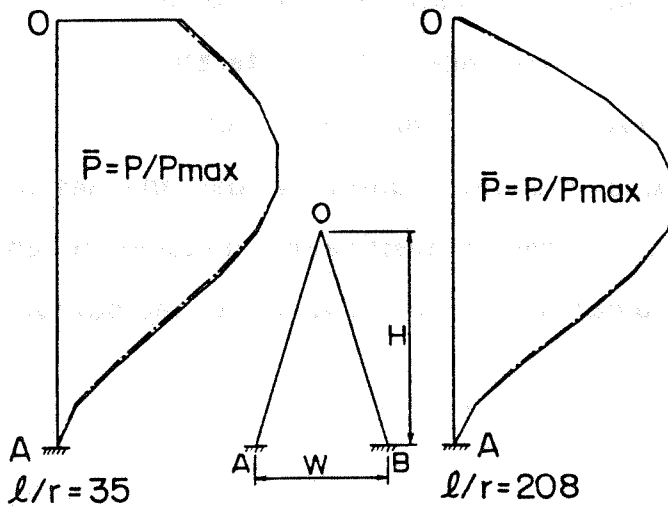
Fig. 4-7  Seismic Lateral Load Distribution of A-Shaped Tower
(W/H = 0.2, 0.4, 0.6, $\ell/r$ = 35, 208)

$E_i = 33W^{1.5}\sqrt{f'c} = 4.42 \times 10^6$ psi

   (W = 144 lb/ft$^3$ based on $E_i = 57000\sqrt{f''_c}$ psi)

$\varepsilon_u = 0.0038$

$f'_t = \gamma_t \sqrt{Wf'_c} = 581$ psi

   ($\gamma_t = 0.625$ based on $f'_t = 7.5\sqrt{f'_c}$

**Creep Constants :**

$a_1(t') = a_2(t') = 0.1586 \times 10^{-6}$

$a_3(t') = 0.1359 \times 10^{-6}$


All the materials of concrete are assumed as constant and independent of time. And no shrinkage is assumed.


(2) Reinforcement Bar

| | | |
|---|---|---|
| $f_y =$ 60 ksi | (Grade 60 steel bar) |
| $E_s = 29000$ ksi | $\therefore \varepsilon_{sy} = 0.00207$ |
| $E'_s =$ 290 ksi | (Monotonic loading) |
| $= 0$ | (Cyclic loading) |

## 5. Nonlinear Behavior against Monotonic Lateral Load Combined with Short Term Gravity Load

### 5.1 Analytical Parameters

Analyses are carried out considering all the parameters described in the previous section since they are essentially geometric nonlinearity related factors when the present model is subjected to gravity load combined with lateral load.

Adopted parameters are as follows :

1) Configuration factor ; $W/H = 0.2, 0.4$ and $0.6$ (3 cases)

2) Slenderness ratio ; $l/r = 35, 69, 104, 156$ and $208$ (5 cases)

3) Gravity load ; $\sigma_0 / f'_c = \dfrac{N_0}{f'_c A_g} = 0.2, 0.4$ and $0.6$ (3 cases)

   where $\sigma_0$ is an average axial stress of columns under gravity load given by a concentrated load at top and is defined by axial force $N_0$ divided by a concrete nominal strength $f'_c$ and by the area of column cross section $A_g$.

4) Reinforcement Ratio ; $p_g = 1.5$ and $3.0\%$ (2 cases)

5) Geometric nonlinearity ; for its estimation on ultimate strength, analyses without considering geometric nonlinearity are additionally conducted for the only $p_g = 3\%$ series.

Therefore, in this chapter, analytical results based on a total of 120 cases ($3 \times 5 \times 3 \times 2$) due to from 1) to 4) will be basically discussed including short column analyses due to 5).

### 5.2 Influence of Geometric Nonlinearity on Ultimate Strength

Both analyses with and without considering geometric nonlinearity are

carried out for $p_g = 3\%$ series to evaluate its effect on ultimate strength.

Non-dimensional ultimate load $(Q_u/Q_u^\circ)$ - slenderness ratio (l/r) relations are shown in Fig.5-1 for the cases of $\sigma_0/f'_c = 0.2$, 0.4 and 0.6, where $Q_u$ is an ultimate load based on the analysis with considering geometric nonlinearity and $Q_u^\circ$ without that. This value varies from 0.99 to 0.25 for $\sigma_0/f'_c = 0.2$, from 0.99 to 0.03 for $\sigma_0/f'_c = 0.4$ and from 0.98 to 0.12 for $\sigma_0/f'_c = 0.6$. As a slenderness ratio increases, the value decreases dependent on the geometric nonlinearity effect. Such a tendency will be dominant with increases of gravity load. Less reduction is observed for smaller configuration factor of W/H, but not significant differences are observed among these values.

In the case of $\sigma_0/f'_c = 0.6$ and $l/r = 208$, a larger value is obtained than expected since the negative overturning moment by a concentrated gravity load on top is encouraged so as to cancel the lateral load moment. This phenomenon will be further discussed later. In general, the influence of geometric nonlinearity appears in the range of l/r larger than 69.

## 5.3 Ultimate Strength

Normalized ultimate strength-slenderness ratio relationships are shown in Fig.5-2 for $\sigma_0/f'_c = 0.1$ and in Fig.5-3 for $\sigma_0/f'_c = 0.6$, where the vertical axis is defined as an maximum average shear stress at base section divided by a conventional uni-axial compressive strength of concrete as follows.

$Q_u$ : Ultimate total lateral load given at base

$\tau_u$ : Maximum shear stress at the base section

$\tau_u = Q_u \cos\theta /2bh$    b : section width    h : section height

$f'_c$ : conventional uniaxial compressive strength of concrete

$\tau_u /f'_c$ : normalized ultimate strength

$$\tau_u /f'_c = \frac{Q_u \cos\theta}{2bhf'_c} \qquad \cdots\cdots\cdots\cdots (5.1)$$

(a) $\dfrac{\sigma_o}{f_c'} = 0.2$

$\begin{cases} \square & \dfrac{W}{H} = 0.2 \\[2mm] + & = \dfrac{W}{H} = 0.4 \\[2mm] \diamond & \dfrac{W}{H} = 0.6 \end{cases}$
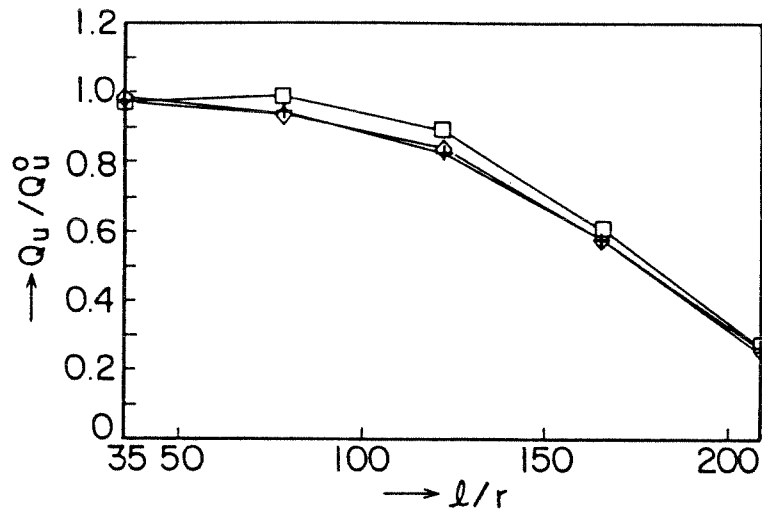
(b) $\dfrac{\sigma_o}{f_c'} = 0.4$
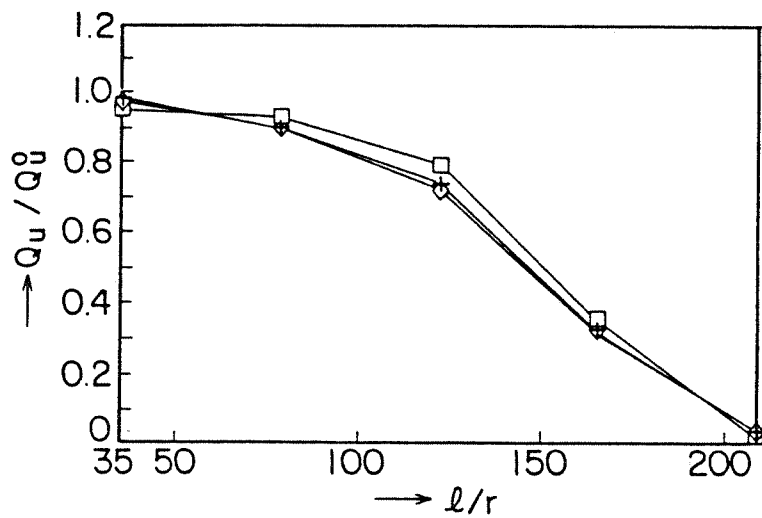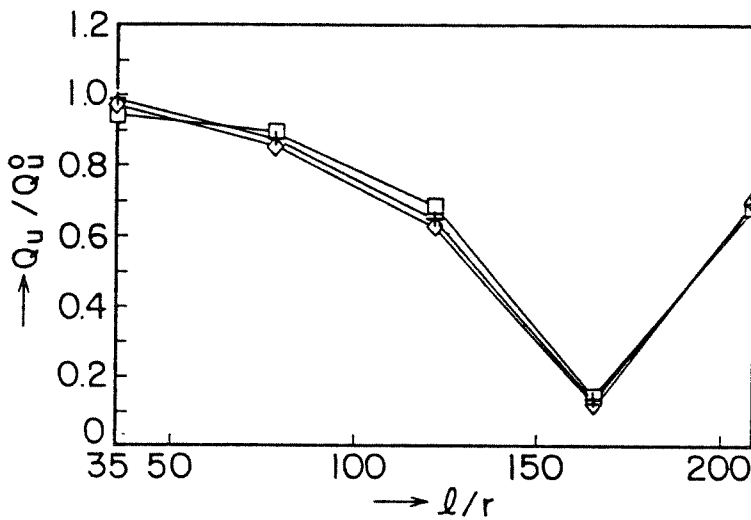
(c) $\dfrac{\sigma_o}{f_c'} = 0.6$

Fig.5-1   Ultimate Load Affected by Geometric Nonlinearity
(Pg = 3%)
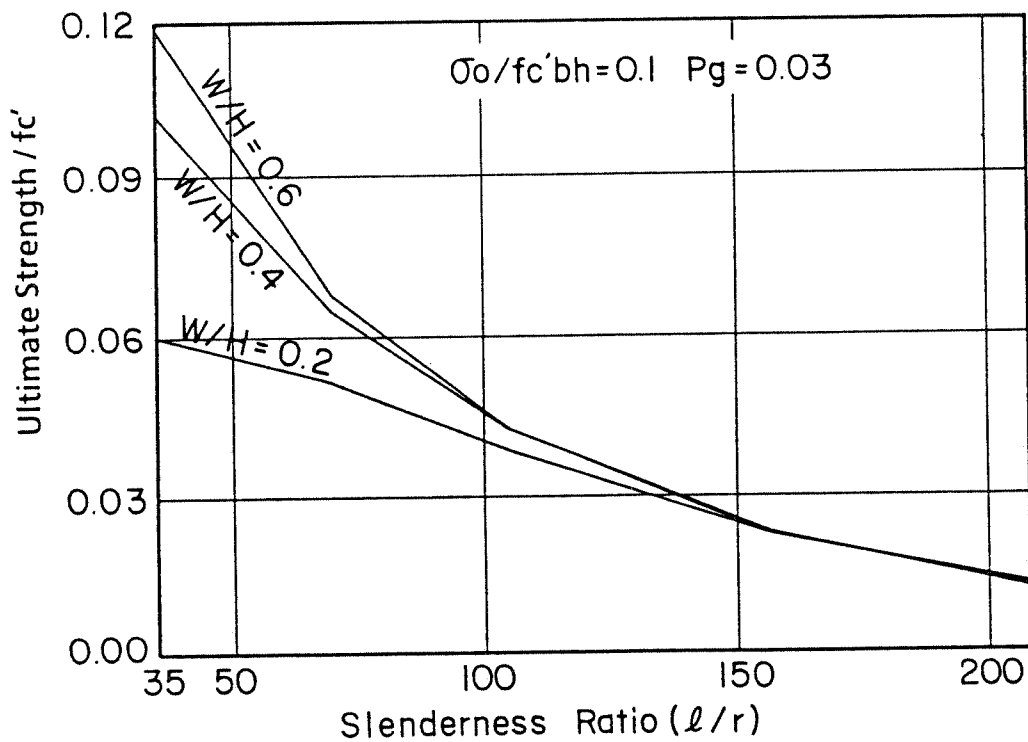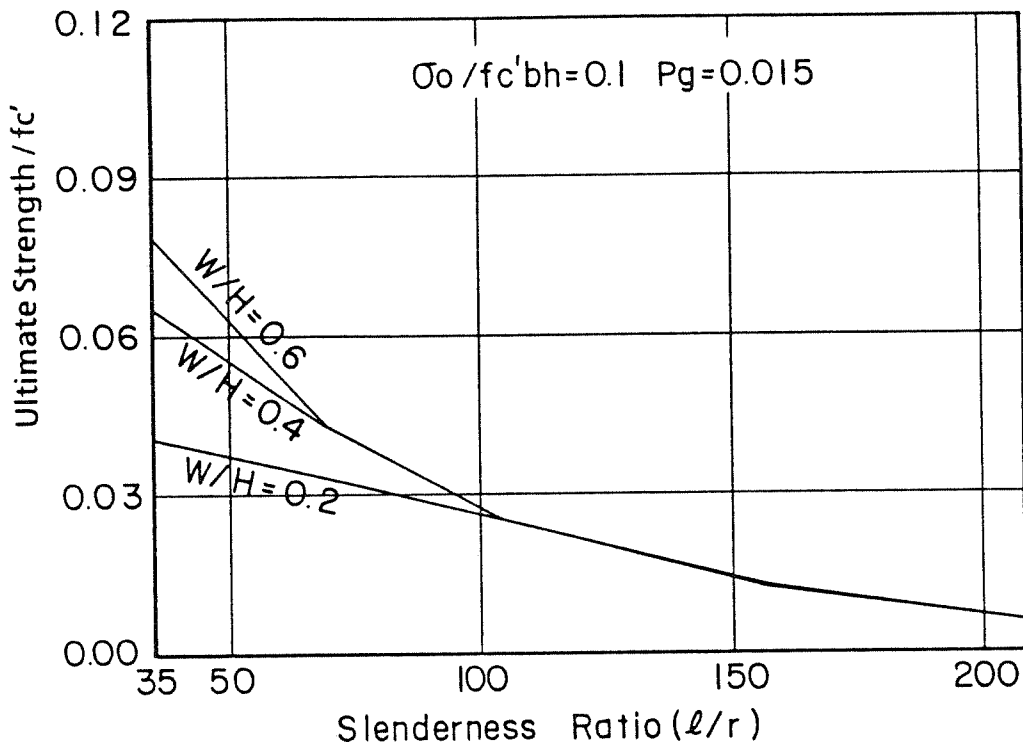
Fig. 5-2   Ultimate Strength − Slenderness Ratio Relationship
($\sigma$o /fc′ = 0.1 )
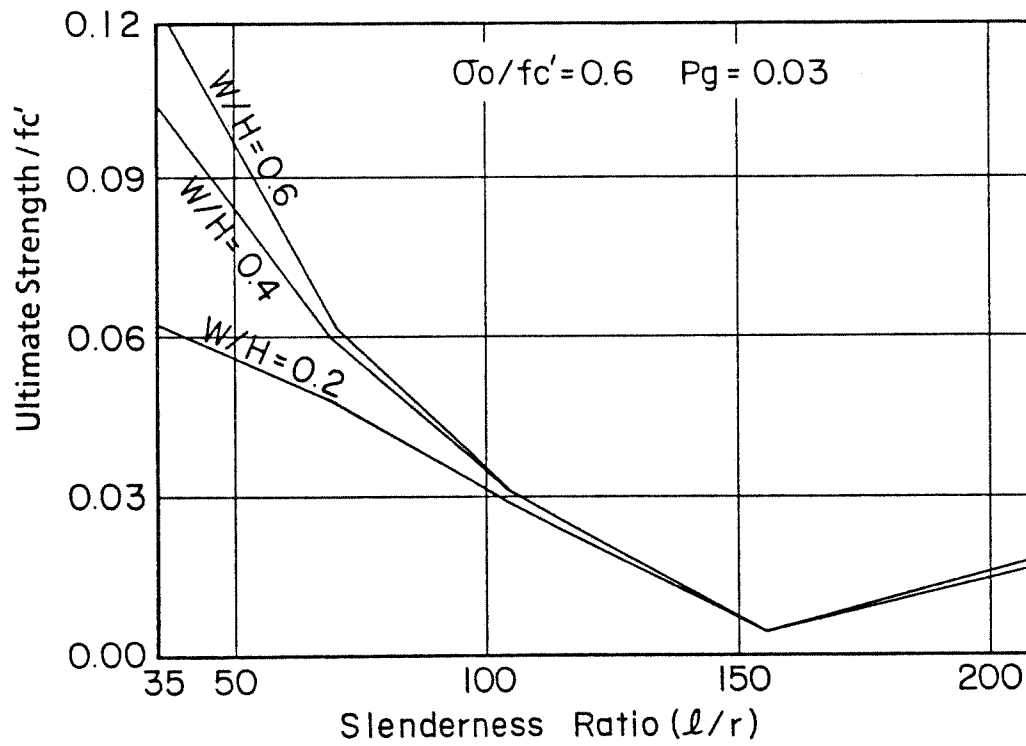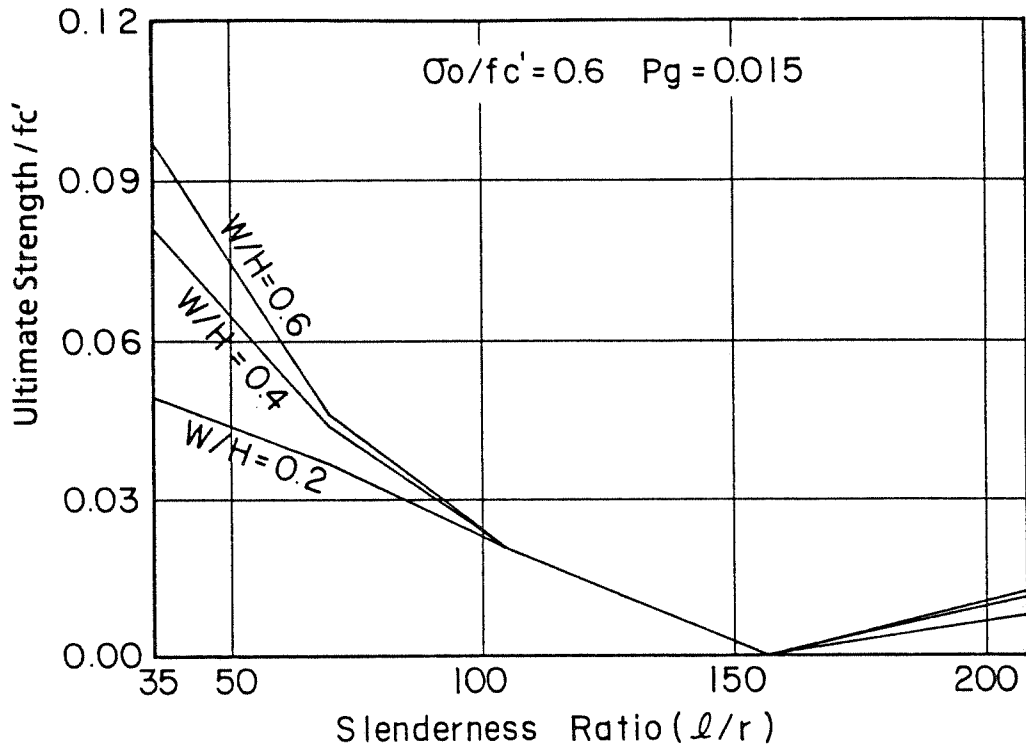
Fig.5−3 Ultimate Strength−Slenderness Ratio Relationship
($\sigma$o/fc' = 0.6 )

Ultimate strength decreases as a slenderness ratio becomes larger. This value seems to be inversely reduced in proportion to a slenderness ratio. This can be theoretically explained by considering a typical ultimate equlibrium as a short column in the following.

Final failure mechanism with yield hinges at both leg ends is assumed as shown in Fig.5-4. It is also assumed that ultimate strength is determined by concrete crush of cross section-A (Node-23).

Equilibrium of vertical, horizontal load and overturning moment can be written as followings.

$$P_v - (N_A^u + N_B^u) \times COS\theta - (Q_A^u - Q_B^u) \times SIN\theta = 0 \qquad \cdots\cdots\cdots\cdots(5.2)$$

$$Q_u + (N_A^u - N_B^u) \times SIN\theta - (Q_A^u + Q_B^u) \times COS\theta = 0 \qquad \cdots\cdots\cdots\cdots(5.3)$$

$$Q_u \times H_c + (N_A^u - N_B^u) \times W/2 \times COS\theta + (Q_A^u + Q_B^u) \times W/2 \times SIN\theta$$
$$- (M_A^u + M_B^u) = 0 \qquad \cdots\cdots\cdots\cdots(5.4)$$

where, $Q_u$ is the total lateral load at ultimate state and $H_c$ is the height from base to the applied centroid of that total load.

From eq.(5.3), the following equation is derived.

$$(Q_A^u + Q_B^u) = \{Q_u + (N_A^u - N_B^u) \times SIN\theta\}/COS\theta \qquad \cdots\cdots\cdots\cdots(5.5)$$

Substituting eq.(5.5) in (5.4), the equation for the lateral load capacity is obtained.

$$Q_u \times H_c + (N_A^u - N_B^u) \times W/2 \times COS\theta + W/2 \times \{Q_u + (N_A^u - N_B^u) \times SIN\theta\}$$
$$\times tan\theta - (M_A^u + M_B^u) = 0$$

Accordingly,

$$Q_u = \frac{2 \times (M_A^u + M_B^u) + W \times (N_B^u - N_A^u) \times (COS\theta + SIN\theta \times tan\theta)}{2 \times H_c + W \times tan\theta} \qquad \cdots\cdots\cdots\cdots(5.6)$$
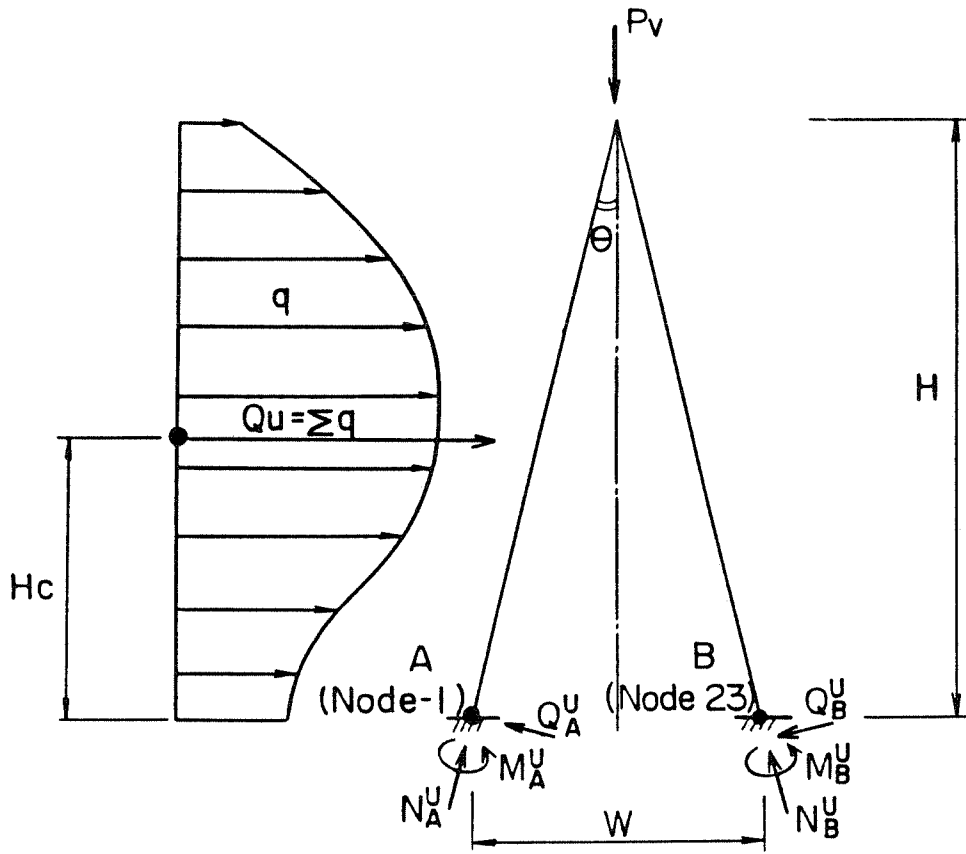
Fig. 5-4  Applied Loads and Reactions at an
Ultimate State
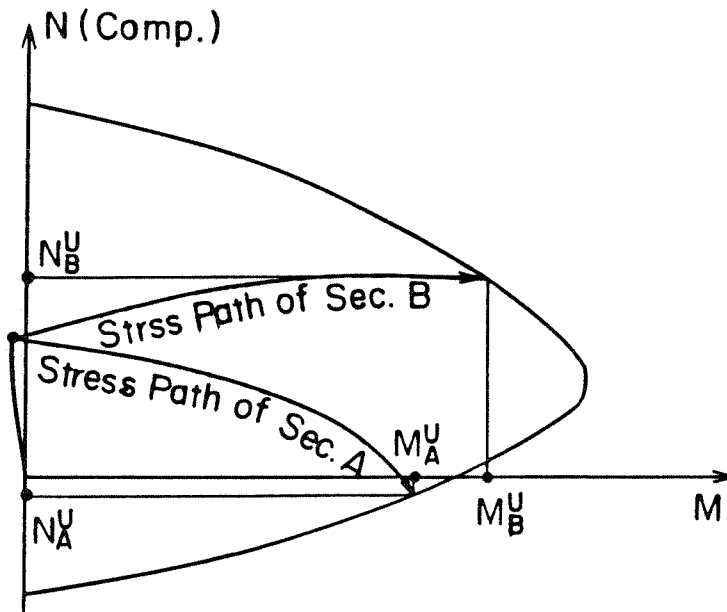


Fig. 5-5  Stress Path of Base Section

Therefore, if flexural moment and axial force at ultimate state are such as shown in Fig.5-5, the ultimate lateral load capacity can be predicated by eq.(5.6)

Substituting the following non-dimensional forms in eq.(5-6),

$$M_A{}^u = f'_c bh^2 m_A{}^u \qquad N_A{}^u = f'_c bh n_A{}^u$$

$$M_B{}^u = f'_c bh^2 m_B{}^u \qquad N_B{}^u = f'_c bh n_B{}^u$$

$$Q_u = \frac{2f'_c h^2}{2H_c + W\tan\theta}(m_A{}^u + m_B{}^u) + \frac{f'_c bW\cos\theta + \sin\theta\tan\theta}{2H_c + W\tan\theta} \times (N_B{}^u - N_A{}^u)h$$

$$\cdots\cdots\cdots\cdots(5.7)$$

Dividing both sides of eq.(5.7) by $A = 2bh/\cos\theta$ with considering $H_c = \alpha H$, $H = \ell\cdot\cos\theta$ and $W = 2\ell\cdot\sin\theta$, the following equation for an average strength, $\tau_u$ is finally derived.

$$\frac{\tau_u}{f'_c} = \frac{(m_A{}^u + m_B{}^u)}{2(\alpha + \tan^2\theta)} \times \frac{h}{\ell} + \frac{\sin\theta\tan\theta(1 + \tan^2\theta)}{2(\alpha + \tan^2\theta)} = C_1\frac{1}{(\frac{\ell}{h})} + C_2 \qquad \cdots\cdots(5.8)$$

From above equation, the ultimate strength is inversely proportinal to a slenderness ratio.

A non-dimentional ultimate strength - slenderness ratio relationship under uniformly distributed lateral load is shown in Fig.5-6 as an example.

With increase of configuration factor for W/H, the value increases because of enlargement of overturning moment resistance.   However, a significant difference is not observed among these values in the range of slenderness ratio of l/r larger than 104 since of less variation of axial force compared with that of flexural moment in legs.   In other words the contribution by axial force becomes independent of the slenderness ratio in that region.

As a gravity load level increases, these values generally become smaller except that of largest slenderness ratio of $\sigma_0/f'_c = 0.6$, apparently the most
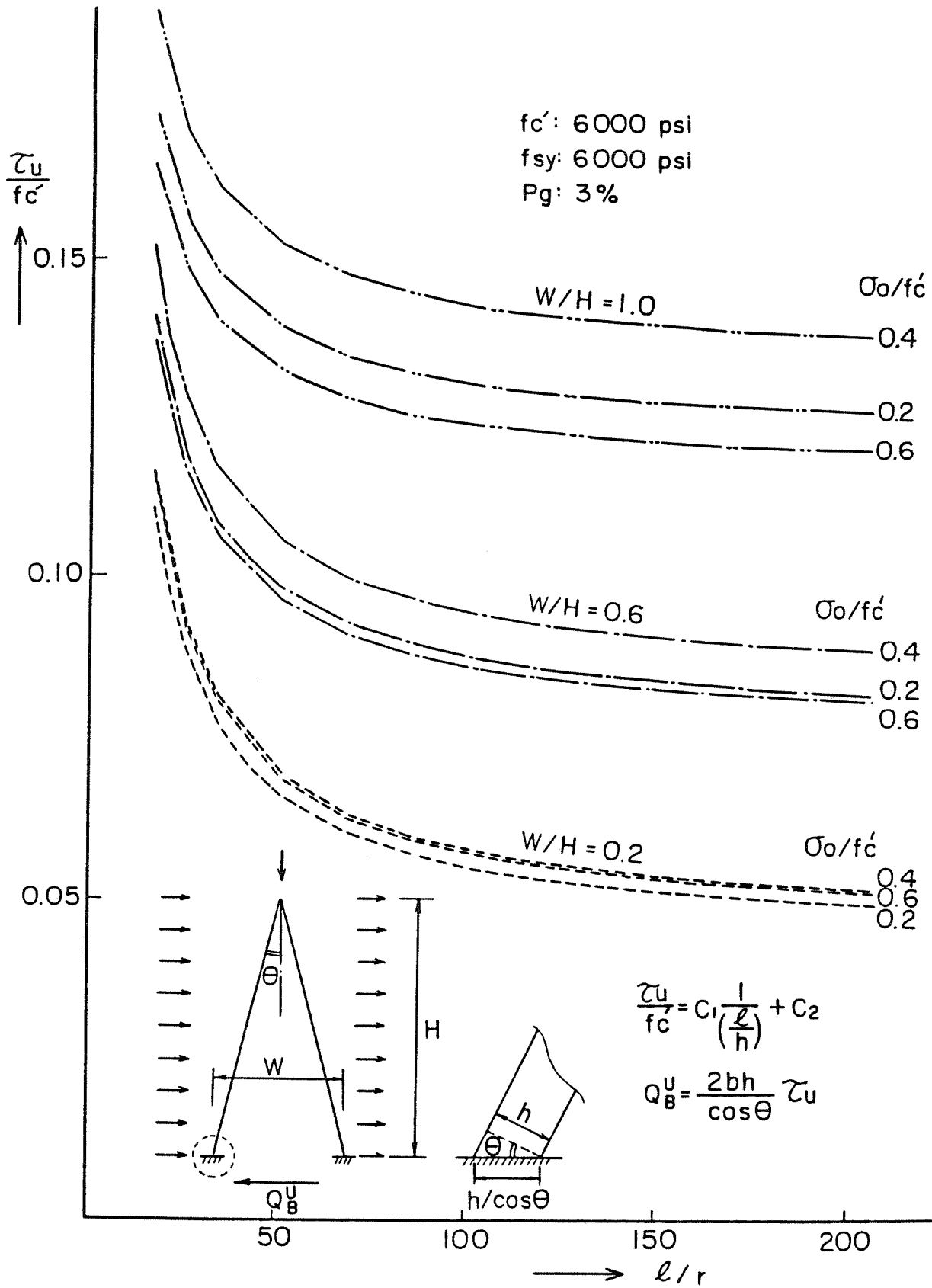
Fig. 5-6  Ultimate Load  based on elastic stress path

dominant case of geometric nonlinearity. Unexpectedly obtained is a relatively larger strength in l/r = 208 than in l/r = 104 case based on the following fact.

The deformation modes under gravity load and under lateral load are shown in Fig.5-7 for the case of l/r = 208 and of l/r = 104 respectively (W/H = 0.2, $\sigma_0/f'_c$ = 0.6 and $p_g$ = 3%). Observed in the former case is the so called pinching mode that lateral deformation of columns in the opposite direction is forced by an additional external moment due to a concertrated gravity load as soon as lateral load being applied. The left side column in which axial force increases in tension will be soon recovered to normal mode under increasing lateral load, while not in the counterpart (right side column). As the result, a flexural moment in the left side column removes to positive, but yet negative in the right side as shown in M-N relationship of Fig.5-8. Such an additinal overturning moment by gravity load is likely to contribute to increase of loading capacity. However, above behavior is not observed for the l/r = 104 case which behaves in a normal deformation mode.

## 5.4 Failure Mode

Failure status at the several representative sections and the failure mechanism as an entire structure are shown in Table5-1 and 5-2 for each $p_g$ = 1.5 and 3.0 percentage series.

A failure mode shown in the table is defined as follows (see Table.5-3);
- Rank 1 : more than 3 yield hinges created including that of bottom leg section in the action of tensile axial force.
- Rank 2 : a total of 2 yield hinges created including that of above section.
- Rank 3 : either one yield hinge created at the above section or concrete compressive failure at bottom leg section, counterpart of the above portion.
- Rank B : buckling failure in an inelastic region

(a) $\dfrac{\ell}{r} = 208$

(b) $\dfrac{\ell}{r} = 104$
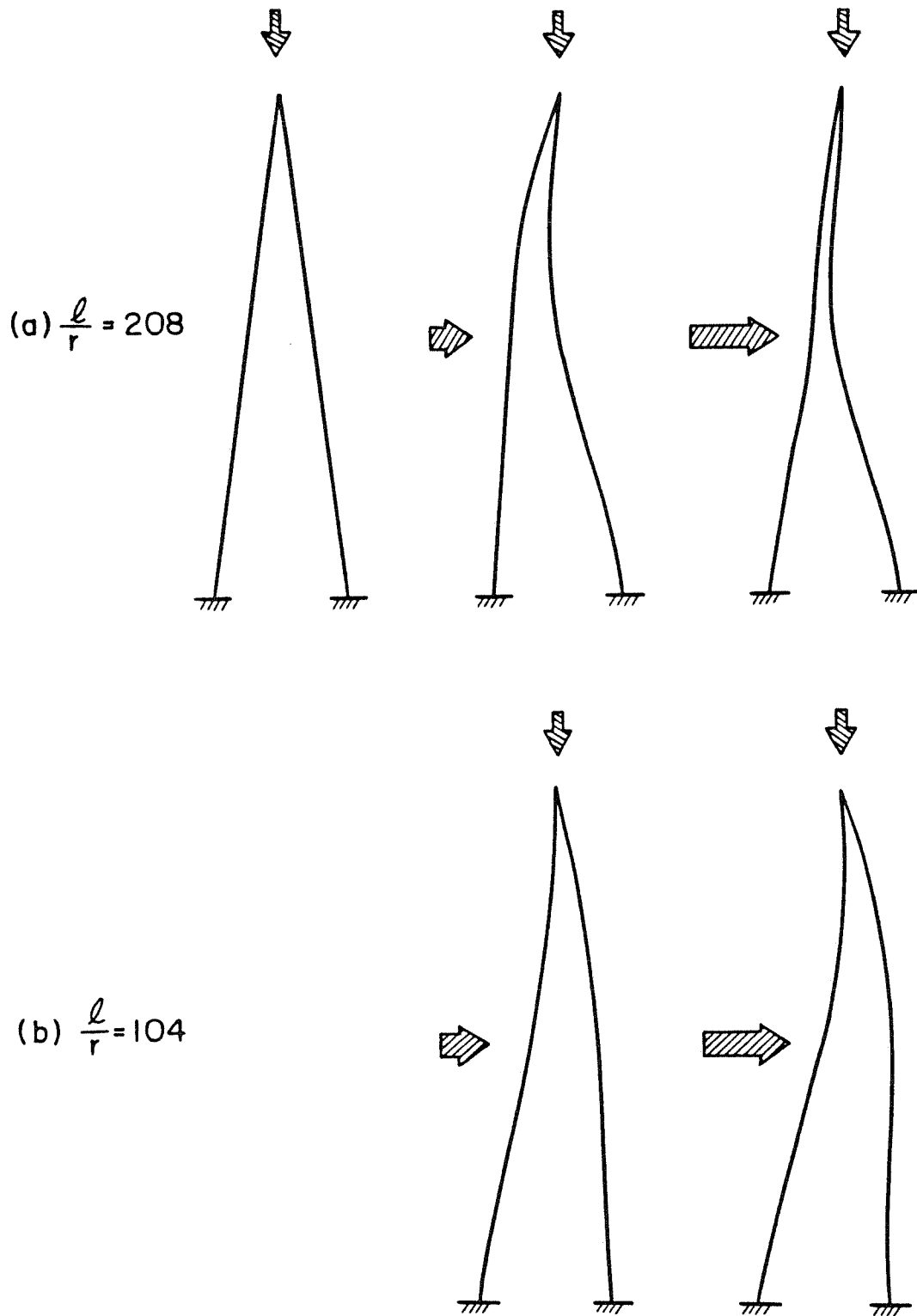
Fig. 5-7  Deformation Mode (W/H = 0.2, $\sigma o/fc' = 0.6$, Pg = 3%)
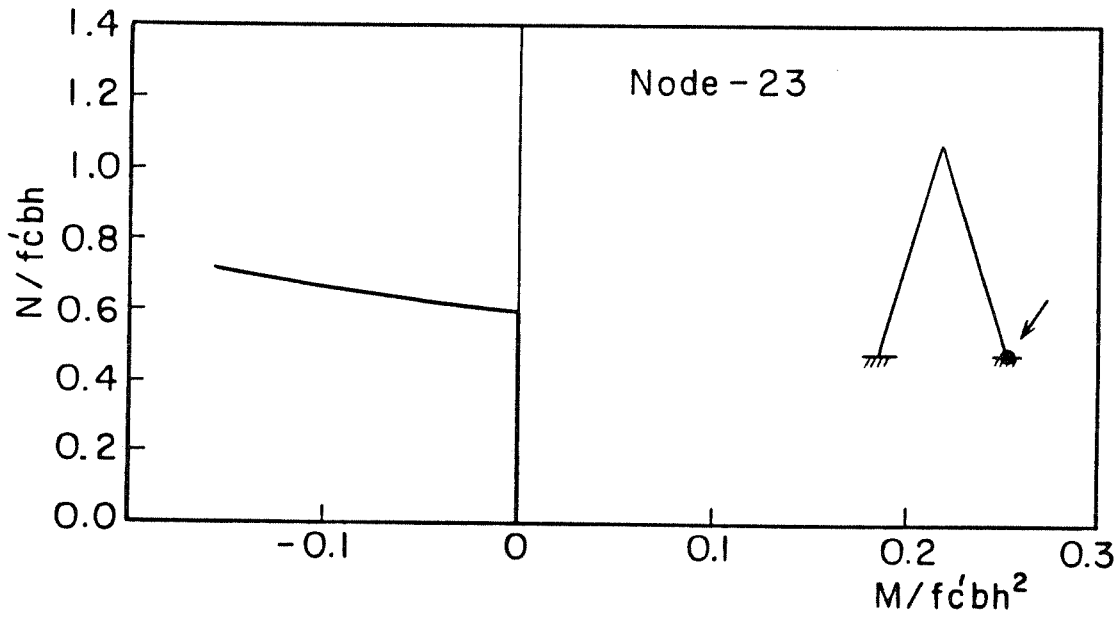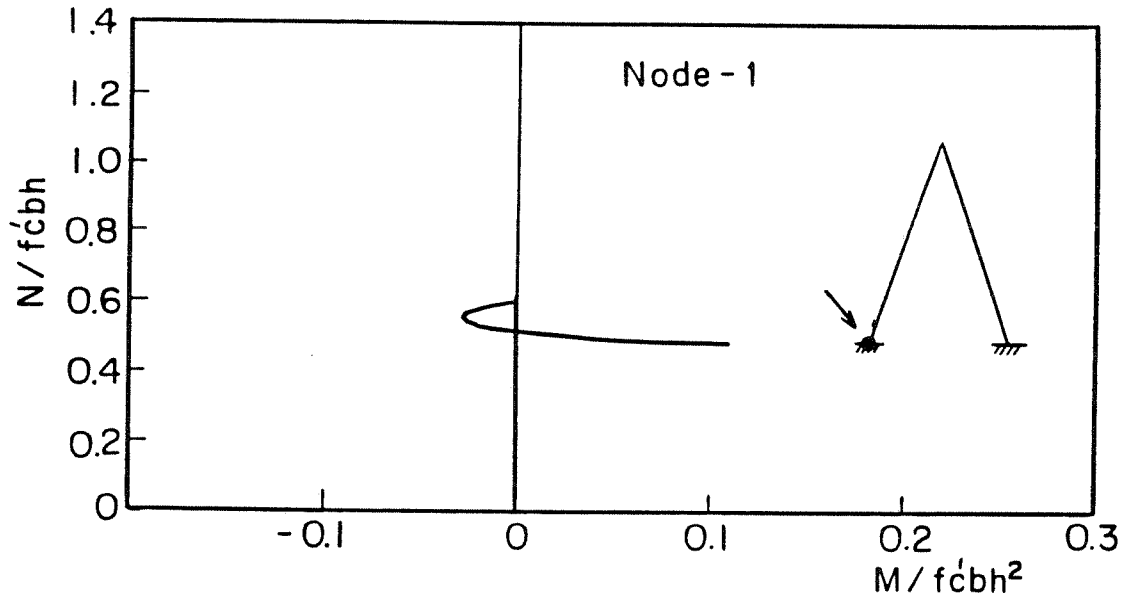
Fig. 5-8  M-N Relationship

$$(W/H = 0.2 \ , \ \ell/r = 208 \ , \ Pg = 3\% \ , \ \frac{\sigma_0}{fc'} = 0.6 \ )$$

Table 5-1 (1)  Ultimate States of A-Shaped Tower (S+H Load)

| Pg | $\sigma_0/f'_c$ | W/H | l/h | l/r | Crack Existence | Elem.1 TRY | 7 TRY | 11 TRY | 17 TRY | Elem.22 TRY | Elem.22 CRY | Elem.22 CC | Fail. Mode Rank | $\tau_u/f'_c$ | $\gamma_{max}/\gamma_y$ | $\delta_{bh}=M_2/M_2^e$ | $\delta_{bh}^{D}$ (ACI) |
|---|---|---|---|---|---|---|---|---|---|---|---|---|---|---|---|---|---|
| 1.5 % | 0.1 | 0.2 | 10 | 35 | ○ | ○ | | ○ | | ○ | ○ | ○ | 1 | 0.0404 | 2.086 | 1.575 | 1.051 |
| | | | 20 | 69 | ○ | ○ | ○ | ○ | | ○ | ○ | ○ | 1 | 0.0334 | 4.296 | 1.509 | 1.215 |
| | | | 30 | 104 | ○ | ○ | ○ | | | ○ | ○ | | 1 | 0.0252 | 2.374 | 1.299 | 1.501 |
| | | | 45 | 156 | ○ | ○ | | | | ○ | | | 2→B | 0.0126 | 1.332 | | 2.054 |
| | | | 60 | 208 | ○ | | | | | | | | B | 0.0058 | | | 3.478 |
| | | 0.4 | 10 | 35 | ○ | ○ | ○ | ○ | | ○ | ○ | ○ | 1 | 0.0651 | 4.152 | 1.492 | 1.048 |
| | | | 20 | 69 | ○ | ○ | ○ | | | ○ | ○ | | 1 | 0.0427 | 3.230 | 1.160 | 1.160 |
| | | | 30 | 104 | ○ | ○ | ○ | | ○ | ○ | | | 1 | 0.0253 | 2.081 | 1.198 | 1.310 |
| | | | 45 | 156 | ○ | ○ | | | ○ | ○ | | | 1→B | 0.0130 | 1.438 | | 1.757 |
| | | | 60 | 208 | ○ | | | | | | | | B | 0.0060 | | | 2.929 |
| | | 0.6 | 10 | 35 | ○ | ○ | ○ | ○ | | ○ | ○ | | 1 | 0.0789 | 3.674 | 1.316 | 1.044 |
| | | | 20 | 69 | ○ | ○ | ○ | | | ○ | | | 1 | 0.0429 | 3.586 | 1.096 | 1.133 |
| | | | 30 | 104 | ○ | ○ | | | ○ | ○ | | | 1 | 0.0253 | 2.063 | 1.150 | 1.271 |
| | | | 45 | 156 | ○ | ○ | | | ○ | ○ | | | 2→B | 0.0122 | 1.000 | | 1.664 |
| | | | 60 | 208 | ○ | | | | | | | | 2→B | 0.0061 | 1.000 | | 2.897 |
| | 0.2 | 0.2 | 10 | 35 | ○ | ○ | ○ | | | | ○ | ○ | 2 | 0.0502 | 1.716 | 1.274 | 1.082 |
| | | | 20 | 69 | ○ | ○ | ○ | | | | ○ | ○ | 2 | 0.0413 | 2.222 | 1.196 | 1.387 |
| | | | 30 | 104 | ○ | ○ | ○ | | | ○ | ○ | | 1 | 0.0281 | 1.433 | 1.329 | 1.985 |
| | | | 45 | 156 | ○ | | | | | | | | B | 0.0115 | | | 5.306 |
| | | | 60 | 208 | ○ | | | | | | | | B | 0.0044 | | | |
| | | 0.4 | 10 | 35 | ○ | ○ | ○ | | | ○ | ○ | | 1 | 0.0834 | 1.900 | 1.219 | 1.077 |
| | | | 20 | 69 | ○ | ○ | ○ | | | ○ | ○ | | 1 | 0.0490 | 1.435 | 1.159 | 1.271 |
| | | | 30 | 104 | ○ | ○ | | | | | | | 1 | 0.0286 | 1.454 | 1.355 | 1.650 |
| | | | 45 | 156 | ○ | | | | | | | | B | 0.0114 | | | 3.824 |
| | | | 60 | 208 | ○ | | | | | | | | B | 0.0045 | | | |
| | | 0.6 | 10 | 35 | ○ | ○ | ○ | | | ○ | ○ | ○ | 1 | 0.0972 | 2.125 | 1.163 | 1.069 |
| | | | 20 | 69 | ○ | ○ | ○ | | | ○ | ○ | | 1 | 0.0509 | 1.510 | 1.134 | 1.236 |
| | | | 30 | 104 | ○ | ○ | ○ | | | ○ | ○ | | 1 | 0.0287 | 1.609 | 1.342 | 1.579 |
| | | | 45 | 156 | ○ | | | | | | | | 2→B | 0.0115 | 1.000 | | 3.736 |
| | | | 60 | 208 | ○ | | | | | | | | B | 0.0046 | | | |

TRY : Tensile Yielding of Rebar   CRY : Compressive Yielding of Rebar   CC : Concrete Crush

Table 5-1 (2)　　Ultimate States of A-Shaped Tower (S+H Load)

| Pg | $\sigma_0/f'_c$ | W/H | l/h | l/r | Crack Existence | Elem.1 TRY | 7 TRY | 11 TRY | 17 TRY | Elem.22 TRY | Elem.22 CRY | Elem.22 CC | Fail. Mode Rank | $\tau_u/f'_c$ | $\gamma_{max}/\gamma_y$ | $\delta_{bh}^e = M_2/M_2^e$ | $\delta_{bh}^D$ (ACI) |
|---|---|---|---|---|---|---|---|---|---|---|---|---|---|---|---|---|---|
| 1.5 % | 0.4 | 0.2 | 10 | 35 | O | O | | | | | O | O | 2 | 0.0585 | 1.000 | 0.8165 | 1.133 |
| | | | 20 | 69 | O | O | | | | | O | O | 2 | 0.0444 | 1.027 | 0.9836 | 1.723 |
| | | | 30 | 104 | O | | | | | | O | O | 3 | 0.0276 | | 1.3760 | 4.655 |
| | | | 45 | 156 | O | | | | | | | | B | 0.0076 | | | |
| | | | 60 | 208 | O | | | | | | | | B' | 0.0131 | | | |
| | | 0.4 | 10 | 35 | O | O | | | | | O | O | 2 | 0.0942 | 1.040 | 0.9554 | 1.122 |
| | | | 20 | 69 | O | | | | | | O | O | 3 | 0.0527 | | 1.0980 | 1.537 |
| | | | 30 | 104 | O | | | | | | O | O | 3 | 0.0281 | | 1.6190 | 3.149 |
| | | | 45 | 156 | O | | | | | | | | B | 0.0076 | | | |
| | | | 60 | 208 | O | | | | | | | | B' | 0.0138 | | | |
| | | 0.6 | 10 | 35 | O | O | | | | | O | O | 2 | 0.1083 | 1.000 | 0.9818 | 1.111 |
| | | | 20 | 69 | O | | | | | | O | O | 3 | 0.0541 | | 1.1205 | 1.484 |
| | | | 30 | 104 | O | | | | | | O | O | 3 | 0.0280 | | 1.6508 | 2.930 |
| | | | 45 | 156 | O | | | | | | | | B | 0.0072 | | | |
| | | | 60 | 208 | O | | | | | | | | B' | 0.0130 | | | |
| | 0.6 | 0.2 | 10 | 35 | O | | | | | | O | O | 3 | 0.0495 | | 0.6954 | 1.166 |
| | | | 20 | 69 | O | | | | | | O | O | 3 | 0.0368 | | 0.8892 | 2.112 |
| | | | 30 | 104 | O | | | | | | O | O | 3 | 0.0205 | | 1.6745 | |
| | | | 45 | 156 | | | | | | | | | EB | 0.0001 | | | |
| | | | 60 | 208 | | | | | | | | | EB' | 0.0076 | | | |
| | | 0.4 | 10 | 35 | O | | | | | | O | O | 3 | 0.0817 | | 0.8204 | 1.157 |
| | | | 20 | 69 | O | | | | | | O | O | 3 | 0.0440 | | 1.1308 | 1.875 |
| | | | 30 | 104 | O | | | | | | O | O | 3 | 0.0206 | | 2.0519 | 21.833 |
| | | | 45 | 156 | | | | | | | | | EB | 0.0002 | | | |
| | | | 60 | 208 | O | | | | | | | | B' | 0.0112 | | | |
| | | 0.6 | 10 | 35 | O | | | | | | O | O | 3 | 0.0980 | | 0.8831 | 1.148 |
| | | | 20 | 69 | O | | | | | | O | O | 3 | 0.0461 | | 1.1720 | 1.813 |
| | | | 30 | 104 | O | | | | | | O | O | 3 | 0.0206 | | 2.1610 | 15.976 |
| | | | 45 | 156 | | | | | | | | | EB | 0.0001 | | | |
| | | | 60 | 208 | | | | | | | | | EB' | 0.0122 | | | |

TRY : Tensile Yielding of Rebar　　CRY : Compressive Yielding of Rebar　　CC : Concrete Crush

Table 5-2 (1)  Ultimate States of A-Shaped Tower (S+H Load)

| $P_g$ | $\dfrac{\sigma_0}{f'_c}$ | $\dfrac{W}{H}$ | $l/h$ | $l/r$ | Crack Existence | Elem.1 TRY | 7 TRY | 11 TRY | 17 TRY | Elem.22 TRY | Elem.22 CRY | Elem.22 CC | Fail. Mode Rank | $\dfrac{\tau_u}{f'_c}$ | $\dfrac{\gamma_{max}}{\gamma_y}$ | $\delta_{bh}=M_2/M_2^e$ | $\delta_{bh}^D$ (ACI) |
|---|---|---|---|---|---|---|---|---|---|---|---|---|---|---|---|---|---|
| 3.0 % | 0.1 | 0.2 | 10 | 35 | ○ | ○ |  |  |  |  | ○ | ○ | 2 | 0.0602 | 1.791 | 1.575 | 1.044 |
|  |  |  | 20 | 69 | ○ | ○ | ○ | ○ |  |  | ○ |  | 1 | 0.0513 | 2.187 | 1.335 | 1.194 |
|  |  |  | 30 | 104 | ○ | ○ | ○ |  |  |  | ○ |  | 2 | 0.0392 | 1.762 | 1.250 | 1.408 |
|  |  |  | 45 | 156 | ○ | ○ |  |  |  | ○ |  |  | 2 | 0.0236 | 1.452 | 1.410 | 1.832 |
|  |  |  | 60 | 208 | ○ | ○ |  |  |  | ○ |  |  | 2→B | 0.0124 | 1.000 |  | 2.429 |
|  |  | 0.4 | 10 | 35 | ○ | ○ | ○ | ○ |  |  | ○ |  | 1 | 0.1008 | 2.475 | 1.414 | 1.043 |
|  |  |  | 20 | 69 | ○ | ○ | ○ |  |  | ○ | ○ |  | 1 | 0.0647 | 2.110 | 1.401 | 1.119 |
|  |  |  | 30 | 104 | ○ | ○ | ○ |  |  | ○ | ○ |  | 1 | 0.0431 | 2.215 | 1.116 | 1.254 |
|  |  |  | 45 | 156 | ○ | ○ |  |  |  | ○ |  |  | 1→B | 0.0240 | 1.478 |  | 1.529 |
|  |  |  | 60 | 208 | ○ | ○ |  |  | ○ | ○ |  |  | 2→B | 0.0126 | 1.000 |  | 2.000 |
|  |  | 0.6 | 10 | 35 | ○ | ○ | ○ |  |  | ○ | ○ |  | 1 | 0.1179 | 2.441 | 1.273 | 1.038 |
|  |  |  | 20 | 69 | ○ | ○ | ○ |  |  | ○ | ○ |  | 1 | 0.0677 | 2.233 | 1.077 | 1.109 |
|  |  |  | 30 | 104 | ○ | ○ | ○ |  |  | ○ |  |  | 1 | 0.0430 | 1.974 | 1.072 | 1.211 |
|  |  |  | 45 | 156 | ○ | ○ |  |  |  | ○ |  |  | 2→B | 0.0234 | 1.447 |  | 1.446 |
|  |  |  | 60 | 208 | ○ | ○ |  |  |  |  |  |  | 2→B | 0.0133 | 1.000 |  | 1.894 |
|  | 0.2 | 0.2 | 10 | 35 | ○ | ○ |  |  |  |  | ○ | ○ | 2 | 0.0654 | 1.332 | 1.312 | 1.061 |
|  |  |  | 20 | 69 | ○ | ○ |  |  |  |  | ○ | ○ | 2 | 0.0559 | 1.858 | 1.175 | 1.284 |
|  |  |  | 30 | 104 | ○ | ○ |  |  |  |  | ○ | ○ | 2 | 0.0412 | 1.492 | 1.246 | 1.665 |
|  |  |  | 45 | 156 | ○ | ○ |  |  |  | ○ |  |  | 2 | 0.0202 | 1.000 | 1.875 | 2.720 |
|  |  |  | 60 | 208 | ○ |  |  |  |  | ○ |  |  | B | 0.0068 |  |  | 8.274 |
|  |  | 0.4 | 10 | 35 | ○ | ○ |  |  |  |  | ○ | ○ | 2 | 0.1101 | 1.577 | 1.215 | 1.059 |
|  |  |  | 20 | 69 | ○ | ○ |  |  |  |  | ○ |  | 2 | 0.0700 | 1.614 | 1.136 | 1.199 |
|  |  |  | 30 | 104 | ○ | ○ |  |  |  |  |  |  | 2 | 0.0421 | 1.307 | 1.263 | 1.423 |
|  |  |  | 45 | 156 | ○ |  |  |  |  | ○ |  |  | 2 | 0.0202 | 1.000 | 1.756 | 2.192 |
|  |  |  | 60 | 208 | ○ |  |  |  |  | ○ |  |  | B | 0.0071 |  |  | 5.970 |
|  |  | 0.6 | 10 | 35 | ○ | ○ | ○ |  |  |  | ○ | ○ | 2 | 0.1338 | 1.842 | 1.136 | 1.054 |
|  |  |  | 20 | 69 | ○ | ○ |  |  |  |  | ○ |  | 2 | 0.0719 | 1.317 | 1.159 | 1.169 |
|  |  |  | 30 | 104 | ○ | ○ |  |  |  | ○ | ○ |  | 2 | 0.0440 | 1.410 | 1.255 | 1.371 |
|  |  |  | 45 | 156 | ○ |  | ○ | ○ |  | ○ |  | ○ | 1 | 0.0205 | 1.549 | 1.889 | 2.079 |
|  |  |  | 60 | 208 | ○ |  |  |  |  | ○ |  |  | B | 0.0069 |  |  | 5.539 |

TRY : Tensile Yielding of Rebar   CRY : Compressive Yielding of Rebar   CC : Concrete Crush

Table 5-2 (2)  Ultimate States of A-Shaped Tower (S+H Load)

| Pg | $\sigma_0/f'c$ | W/H | l/h | l/r | Crack Existence | Elem.1 TRY | 7 TRY | 11 TRY | 17 TRY | Elem.22 TRY | Elem.22 CRY | Elem.22 CC | Fail. Mode Rank | $\tau_u/f'c$ | $\gamma_{max}/\gamma_y$ | $\delta_{bh}=M_2/M_2^e$ | $\delta_{bh}^D$ (ACI) |
|---|---|---|---|---|---|---|---|---|---|---|---|---|---|---|---|---|---|
| 3.0 % | 0.4 | 0.2 | 10 | 35 | ○ | | | | | | ○ | ○ | 3 | 0.0705 | | 0.909 | 1.092 |
| | | | 20 | 69 | ○ | ○ | | | | | ○ | ○ | 2 | 0.0561 | 1.000 | 1.001 | 1.446 |
| | | | 30 | 104 | ○ | | | | | | ○ | ○ | 3 | 0.0376 | | 1.290 | 2.350 |
| | | | 45 | 156 | ○ | | | | | | | | B | 0.0122 | | | 56.099 |
| | | | 60 | 208 | | | | | | | | | EB | 0.0008 | | | |
| | | 0.4 | 10 | 35 | ○ | ○ | | | | | ○ | ○ | 2 | 0.1167 | | 0.986 | 1.086 |
| | | | 20 | 69 | ○ | | | | | | ○ | ○ | 3 | 0.0694 | 1.000 | 1.090 | 1.338 |
| | | | 30 | 104 | ○ | | | | | | ○ | ○ | 3 | 0.0401 | | 1.440 | 1.956 |
| | | | 45 | 156 | ○ | | | | | | | | B | 0.0120 | | | 16.513 |
| | | | 60 | 208 | | | | | | | | | EB | 0.0012 | | | |
| | | 0.6 | 10 | 35 | ○ | ○ | | | | | ○ | ○ | 2 | 0.1370 | | 0.999 | 1.079 |
| | | | 20 | 69 | ○ | | | | | | ○ | ○ | 3 | 0.0728 | 1.066 | 1.102 | 1.303 |
| | | | 30 | 104 | ○ | | | | | | ○ | ○ | 3 | 0.0402 | | 1.463 | 1.867 |
| | | | 45 | 156 | ○ | | | | | | | | B | 0.0117 | | | 16.409 |
| | | | 60 | 208 | | | | | | | | | EB | 0.0012 | | | |
| | 0.6 | 0.2 | 10 | 35 | ○ | | | | | | ○ | ○ | 3 | 0.0619 | | 0.7809 | 1.114 |
| | | | 20 | 69 | ○ | | | | | | ○ | ○ | 3 | 0.0475 | | 0.9230 | 1.611 |
| | | | 30 | 104 | ○ | | | | | | ○ | ○ | 3 | 0.0288 | | 1.4138 | 3.720 |
| | | | 45 | 156 | | | | | | | | | EB | 0.0044 | | | |
| | | | 60 | 208 | ○ | | | | ○ | | ○ | | B´ | 0.0162 | | | |
| | | 0.4 | 10 | 35 | ○ | | | | | | ○ | ○ | 3 | 0.1034 | | 0.8731 | 1.108 |
| | | | 20 | 69 | ○ | | | | | | ○ | ○ | 3 | 0.0594 | | 1.0814 | 1.493 |
| | | | 30 | 104 | ○ | | | | | | ○ | ○ | 3 | 0.0311 | | 1.7016 | 3.001 |
| | | | 45 | 156 | | | | | | | | | EB | 0.0043 | | | |
| | | | 60 | 208 | ○ | | | | ○ | | ○ | | B´ | 0.0171 | | | |
| | | 0.6 | 10 | 35 | ○ | | | | | | ○ | ○ | 3 | 0.1227 | | 0.9054 | 1.102 |
| | | | 20 | 69 | ○ | | | | | | ○ | ○ | 3 | 0.0620 | | 1.1134 | 1.456 |
| | | | 30 | 104 | ○ | | | | | | ○ | ○ | 3 | 0.0311 | | 1.7248 | 2.839 |
| | | | 45 | 156 | | | | | | | | | EB | 0.0040 | | | |
| | | | 60 | 208 | ○ | | | | ○ | | ○ | | B´ | 0.0177 | | | |

TRY : Tensile Yielding of Rebar    CRY : Compressive Yielding of Rebar    CC : Concrete Crush
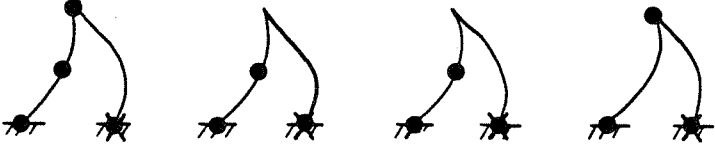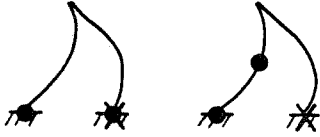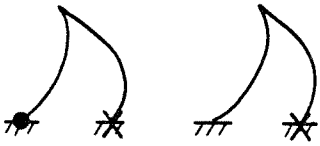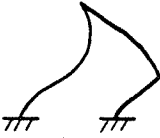
●:Yield Hinge    x : Concrete Crush
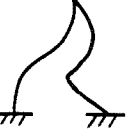
| Rank | Failire Mode |
|------|--------------|
| I | |
| 2 | |
| 3 | |
| B | Inelastic Buckling |
| EB | Elastic Buckling |
| B' | Inelastic Buckling with Pinching Mode |
| EB' | Elastic Buckling with Pinching Mode |

Table. 5- 3  Failure Mode

●Rank EB : buckling failure in an elastic region

●Rank B' or EB' : inelastic or elastic buckling failure accompanied by an

pinching mode explained in the previous section.

In the above definision, 'Yield Hinge' is assumed to be created by a tensile yielding of rebar.

More ductility can be expected in smaller failure mode rank which creates as many yield hinges as, or close to collapse mode of structure in flexure. Therefore, a brittle failre is potentially caused for rank 3 and for buckling failure such as rank B or EB and B' or EB', which are not recommendable from a ductility design point of view.

Some results with intermediate slenderness ratio present no convergence in numerical solution in spite of no occurence of crush after rebar yielding.

It is possibly considered that a convergent solution is not reach during interation for unbalanced force because of a relatively rapid failure appearance by concrete crushing at Elem-22.

Furthermore, there are some cases which reach failure without any yielding and crushing after some or no crack occurence especially for larger slenderness ratio cases. Even when fairly small load increments are intentionally applied near ultimate load, deformation suddenly increases without any appearance of yielding and crushing followed by divergence of solution. Based on these facts in the numerical solution, this type of failure can be defined as buckling.

In the practical range of slenderness ratio less than 104, it can be said that the cases of gravity load of $\sigma_0/f'_c$ less than 0.2 indicate Rank 1 Mode in general, but some of them Rank 2 mode especially for rebar ratio of $p_g = 3\%$. And a brittle failure may be encouraged with such as rank 2 or 3 for $\sigma_0/f'_c = 0.4$ and rank 3 for $\sigma_0/f'_c = 0.6$.

In the range of slenderness ratio larger than 156, extremely brittle buckling failure seems to occur even with low gravity load, particularly elastic buckling with high gravity load.

Low gravity load cases of $\sigma_0/f'_c \leqq 0.2$ indicate yielding of tensile rebar of Elem-1, predominant section in axial tension due to overturning moment, prior to compressive yielding or crushing of Elem-22, counterpart of Elem-1 except for large slenderness ratio cases. And compressive yilding of rebar or concrete crushing occurs afrewards at Elem-22 for relatively small slenderness ratio, and additional tensile yielding of rebar at that section for large slenderness ratio. The increase of configuration factor,W/H provides slightly dominant flexural moment behavior with less variation of axial force, which encourage tensile rebar yielding of Elem-22. With decrease of gravity load and of a slenderness ratio, a yield hinge tends to be produced even at mid part legs.

For larger slenderness ratio, especially larger than 156, highly possible is a buckling failure. And even an elastic buckling failure may occur if the gravity load is large. In the case with the largest slenderness ratio of $l/r = 208$ and with high gravity load of $\sigma_0/f'_c = 0.4$, possibly observed is a buckling as well with the pinching mode previously described.

In general, it can be said that a ductile failure is not obtained for gravity load of $\sigma_0/f'_c$ larger than 0.2 and that no significant differences of failure mode by a configuration factor, W/H and by rebar ratio, $p_g$ are observed.

## 5.5 Moment Magnification Factor

It is one of objectives to evaluate the applicability of the moment magnifier method specified in the current design code[4] to a bridge tower such as the present structure.

In order to discuss the moment magnification factor, it is appropriate to

focus on the forces at the bottom leg section such as Node-23 under a large compressive axial force since analytical results provide that section as critical in failure.

A typical stress path at that particular section under lateral load combined with gravity load is shown in Fig.5-9, where the solid line shows a nonlinear stress path, while the dashed line, linear path is based on a conventional elastic analysis. $(M_1, N_1)$ and $(M_1^e, N_1^e)$ are the stress points respectively for the nonlinear and the linear analysis under gravity load, and $(M_2, N_2)$ and $(M_2^e, N_2^e)$ under ultimate load.

$M_G$ and $M_G^e$ are the absolute values of that moment under gravity load, while $M_H$ and $M_H^e$ are the differences under gravity load and under lateral load respectively.

The gravity load behavior up to $N = N_1 = N_1^e$ shows that the nonlinear moment, $M_1$ is less than the linear moment, $M_1^e$ because of stress relaxation based on the stiffness reduction of the botom leg section.

The subsequent linear moment, $M_H^e$ is calculated so that an axial force, $N_2^e$ equals the ultimate value, $N_2$ in nonlinear analysis. In the current design code, a magnified moment is specified by following equations.

$$Mc = \delta_b M_{2b} + \delta_s M_{2s} \qquad \cdots\cdots\cdots\cdots(5.9)$$

where

$$\delta_b = \frac{C_m}{1 - \phi P_u / P_c} \geqq 1.0 \qquad \cdots\cdots\cdots\cdots(5.10)$$

$$\delta_s = \frac{C_m}{1 - \dfrac{\Sigma \phi P_u}{\Sigma P_c}} \geqq 1.0 \qquad \cdots\cdots\cdots\cdots(5.11)$$

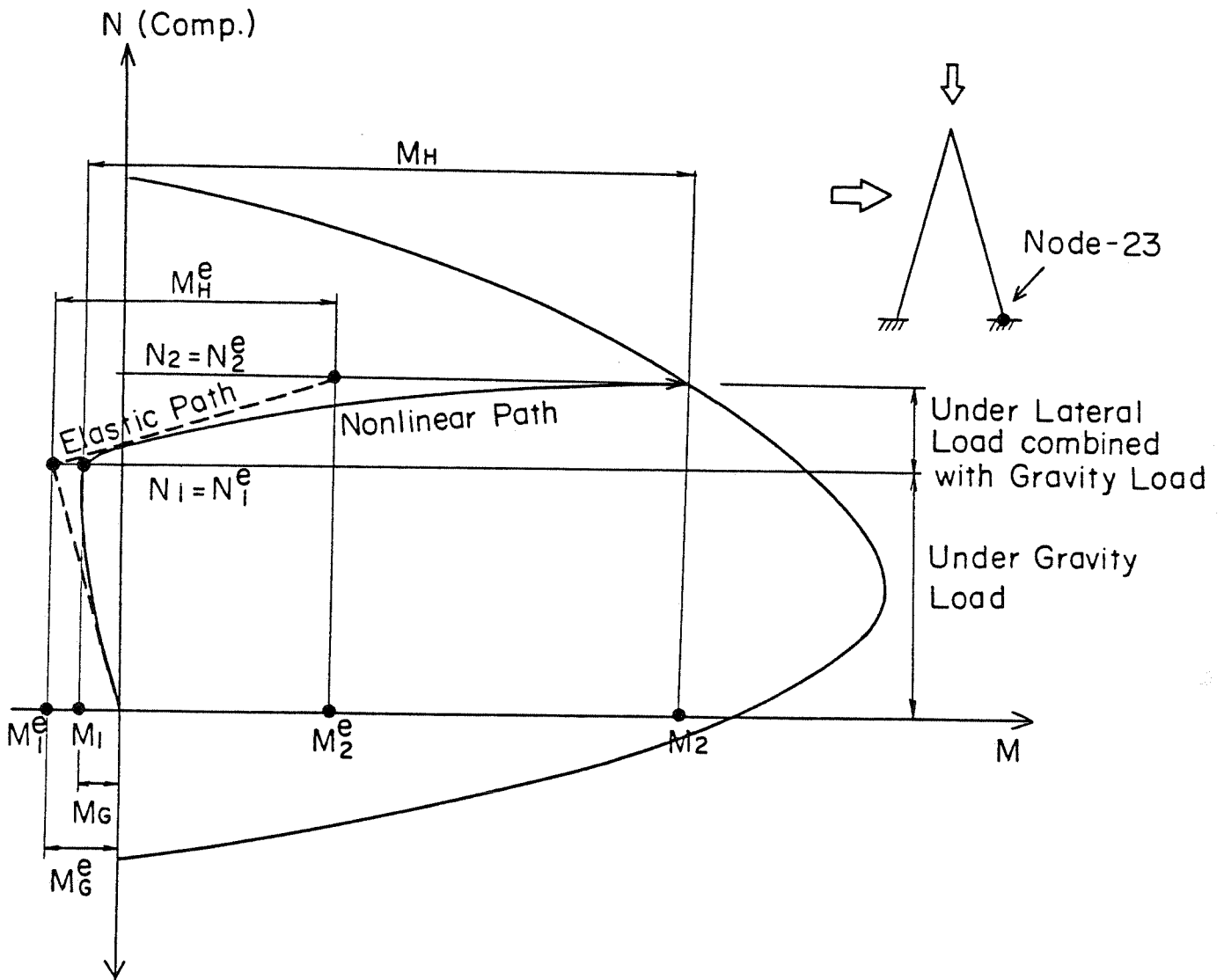$$Pc = \frac{\pi^2 EI}{(kl_u^2)} \qquad \cdots\cdots\cdots\cdots(5.12)$$

Fig.5-9  A Typical Stress Path at the Bottom Leg Section
(Node-23)

In the eq.(5-9), the first term is the moment for frames braced against sildeway and the second is for frames not braced against sideway. In the present study, the comparison between analytical and design values calculated as a braced frame both under gravity and lateral load, will be carried out since the both legs are connected at top with to other and the prediction as an unbraced frame may produce a too conservative value. Therefore, the second term in eq.(5.9) will be neglected in the present study.

(1) Design Moment Magnification Factor

The moment magnification factor as a design value will be calculated as follows.

The flexural stiffness in eq.(5.12) is specified as

$$EI = \frac{(\frac{E_c I_g}{5}) + E_s I_{se}}{1 + \beta_d} \qquad \cdots\cdots\cdots\cdots(5.13)$$

where $\beta_d$ can be assumed as zero because the gravity load moment is far smaller than that of a total moment including lateral load moment. In eq.(5.12), $l_u = 1$, is a full length of the leg and $k = 0.625$ is based on the assumption as a braced frame in which $f_a = 0$ at a fixed end and $f_b = 1$ at a top end are to be used[20]. The assumption, $f_b = 1$ is based on that of a column laterally supported and rotationally restricted by each other with the same flexural rigidity $EI/1$.

In the eq.(5.10), a factored axial load, $\phi P_u$ is to be equal to the analytical values, $N_1 = N_1^e$ for a gravity load and $N_2 = N_2^e$ for a combined load respectively as shown in Fig.5-9. $\phi = 1$ as a strength reduction factor is assumed, which can be rather comparable to an analytical result with no reduction of material strength.

Additionally assumed is $C_m = 1$ since the member of the present structure has transverse loads between supports.

(2)  Analytical Moment Magnifiction Factor

An analytical moment magnification factor is to be calculated on the following basis.

Based on the previous assumption of a braced frame ,eq.(5.9) can be rewritten referring to the Fig.5-9 as

$$M_1 = \delta_{bg}M_1{}^e, \quad M_2 = \delta_{bh}M_2{}^e \qquad \cdots\cdots\cdots\cdots(5.14)$$

Moment magnification factors for the gravity and the combined load can be estimated respectively by rewriting eq.(5-14).

$$\delta_{bg} = \frac{M_1}{M_1{}^e} \qquad \cdots\cdots\cdots\cdots(5.15)$$

$$\delta_{bh} = \frac{M_2}{M_2{}^e} \qquad \cdots\cdots\cdots\cdots(5.16)$$

In the present model, the gravity load moments, $M_1 = M_G$ and $M_1{}^e = M_G{}^e$ are both far smaller compared to the combined load moment $M_2$ and $M_2{}^e$. Therefore, $M_2$ and $M_2{}^e$ can be almost equal to $M_h$ and $M_h{}^e$ respectively.

In the following section, a comparison will be carried out between the design value expressed by eq.(5.10) and the analytical values by eq.(5.15) or (5.16).

(3) Moment Magnification Factor $\delta_{bg}$ for Gravity Load.

The moment magnification factor-slenderness ratio relationships for the bottom leg section are shown in Fig.5-10~5-11.   As shown in the figures, the values of $\delta_{bg}$ are all less than one and the reduction becomes larger with increase of $l/r$ and with that of $\sigma_0/f'_c$.

The governing factors for moment behavior under gravity load are 1) stiffness variation along legs and 2) secondary moment effect.

For small slenderness ratio, less flexural moment reduction is obtained
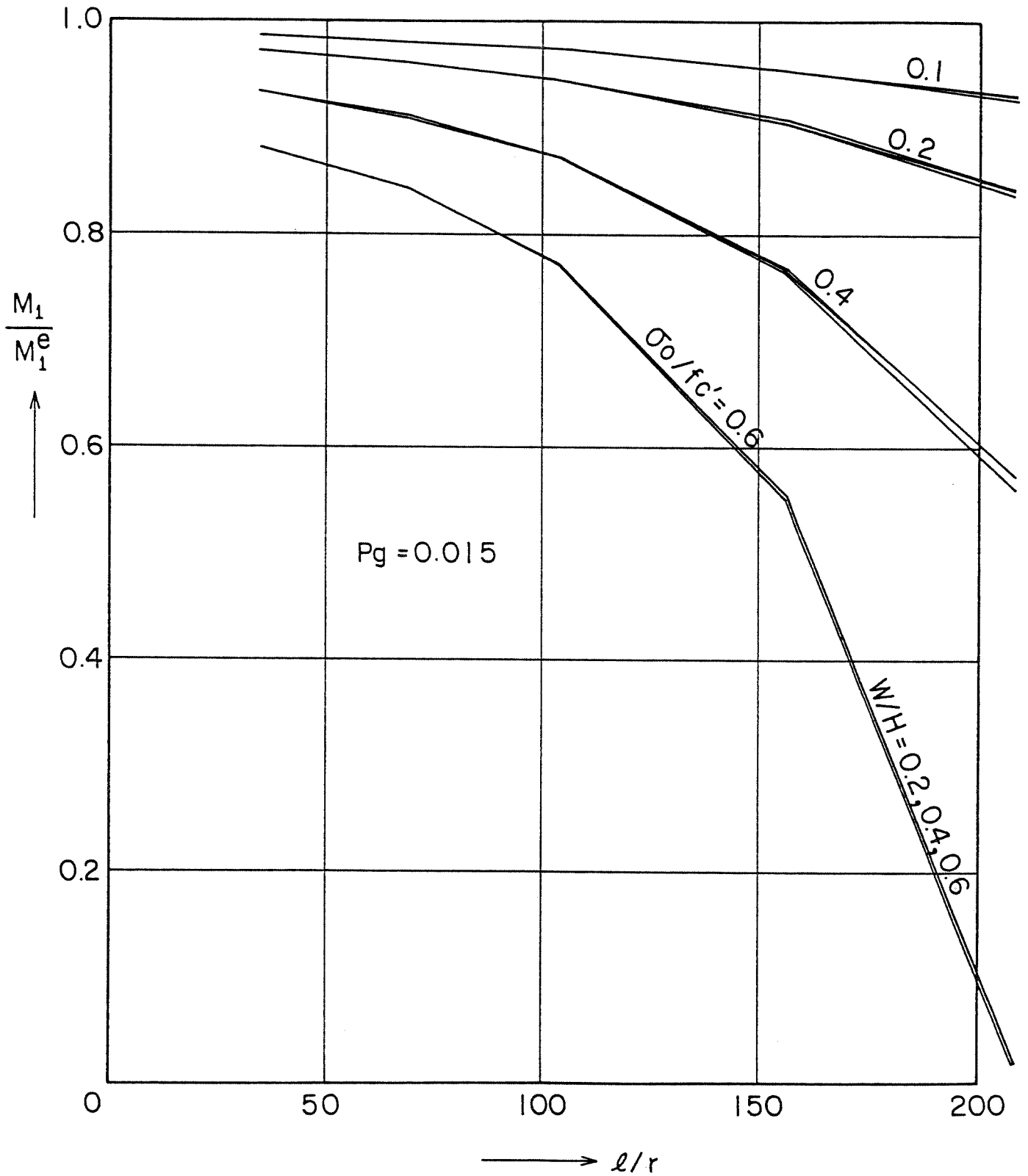
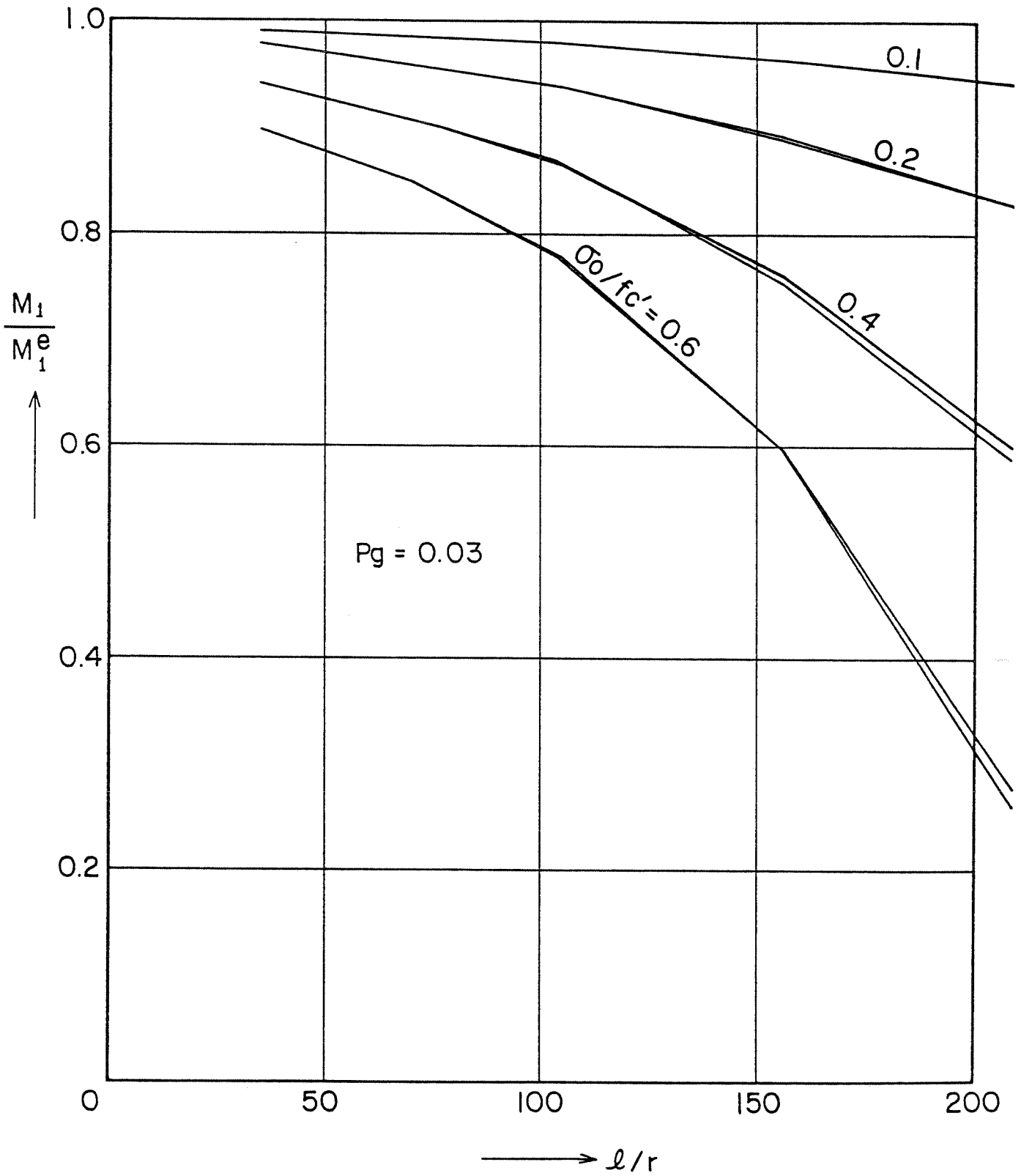Fig. 5-10   Moment Magnification Factor δbg for Gravity Load
( Pg = 0.015 )

Fig. 5-11   Moment   Magnification   Factor   δbg   for   Gravity   Load
(Pg = 0.03)

dependent on less flexural stiffness reduction near the column ends. The moment reduction, in other words the value of $\delta_{bg}$ less than one obtained for smaller l/r region is corresponding to this behavior as shown in the Fig.5-12a.

On the other hand, a secondary moment becomes larger dependent on deformation. As shown in Fig.5-12b, lateral deformation increase near the intermediate part of legs makes flexural moments of that part larger and end moments smaller. As a result, the value of $\delta_{bg}$ decreases dependent on the slenderness ratio, l/r and the axial load, $\sigma_0/f'_c$, . Subsequently more reduction is obtained for the large slenderness ratio region as a result.

A configuration factor, W/H does not provide any sigificant difference on the value.

(4) Moment Magnification Factor $\delta_{bh}$ for Combination of Lateral and Garvity Load

The moment magnification factor-slenderness ratio relationships are shown in Fig.5-13~5-16 for each gravity load case with rebar ratio of $p_g = 3\%$. Each solid line is design value, while round marks show analytical results including buckling failure case for reference. In general, both design and analytical values as expected become larger with increases of the slenderness ratio and that of the gravity load. In addition, design values are generally on the conservative side except in the particular region, small l/r.

Follows are some of noticeable phenomena observed in these figures.

●Influence of configuration factor

That the design value generally becomes smaller as the configuration factor of W/H increases for all gravity load cases, is easily realized by the fact that the variation at a factored axial load, $\phi P_u$ in eq.(5.10) becomes smaller with increase of leg width of W. This trend, however is not necessarily observed in the
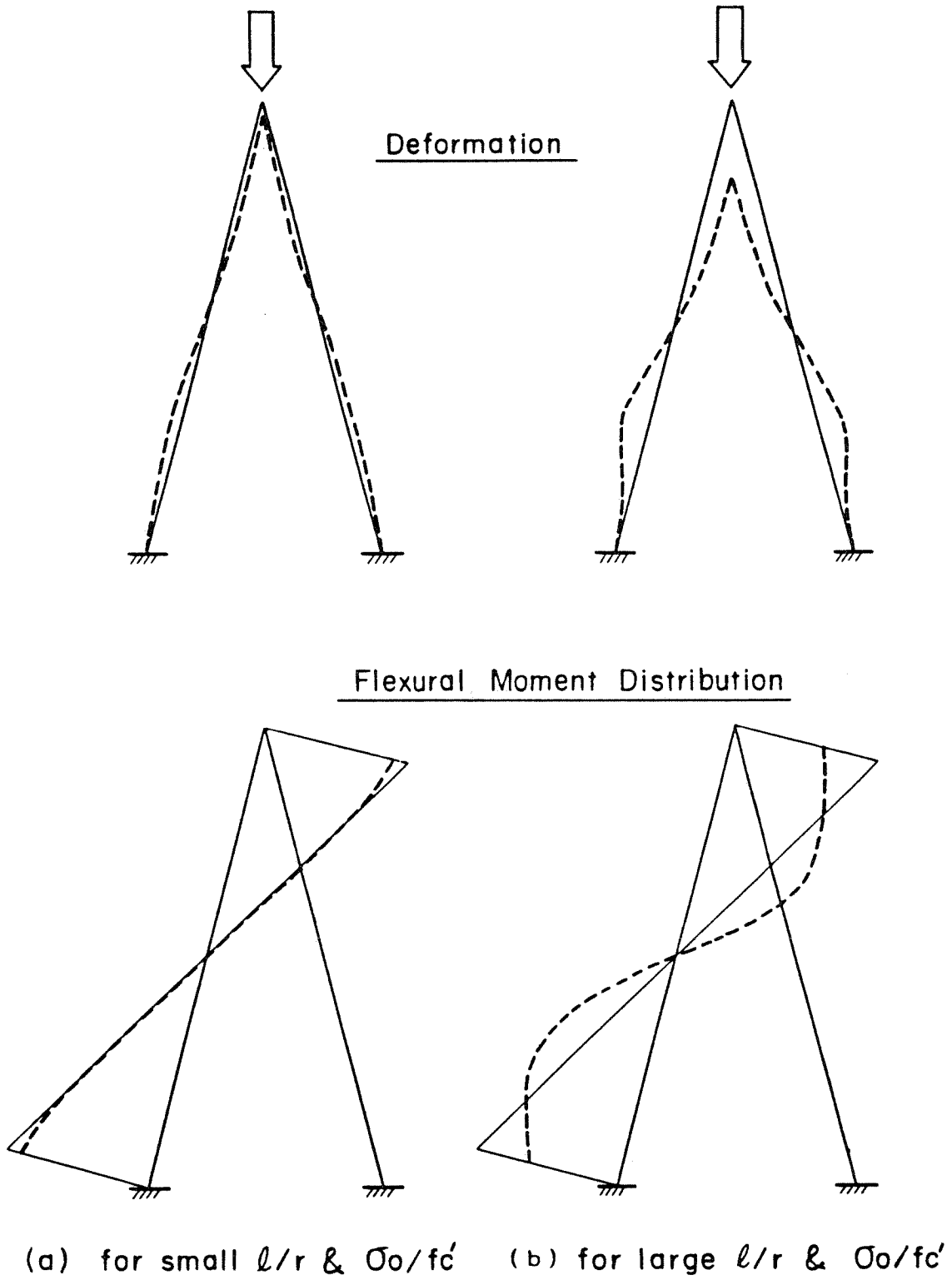
Deformation

Flexural Moment Distribution

(a) for small $\ell/r$ & $\sigma_o/f_c'$    (b) for large $\ell/r$ & $\sigma_o/f_c'$

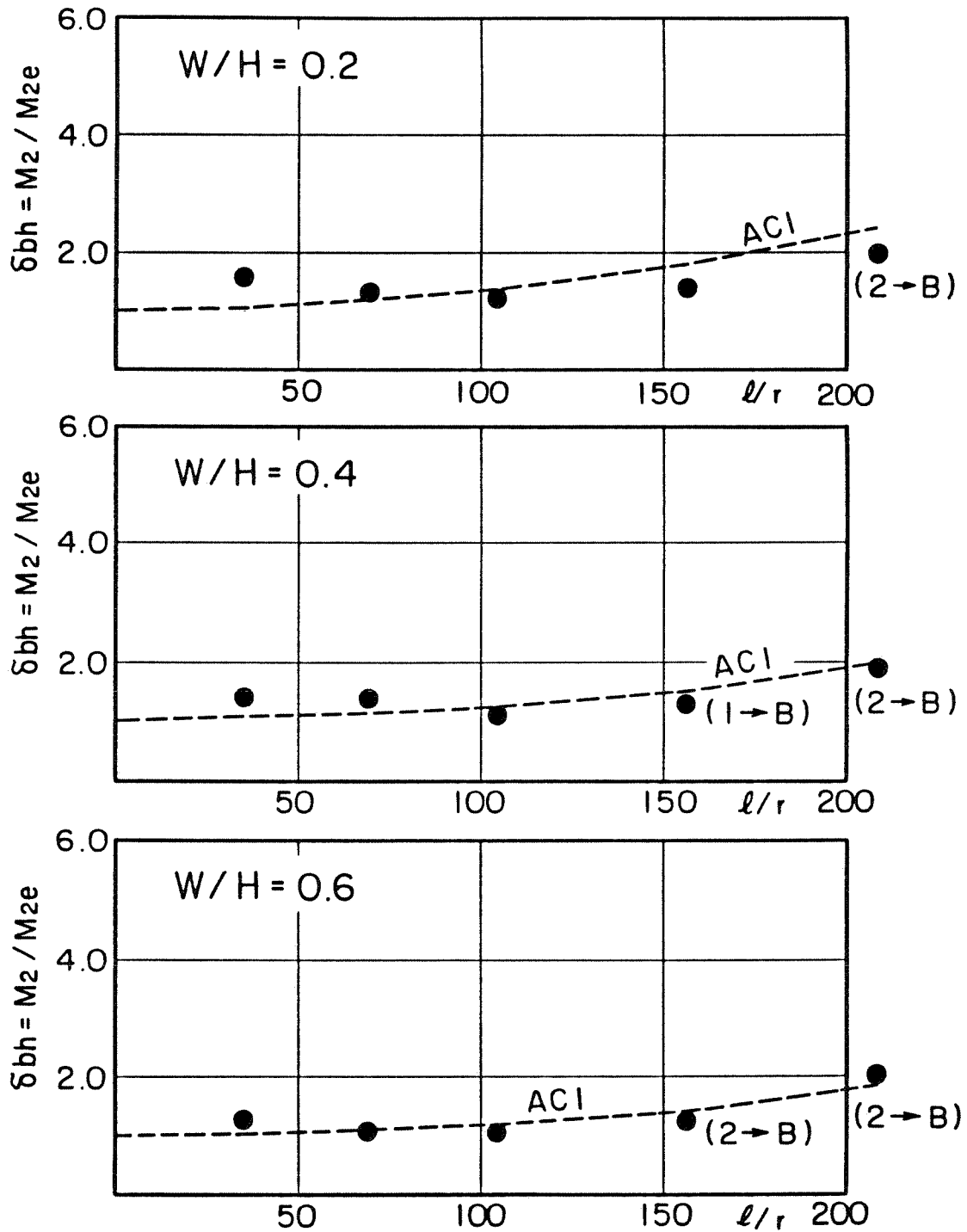Fig. 5-12 Flexural Behavior under Gravity Load

Fig. 5−13   Moment Magnification Factor $\delta_{bh}$ for S+H Load
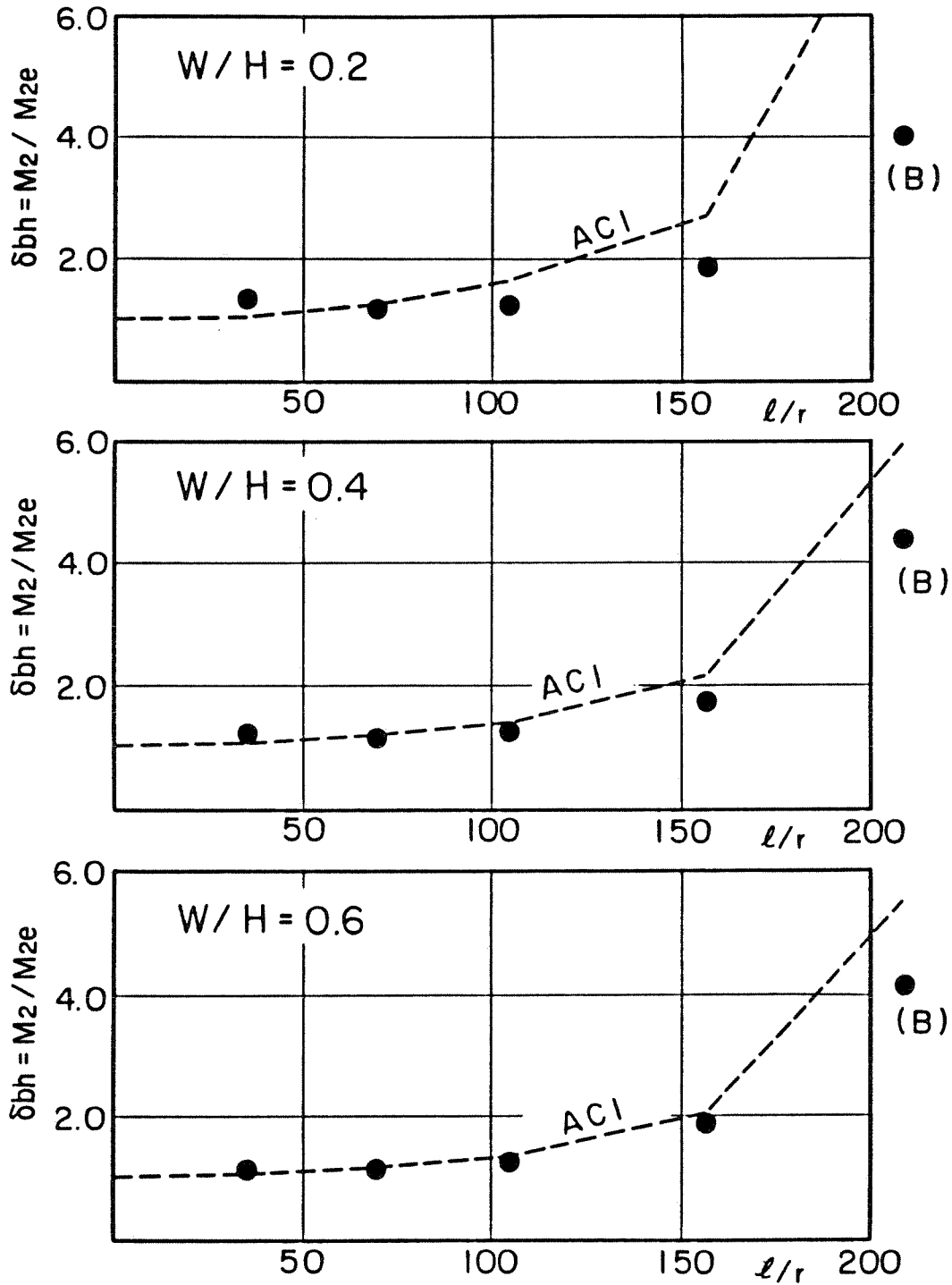($\sigma_o/f_c'=0.1$, $P_g=0.03$)

Fig.5 – 14 Moment Magnification Factor δbh for S + H Load
($\sigma_o / fc' = 0.2$, Pg = 0.03)

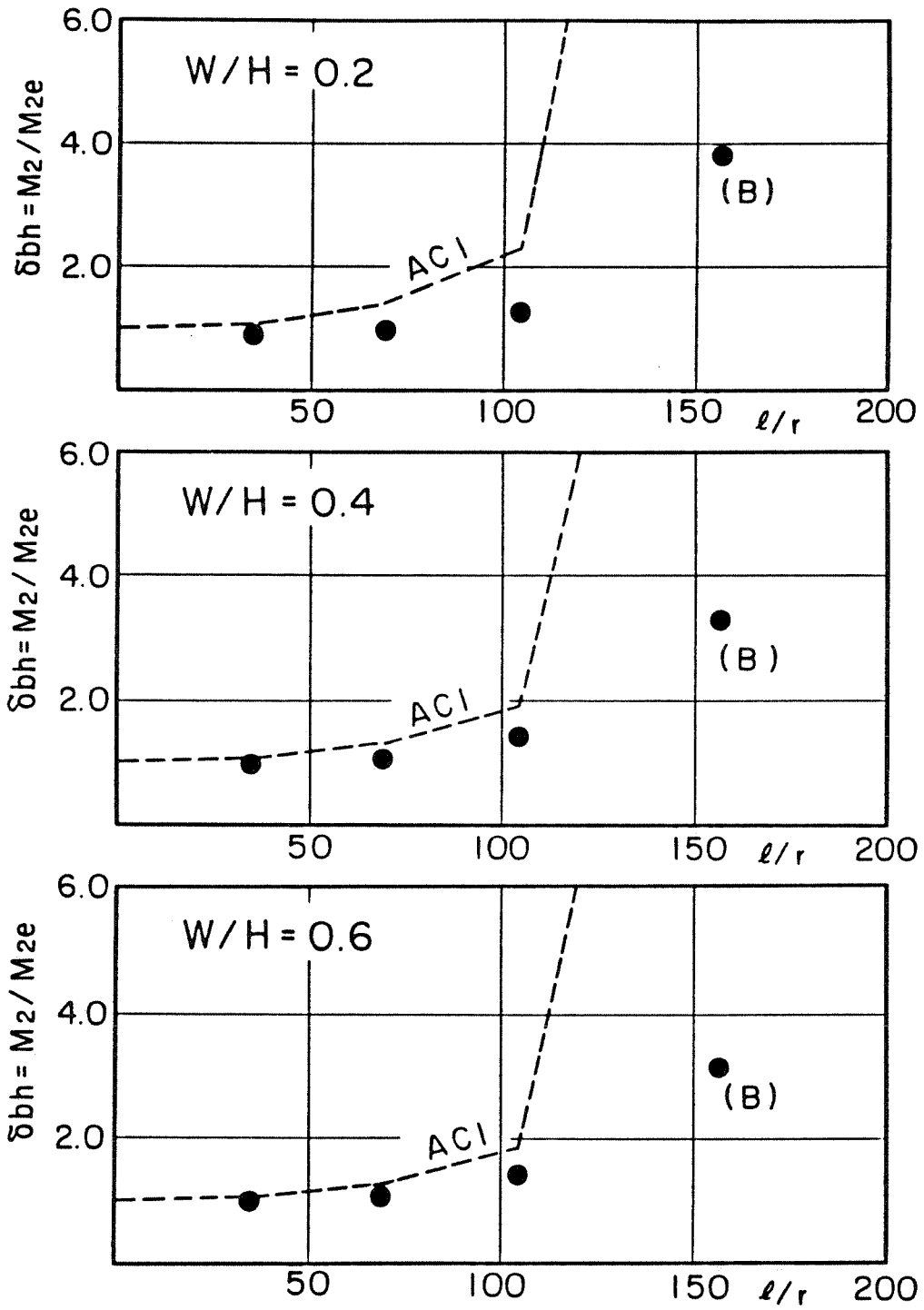Fig. 5-15   Moment Magnification Factor $\delta_{bh}$ for S+H Load
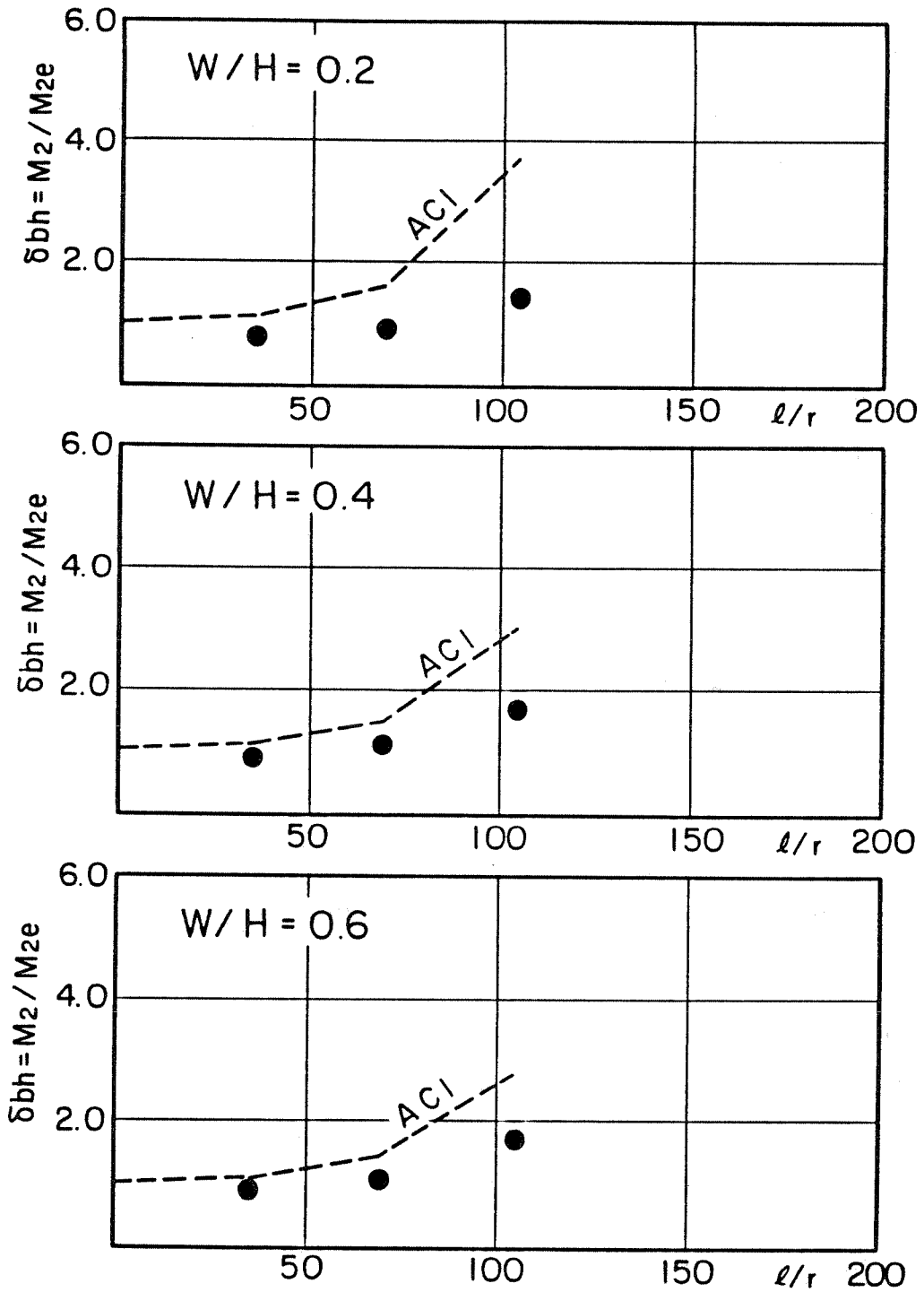($\sigma_o / fc' = 0.4$ , $Pg = 0.03$)

Fig. 5−16  Moment Magnification Factor δbh for S +H Load
($\sigma_o / fc' = 0.6$, Pg = 0.03)

analyses, i. e. the above mentioned is true in lower gravity load cases with $\sigma_0/f'_c \leqq$ 0.2, but not in higher cases.

The stress paths on the bottom leg section are shown in Fig.5-17 and 5-18 for W/H = 0.2 and 0.4 cases respectively with same gravity load of $\sigma_0/f'_c = 0.4$ (l/r = 35 and $p_g = 3\%$). The stress path of the Node-23 is slightly above the elastic line in the W/H = 0.2 case , but almost on that line in the W/H = 0.4 case. Slightly larger axial force variation is observed in the former case than in the latter, and this phenomenon appears simultaneously on the Node-1 stress path under incremental tensile axial force.

The contribution of each moment and of axial force at a bottom leg are represented through the lateral loading stage as shown in Fig.5-19, where $M_N$ is the resisting overturing moment due to axial force with neglection of lateral shear force, and $M_T$ the total internal moment as summation in equlilbrium with the external moment, $M_{ext}$ excluding gravity load participation. These moments are all expressed in non-dimensional form divided by an external moment, $M_{ext}$ and similarly is an external lateral load, $Q_{ext}$ divided by the ultimate load, $Q_u$. A slight difference between $M_T$ and $M_{ext}$ is likely caused by no consideration of the lateral shear force at the bottom section and of the secondary external moment due to a gravity load.

The main concern in this discussion is the difference of a resisting overturning moment, $M_N$ between W/H = 0.2 and 0.4 . The former case (solid line) presents a slightly larger increase around the ultimate region than the latter one (dashed line). This implys that the contribution of a resisting overturning moment becomes larger and on the contrary, that of local end moment smaller in the former case. This can be the main reason why a smaller moment magnification factor of analysis is obtained in the smaller configuration factor case.
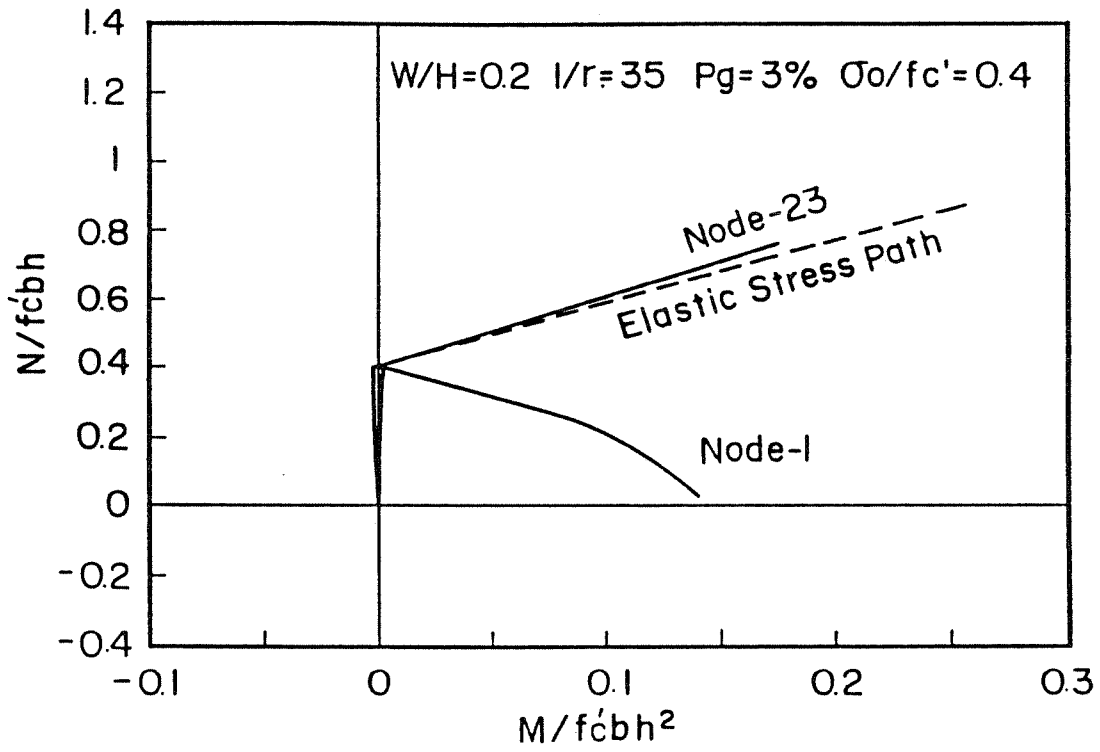
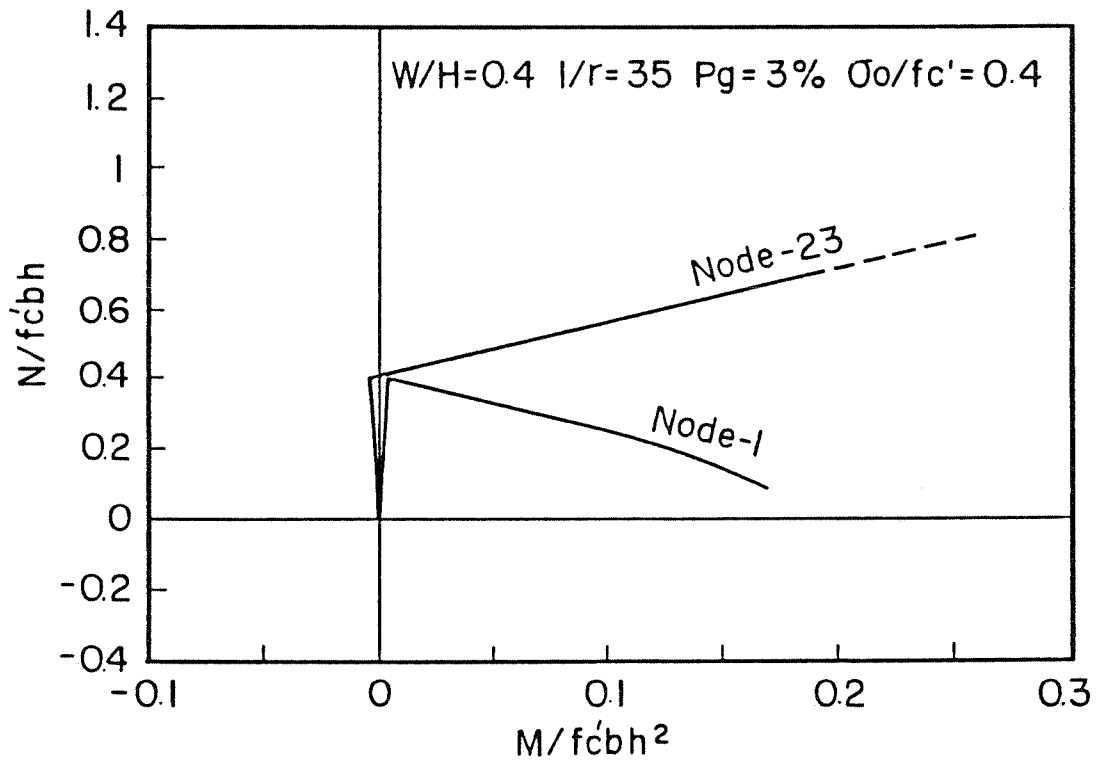Fig. 5-17   M-N   Relationship



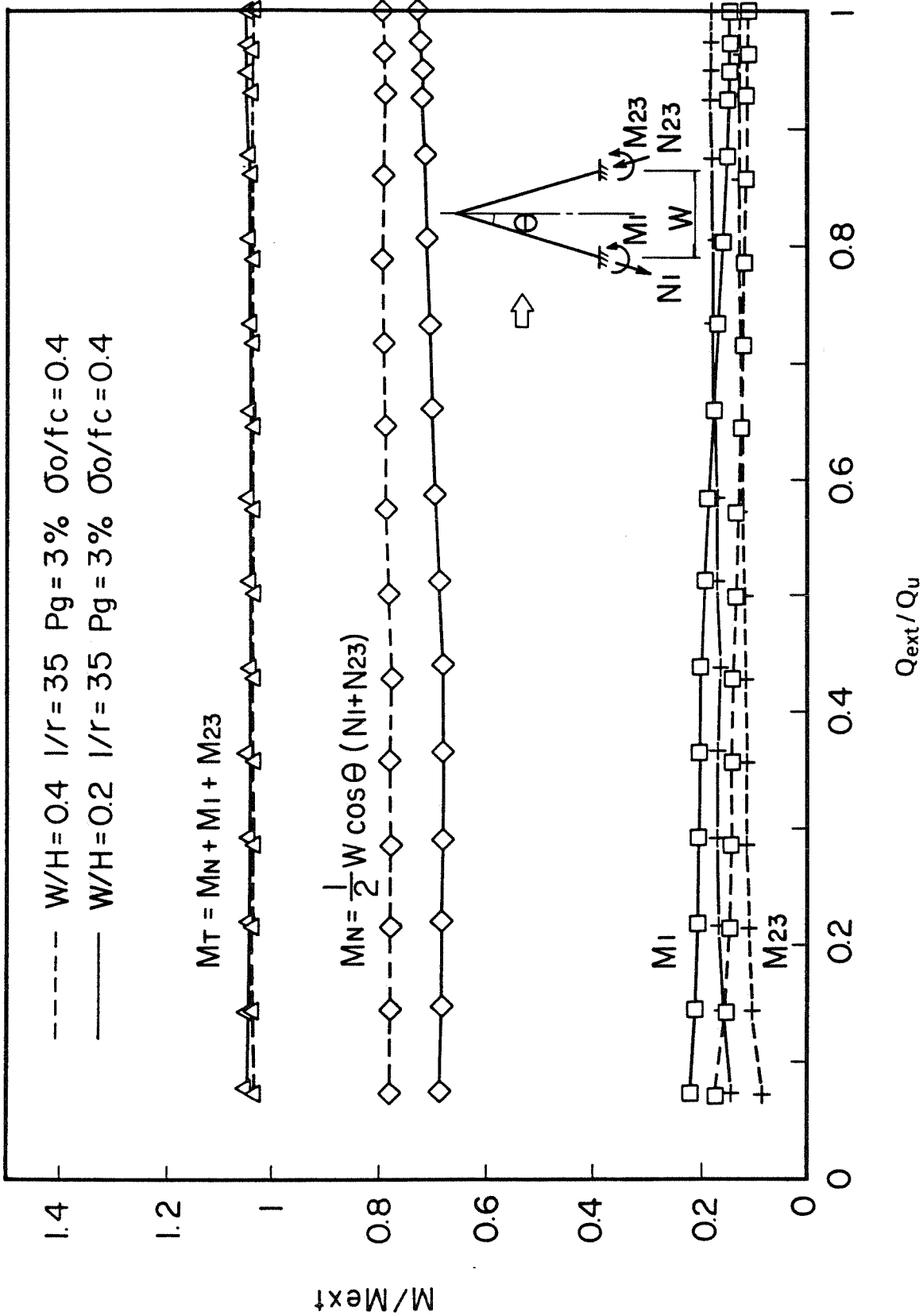Fig. 5-18   M-N   Relationship

Fig. 5-19   REDISTRIBUTION of RESISTING MOMENT

●Moment redistribution effect in small slenderness ratio range

It was previously described that design value generally provides a conservative value. However this is not necessarily true in the relatively small slenderness ratio range, especially $l/r \leq 56$, in which an analytical value larger than the design value is obtained. The main reason is that the flexural moment at Node-23 is enlarged for moment redistribution accompanied by axial force variation.

The stress paths and contribution of moment are shown for two different axial load cases of $\sigma_0/f'_c = 0.4$ and 0.2 (w/H = 0.2, $l/r = 36$ and $p_g = 3\%$) in the Fig.5-20~5-21. As shown in Fig.5-20, the stress vector at Node-1 drops a bit sharply after cracks and moves downwards along yield surface. Such a weakened moment of that section must be compensated by a increasing moment at the counterpart, Node-23. The Fig.5-21 shows a sharper increase for $\sigma_0/f'_c = 0.2$ case than the former one for $\sigma_0/f'_c = 0.4$.

An analytical moment larger than the design value is likely encouraged with the decrease of $\sigma_0/f'c$ and that of W/H. Therefore, in case of a structure such as the present bridge tower in which a frame action is more expected, influence of moment redistribution must be considered rather than the secondary moment effect especially in the small slenderness ratio region less than 56 with gravity load, $\sigma_0/f'_c$ less than 0.2.


●High gravity load effct

Analytical values of $\delta_{bh}$ less than one are presented for higher gravity load cases with small slenderness ratios as shown in Fig.5-15 and 5-16 . With increase of gravity load, the bottom section (Node-1) bears more flexural moment under high axial force. In addition, axial force contribution on the resisting overturning moment becomes greater. The flexural moment at Node-23 as a result is reduced less than an elastic moment as shown in the Fig.5-20.
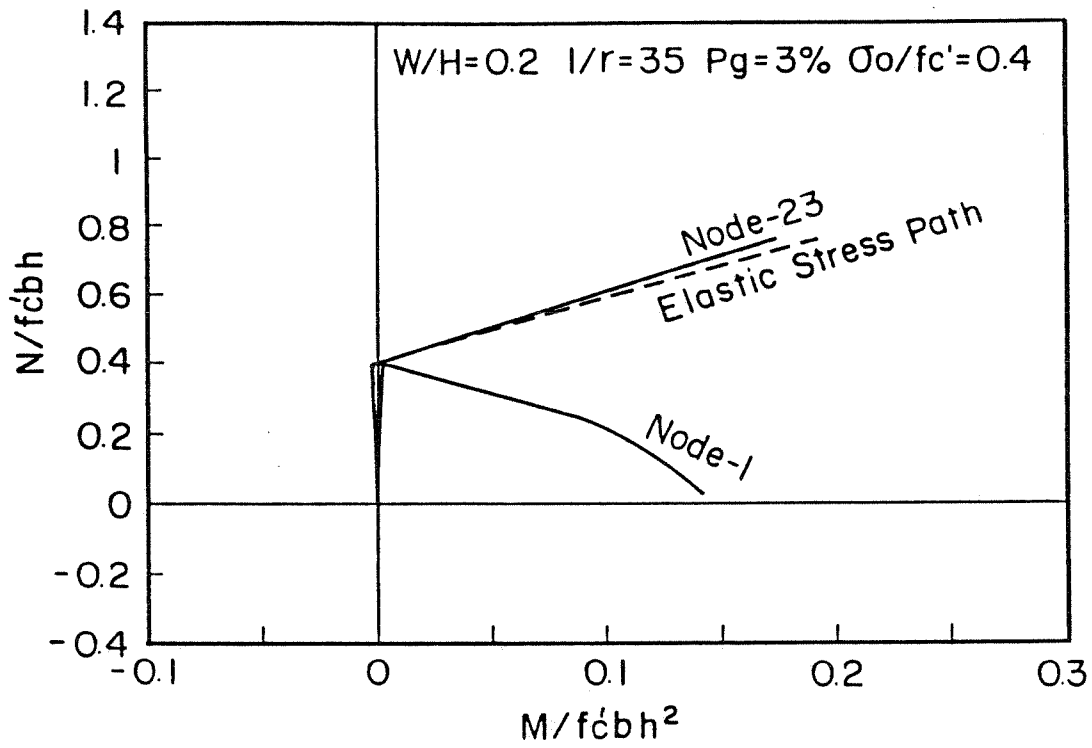
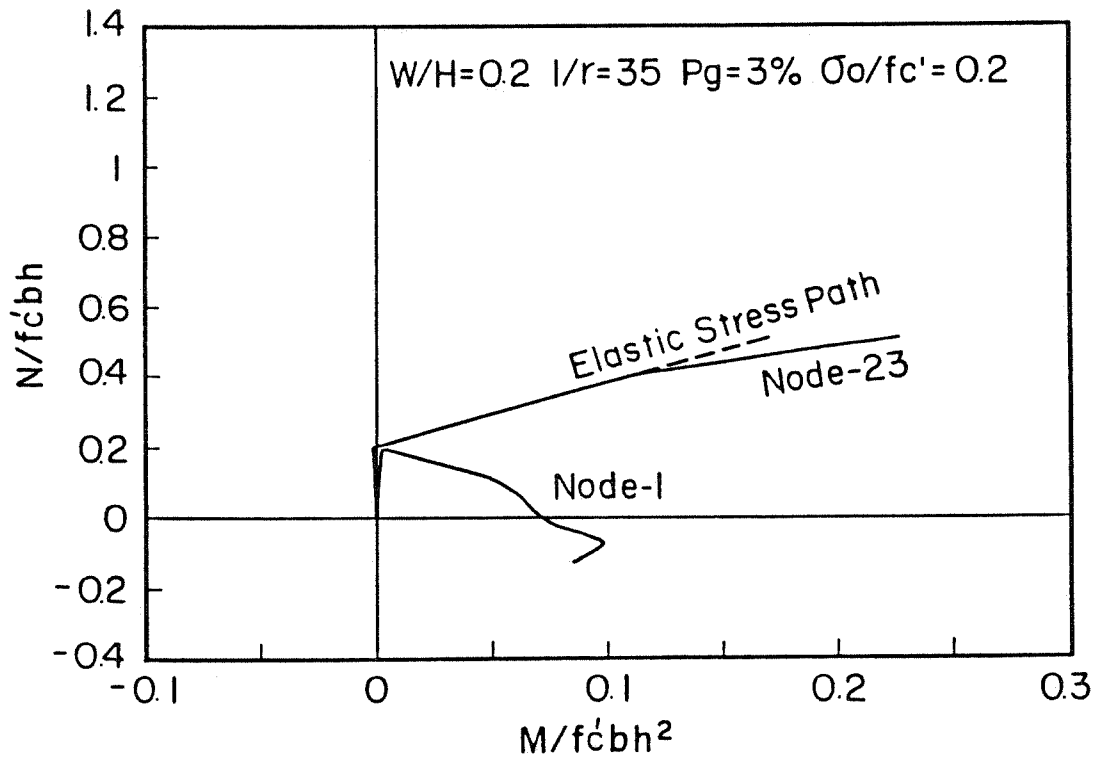Fig. 5-20   M-N   Relationship



Fig. 5-21   M-N   Relationship

● Buckling Failure

Fig.5-22 represents several stress paths due to buckling failure. The type-A corresponds to a intermediate severe case in this failure such as $\sigma_0/f'_c \leq 0.2$ and $l/r = 208$ or $\sigma_0/f'_c = 0.4$ and $l/r = 156$ case. As shown in the figure, the actual ultimate stress cannot be predicted since the drastic failure appears prior to reaching the failure surface.

The moment magnification factor is temporarily evaluated based on stresses in the stable condition directly prior to failure. Therefore, the values in Fig.5-13 5-16 corresponding to this failure case are shown for refernce.

The type-B generally represents a fairly severe case such as $\sigma_0/f'_c = 0.4$ and $l/r = 208$, or $\sigma_0/f'_c = 0.6$ and $l/r = 156$ case. The corresponding values are excluded in Fig.5-13 5-16 since the negative value obtained for $\delta_{bh}$ in addition to no possibility of accurate stress evaluation in ultimate. Moment contribution by each component is presented in the Fig.5-23 as well as previously shown. Negative resisting overturning moment unexpectedly appears with the opposite action of axial force in each bottom leg.

The type-C represents the most severe case in geometric nonlinearity with $\sigma_0/f'_c = 0.6$ and $l/r = 208$. The corresponding values are also removed in Fig.5-13~5-16 because of the negative value obtained as in the former case. As shown in the Fig.5-8 the flexural moment at Node-1 moves from the negative to the positive side under lateral load increasing, while that at Node-23 remains increasing monotonically on the negative side and is strongly affected by a negative external overturning moment due to gravity load. The final failure of this type presents B' or EB' as previously described in the section 5.4.
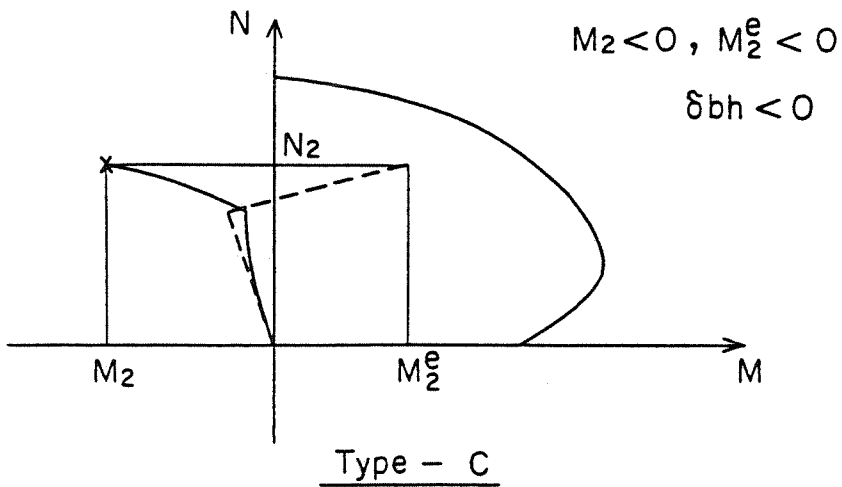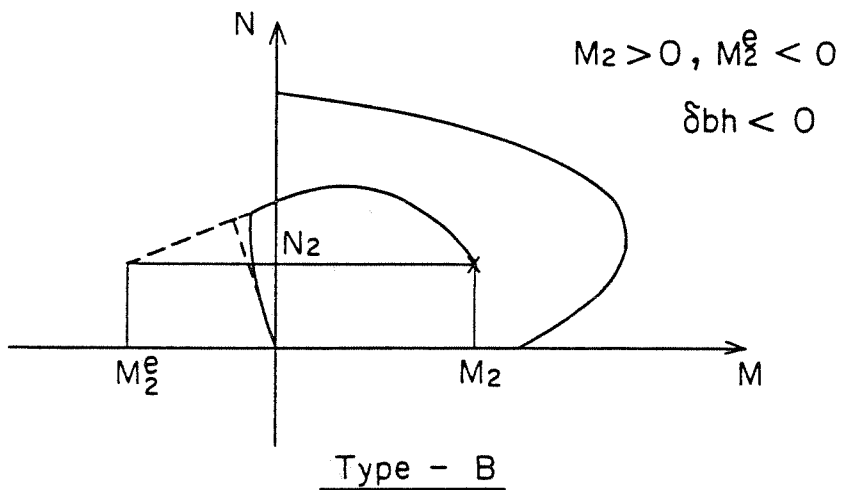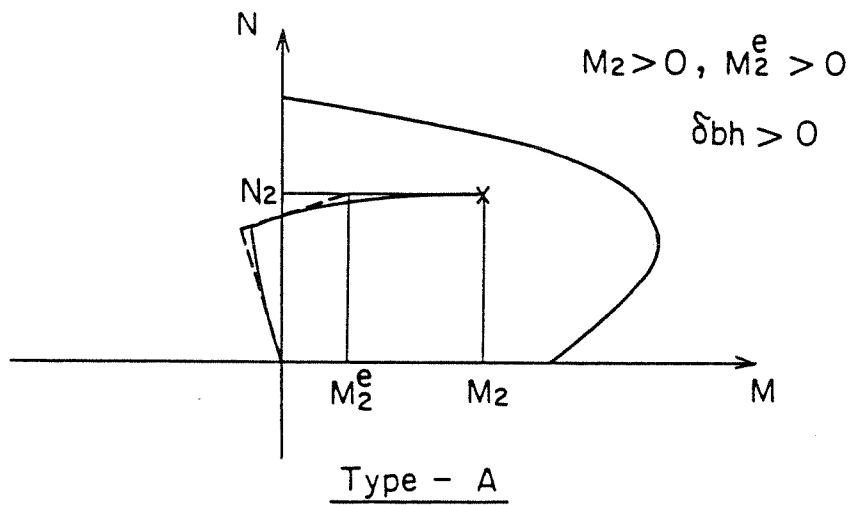
Fig.5-22  Typical Stress Pathes of Node-23 for
A Model with Buckling Failure

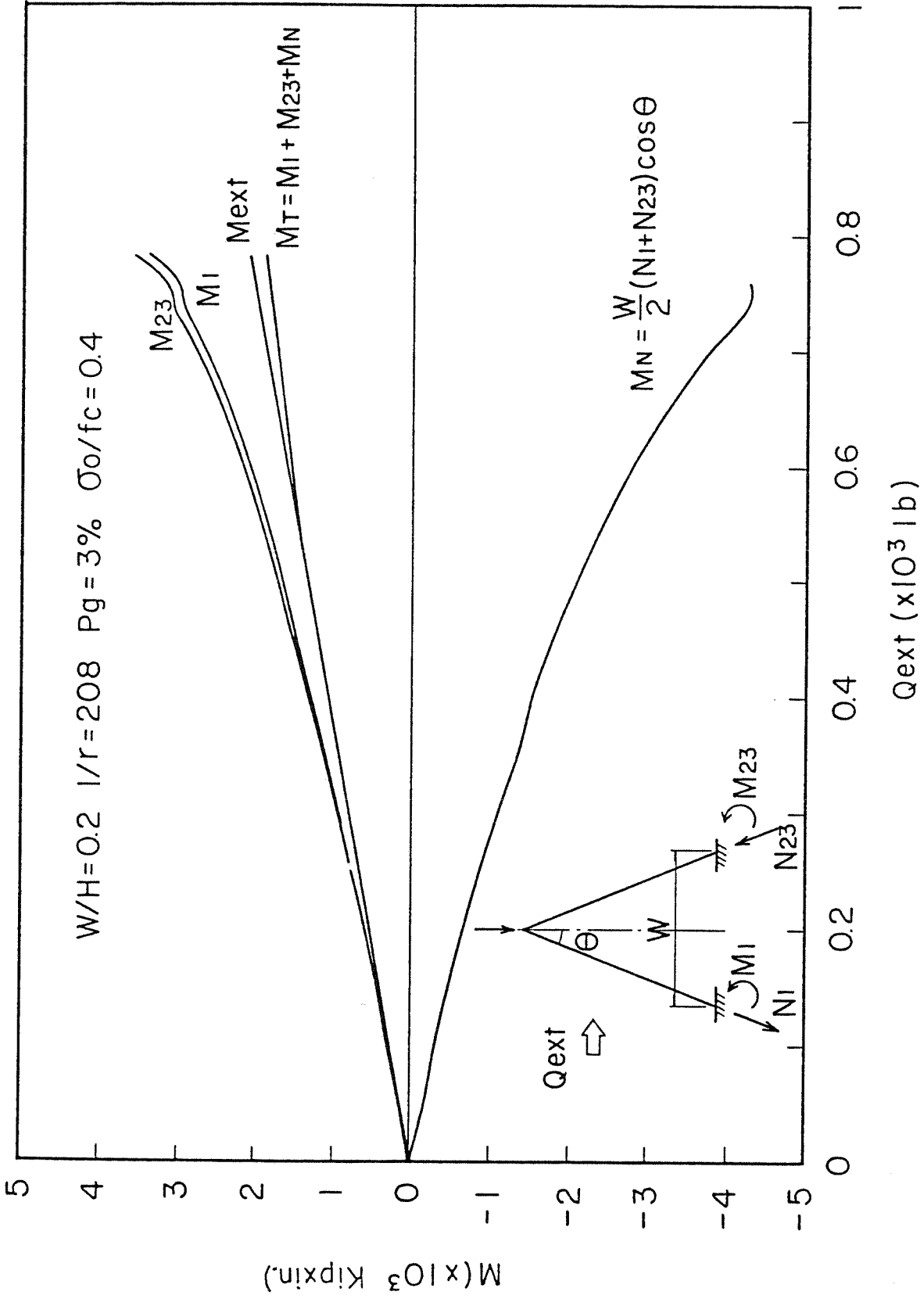Fig. 5-23 M-Qb RELATIONSHIP

## 6. Nonlinear Behavior against Monotonic Lateral Load Combined with Sustained Gravity Load

### 6.1 Analytical Parameters

It was described in the previous chapter that a loading capacity is increased by a larger resistance against overturnig moment with increase of leg width. No significant differences of substantial behavior except loading capacity, however, were observed between different configuration factors of W/H. Therefore, parametric analyses will be carried out on the particular cases of W/H $= 0.4$ with several parameters of $p_g$, $\sigma_0/f'_c$ and l/r as shown in Table6-1. The influence of creep deformation due to gravity load in the inelastic range should be particularly noted. This influence could be of importance as the axial load and slenderness ratio become larger. The slenderness ratio range up to l/r $= 156$ as a parameter is considered practically sufficient.

### 6.2 Behavior during Sustained Gravity Load

The Fig.6-1~6-6 show the bottom leg moment under gravity load followed by its time dependent variation, where a nondimensional form is provided for the gravity load coordinate divided by its instant target value. The greater nonlinear behavior obtained under instant higher gravity load is considered to be caused by the moment reduction due to a concrete plasticity at the bottom of the legs. This moment, for the smaller slenderness ratio, also indicates an ascending variation with time since the flexural moment is enlarged because the structure is entirely shortended under gravity load. This moment, however declines as the gravity load of $\sigma_0/f'_c$ and slenderness ratio of l/r become larger respectively. The reason is that the stiffness of the bottom leg is relatively reduced by creep deformation.

The Fig.6-7 indicates column moment distributions for slenderness ratios of l/r $= 35$ and 156. The former case shows a uniform increase of moment, while the
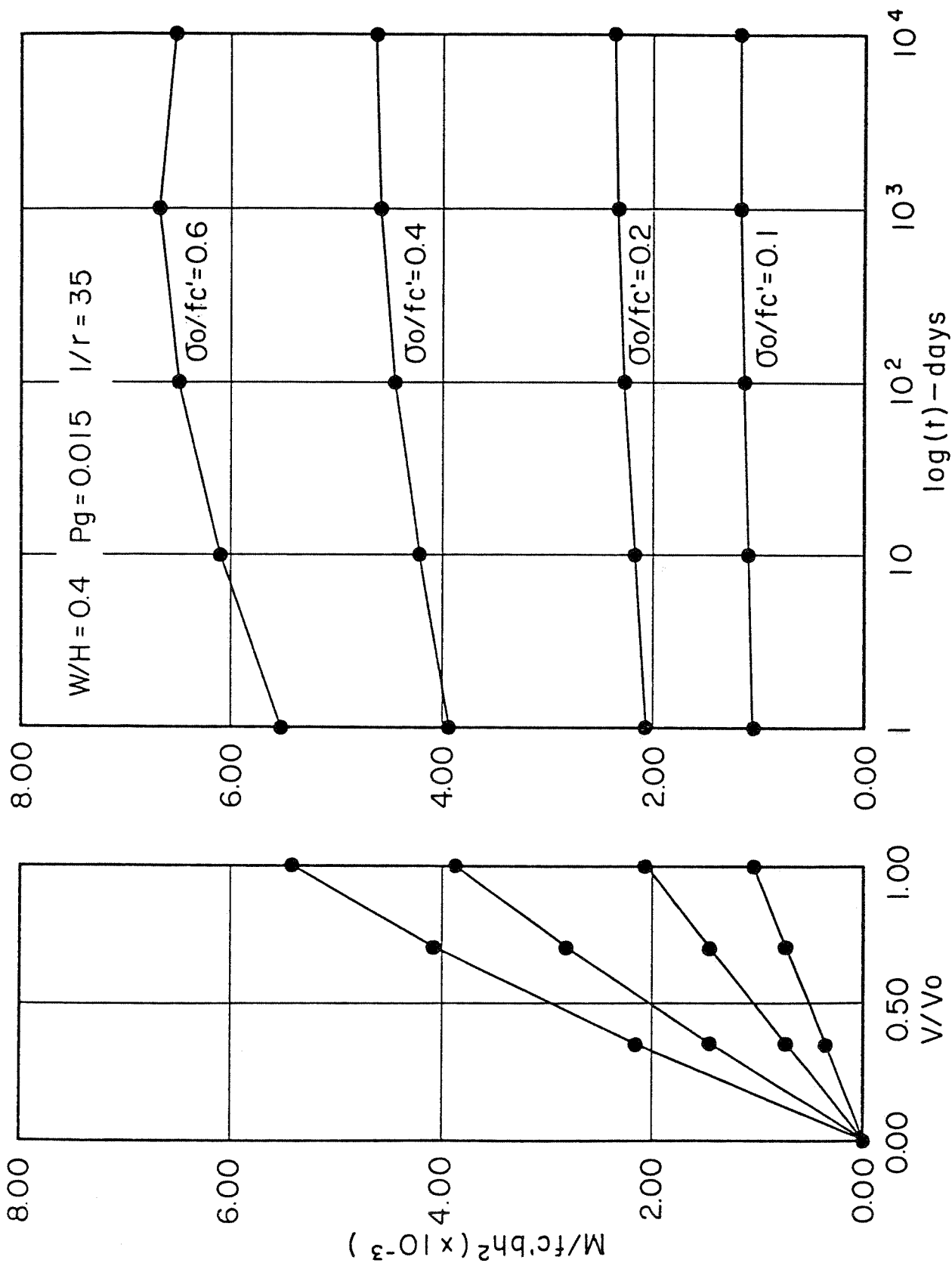
Table 6-1  Ultimate States of A-Shaped Tower (L+H Load)

| $P_g$ | $\dfrac{\sigma_0}{f'_c}$ | $\dfrac{W}{H}$ | $l/h$ | $l/r$ | Crack | Elem.1 TRY | 7 TRY | 11 TRY | 17 TRY | Elem.22 TRY | Elem.22 CRY | Elem.22 CC | Fail. Mode Rank | $\dfrac{\tau_u}{f'_c}$ | $\dfrac{\tau_u}{\tau^0_u}$ *1) | $\dfrac{\gamma_{max}}{\gamma_y}$ | $\dfrac{\gamma_{max}}{\gamma^0_{max}}$ *2) | $\delta_{bh}=M_2/M_2^e$ |
|---|---|---|---|---|---|---|---|---|---|---|---|---|---|---|---|---|---|---|
| 1.5 % | 0.1 | 0.4 | 10 | 35 | ○ | ○ | ○ | ○ | | ○ | ○ | | 1 | 0.0642 | 0.986 | 3.294 | 0.793 | 1.525 |
| | | | 30 | 104 | ○ | ○ | ○ | | | ○ | | | 1 | 0.0253 | 1.000 | 2.086 | 1.002 | 1.205 |
| | | | 45 | 156 | ○ | ○ | ○ | | ○ | ○ | | | 1 | 0.0124 | 0.954 | 1.484 | 1.032 | 1.673 |
| | 0.2 | | 10 | 35 | ○ | ○ | | | | | | ○ | 2 | 0.0817 | 0.980 | 1.688 | 0.888 | 1.244 |
| | | | 30 | 104 | ○ | ○ | | | | ○ | ○ | | 2 | 0.0281 | 0.982 | 1.277 | 0.878 | 1.411 |
| | | | 45 | 156 | ○ | | | | | | ○ | | B | 0.0105 | 0.921 | | | |
| | 0.4 | | 10 | 35 | ○ | | | | | ○ | ○ | ○ | 3 | 0.0901 | 0.956 | | | 0.960 |
| | | | 30 | 104 | ○ | | | | | ○ | ○ | | 3 | 0.0251 | 0.893 | | | 1.678 |
| | | | 45 | 156 | ○ | | | | | ○ | ○ | | 3→B | 0.0071 | 0.941 | | | |
| | 0.6 | | 10 | 35 | ○ | | | | | ○ | ○ | ○ | 3 | 0.0800 | 0.980 | | | 0.796 |
| | | | 30 | 104 | ○ | | | | | ○ | ○ | | 3 | 0.0170 | 0.829 | | | 2.485 |
| | | | 45 | 156 | | | | | | | | | EB | 0.0006 | 3.826 | | | |
| 3.0 % | 0.1 | | 10 | 35 | ○ | ○ | ○ | ○ | | ○ | | | 1 | 0.1001 | 0.993 | 2.220 | 0.897 | 1.404 |
| | | | 30 | 104 | ○ | ○ | ○ | | ○ | ○ | | | 1 | 0.0426 | 0.988 | 1.762 | 0.795 | 1.170 |
| | | | 45 | 156 | ○ | ○ | | | | | | | 2 | 0.0234 | 0.975 | 1.333 | 0.902 | 1.327 |
| | 0.2 | | 10 | 35 | ○ | ○ | | | | ○ | ○ | | 2 | 0.1101 | 1.000 | 1.536 | 0.974 | 1.221 |
| | | | 30 | 104 | ○ | ○ | | | | | | | 2 | 0.0411 | 0.976 | 1.269 | 0.971 | 1.301 |
| | | | 45 | 156 | ○ | | | | | | | | 2 | 0.0195 | 0.963 | | | 2.076 |
| | 0.4 | | 10 | 35 | ○ | | | | | ○ | ○ | | 3 | 0.1109 | 0.950 | | | 1.004 |
| | | | 30 | 104 | ○ | | | | | ○ | ○ | | 3 | 0.0366 | 0.913 | | | 1.532 |
| | | | 45 | 156 | | | | | | | ○ | | B | 0.0102 | 0.850 | | | |
| | 0.6 | | 10 | 35 | ○ | | | | | ○ | ○ | ○ | 3 | 0.0984 | 0.952 | | | 0.869 |
| | | | 30 | 104 | ○ | | | | | ○ | ○ | | 3 | 0.0256 | 0.823 | | | 1.932 |
| | | | 45 | 156 | | | | | | ○ | ○ | | 3→B | 0.0048 | 1.123 | | | |

TRY : Tensile Yielding of Rebar    CRY : Compressive Yielding of Rebar    CC : Concrete Crush

*1) Rate of ultimate shear Stress under +H.Load to that under S+H.Load

*2) Rate of ductility factor under L+H Load to that under S+H.Load

Fig. 6-1 Flexural Moment - Gravity Load & Time Relationship (Node-23)

Fig. 6-2  Flexural  Moment - Gravity  Load  &  Time  Relationship ( Node - 23 )
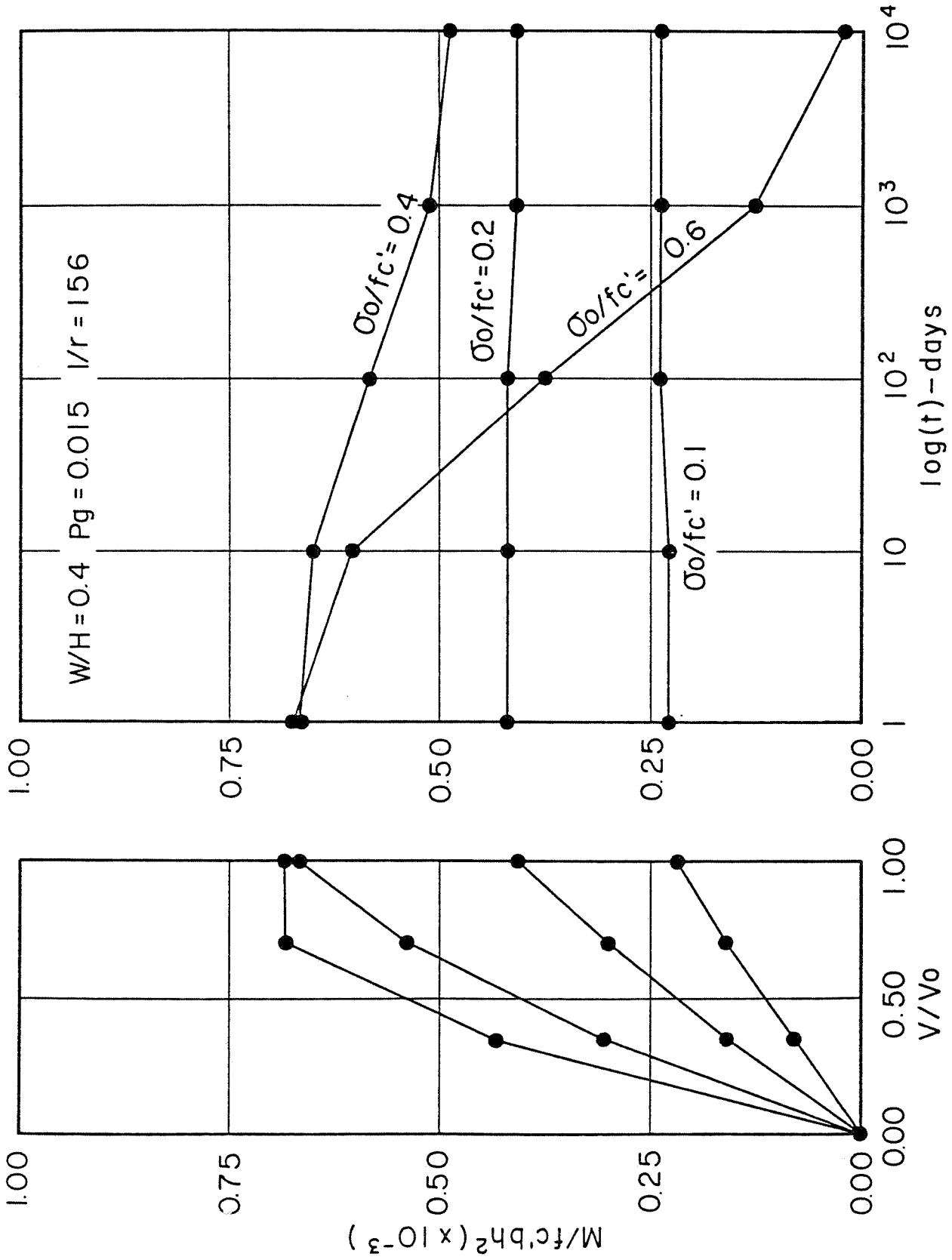
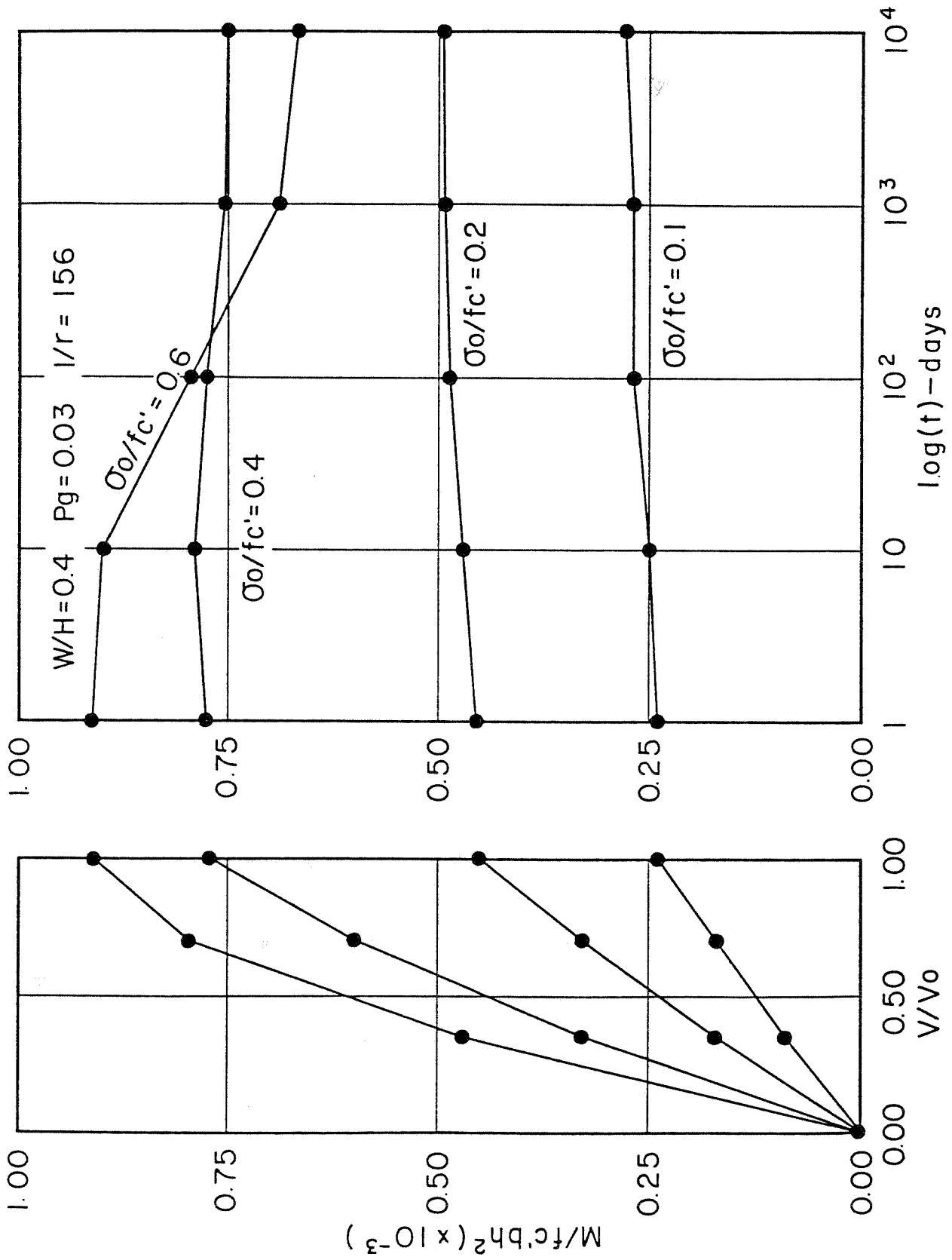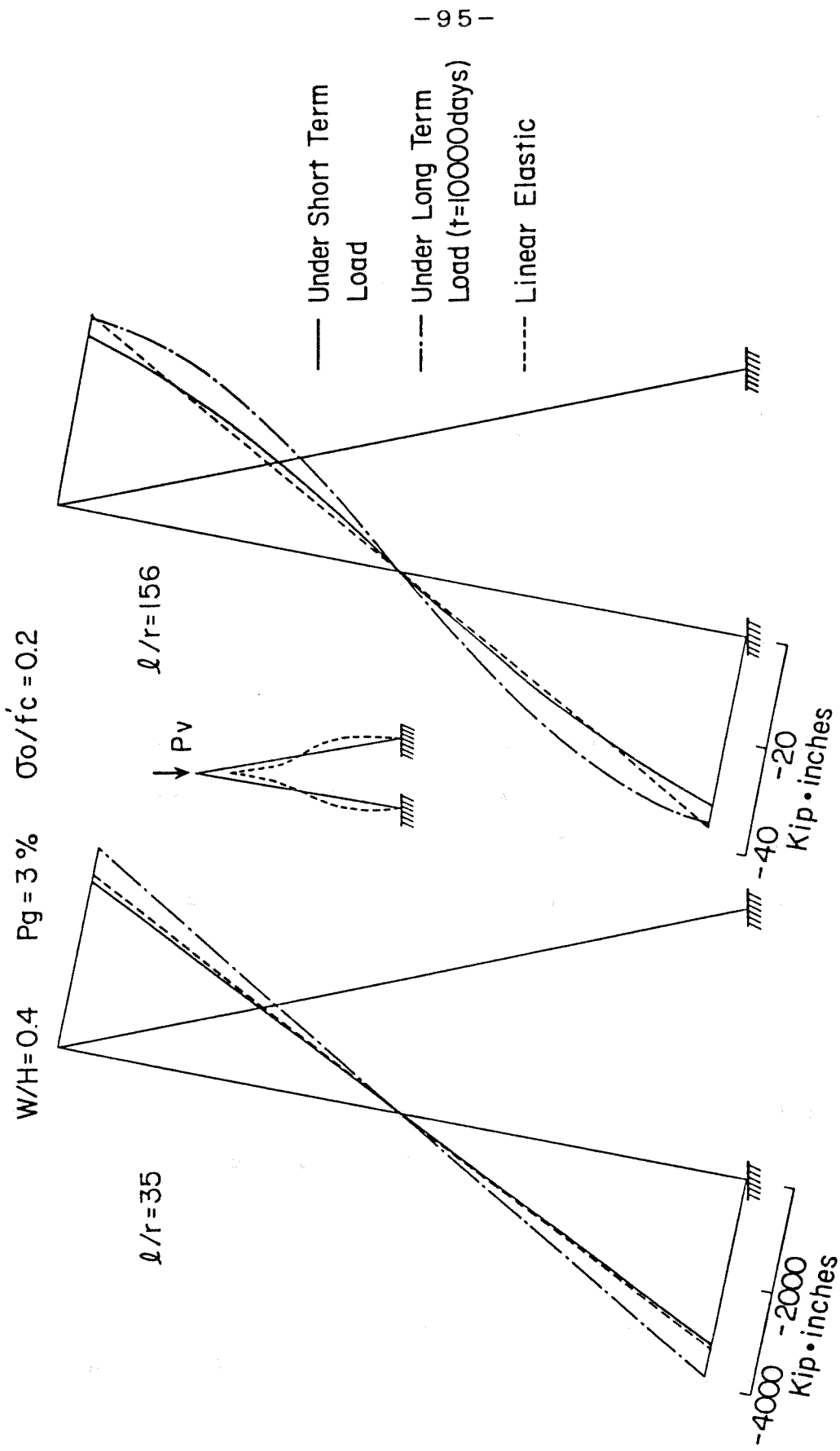Fig. 6-3 Flexural Moment — Gravity Load & Time Relationship (Node-23)
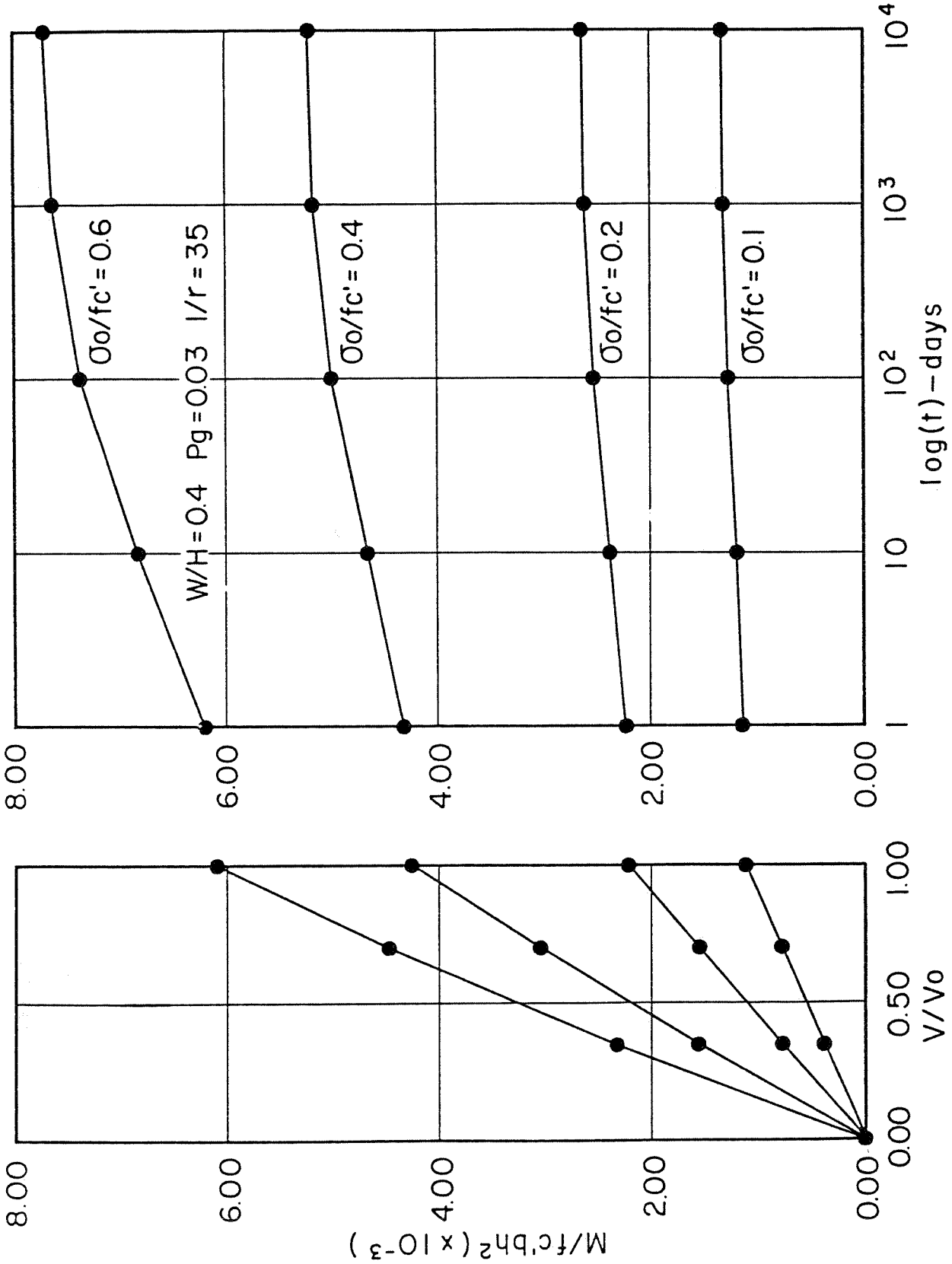
Fig.6-4  Flexural Moment –Gravity Load & Time Relationship (Node – 23)
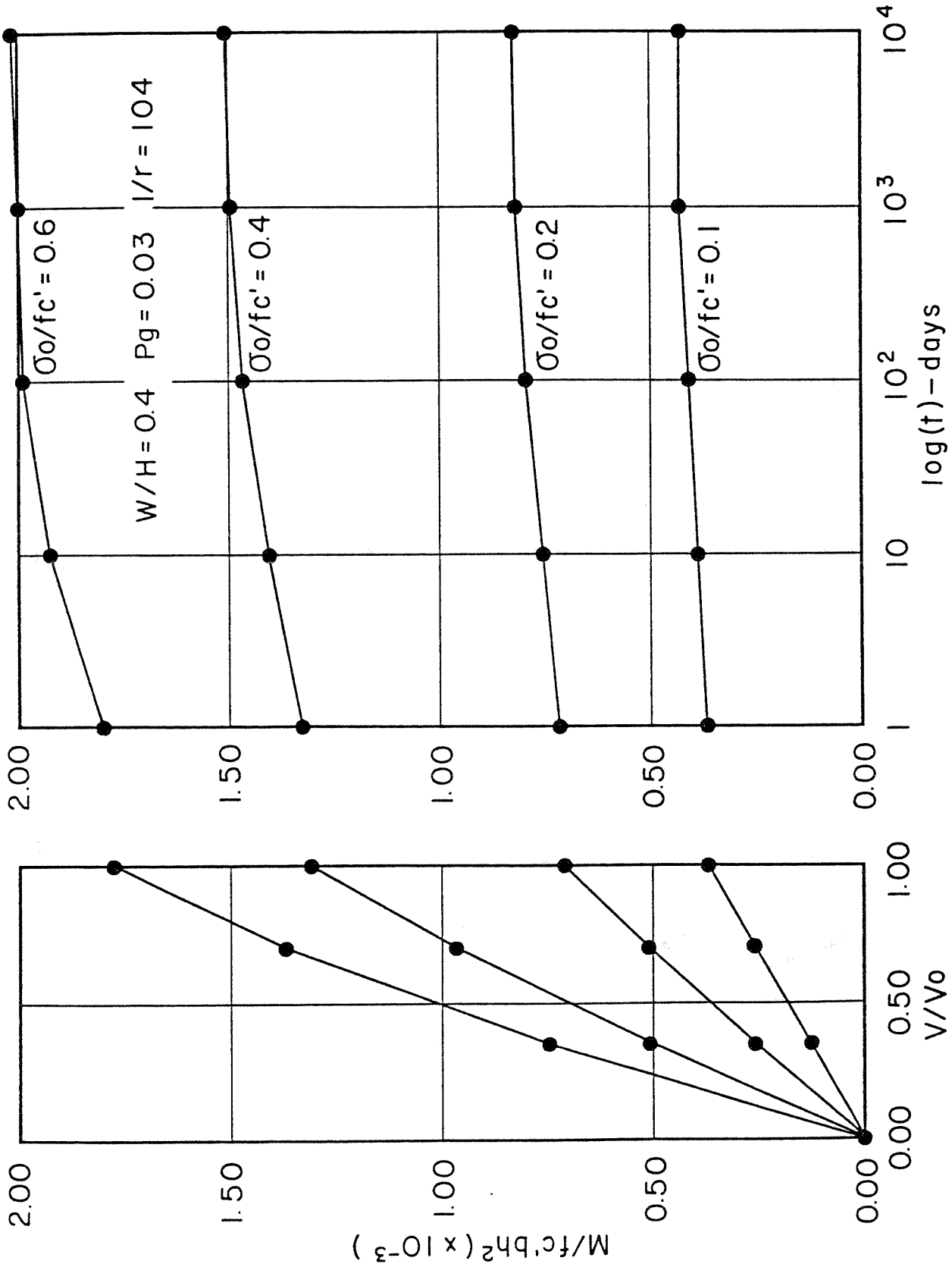
Fig. 6-5  Flexural Moment-Gravity Load & Time Relationship (Node-23)

Fig. 6-6  Flexural  Moment - Gravity  Load  &  Time  Relationship  (Node - 23 )

Fig. 6-7  Flexural  Moment  Distribution  of  A-Shaped  Tower  under  Gravity  Load

latter shows more moment increase at the mid-part and less at the bottom due to a larger secondary moment effect and a change of flexural stiffness along the leg.

The moment magnification factors for gravity load shown in Fig.6-8~6-9 indicate that these factors are generally encouraged by creep deformation, but not in the case of larger $\sigma_0/f'_c$ and l/r values in comparison with short term gravity load cases as explained in the Fig.6-7. However it should be noted that these moments due to gravity load are far smaller than those due to lateral load.

## 6.3  Creep Effect on Deformation Characteristics during Lateral Load

The load-lateral dispalcement of the mid-height (Node-7) and the load-concrete mechanical strain of the bottom section (Elem-22) are shown in Fig.6-10~6-13 for small axial load cases. As a result of stress relaxation in the concrete and a corresponding compressive stress increase in the rebar due to creep deformation during gravity load, a crack occurence and a stiffness reduction are encouraged in the early stage of lateral load applied for the L + H case in comparison with that for the S + H case. However, no significant difference is observed of both loading capacity and maximum displacement as well as concrete stress behavior of the bottom section.

Similar relations are shown in Fig.6-14~6-19 for the largest axial load case $\sigma_0/f'_c = 0.6$ with l/r = 108. As a concrete creep deformation becomes larger under gravity load, concrete is unloaded back to elastic stress state as shown in Fig.6-17~6-18, while a considerable amount of compressive stress is imposed in the rebar to compensate for this (Fig.6-19). As the result, initial stiffness in the load-displacement relation becomes fairly larger followed by a considerable stiffness reduction due to concrete cracks and lower loading capacity due to compressive yielding of the rebar than in the case of S + H (Fig.6-14 and 6-16).

## 6.4  Creep Effect on Moment Behavior during Lateral Load

The load-axial force and the load-moment relations at the bottom leg
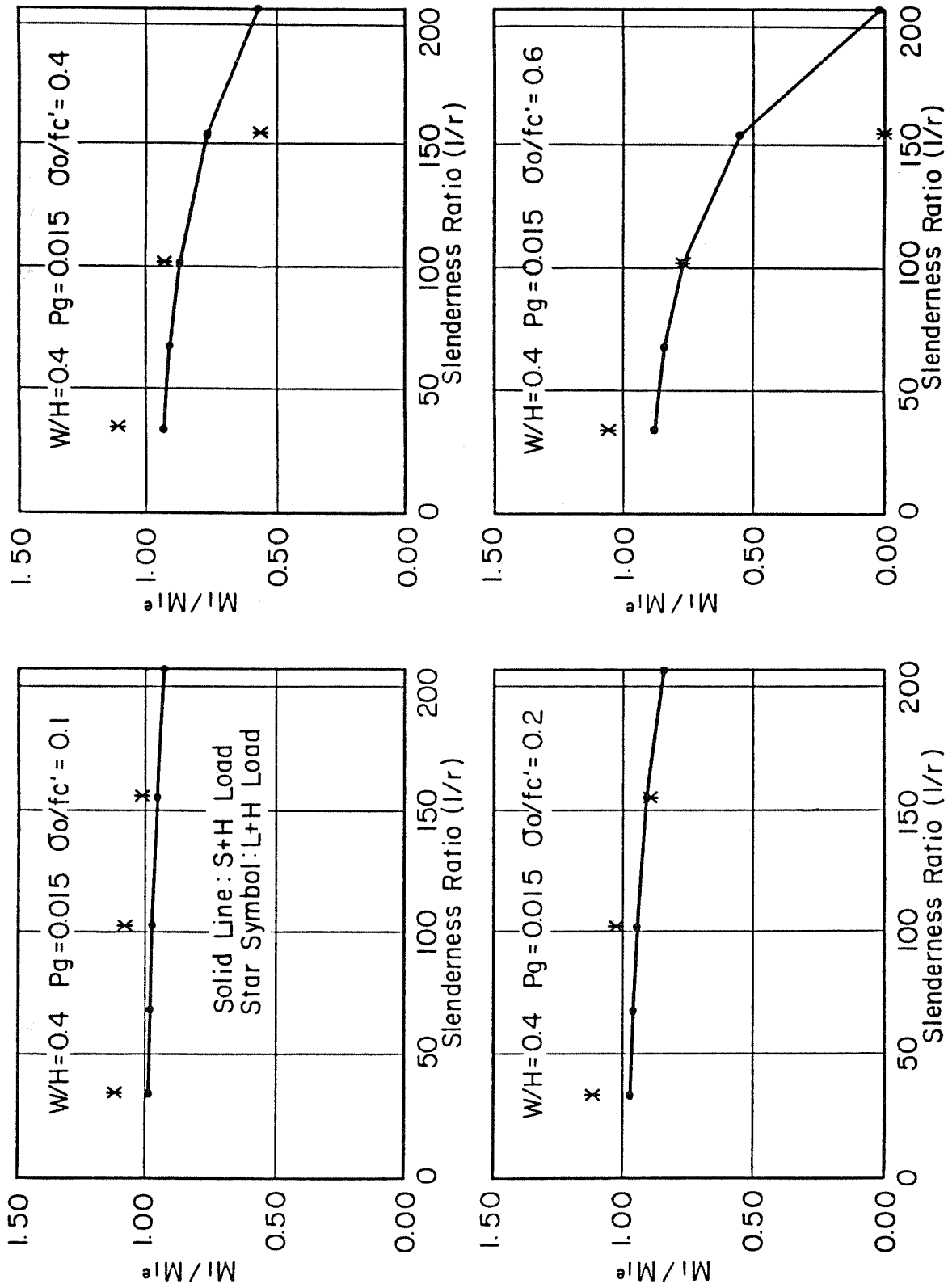
Fig.6-8 Moment Magnification Factor - Slenderness Ratio Relationship for Gravity Load (p$_g$=0.015)
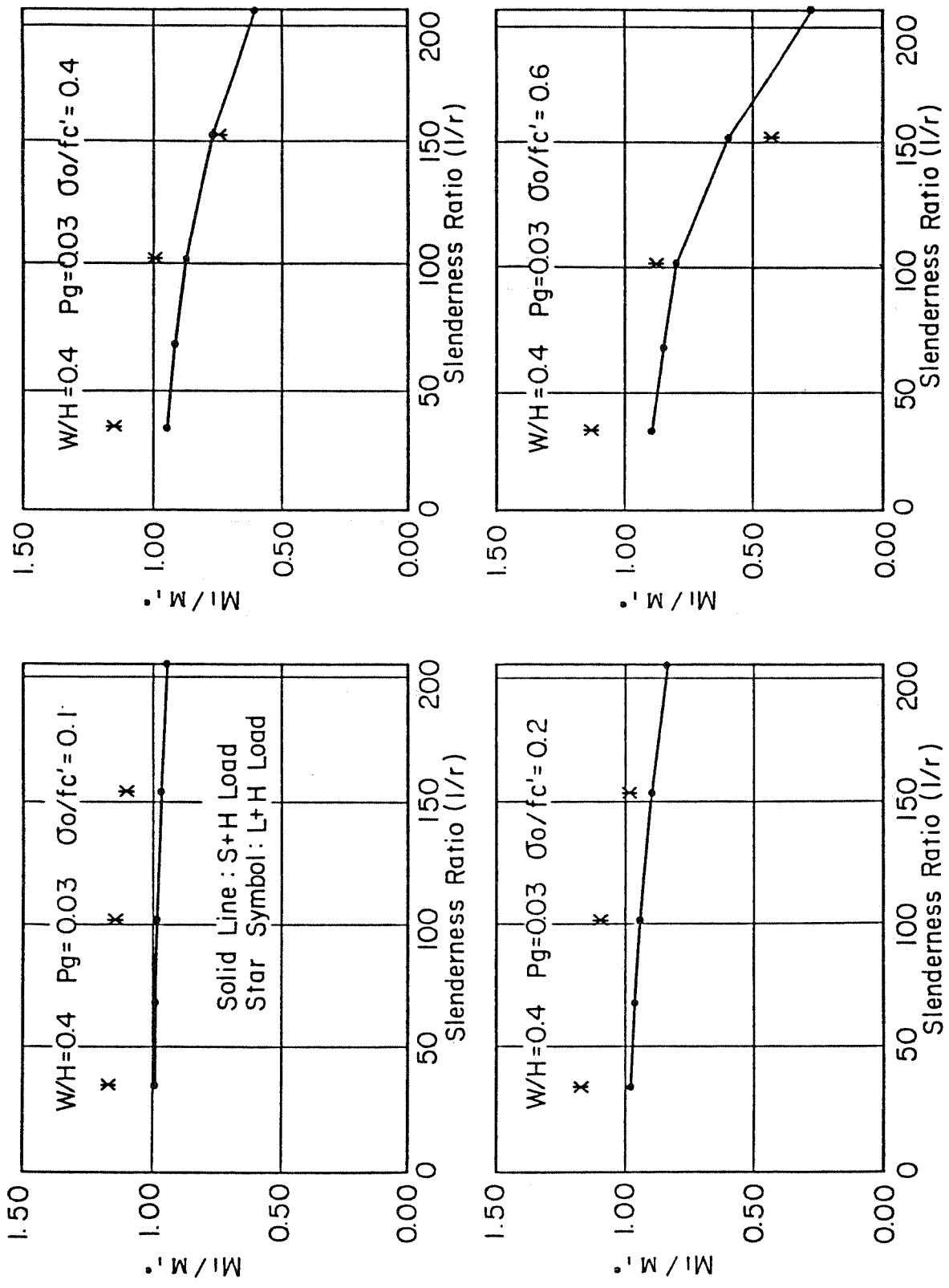
Fig. 6-9  Moment Magnification Factor-Slenderness Ratio Relationship for Gravity Load (Pg=0.03)
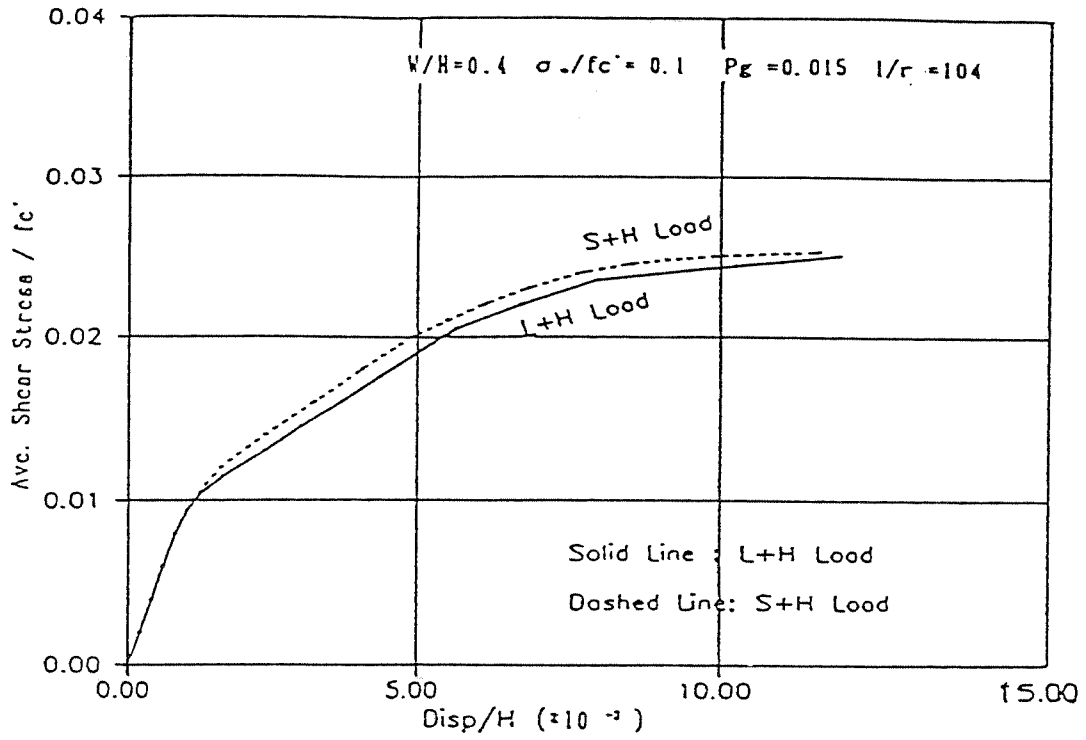
Fig. 6—10    Load-Displacement Relationship ( Node - 7 )
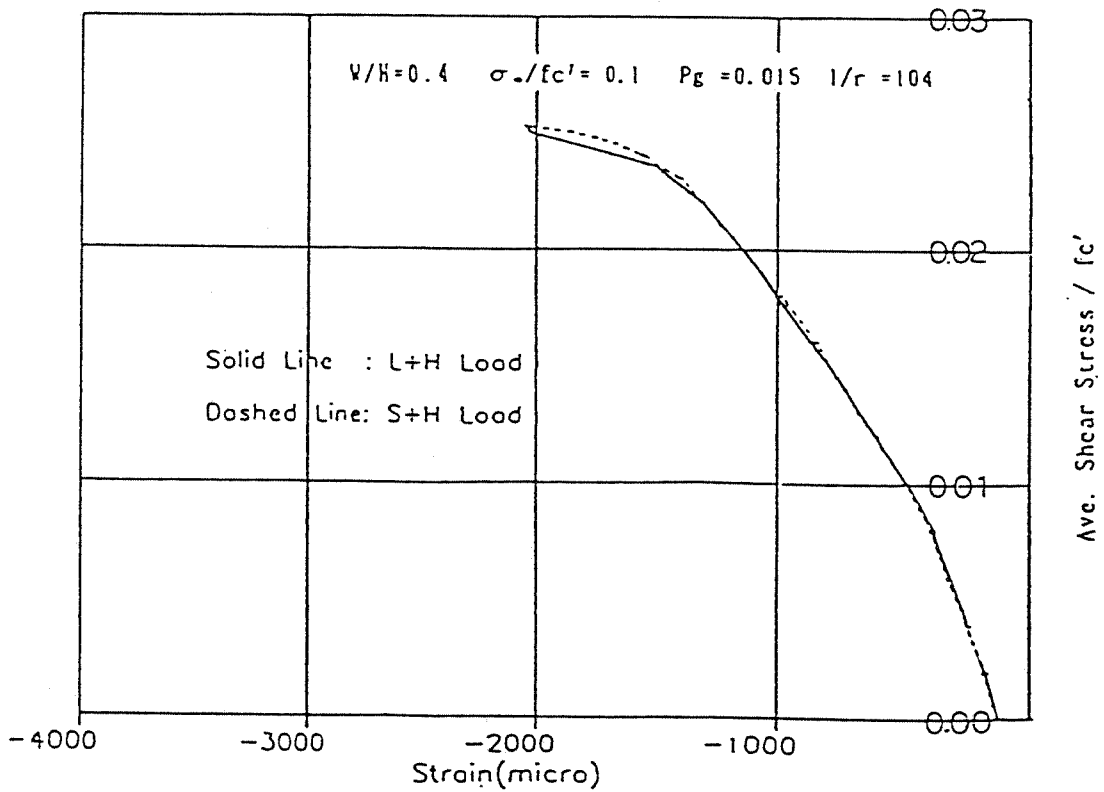


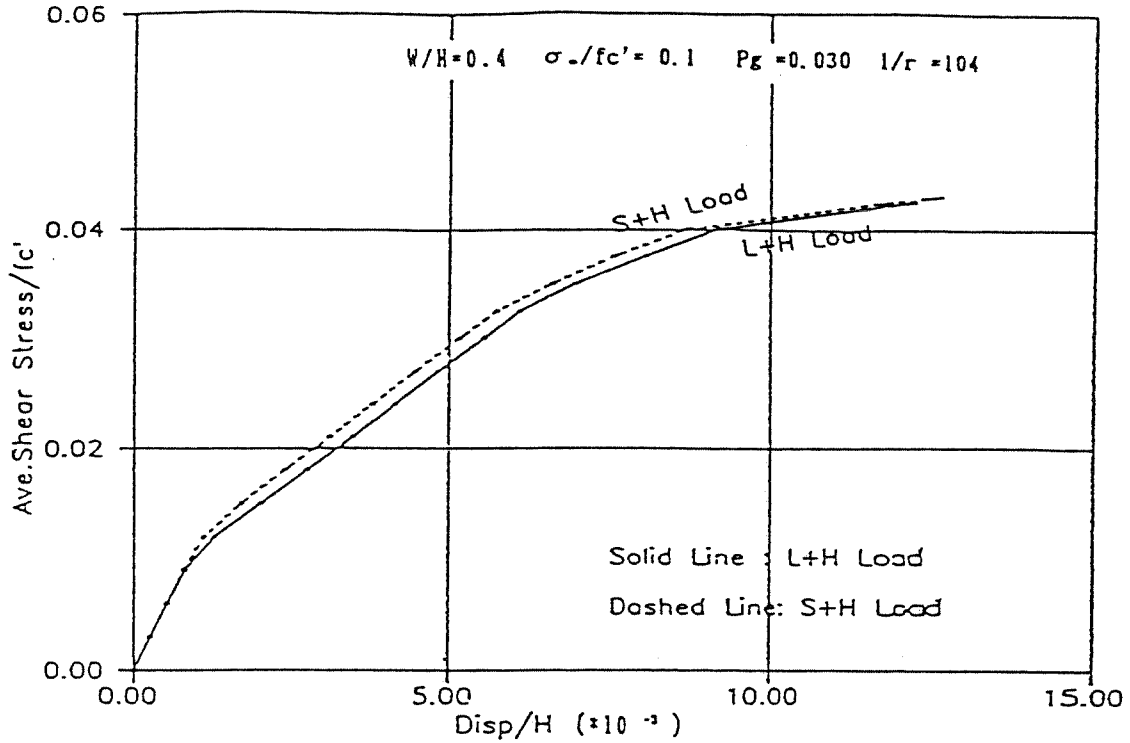Fig. 6—11    Load-Concrete Strain Relationship (Elem - 22.Out )
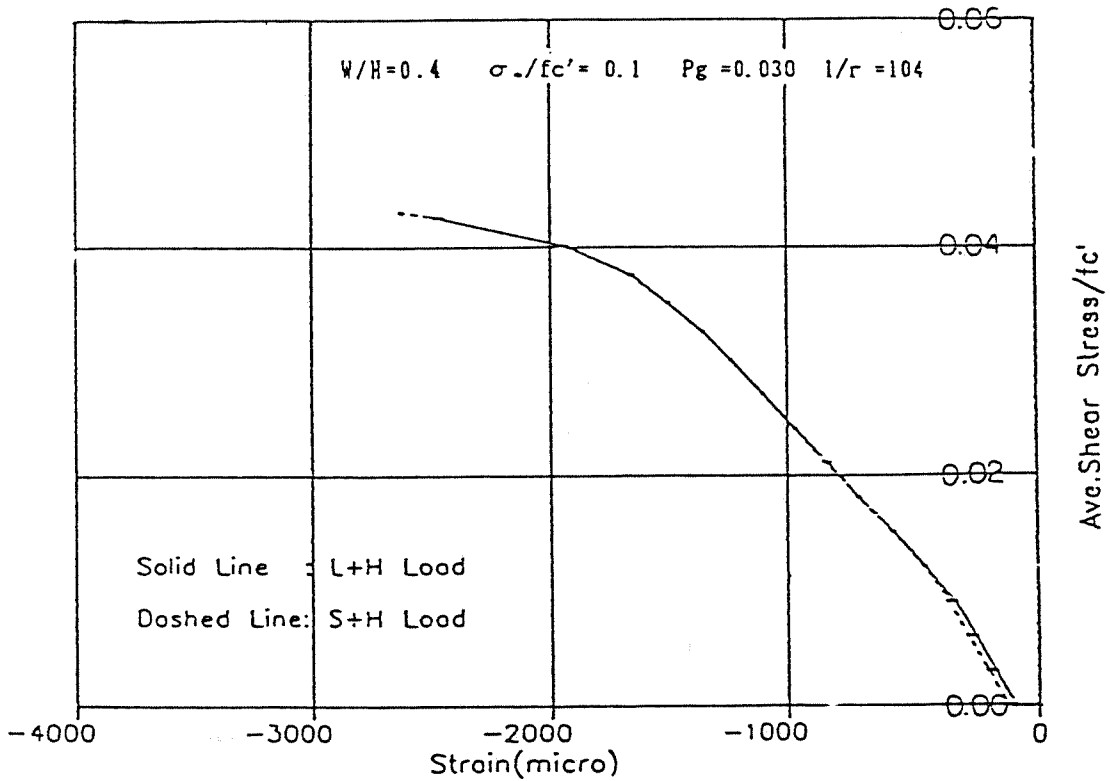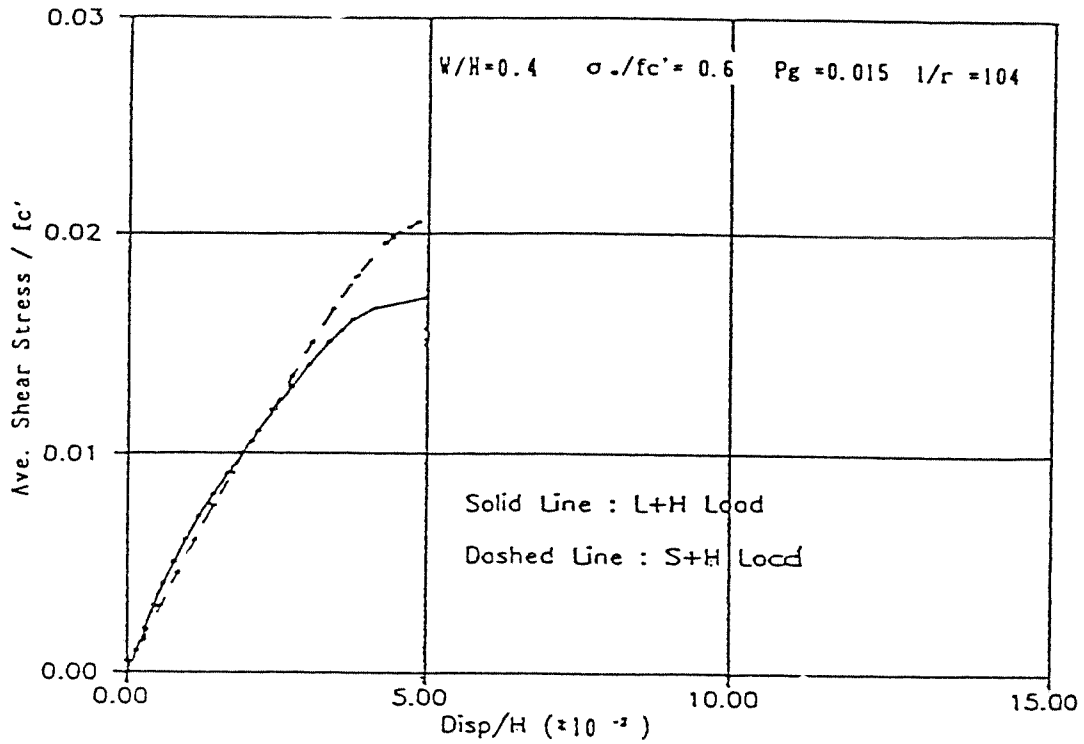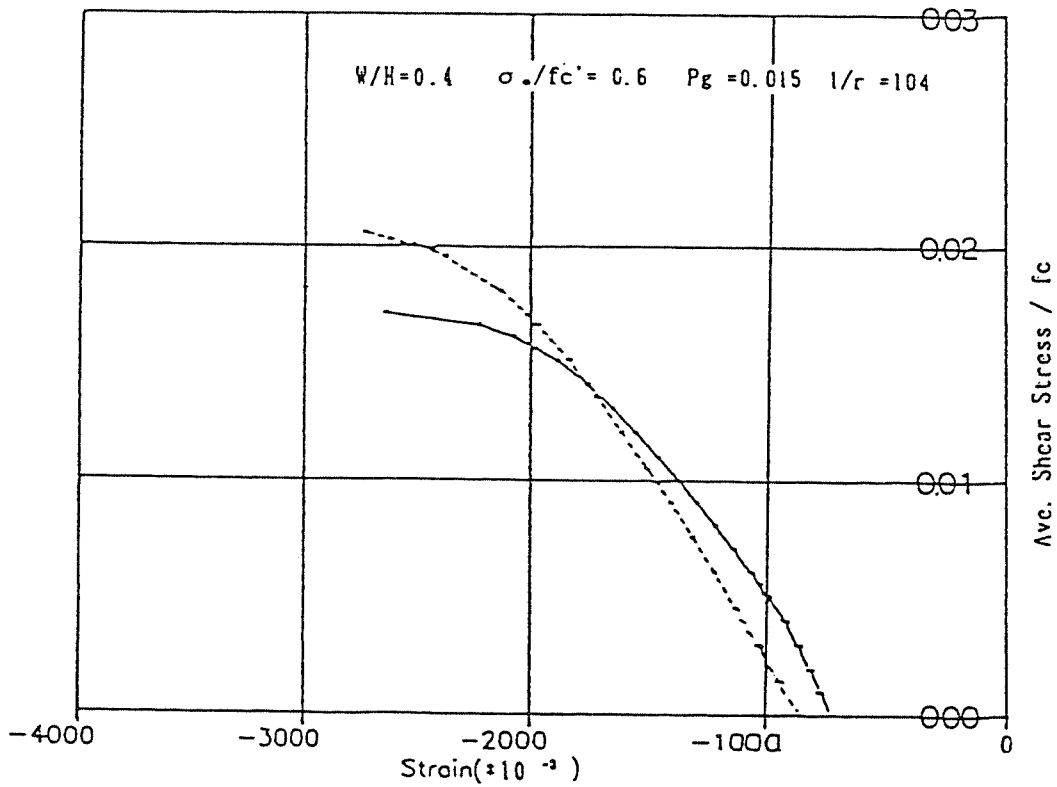
Fig. 6 − 12   Load-Displacement Relationship ( Node − 7 )

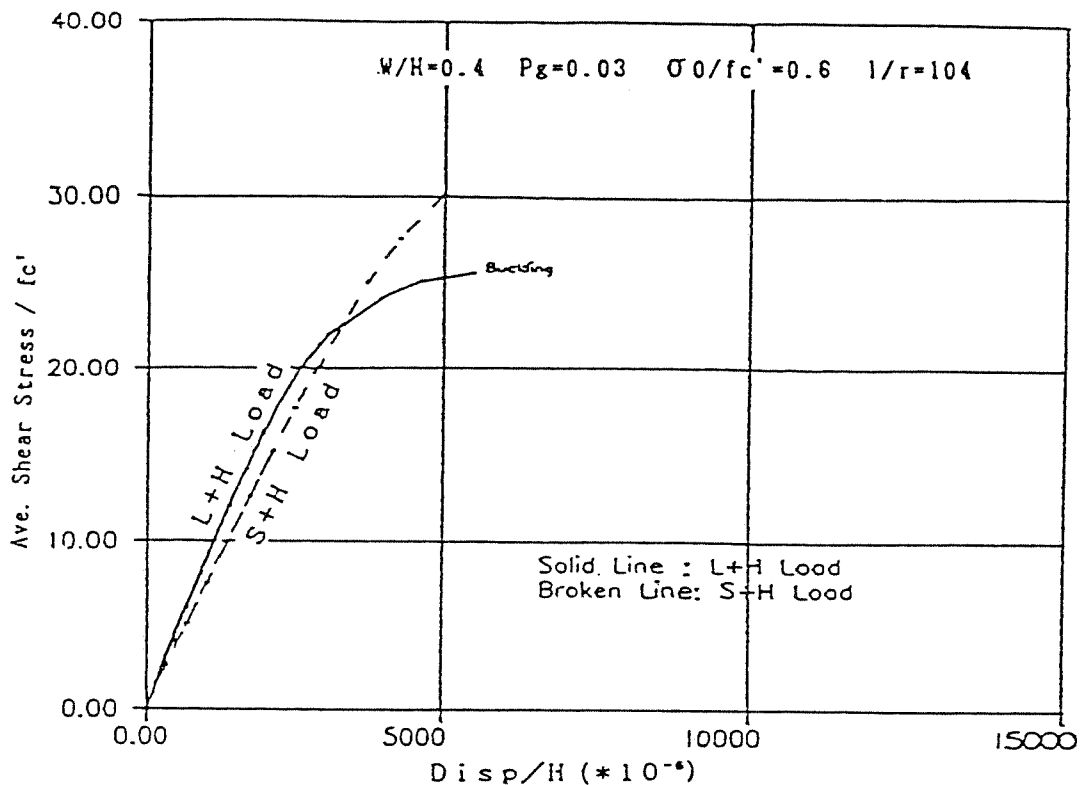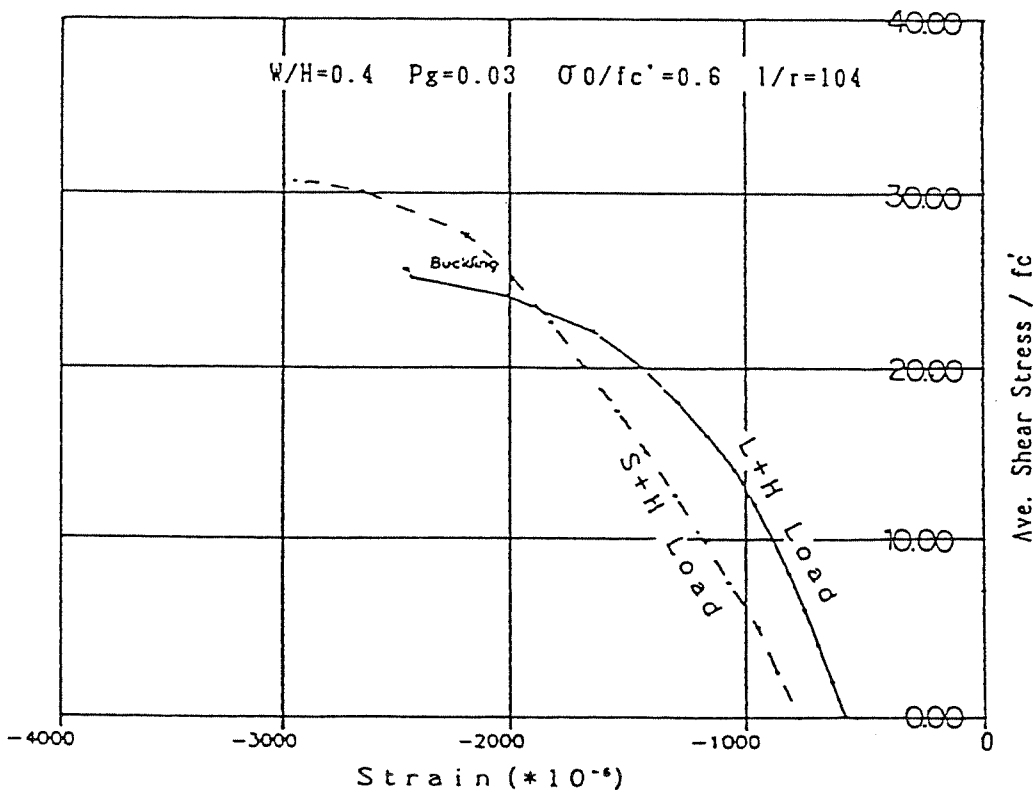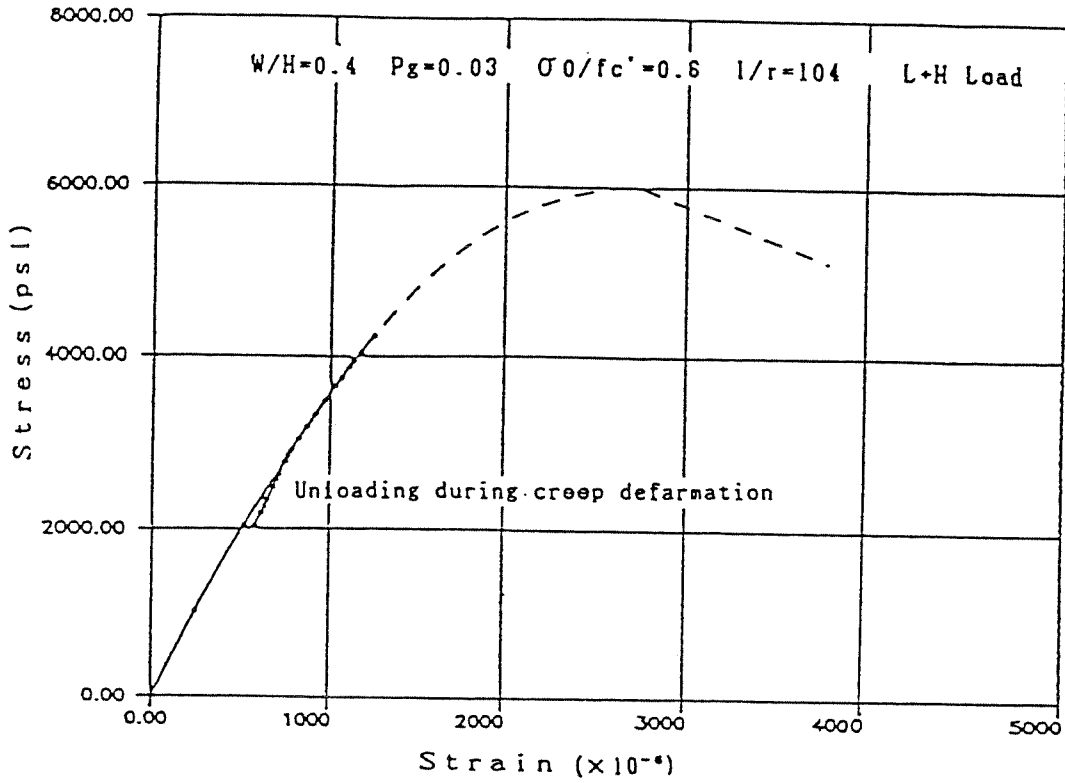

Fig. 6 − 13   Load-Concrete Strain Relationship (Elem − 22.Out )

W/H=0.4    $\sigma._{\circ}/fc' = 0.6$    Pg =0.015  1/r =104

Solid Line : L+H Load

Doshed Line : S+H Locd

Disp/H ($\pm$10$^{-2}$)

F i g. 6－14   Load-Displacement Relationship ( Node - 7 )



W/H=0.4    $\sigma._{\circ}/fc' = 0.6$    Pg =0.015  1/r =104

Strain($\pm$10$^{-3}$)

F i g. 6－15   Load-Concrete Strain Relationship (Elem - 22.Out )

F i g. 6 — 1 6  Lord-Displacement Relationship ( Node - 7 )



F i g. 6 — 1 7 Load-Concrete Strain Relationship (Elem - 22.Out )

Fig. 6−18 Concrete  Stress − Strain Relationship (Elem − 22.Out)
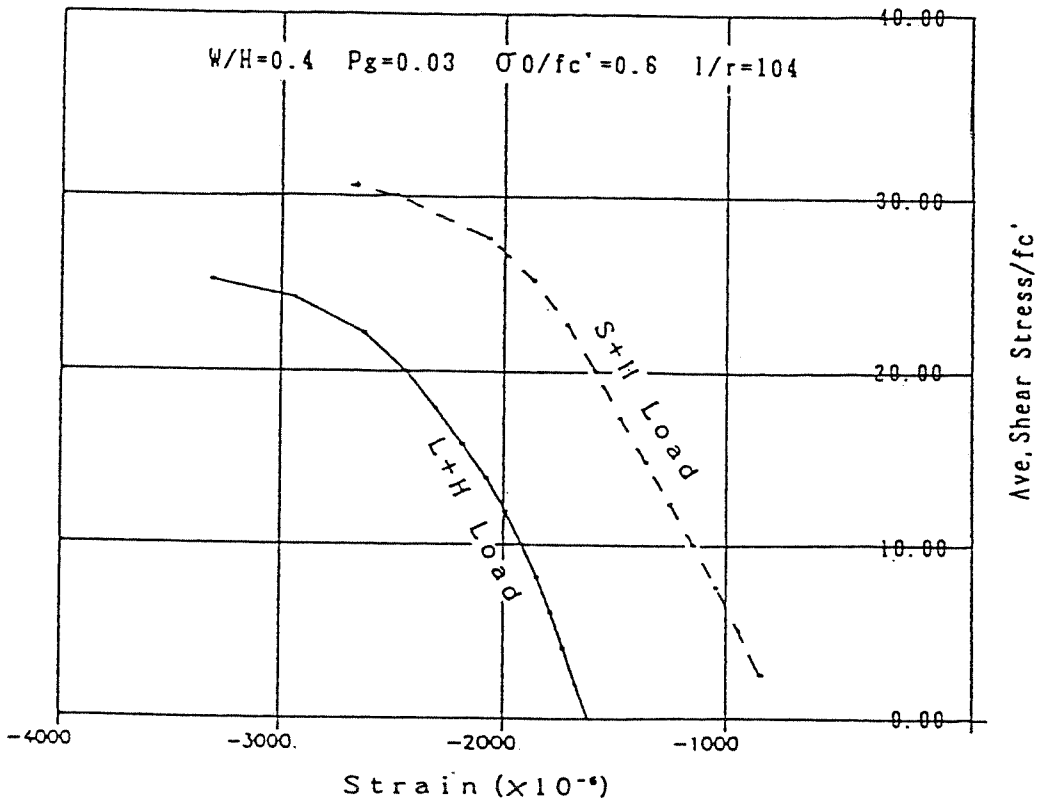


Fig. 6−19  Load − Rebar  Strain Relationship (Elem − 22.Out)

sections (Node-1 and -23) are shown in Fig.6-20~6-21 for the case of $\sigma_0/f'_c = 0.1$, $p_g = 1.5\%$, and $l/r = 104$. At node 1 where a tensile axial force acts, the postcracking moment increase is weakened followed by less increase after rebar yielding. At node 23 (Fig.6-21), meanwhile, in which axial compressive force acts, the moment increase is larger to compensate for the smaller moment at opposite side, node 1, and then increases with constant gradient. The load-moment relation for the $l/r = 35$ case indicates a larger axial force variation (Fig.6-22). There is no significant difference between the result of L + H case with creep influence and that of S + H case. Similar results are shown in the Fig.6-23~6-24 for the largest axial load case of $\sigma_0/f'_c = 0.6$. Less moment increase is observed for the L + H case in the early stage, because of stress redistribution influence and then yielding of rebar and cracking cause it to be larger across the curve of S + H case. It should be noticed that the axial force variation is remarkably small as compared to the small axial load case of $\sigma_0/f'_c = 0.1$. In other words, the moment variation becomes much larger than the axial force variation. Similar relations are presented in Fig.6-25~6-26 for the larger reinforcement ratio of $p_g = 3\%$, in which little difference is observed between the results of S + H and L + H for $\sigma_0/f'_c = 0.1$ case.

Fig.6-27~6-28 represent the moment magnification factors from these analyses accompanied by those by the current ACI code, that are calculated based on the moment of node 23 critical in comparison with that of another node.

Usage of flexural stiffness

$$EI = \frac{(\frac{E_c I_g}{5}) + E_s I_{se}}{1 + \beta_d} \qquad \cdots\cdots\cdots\cdots(6.1)$$

is specified in the design[4] in which the creep effect is involved as $\beta_d$, the ratio of gravity load moment to combined moment of gravity and lateral loads. A $\beta_d$

Fig. 6-20 Load-Axial Force & Flexural Moment Relationship(Node-1)

W/H = 0.4    σo/fc' = 0.1    Pg=0.015    l/r=104

Solid Line : L+H Load
Dashed Line:S+H Load

M/fc'bh²

Ave.Shear Stress/fc'

N/fc'bh

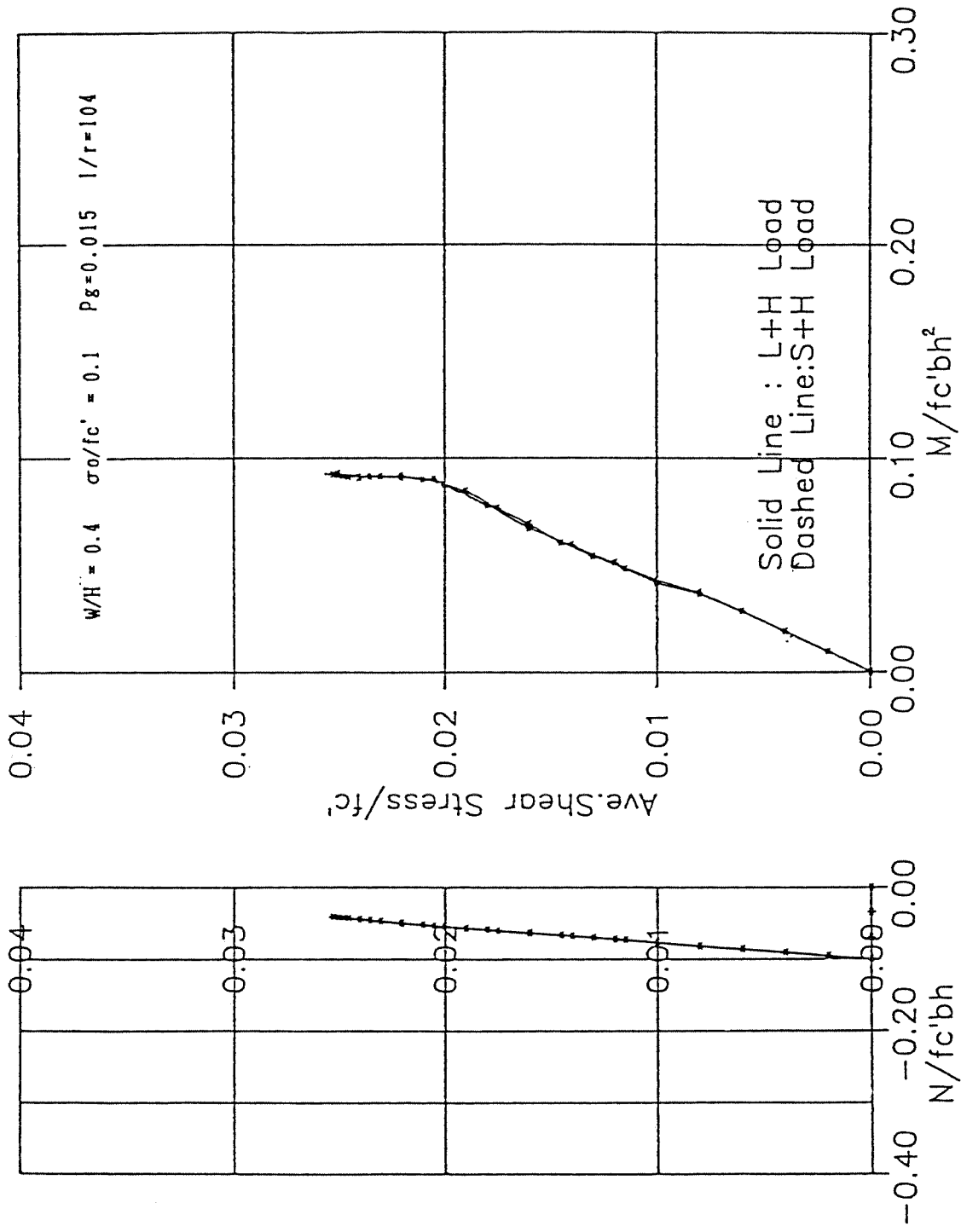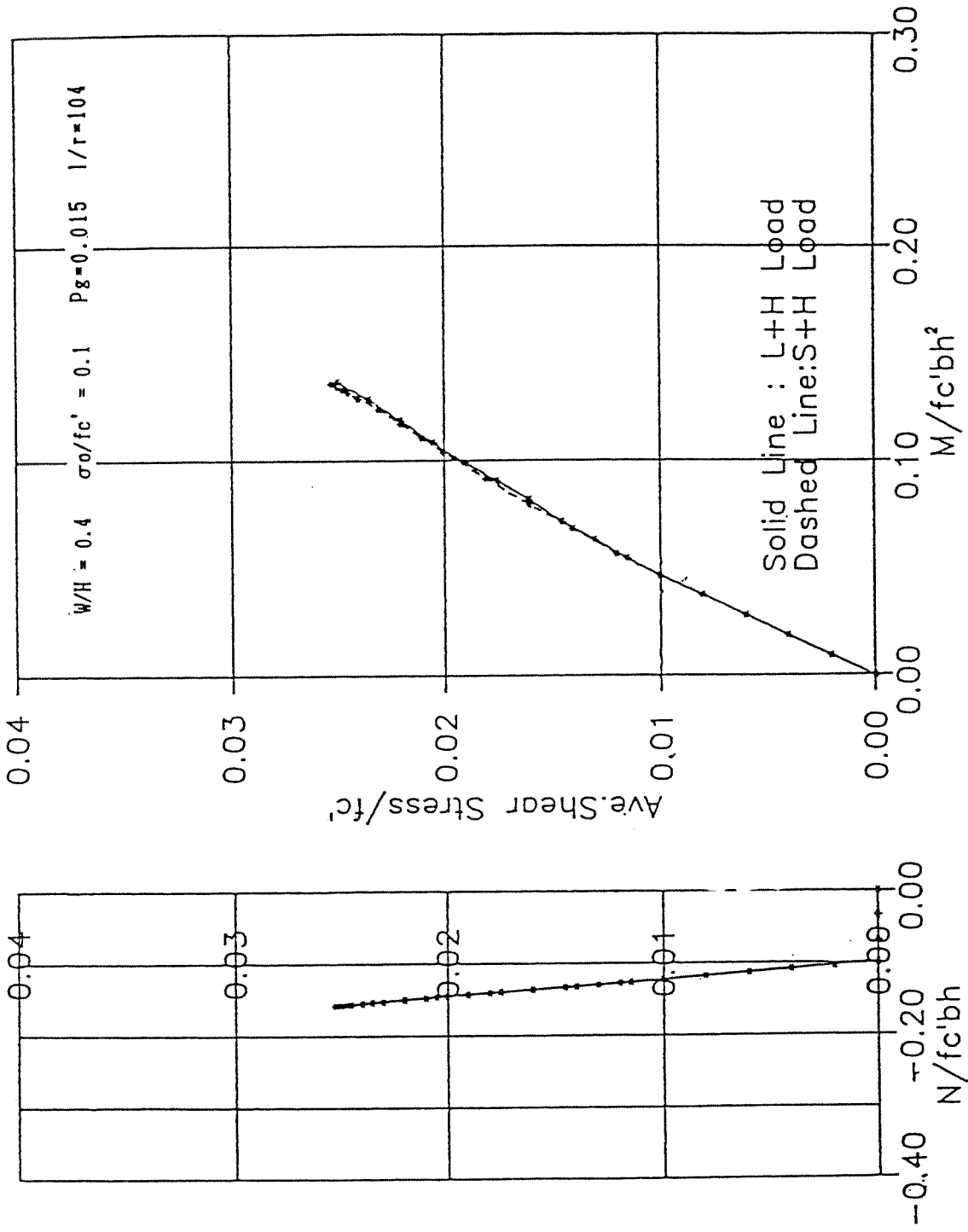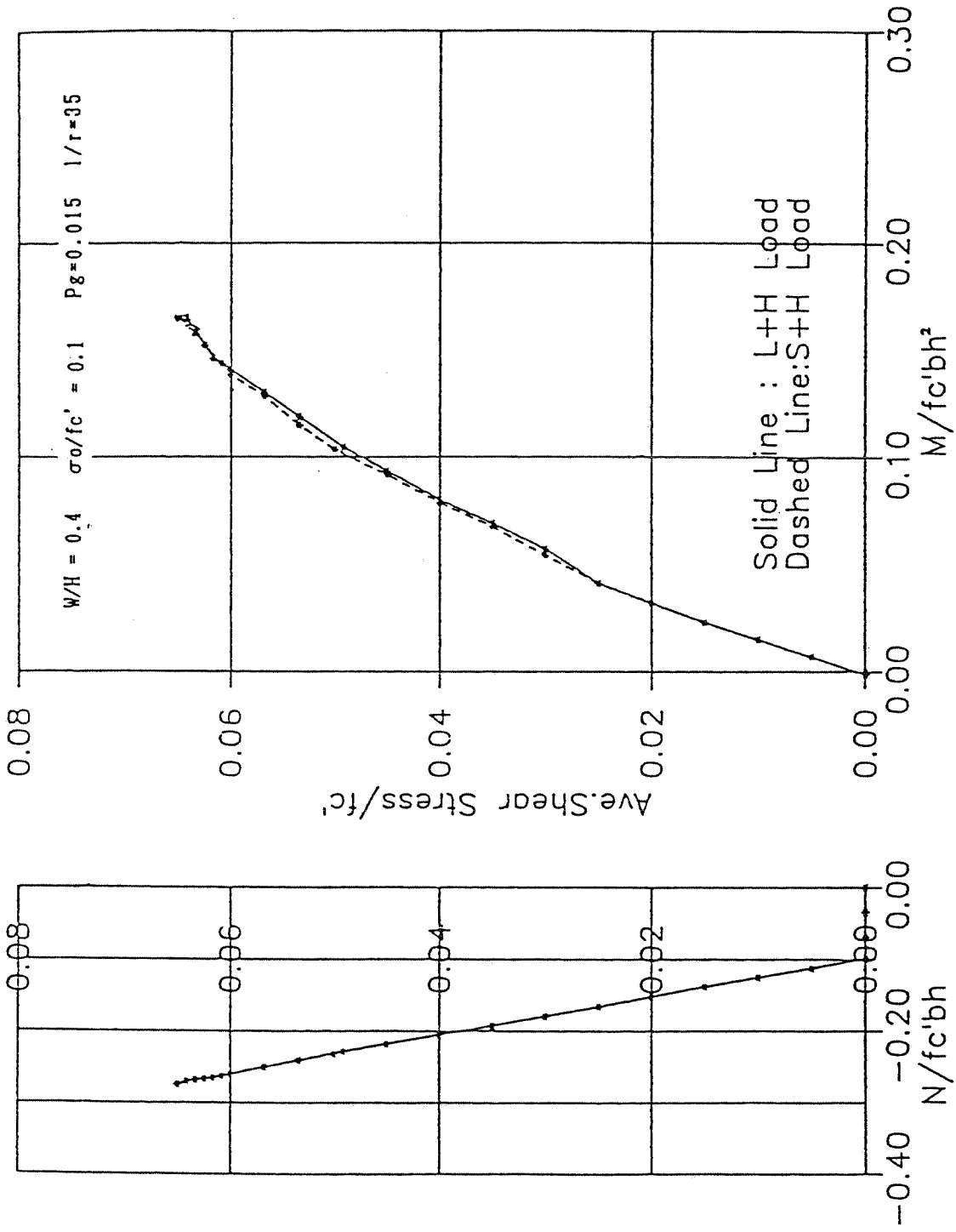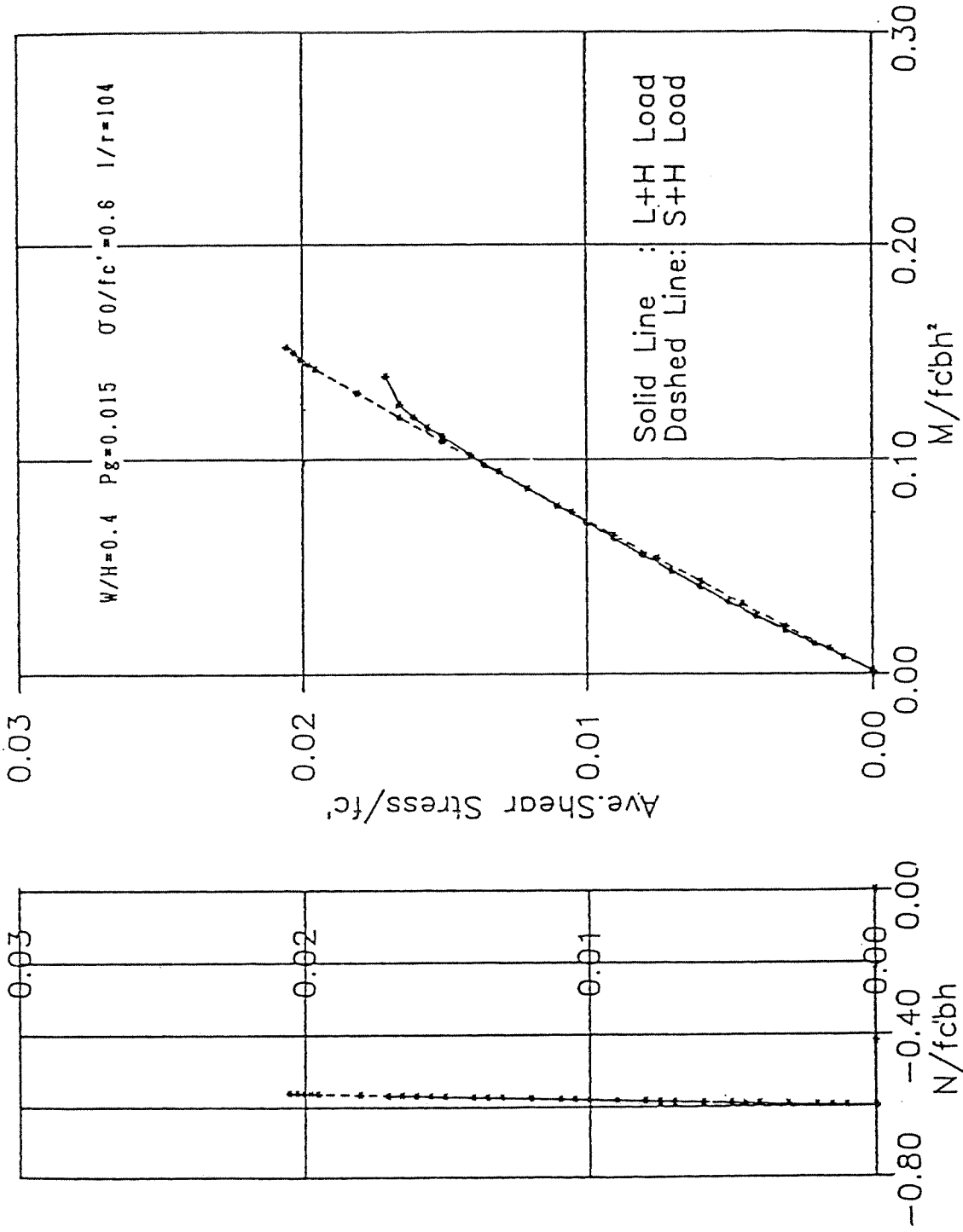Fig. 6-21 Load-Axial Force & Flexural Moment Relationship(Node-23)

Fig. 6-22 Load—Axial Force & Flexural Moment Relationship(Node—23)

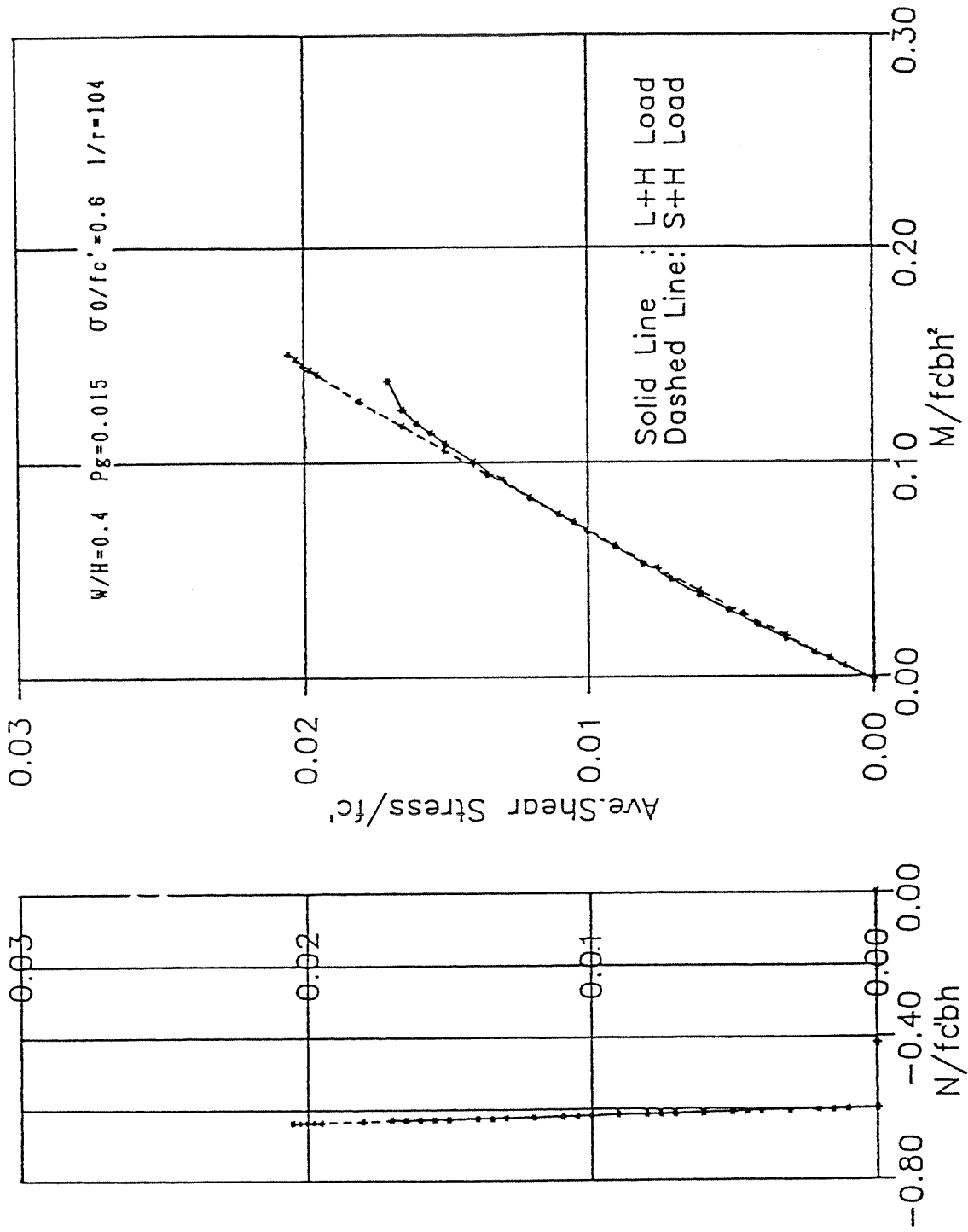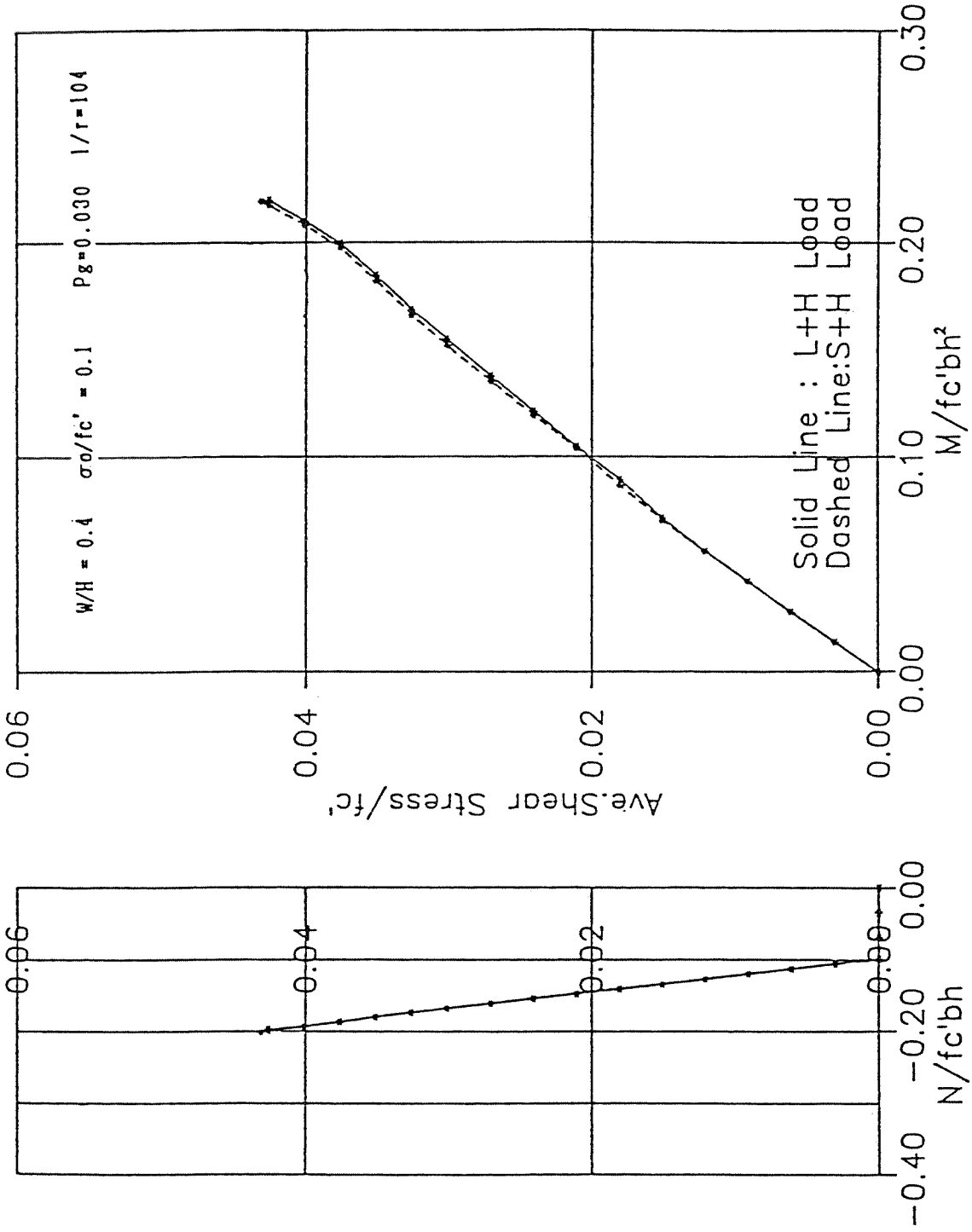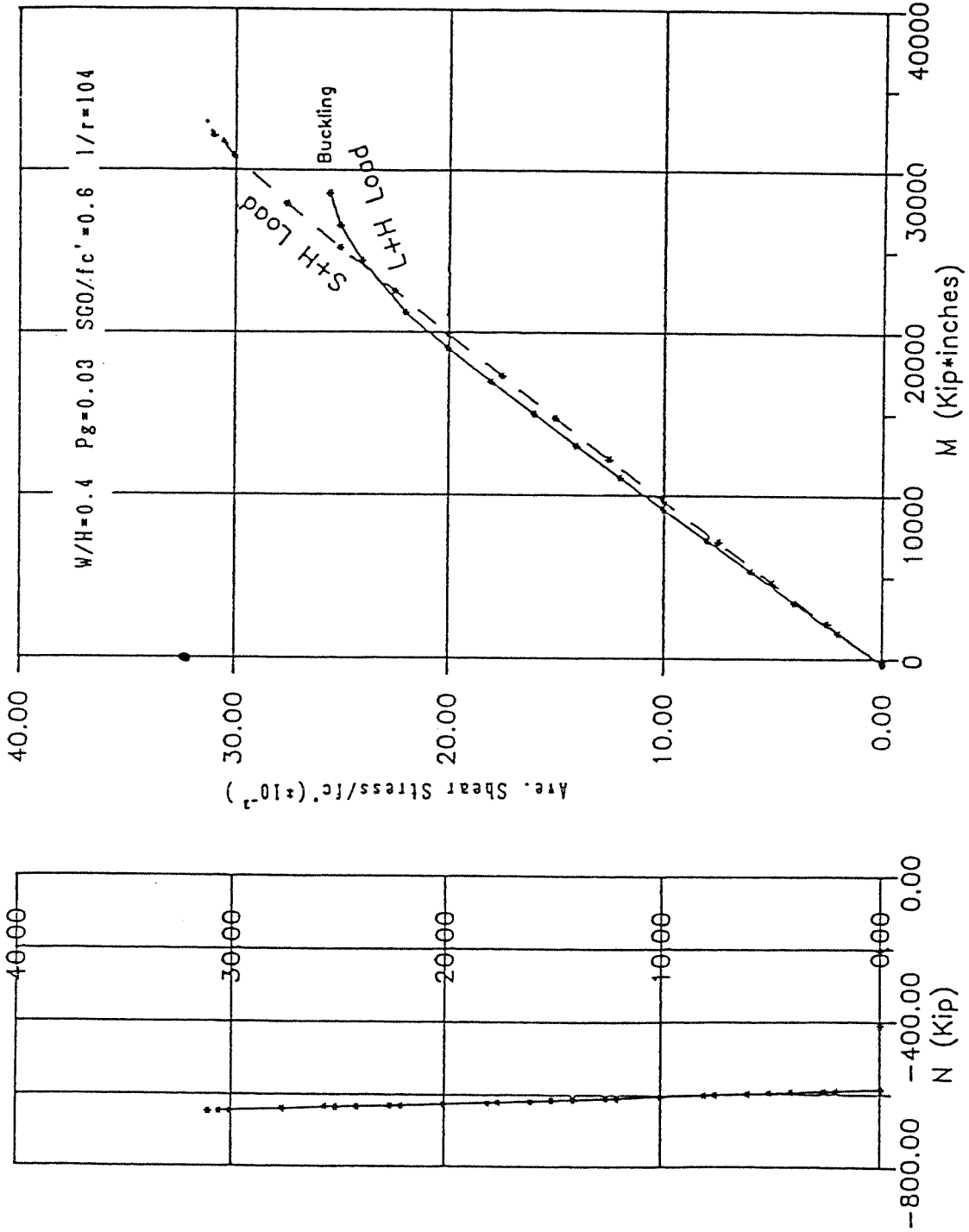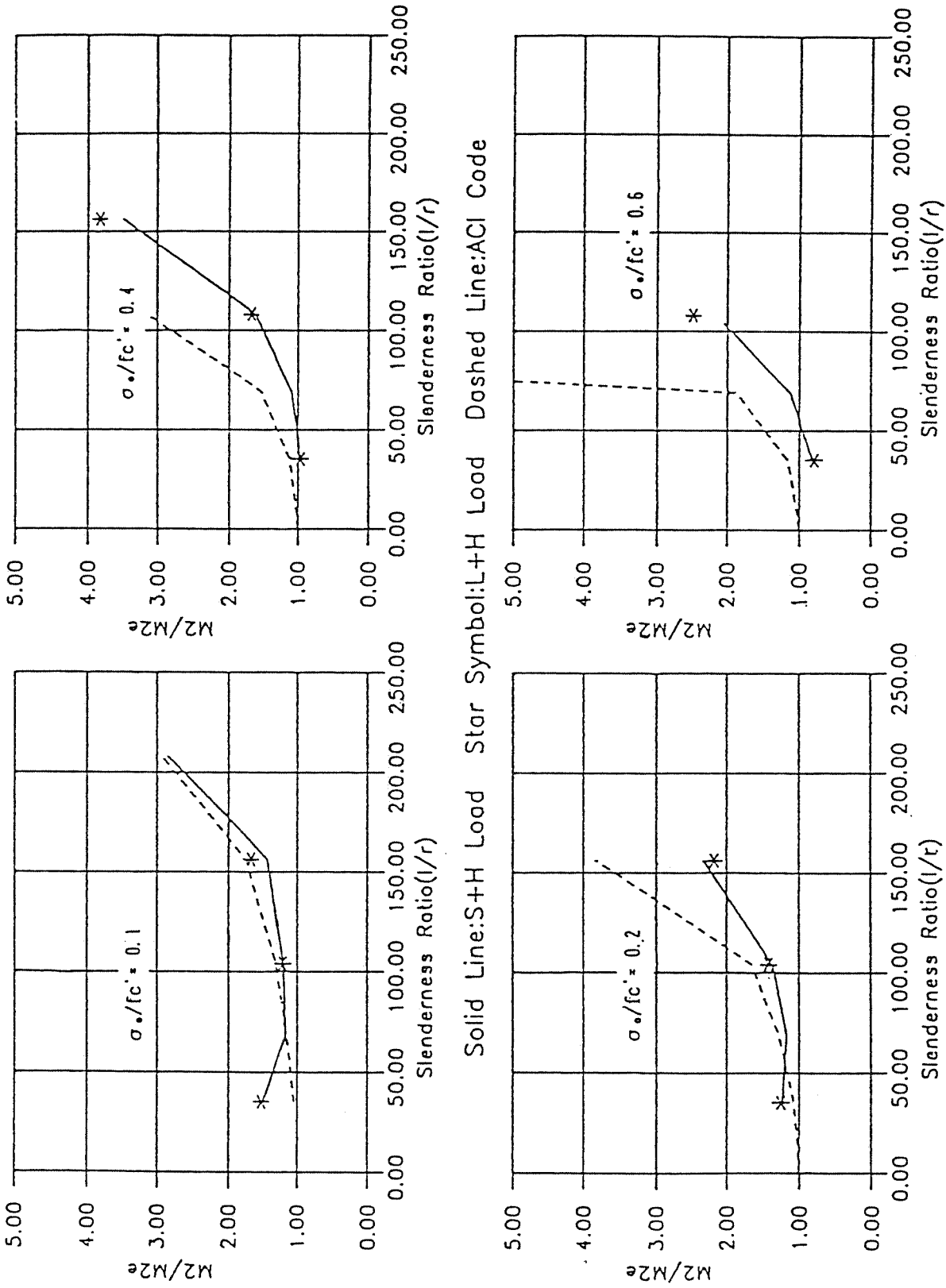Fig.6-23 Load−Axial Force & Flexural Moment Relationship(Node−1)

Fig. 6-24 Load—Axial Force & Flexural Moment Relationship(Node—23)

Fig. 6-25 Load-Axial Force & Flexural Moment Relationship(Node-23)

Fig. 6-26  Load—Axial Force & Flexural Moment Relationship (Node-23)

Fig. 6-27 Moment Magnification Factor-Slenderness Ratio(W/H=0.4,Pg=0.015)
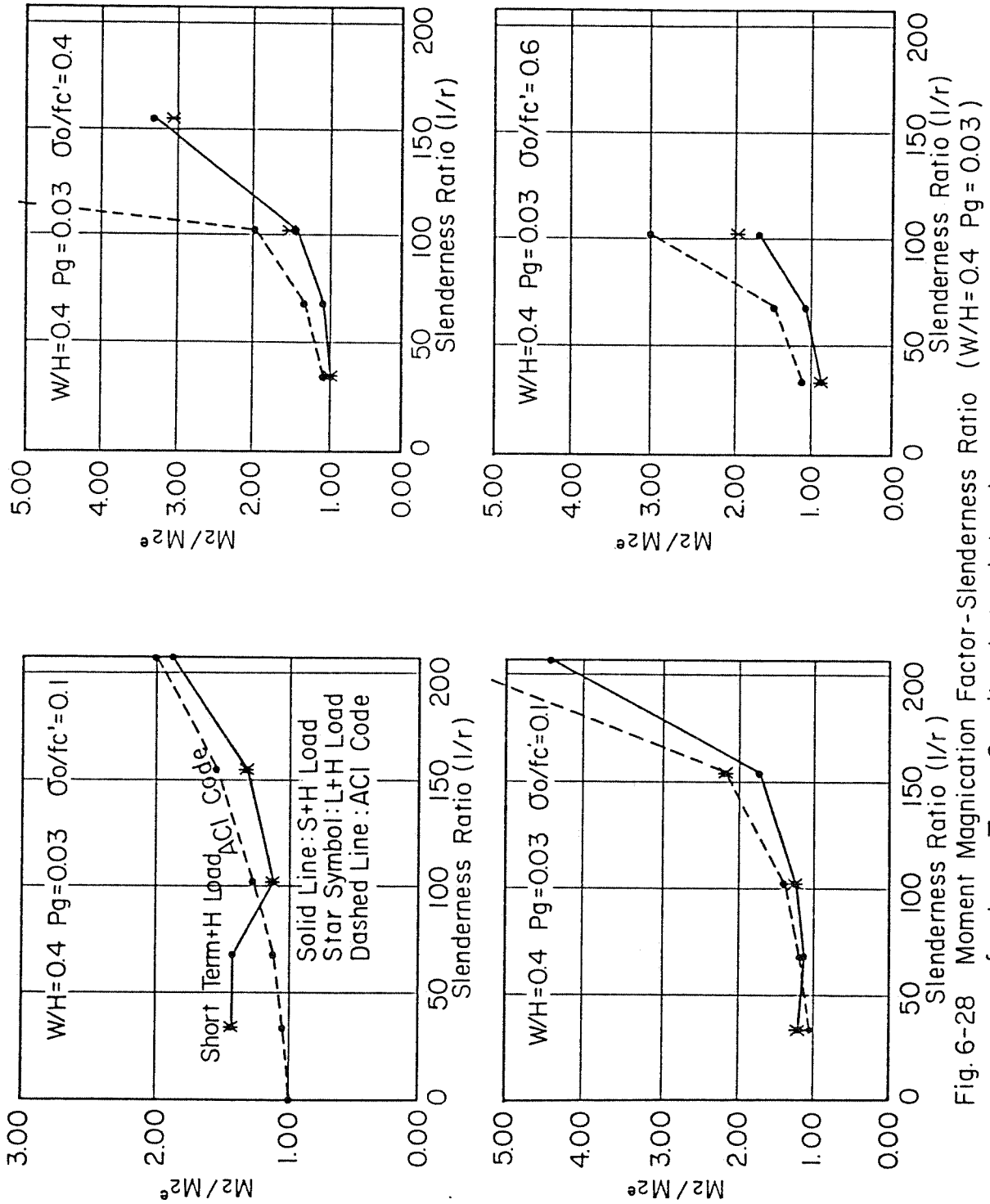
Fig. 6-28 Moment Magnication Factor-Slenderness Ratio (W/H=0.4 Pg=0.03)
for Long Term Gravity+ Lateral Load

=0, however is assumed in the calculation of design value in these figures since the moment due to gravity load is much smaller than that due to a combination of lateral and gravity loads.

In the case of lower axial load ,the analytical results provide a higher value than the design value in the low slenderness region, based on the effect of moment redistribution previously described that the additional moment is loaded in the compressive side leg (Node-23) to compensate for its reduction in the tensile side (Node-1). Such a tendency will be larger with lower slenderness ratio and with lower gravity load in which the flexural stiffness reduction in the tensile side is remarkable. These phenomena could be brought on by stress redistribution based on material nonlinearity rather than geometric nonlinearity.

On the other hand, analytical values less than one are obtained with an increase of $\sigma_0/f'_c$. Less reduction of flexural stiffness at the bottom of the tensile leg causes less moment redistribution. In addition, another reason could be more contribution of the axial forces due to the overturning moment.

Some difference is observed between the analytical values of L + H and S + H cases for larger slenderness ratios failed by buckling. Since an analytical value is defined based on moment at the previous step directly before failure, some error could be included for a drastic failure case such as a buckling.

Except for the large slenderness ratio cases with the above drastic failure, the L + H cases provide almost the same results as that of S + H without considering creep. It is indicated that the predicted moment magnification factor less than the design value is generally obtained excluding the low axial load and low slenderness ratio regions and that a larger difference appears with increase of axial load.

## 6.5 Creep Effect on Ultimate Strength, Ductility and Failure Mode

Various quantities on the ultimate state are shown in the Table6-1. As shown in the ultimate strength-slenderness ratio relation of Fig.6-29~6-30, L + H
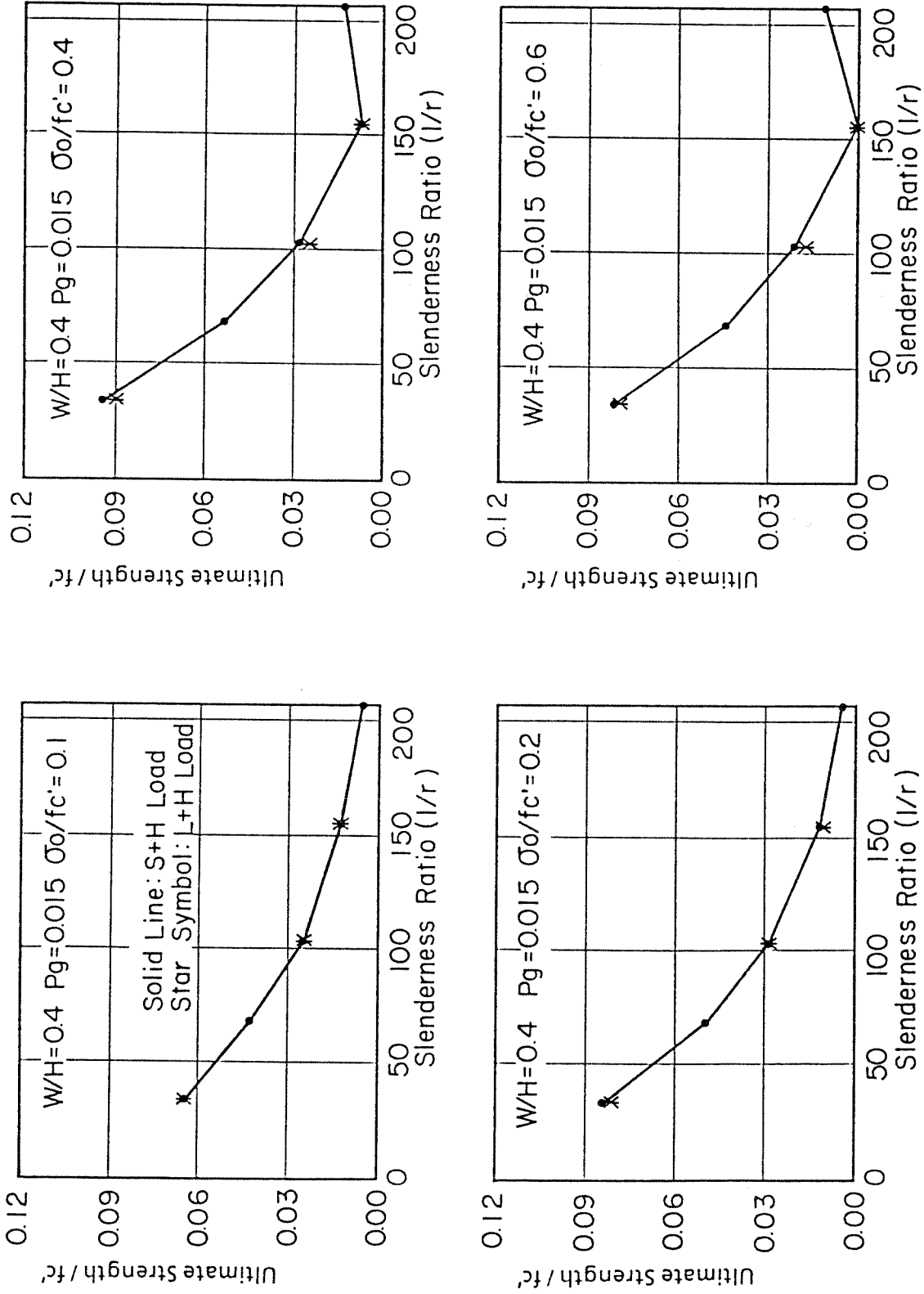
Fig.6-29  Ultimate Strength - Slenderness Ratio Relationship (W/H = 0.4, Pg = 0.015)
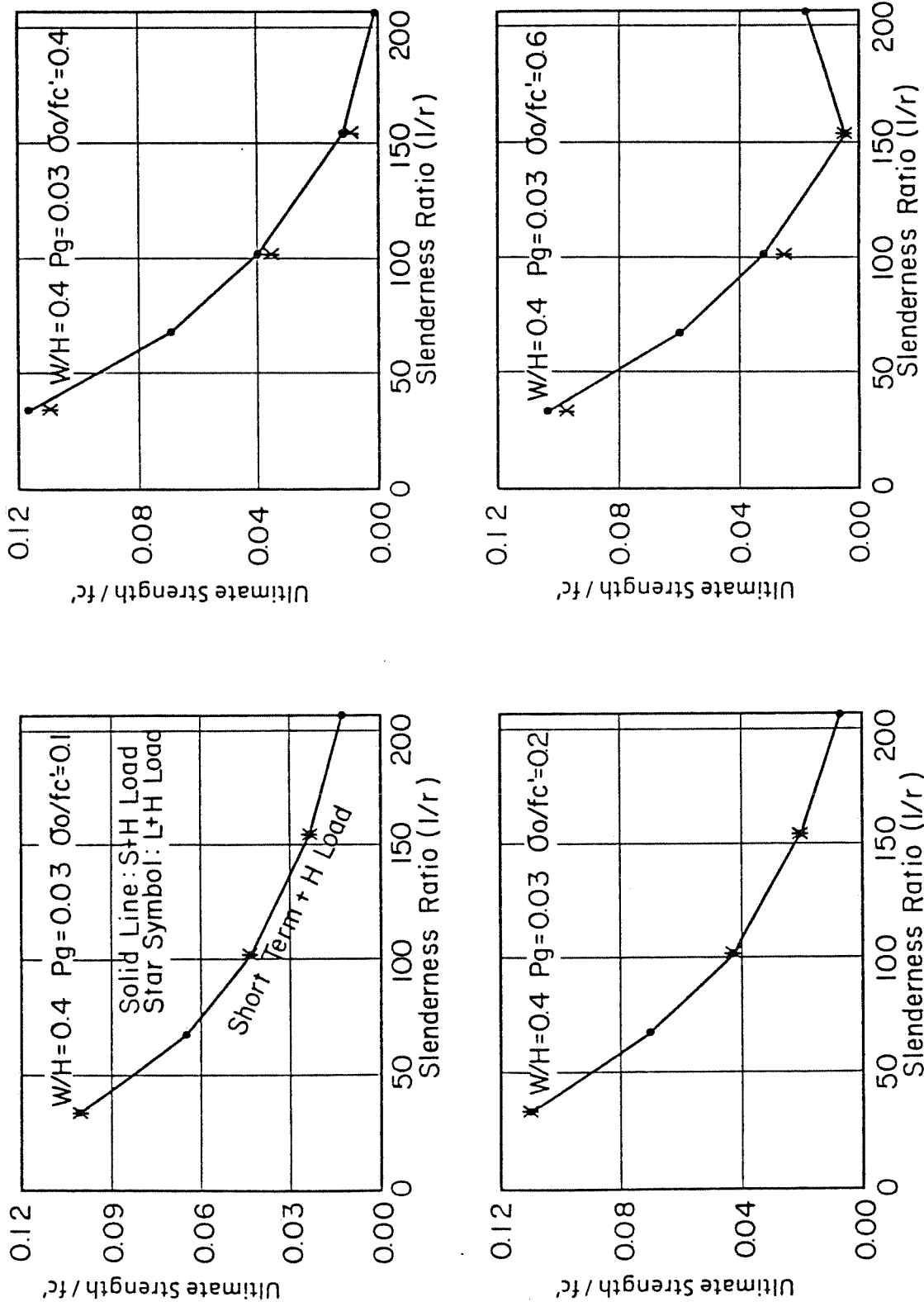for Long Term Gravity + Lateral Load

Fig. 6-30  Ultimate Strength-Slenderness Ratio Relationship (W/H=0.4, Pg=0.03)
for Long Term Gravity+ Lateral Load

load cases provide almost the same ultimate strength as S + H load cases in wide range of slenderness ratio for relatively low axial load up to $\sigma_0/f'_c = 0.2$. For high axial loads such as $\sigma_0/f'_c = 0.4$ and 0.6, similar results are obtained for both cases in the low range of slenderness ratio (l/r = 35), but some difference occurs as the slenderness ratio increases because of stronger influence of creep on ultimate strength.

Table6-1 shows $\gamma_{max}/\gamma^0_{max}$, the ratio of maximum displacement of a L + H case divided by that of a S + H case for ductility estimation. Slightly reduced values by 80~100% are generally obtained in the lower range of axial loads such as $\sigma_0/f'_c = 0.1$~0.2. In the table, the ductility factor $\gamma_{max}/\gamma_y$ less than one obtained with no yielding of tensile rebar is not presented.

Yielding of the tensile rebar at the bottom leg (Node-1) followed by either a yielding of the compressive rebar or concrete crushing at opposite bottom leg (Node-23) is the typical failure pattern in the lower axial load case less than 0.2.

Higher axial load cases, larger than $\sigma_0/f'_c = 0.4$, on the other hand, provide critical conditions in compressive yielding or crushing.

These failure patterns are almost similar for both L + H and S + H cases.

## 7. Nonlinear Behavior during Cyclic Lateral Load Combined with Sustained Gravity Load

### 7.1 Analytical Parameters

#### (1) Absorbed Energy

The usage of structural members with sufficient ductility is cost effective in a seismic resistant design. As shown in Table5-1~5-4, the ductility demand does not occur in the high axial load cases such as $\sigma_0/f'_c = 0.4$ and $0.6$ with no tensile rebar yielding showing failure mode rank of 3 or Buckling.

Fig.7-1~7-2 show non-dimensional absorbed energy calculated by an area of load-displacement curve from elastic up to ultimate for the case of $\sigma_0/f'_c = 0.1$ and $0.2$ for which ductility design could be possible. The absorbed energy above mentioned is defined here as an equivalent external work by applied nodal forces.

It becomes difficult to specify the particular nodal point for the representative displacement for absorbed energy estimation because distributed lateral loads are applied along legs. Therefore, a representative displacement, $\delta_{eq}$ will be defined by considering an equivalence with an actual external work as shown in eg.(7.1) in incremental form (Fig.7-3).

$$\Delta W = \Sigma \int P_i \Delta \delta_i = \int (\Sigma P_i) \Delta \delta_{eq} \quad \cdots\cdots\cdots\cdots(7.1)$$

$$\therefore \Delta \delta_{eq} = \frac{\Sigma P_i \Delta \delta_i}{\Sigma P_i} \quad \cdots\cdots\cdots\cdots(7.2)$$

Useful is the non-dimensional form dividing both sides by tower height, H.

$$\therefore \Delta \gamma_{eq} = \frac{\Sigma P_i \Delta \delta_i}{H \Sigma P_i} \quad \cdots\cdots\cdots\cdots(7.3)$$

As shown in Fig.7-4, a non-dimensional expression with a load axis divided by section area and $f'_c$ and with a displacement axis divided by a tower height
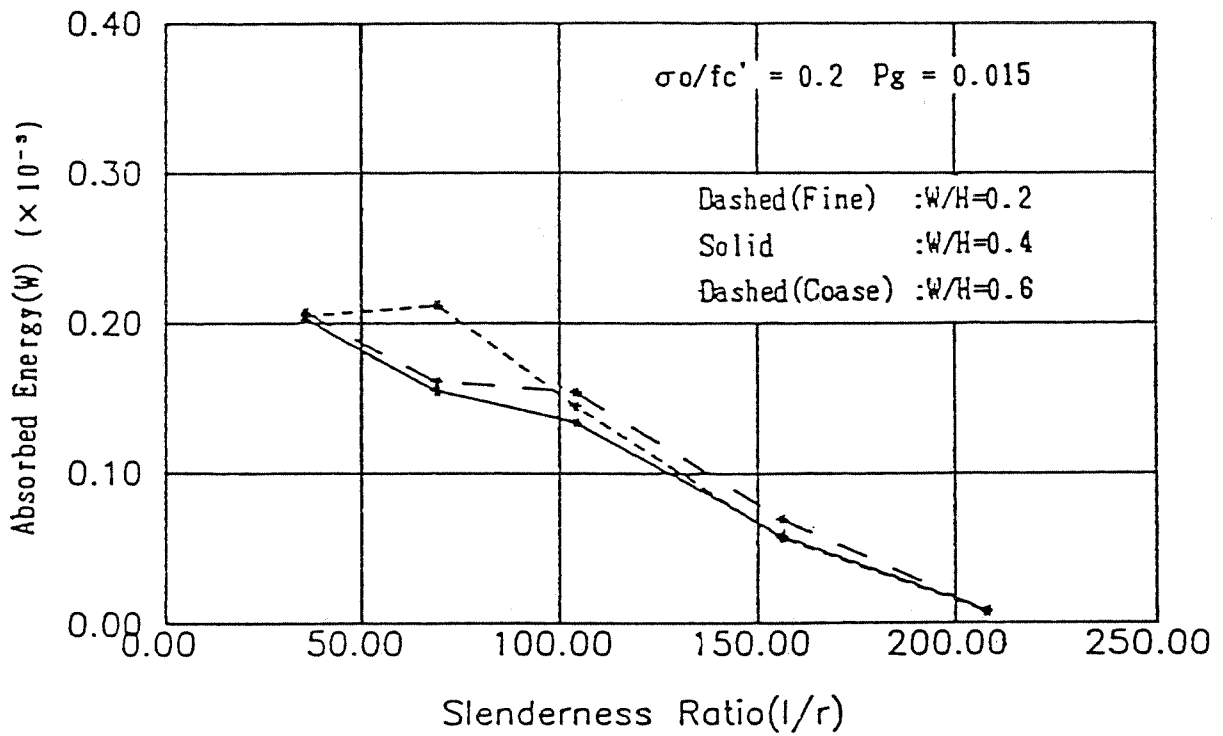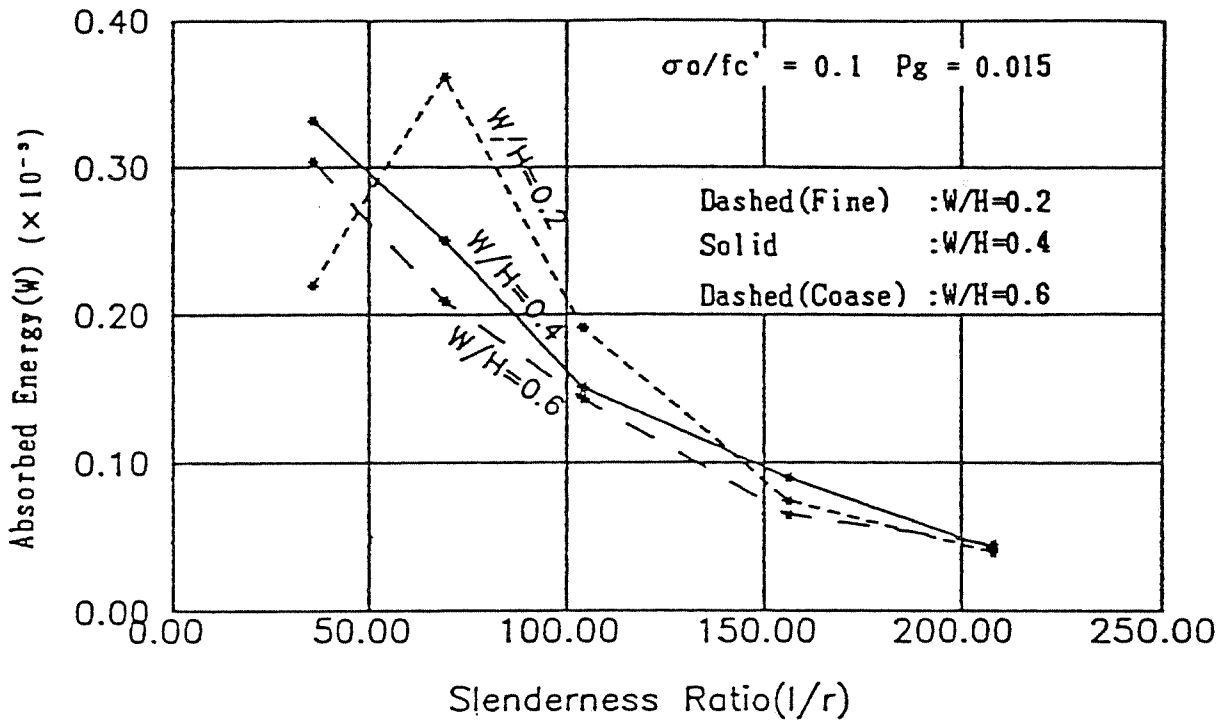
Fig. 7−1
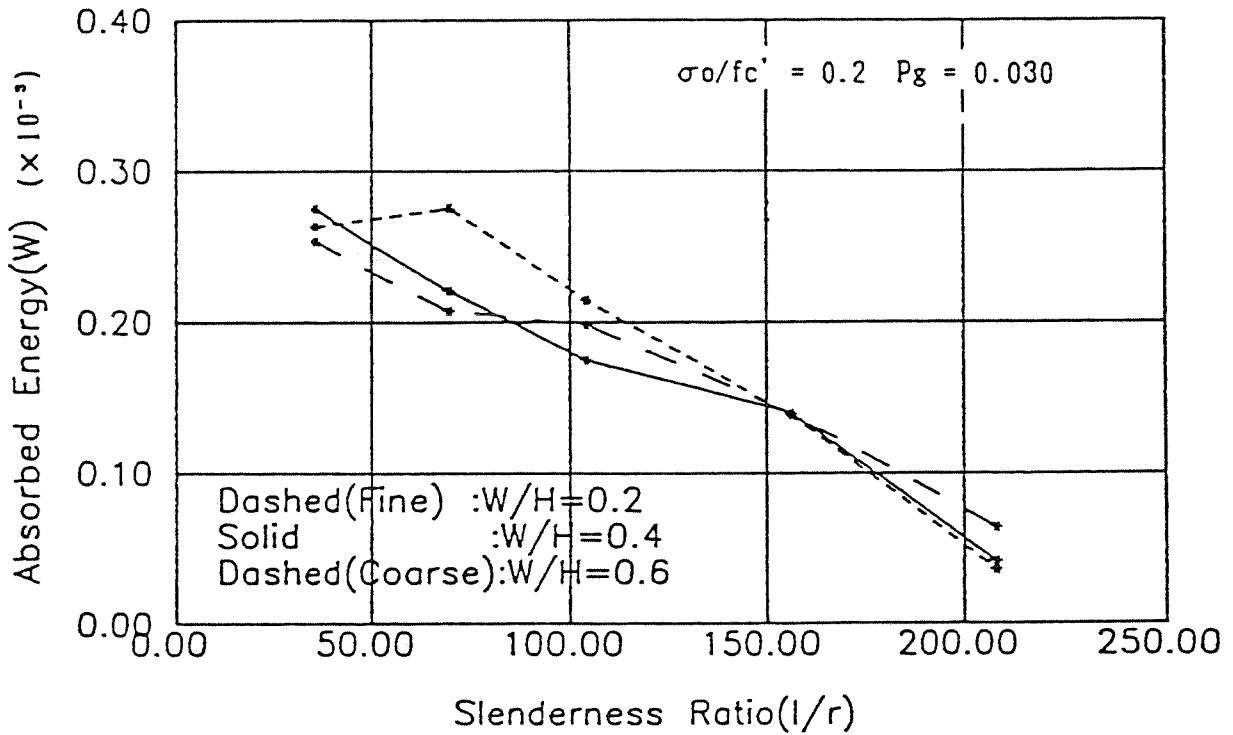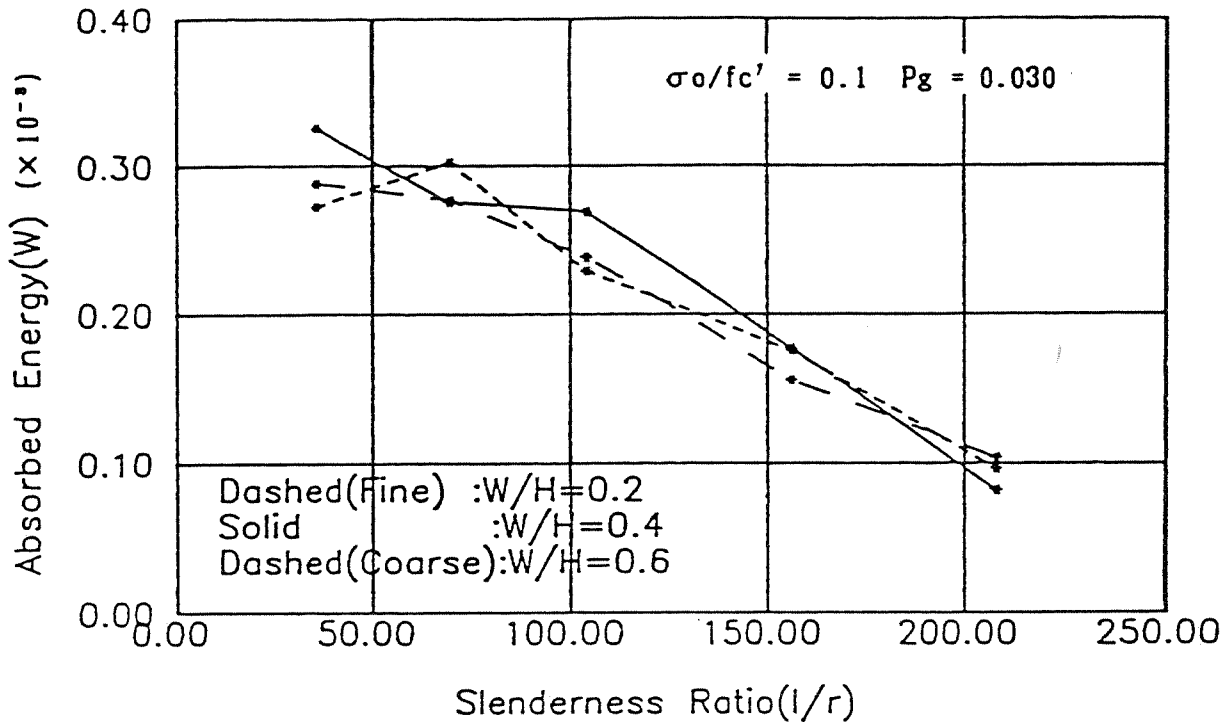Absorbed Energy−Slenderness Ratio Relationship(Pg=0.015)

Fig. 7-2
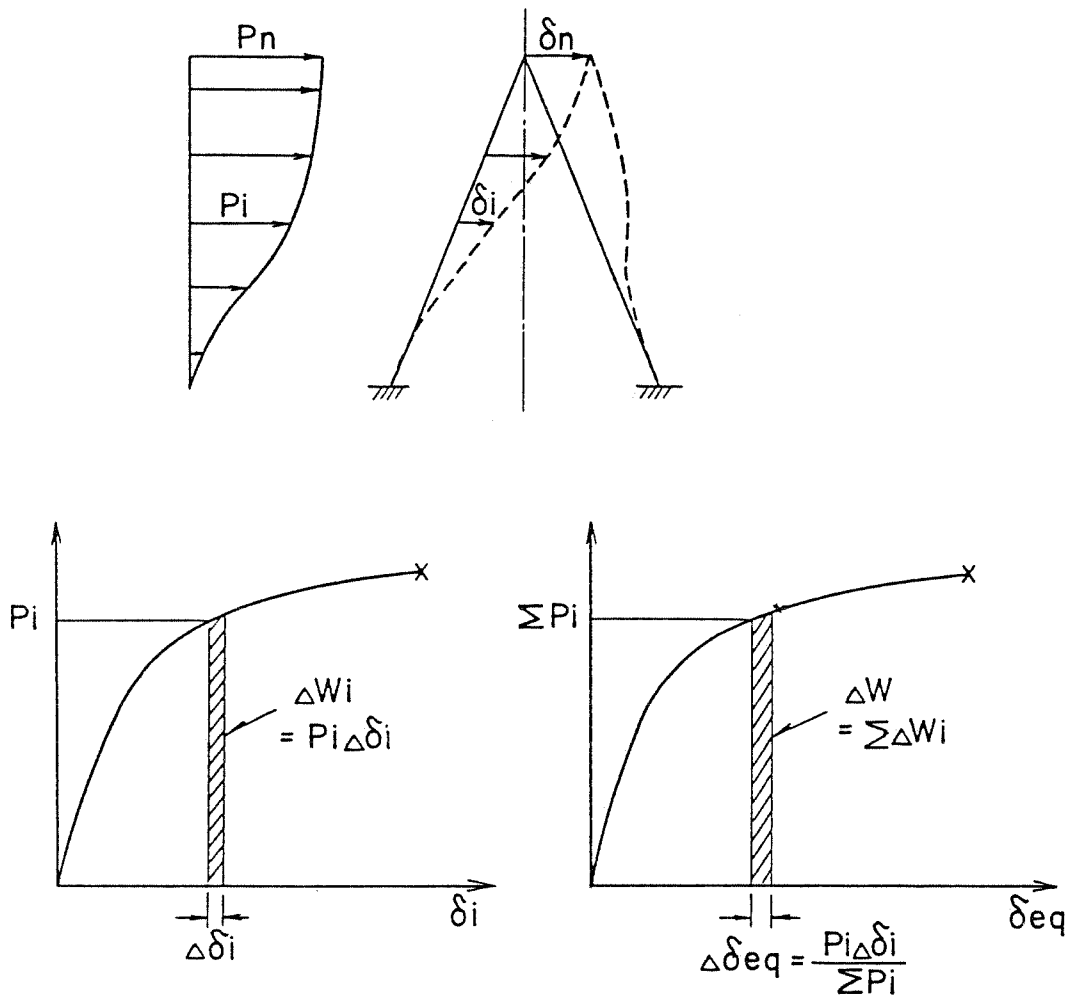Absorbed Energy-Slenderness Ratio Relationship(Pg=0.030)

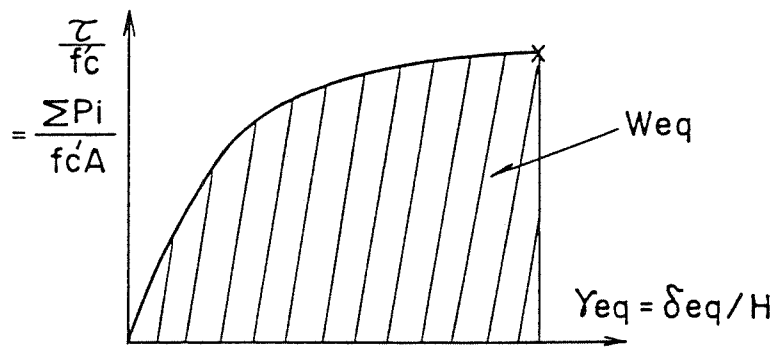Fig 7-3 A Reprentative Displacement Based on External Work
Equivalence



Fig 7-4  Non-dimensional Load-Displacement Relationship

shown in (7.3), makes it possible to compare substantial characteristics of structures with different dimensions. Finally a non-dimensional form of absorbed energy is expressed in eq.(7.4).

$$W_{eq} = \int \frac{\tau}{f'_c} d\gamma_{eq} \qquad \cdots\cdots\cdots\cdots(7.4)$$

An absorbed energy decreases in general as a slenderness ratio becomes larger since ultimate strength, $\tau_u$ is getting smaller.

The case of low axial load of $\sigma_0/f'_c = 0.1$ and small reinforcement ratio of $p_g = 1.5\%$ provides a drastic increase of absorbed energy in the smaller slenderness ratio region since a fair amount of plastic deformations can be accumulated under the action of tensile axial force (Fig.7-1 above). This tendency becomes remarkable for the smaller configuration case with W/H = 0.2. However, an unexpected result is obtained for the W/H = 0.2 and l/r = 35 case based on the reason that the opposite bottom leg section (Elem-22) is possibly critical in compressive failure under a larger variation of axial force.

The larger axial load case, meanwhile, provides a rather smaller absorbed energy as shown in Fig. 7-1 below with increased ultimate strength, but smaller ductility and critical in compression failure of concrete.

On the other hand, in case of larger reinforcement ratio with a $p_g = 3\%$ (Fig.7-2), a larger value is obtained than former case with a $p_g = 1.5\%$ in the entire region of l/r due to an increased ultimate capacity, but it is apparently limited by concrete failure particularly in the smaller slenderness ratio region.

Generally speaking, energy absorptoin capability decreases significantly in the region of l/r larger than 100 and therefore slenderness ratio usage in that region is not effective in the practical design .

(2) Analytical Parameters

Based on the description discussed above, the usage of members with large slenderness ratio is not recommendable.   In that sense, it can be practically sufficient to investigate cyclic characteristics of structures with a slenderness ratio up to $l/r = 104$.

Therefore, the following parameters are adopted for cyclic load analysis as shown in Table7-1.

Configuration Factor : $W/H = 0.4$

Reinforcement Ratio : $p_g = 1.5$ and $3.0\%$

Slenderness Ratio    : $l/r = 35$ and $104$ ($l/h = 10$ and $30$)

The examples of slenderness ratio used in practice are in the references as $44\sim69$ for Pasco Kennewnwick[15], 74 for East Huntington[14], 71 for James River bridge[12], all of which exist between 35 and 104 as parameters adopted in the present section.
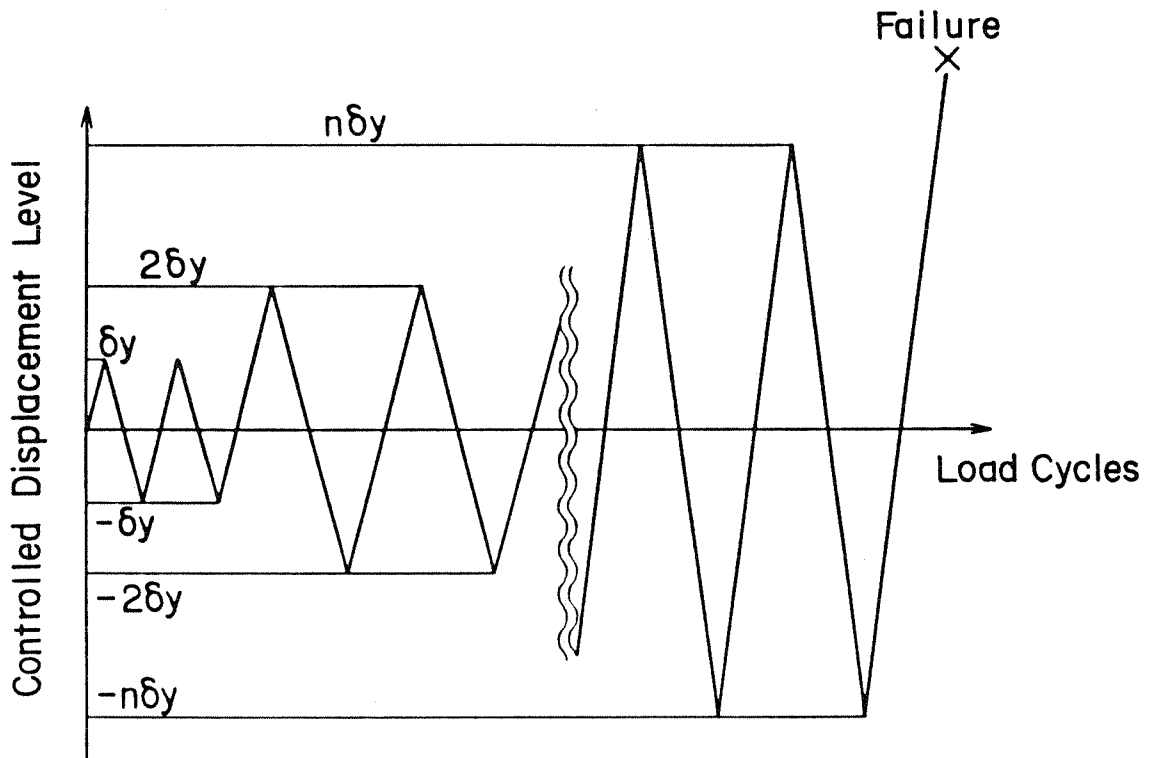

## 7.2  Cyclic Loading

It is appropriate to investigate a hysteretic behavior of the present structure under cyclic lateral load for estimation of its seismic resistant capability.
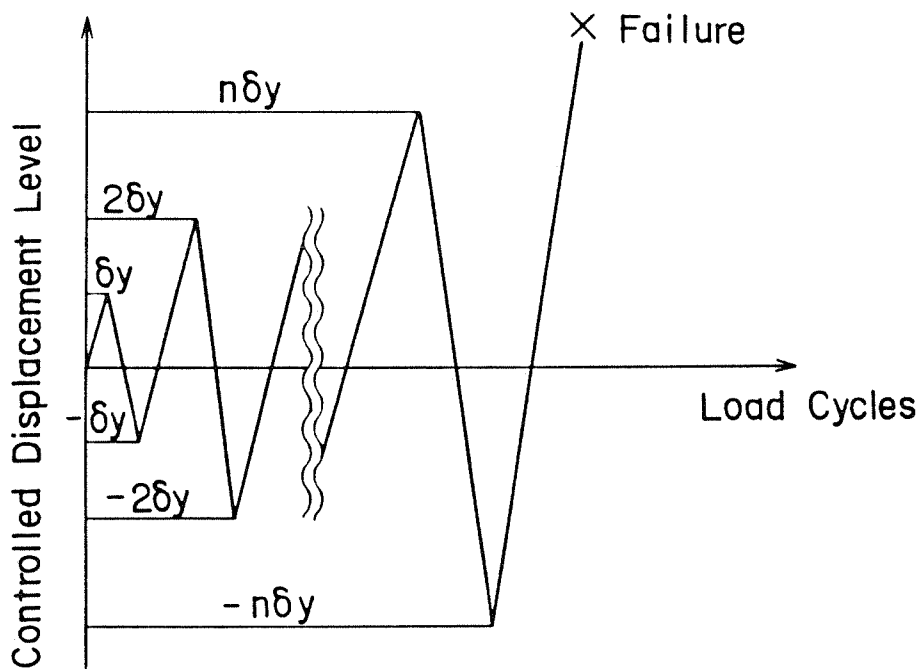
A displacement control type load application, as shown in Fig.7-5, is adopted based on the yield displacement, $\delta^y_{eq}$ defined by a tensile yielding of rebar at the bottom leg section.   Loaded are two cycles at each displacement level for the 1.5% reinforcement ratio series.   Meanwhile, as no influence of a cyclic number is found on the behavior through above studies as described later, only one cycle loading for each displacement level is applied with 3.0% reinforcement ratio series.


## 7.3  Deformation Characteristics and Cyclic Load Effect

In Fig.7-6~7-8, load-displacement relations are shown regarding the

Table 7-1　Ultimate States of A-Shaped Tower (L + Cyclic H Load)

| $P_g$ | $\dfrac{\sigma_o}{f'_c}$ | $\dfrac{W}{H}$ | Slenderness Ratio $l/h$ | $l/r$ | Crack | Eleml. TRY | 7 TRY | 11 TRY | 17 TRY | Elem.22 TRY | Elem.22 CRY | Elem.22 CC | Fail. Mode Rank | $\dfrac{\tau_u}{f'_c}$ | *1) $\dfrac{\tau_u}{\tau^0_u}$ | $\dfrac{\gamma_{max}}{\gamma_y}$ | *2) $\dfrac{\gamma_{max}}{\gamma^0_{max}}$ | $\delta_{bh}=M_2/M_2^e$ |
|---|---|---|---|---|---|---|---|---|---|---|---|---|---|---|---|---|---|---|
| 1.5 % | 0.1 | 0.4 | 10 | 35 | ○ | ○ | ○ | ○ | | ○ | ○ | | 1 | 0.0626 | 0.962 | 4.222 | 1.017 | 1.524 |
| | | | 30 | 104 | ○ | ○ | ○ | ○ | | ○ | ○ | | 1 | 0.0246 | 0.972 | 2.343 | 1.126 | 1.270 |
| | 0.2 | | 10 | 35 | ○ | ○ | | | | | ○ | ○ | 2 | 0.0817 | 0.980 | 2.096 | 1.103 | 1.223 |
| | | | 30 | 104 | ○ | ○ | | | | ○ | ○ | ○ | 2 | 0.0276 | 0.965 | 1.532 | 1.054 | 1.405 |
| 3.0 % | 0.1 | | 10 | 35 | ○ | ○ | ○ | ○ | | ○ | ○ | | 1 | 0.0959 | 0.951 | 2.452 | 0.991 | 1.413 |
| | | | 30 | 104 | ○ | ○ | ○ | | | | ○ | ○ | 1 | 0.0421 | 0.977 | 2.197 | 0.992 | 1.116 |
| | 0.2 | | 10 | 35 | ○ | ○ | | | | ○ | ○ | ○ | 2 | 0.1068 | 0.970 | 1.721 | 1.091 | 1.223 |
| | | | 30 | 104 | ○ | ○ | | | | ○ | ○ | ○ | 2 | 0.0401 | 0.952 | 1.270 | 0.972 | 1.253 |

TRY : Tensile Yielding of Rebar　　CRY : Compressive Yielding of Rebar　　CC : Concrete Crush

*1) Rate of ultimate strength under L + cyclic H.Load to that under S + H Load

*2) Rate of ductility factor $\gamma_{max}/\gamma_y$　under L + cyclic H.Load to that under S + H Load

(a) Two Cycles for Each Displacement Level
(Pg=1.5% Series)

(b) One Cycle for Each Displacement Level
(Pg=3.0% Series)

Fig. 7-5  A Displacement Control Cyclic Load Application
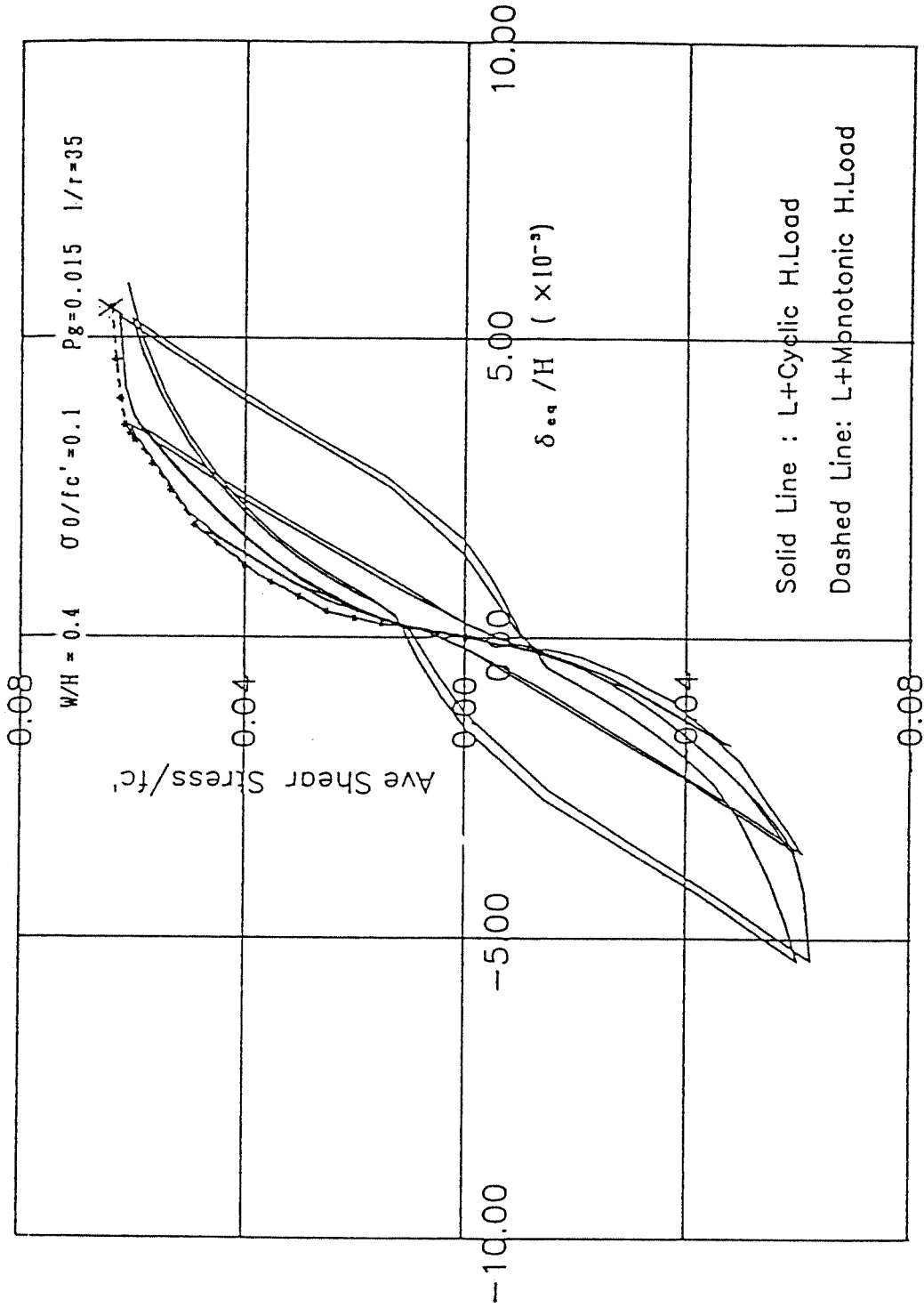
Fig. 7-6  Load-Displacement Relationship(Equivalent Displacement)
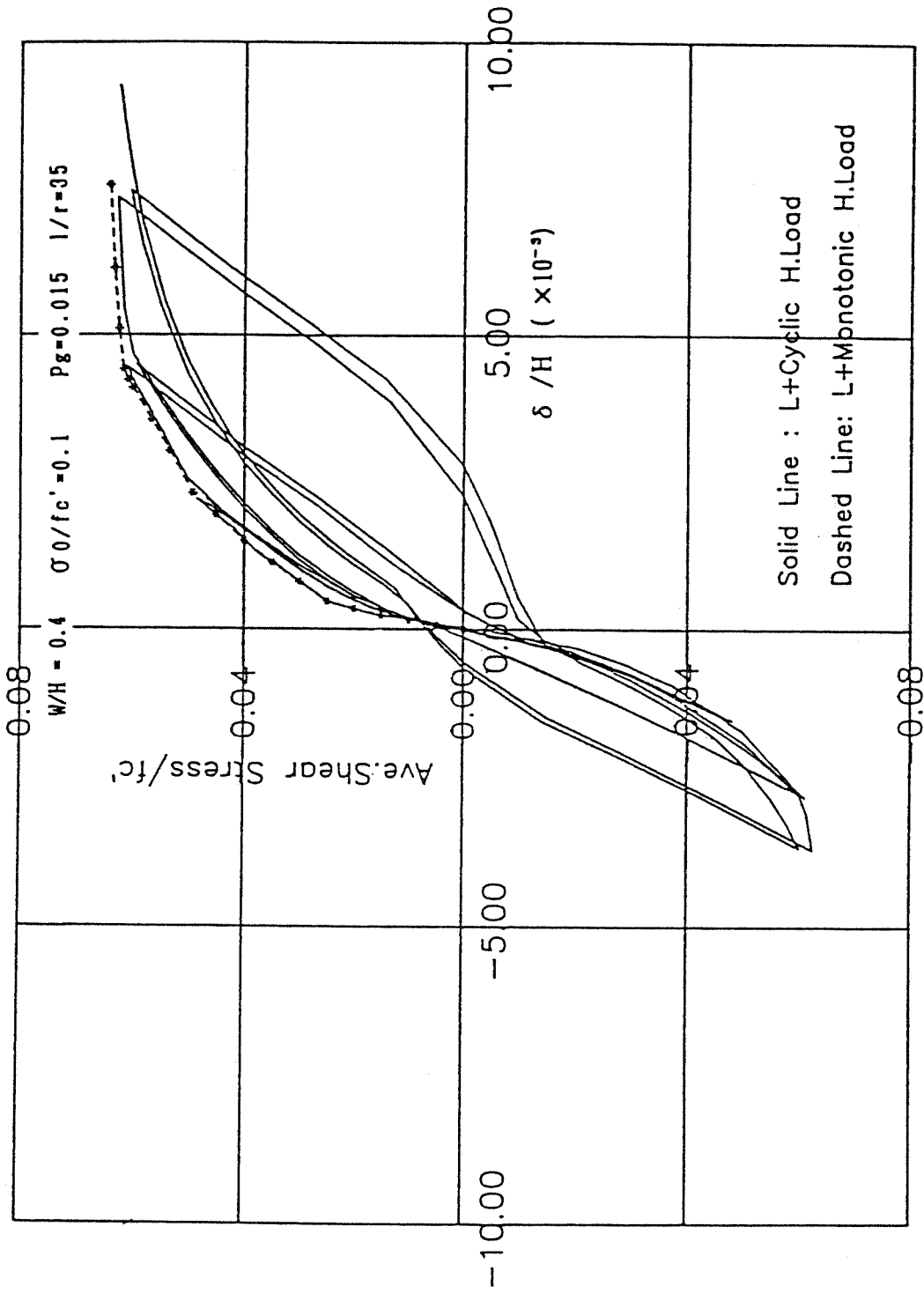
Fig. 7-7  Load–Displacement Relationship(Node—7)
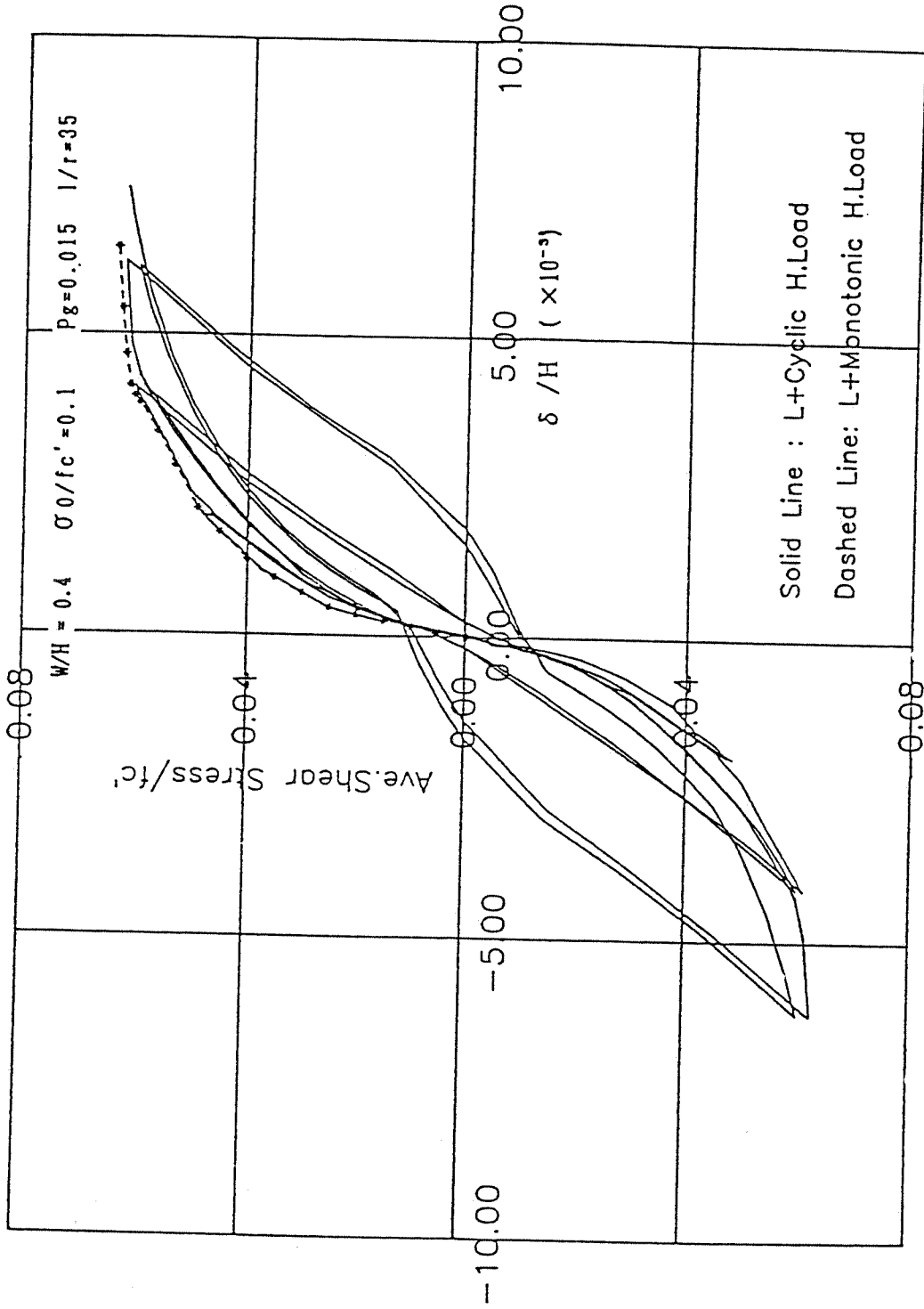
Fig. 7-8   Load-Displacement Relationship(Node-12)

equivalent displacement defined by eq.(7.3), the mid-part displacement (Node-7) and the top displacement (Node-12) for the case of $\sigma_0/f'_c = 0.1$, $p_g = 1.5\%$ and $l/r = 35$, where each coordinate is respectively provided as the average shear stress at bottom leg section divided by $f'_c$ and as the displacement divided by a tower height, H.

Based on the definition of section 7.1, the load-equivalent displacement relationship of Fig.7-6 can represent hystretic characteristic as an entire structure. With failure directly before reaching $4\delta_y$, the loading capacity is slightly smaller, but the maximum displacement is rather larger than the monotonic loading case. An S-shaped loop exists in the appearance, but a fairly good energy absorption capability is obtained. An unsymmertric loop shape is observed for the mid-part displacement (Node-7) as shown in Fig.7-7. The reason for this is that the column member where that node is located has larger plastic deformation under the tensile axial force against positive load, but has larger stiffness under the compressive axial force against negative load. However, an antisymmetric relationship is expectedly observed for the top displacement (Node-12) because of the appearance of the averaged behavior as shown in Fig.7-8.

Fig.7-9~7-11 show similar load-displacement relations for larger slenderness ratio cases with $l/r = 104$. With failure in the loading cycle around $2\delta_y$, a plastic deformation less than the previous series exists because of a smaller variation of axial force. The ultimate strength and the ultimate displacement are both similar to the values of the monotonic loading case. It can be said that comparatively good capability in absorbed energy appears despite the lack of ductility. Unsymmetric behavior is also observed for the mid-part displacement (Fig.7-10). The top displacement is considerably smaller as shown in Fig.7-11 because of less overturning deformation compared with flexural deformation which dominates more in the mid-part of legs.

Fig. 7-12~7-13 show load-equivalent displacement relations for the higer
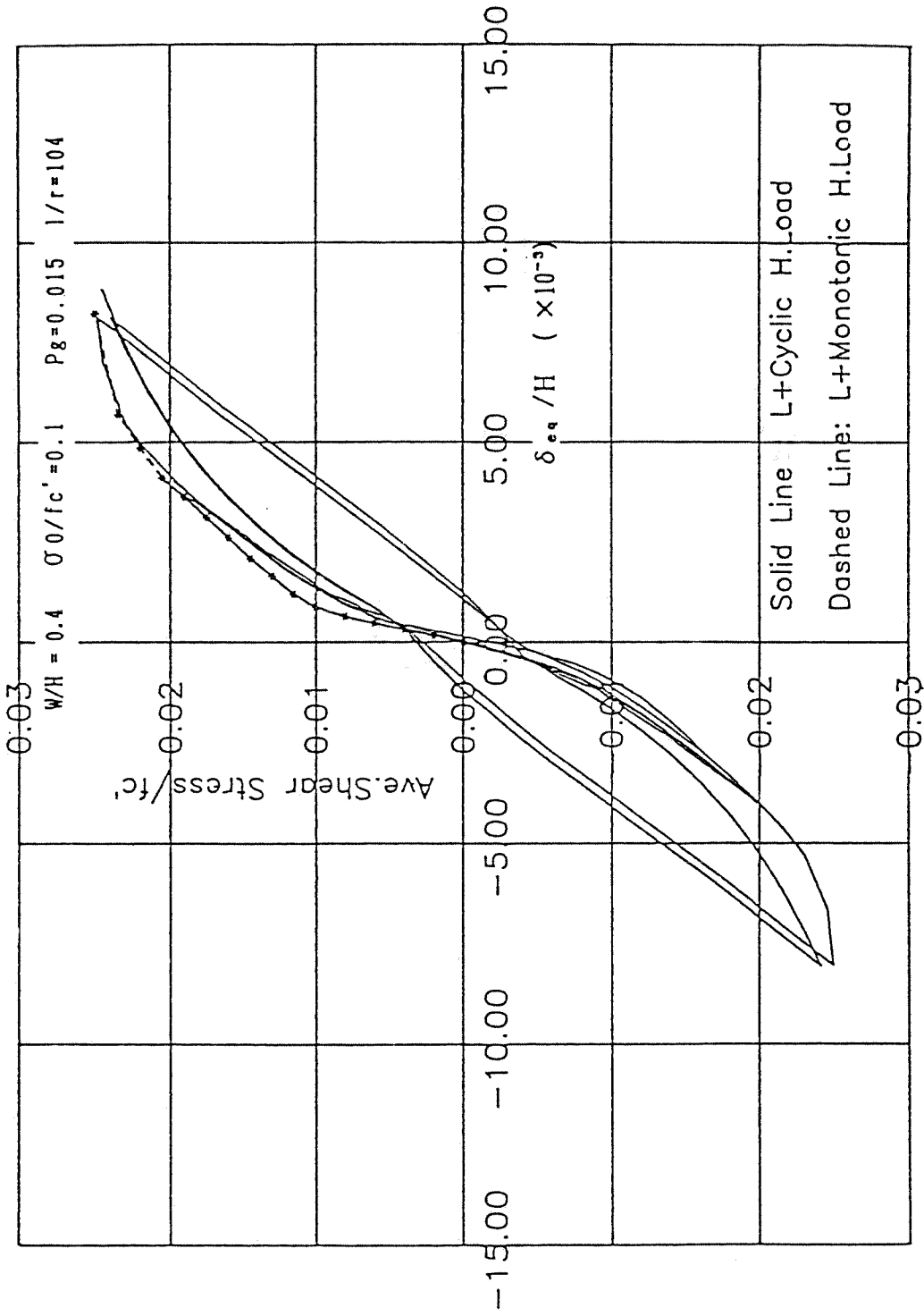
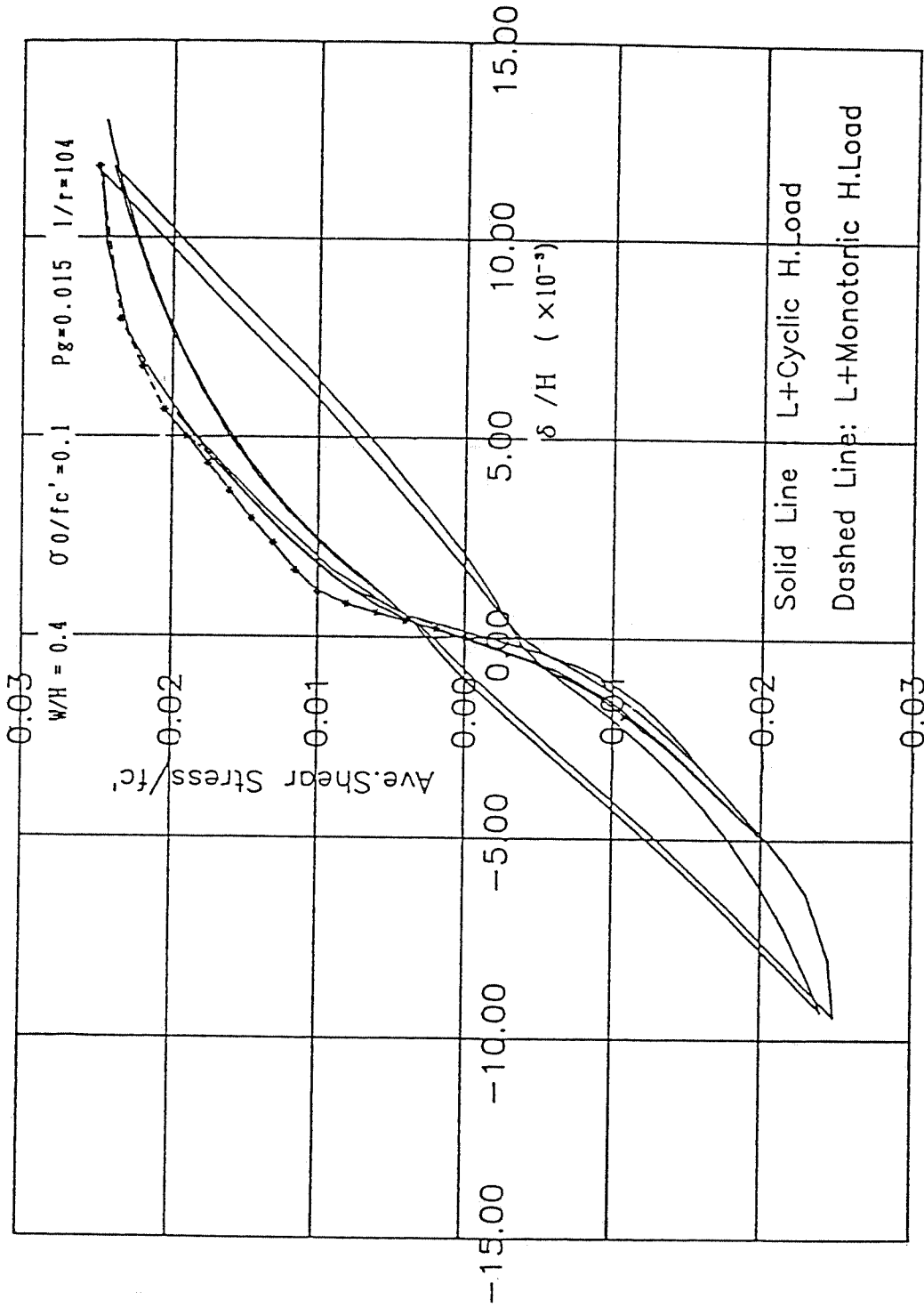Fig. 7-9  Load–Displacement Relationship(Equivalent Displacement)
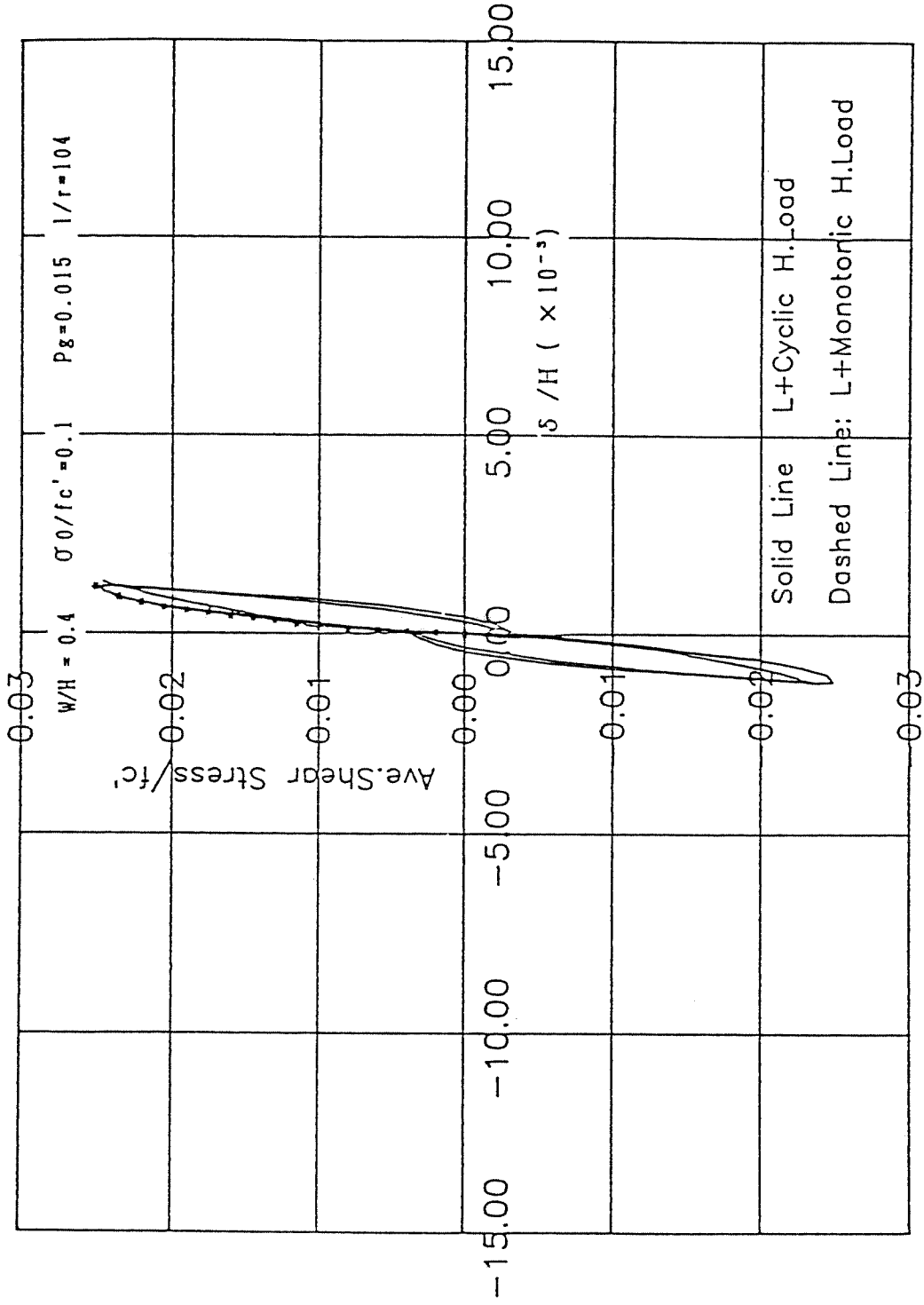
Fig. 7-10  Load−Displacement Relationship(Node−7)
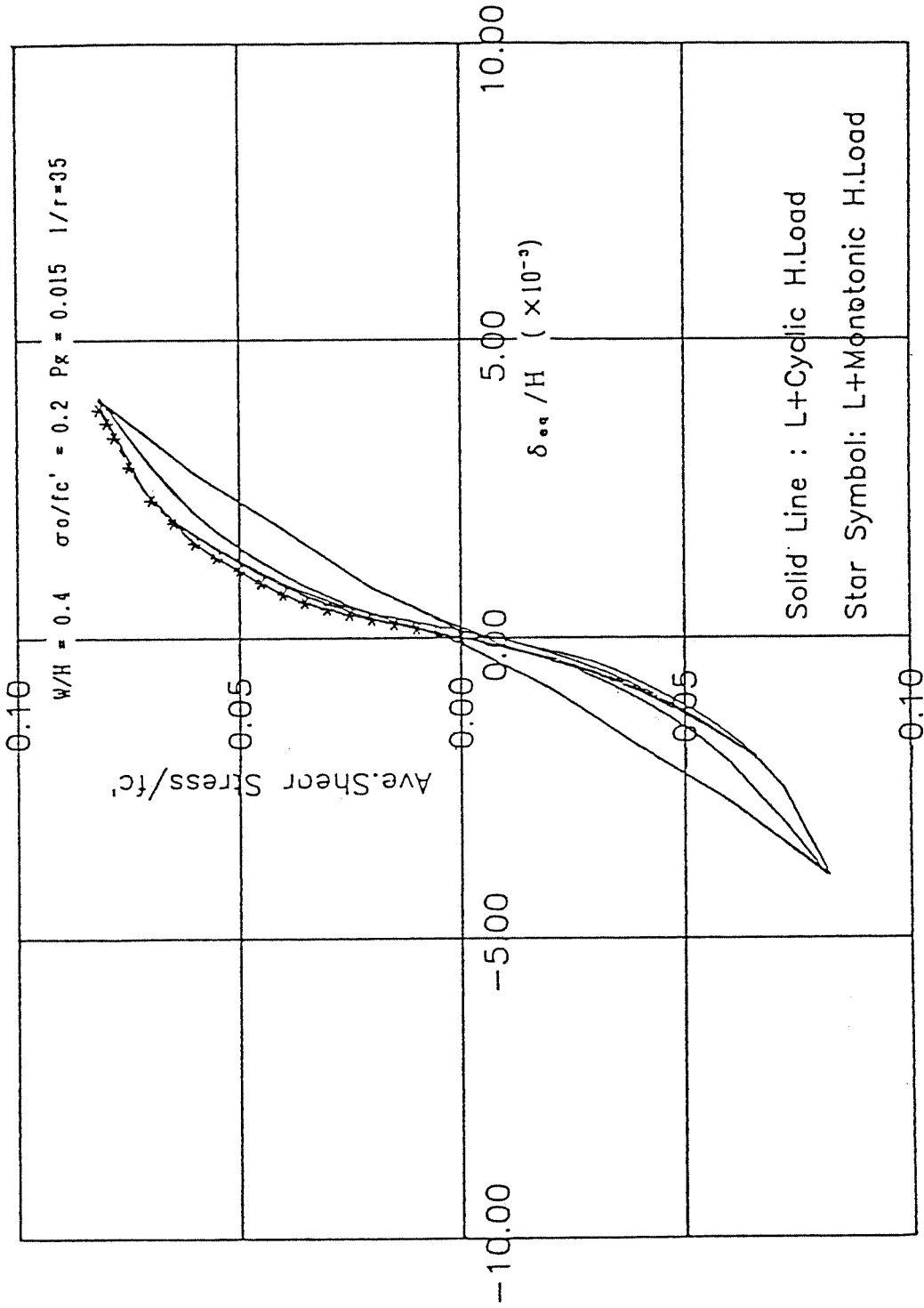
Fig. 7-11　Load—Displacement Relationship(Node—12)

Fig. 7-12 Load-Displacement Relationship(Equivalent Displacement)
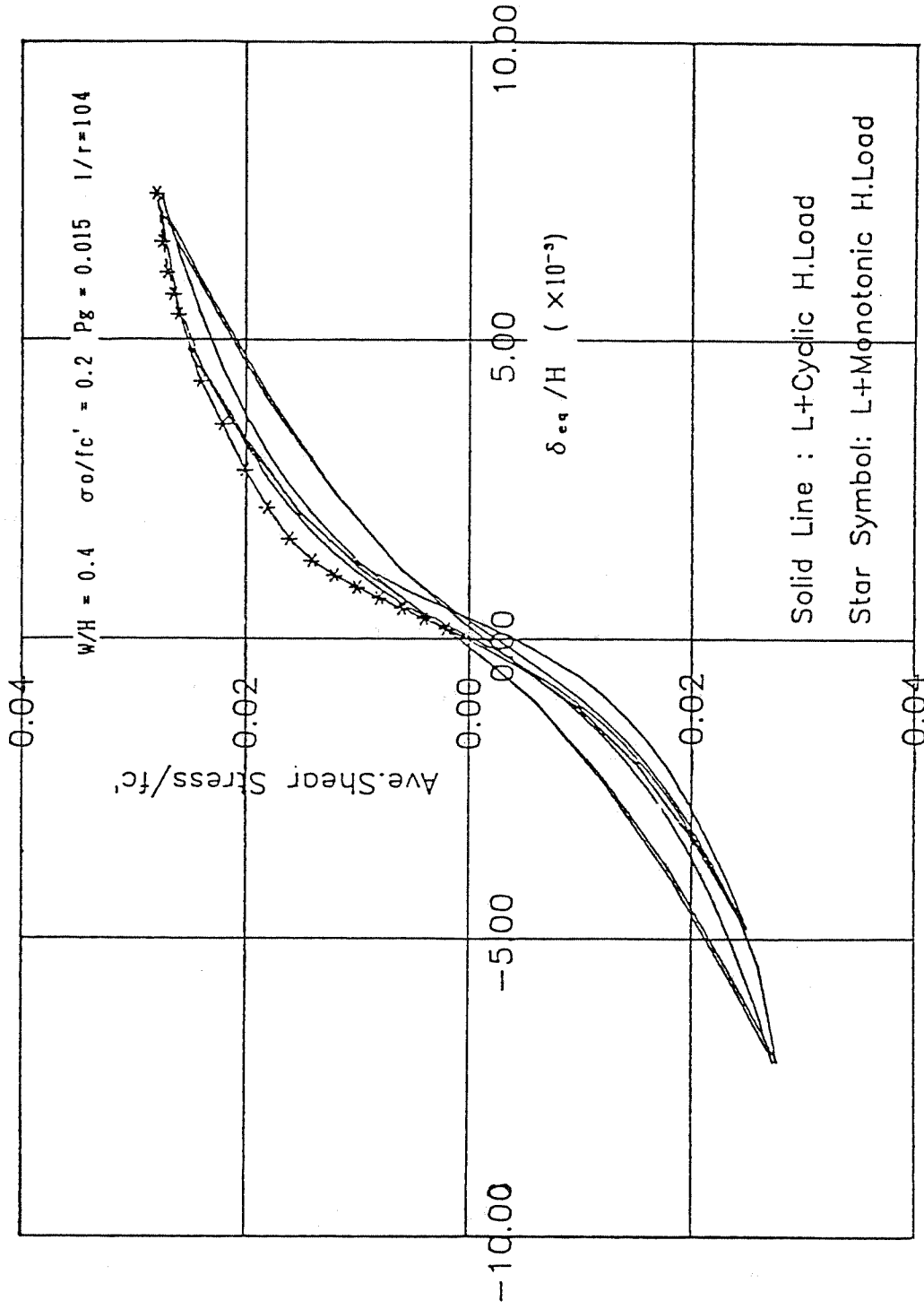
Fig. 7-13   Load-Displacement Relationship(Equivalent Displacement)

axial load case of $\sigma_0/f'_c = 0.2$.   Both of them fail with an ultimate displacement around $2\delta_{eq}$ since the concrete becomes critical in a compressive failure.

The loop shape becomes thin as affected by higher axial load, and the ultimate strength, ductility and skelton curves are similar to the monotonic loading case.

In the Fig.7-14~7-17, load-rebar strains at the bottom section are shown for $p_g = 1.5\%$ cases.  Larger plastic strain is observed in the lower slenderness ratio case which provide a larger axial load variation and the unloading curve moves back to origin more as an axial load becomes larger.   These phenomenon correspond to the displacement characteristics discussed above.

Fig. 7-18~7-21 also show load-equivalent displacement relation for the larger rebar ratio series of $p_g = 3\%$.   As for the $p_g = 1.5\%$ series, the lower axial load case with $\sigma_0/f'_c = 0.1$ indicates good energy absorption capability, but the higher case with $\sigma_0/f'_c = 0.2$ provides less.   The concrete becoming more critical in compressive failure is one of reasons why only about two as a ductility factor is obtained in the larger rebar ratio case.   However, because no considerable differences of ultimate strength and ductility in comparison with monotonic loading occur, it suggests that the influence of cyclic load is less.

## 7.4 Cyclic Load Effect on Moment Behavior
### (1) M-N Relationships

Fig.7-22 show the M-N relationships of nodes 1, 8 and 23 for the $p_g = 1.5\%$, $\sigma_0/f'_c = 0.1$ and $l/r = 35$ case.   The unloading path becomes different from the loading one in the region where the axial force moves to tensile side and when large plastic strain is loaded in tensile rebar with a larger variation of axial force. These are dependent on the fact that the resisting section stiffness during unloading becomes different from that during loading if a certain amount of residual deformation remains due to the existence of crack and rebar yielding.
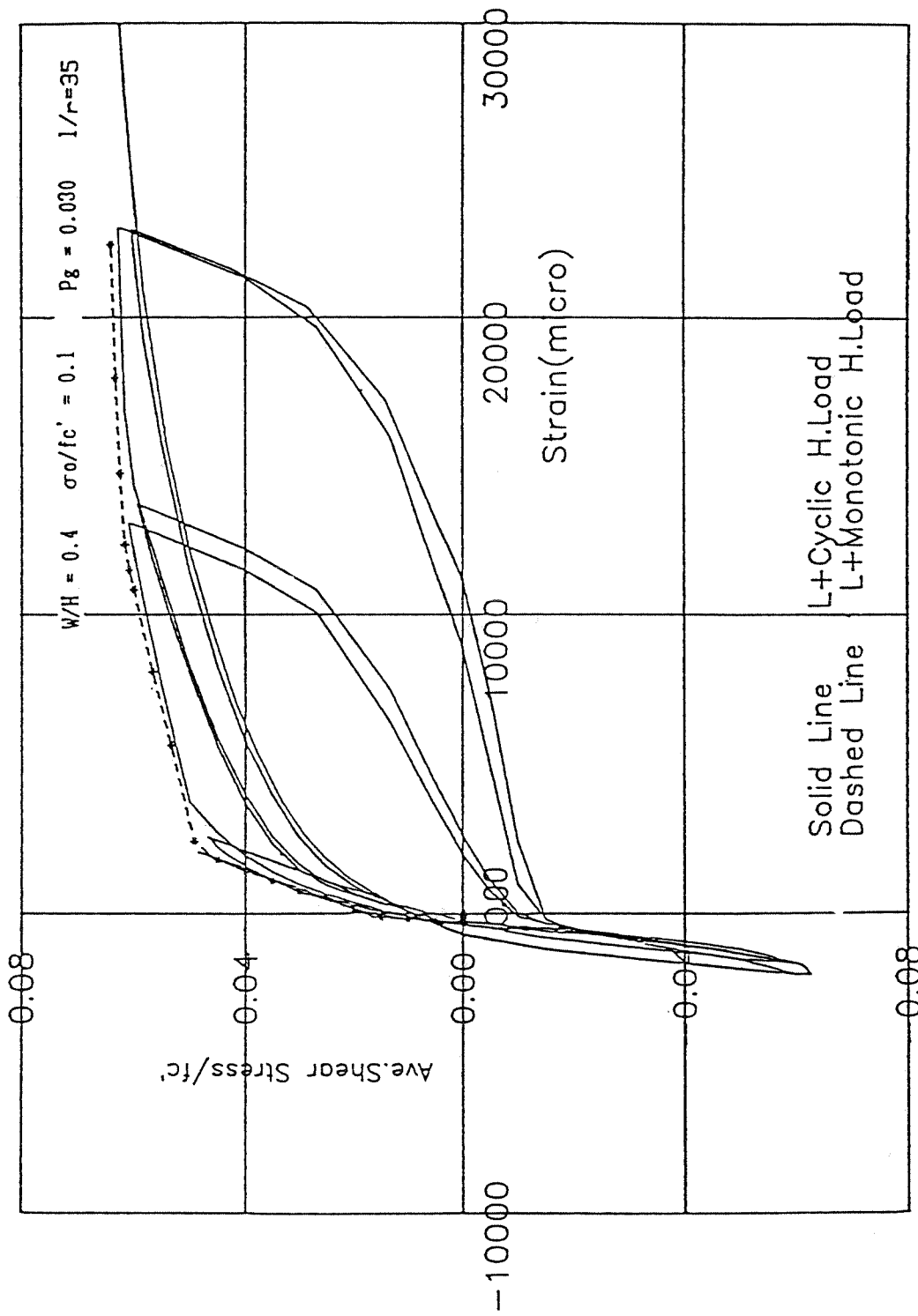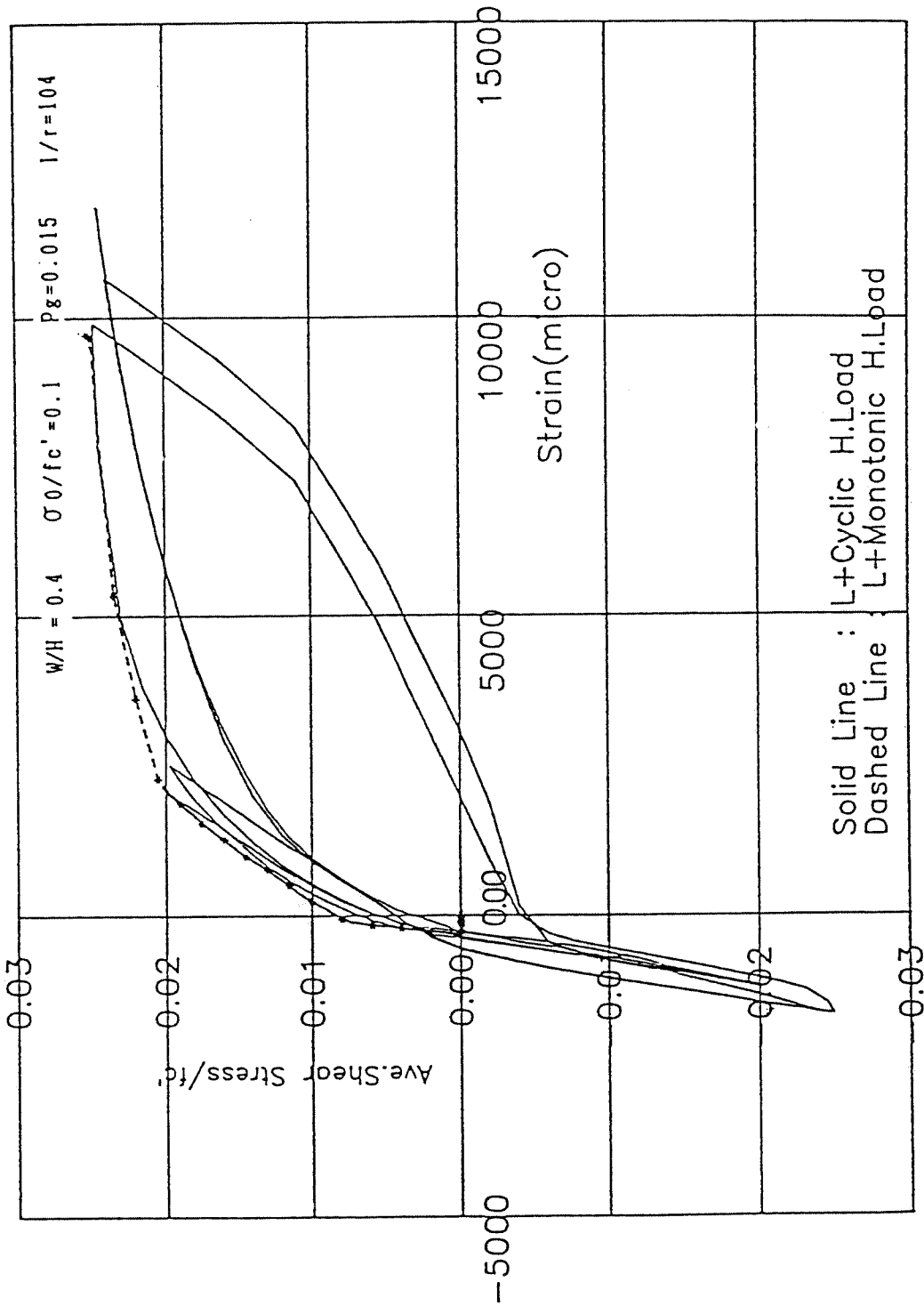
Fig. 7-14   Load-Rebar Strain Relationship(Elem-1,Outer)
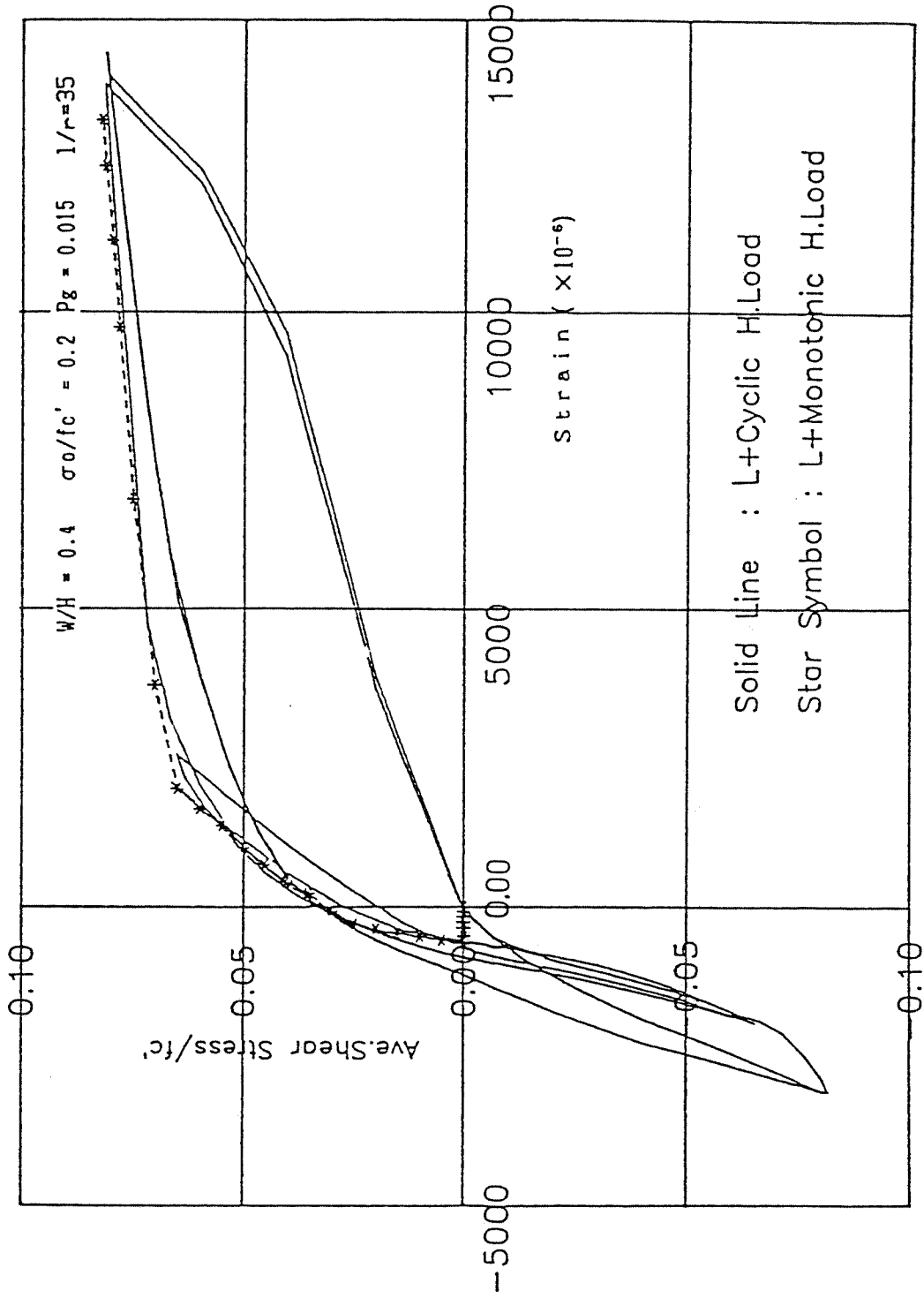
Fig. 7-15  Load–Rebar Strain Relationship(Elem–1,Outer)

Fig. 7-16  Load-Rebar Strain Relationship(Elem-1,Outer)

W/H = 0.4    σo/fc' = 0.2  Pg = 0.015   l/r = ln4

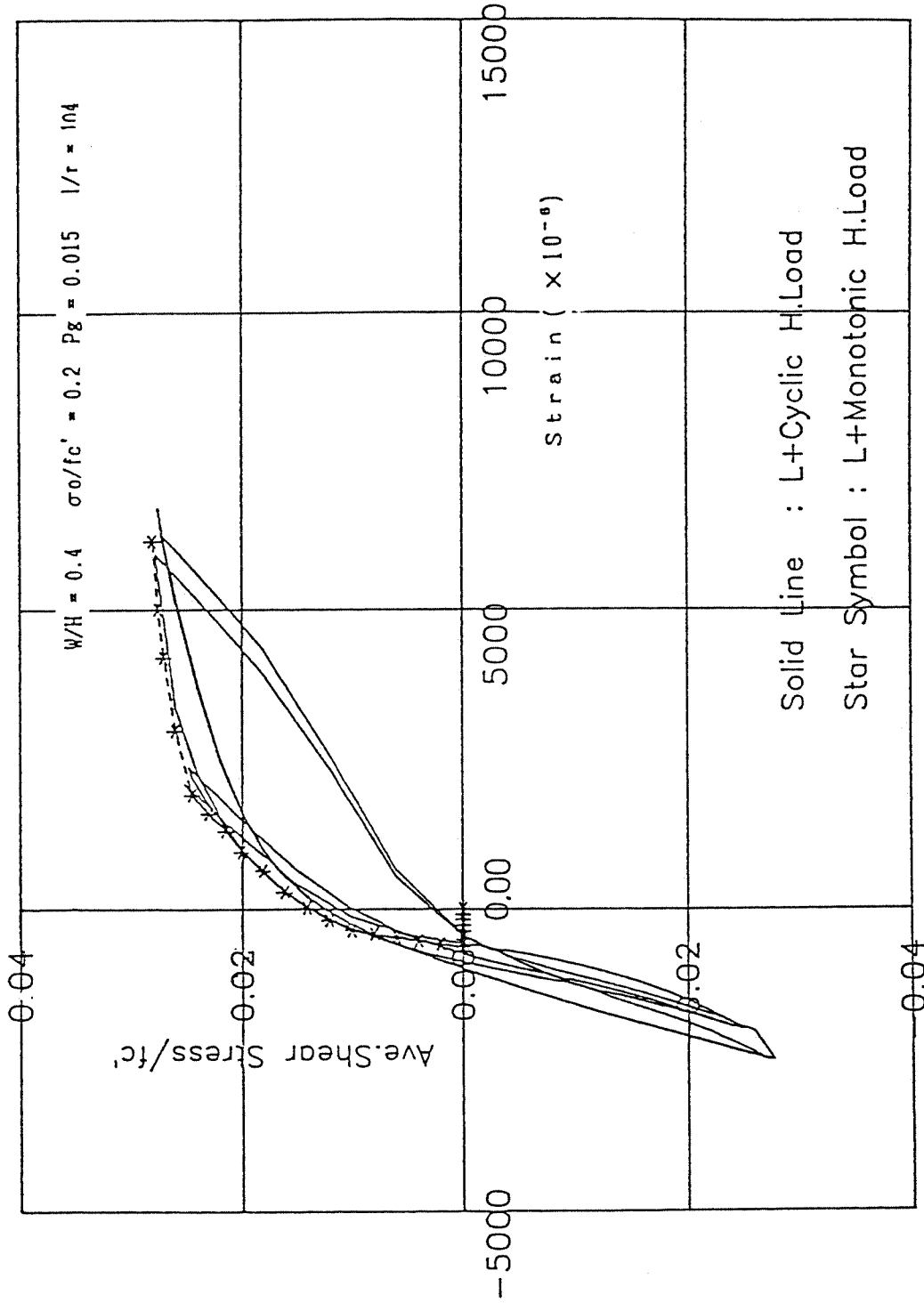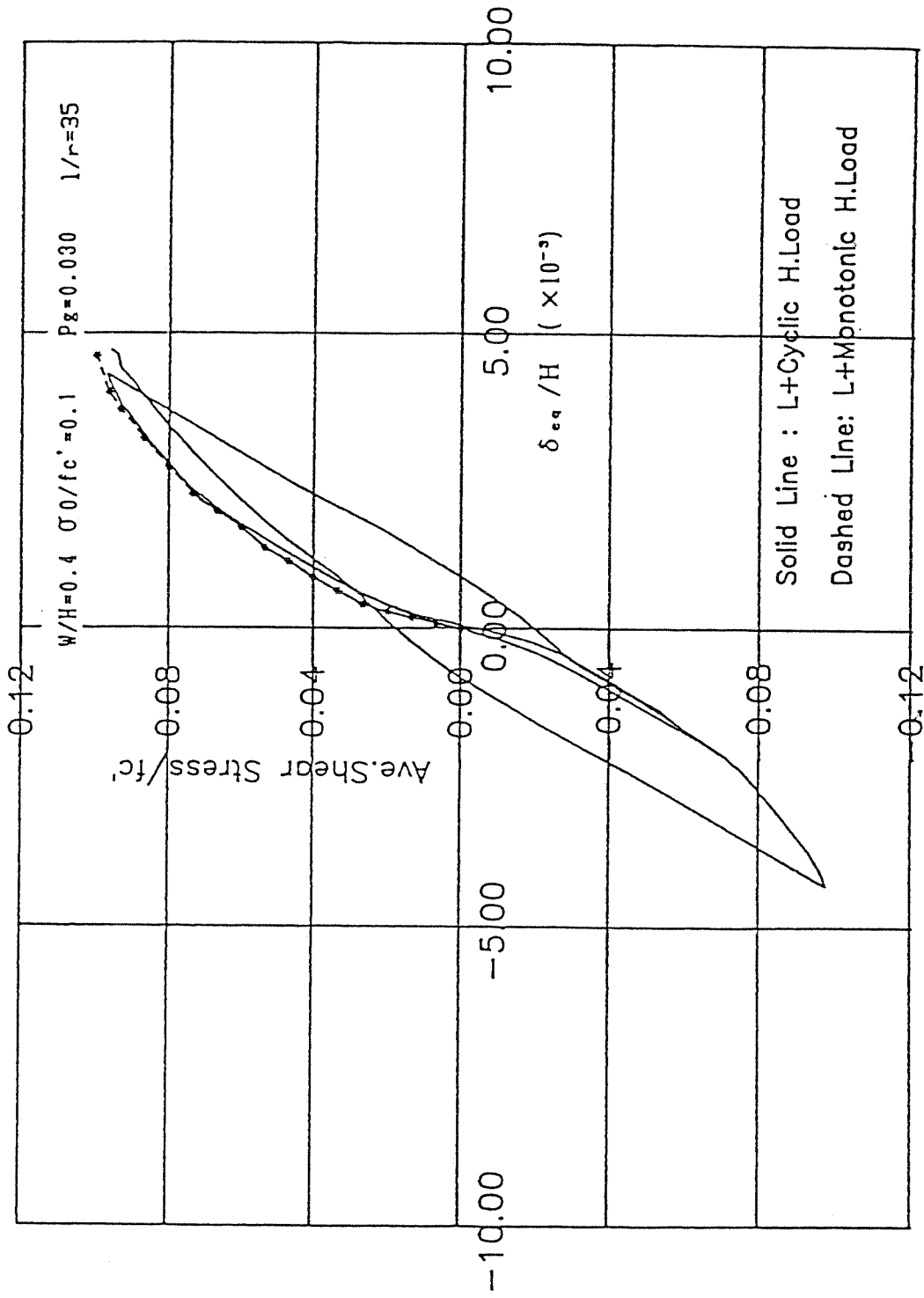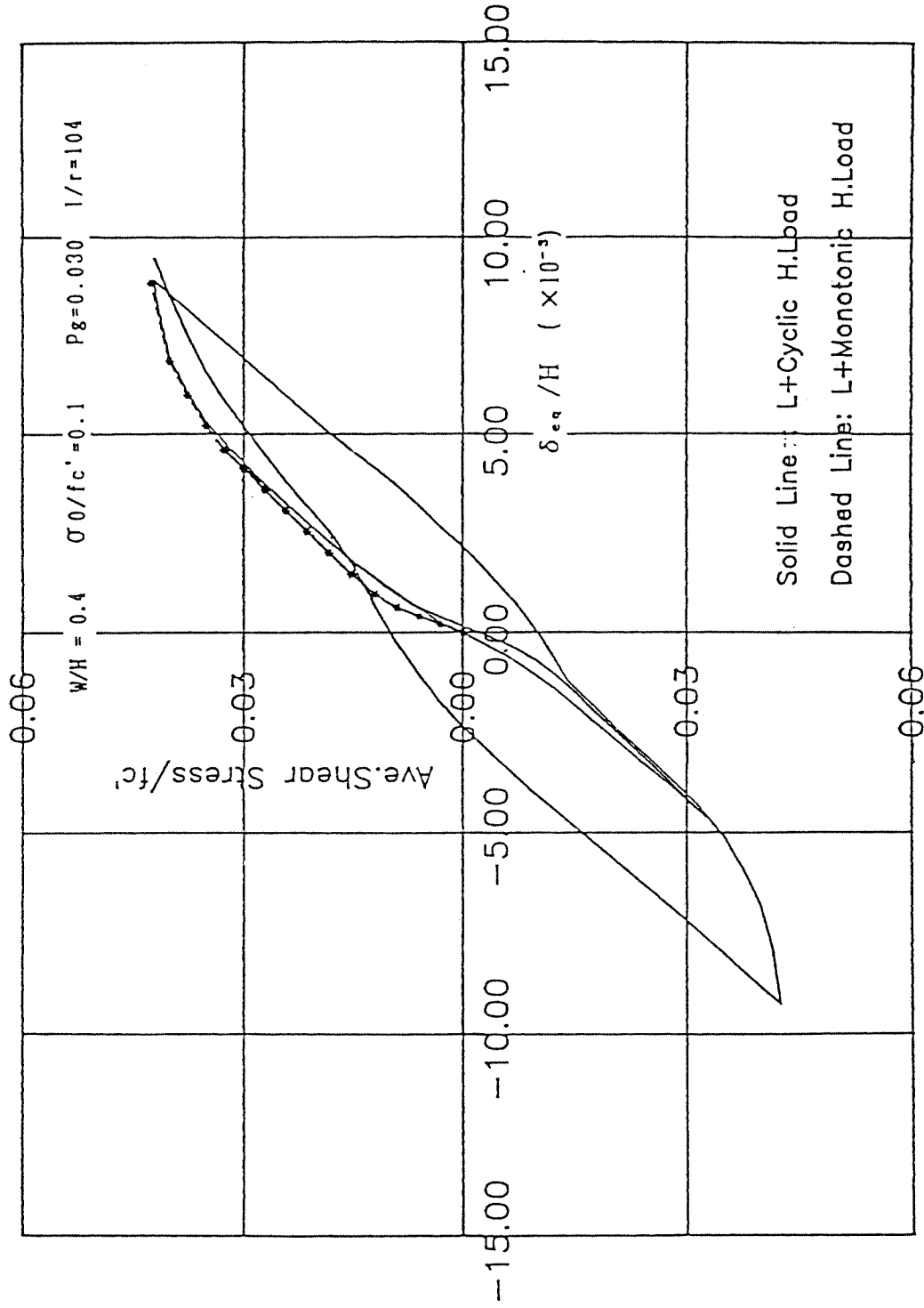Solid Line  : L+Cyclic H.Load

Star Symbol : L+Monotonic H.Load
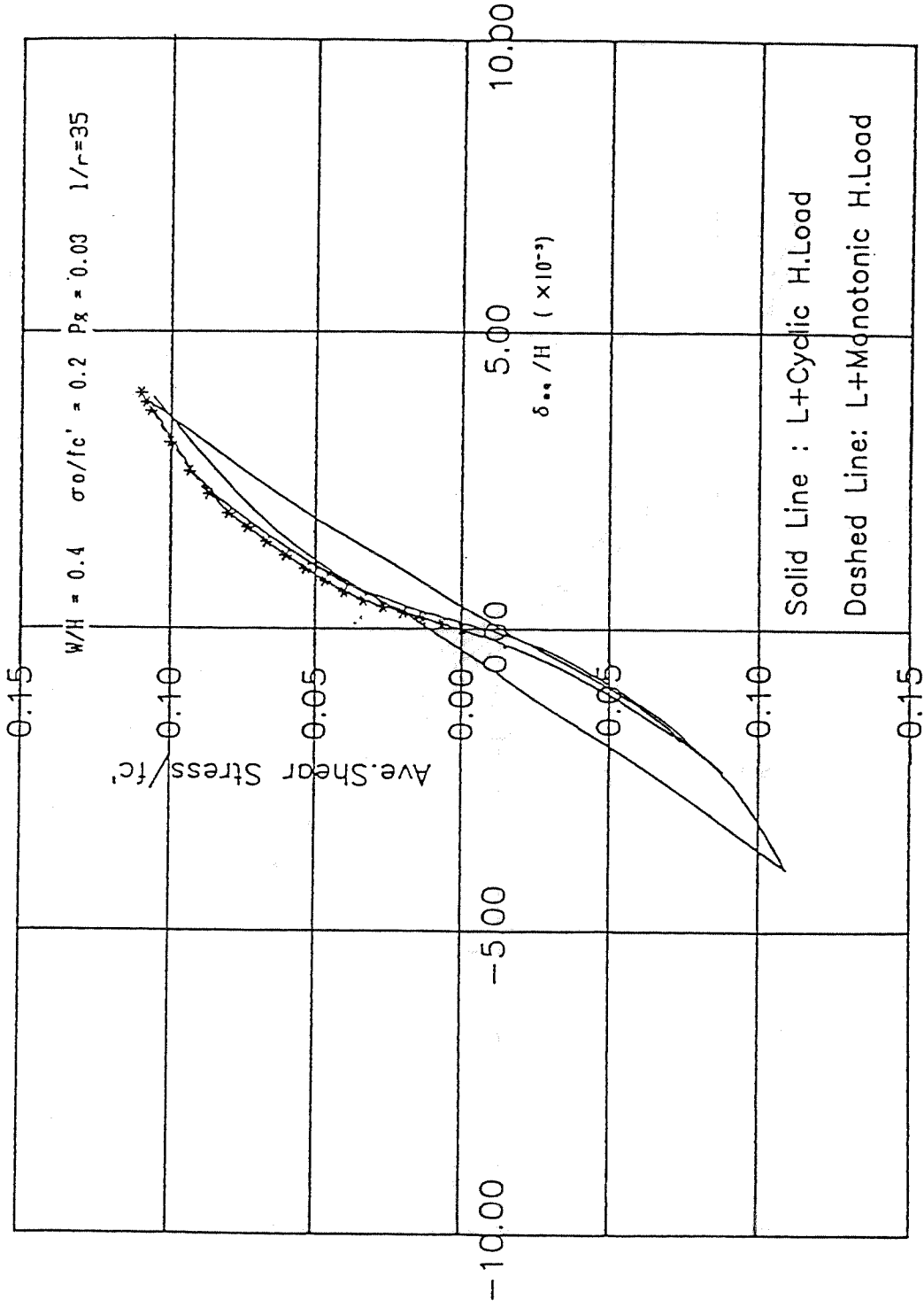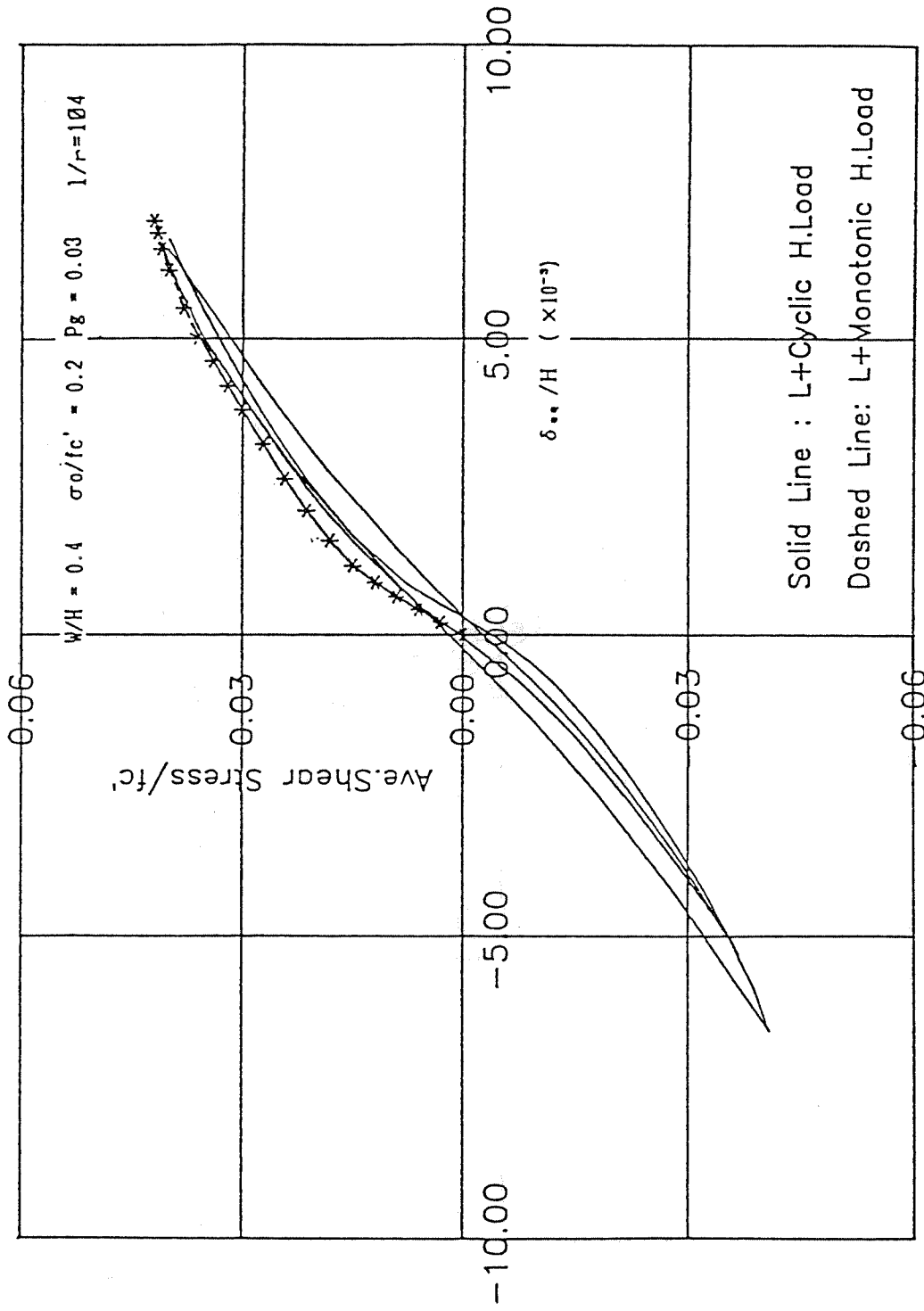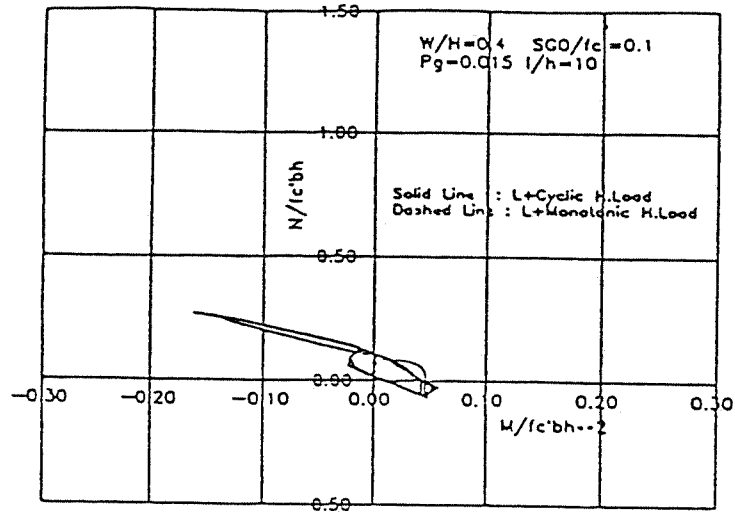
Fig. 7-17  Load-Rebar Strain Relationship(Elem-1,Outer)

Fig. 7-18 Load-Displacement Relationship(Equivalent Displacement)

Fig. 7-19   Load-Displacement Relationship(Equivalent Displacement)
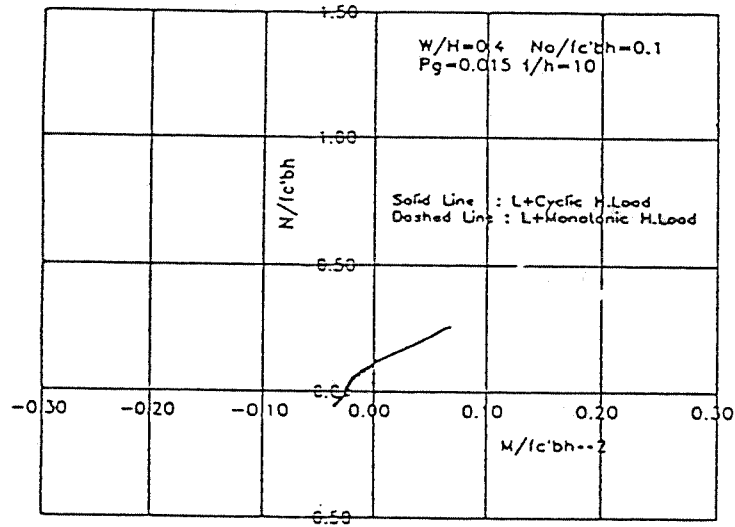
Fig. 7-20 Load-Displacement Relationship(Equivalent Displacement)

Fig. 7-21 Load-Displacement Relationship(Equivalent Displacement)
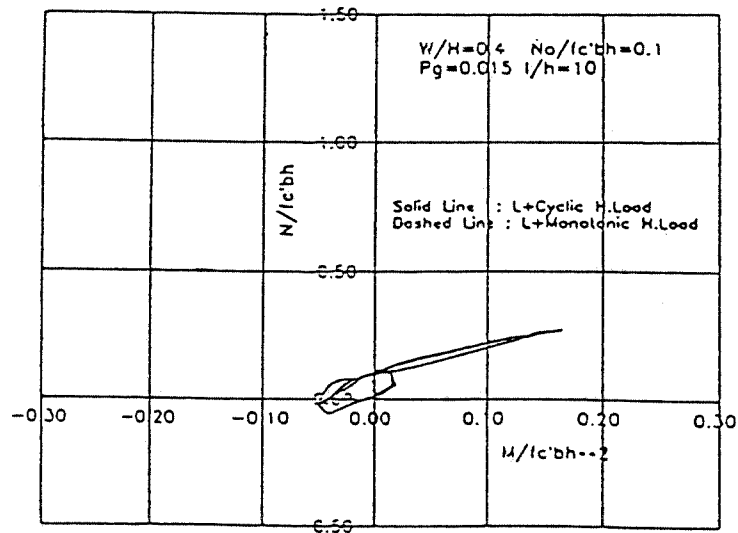
(a) Node-1

(b) Node-8

(c) Node-23

Fig.7-22  M-N Relationship (W/H=0.4   σo/fc'=0.1   Pg=0.015  1/r=35)

For the larger compressive axial force level, similar stress paths are obtained in general, but in the maximum displacement cycle, a slight difference exists between loading and unloading paths. The unloding path is below the loading one, which means a larger moment is imposed during unloading to compensate for the reduced moment in the opposite bottom leg section . Such stress path differences are not observed in the mid-section as shown in the Fig.7-22b because less plastic deformation is imposed.

Fig.7-23 are the similar M-N relationships for node 23 for different slenderness ratio and axial load cases. The $l/r = 104$ cases with less axial force variation provide little difference between loading and unloading paths, and in other words, impose very little residual strain.

## (2) P-M and P-N Relationships

Load-axial force and load-flexural moment relationships are shown in Fig.7-24 for $p_g = 1.5\%$, $\sigma_0/f'_c = 0.1$ and $l/r = 35$ case. After the large tensile plastic strain is imposed up to the maximum load of cycle, a resisting moment during unloading decreases by residual stain due to crack and rebar yielding. As a result, the P-M loop shows a different path between loading and unloading, which has already been described.

The reason why the moment reaches the negative region during unloading after positive maximum load as shown in the Fig.7-24a, c, can be explained as follows. An axial force variation causes the tensile rebar to recover and reach a large compressive stress and as a result, moment sign can be changed. It should be noted that the moment path could be varied, but axial force path varies very little under cyclic load. Antisymmetric behavior are expectedly observed between Node-1 and Node-23 (Fig.7-24a and c) and less variation of moment for Node-8.

Fig.7-25 are also added for another case with similar phenomenon. Although the moment path could be different in the intermediate load region
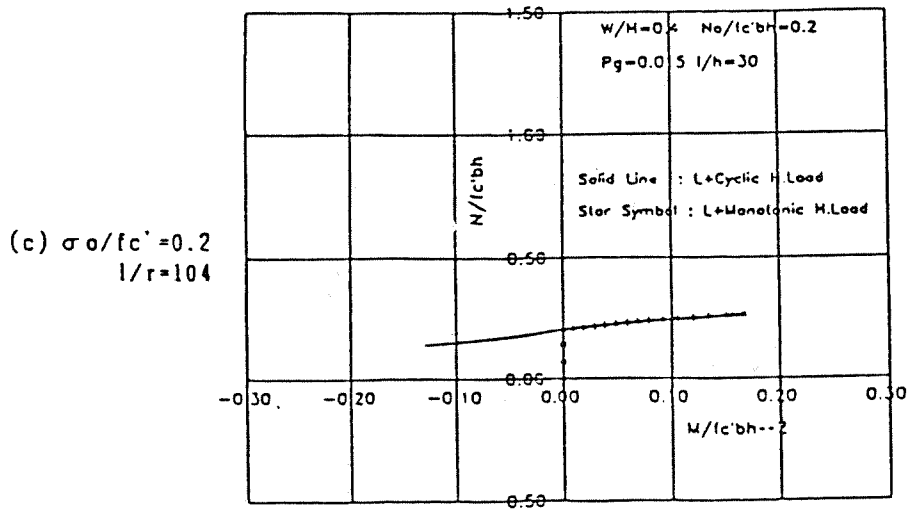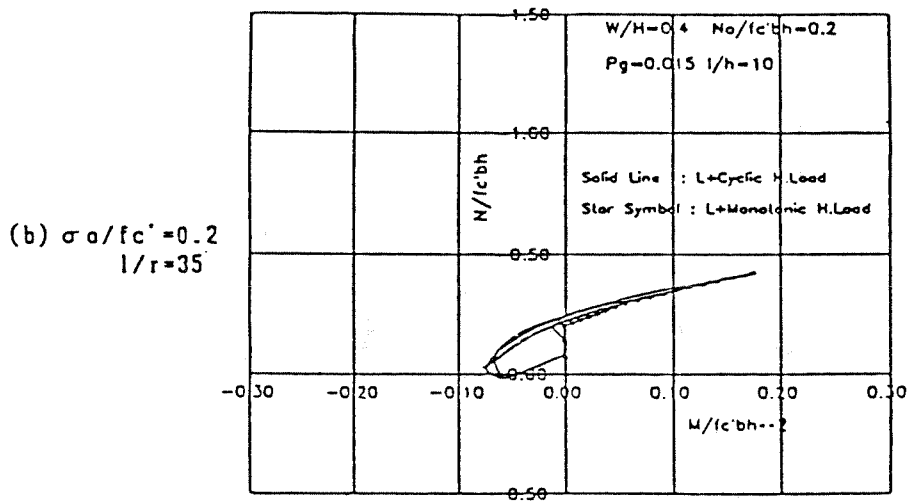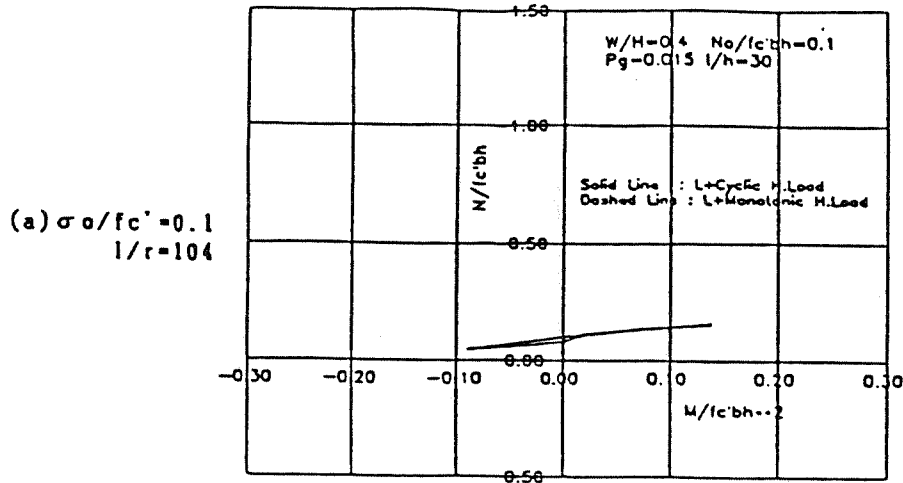
(a) $\sigma o / f c' = 0.1$
    $1/r = 104$

(b) $\sigma o / f c' = 0.2$
    $1/r = 35$

(c) $\sigma o / f c' = 0.2$
    $1/r = 104$

Fig.7-23   M-N Relationship (W/H=0.4, Pg=0.015)
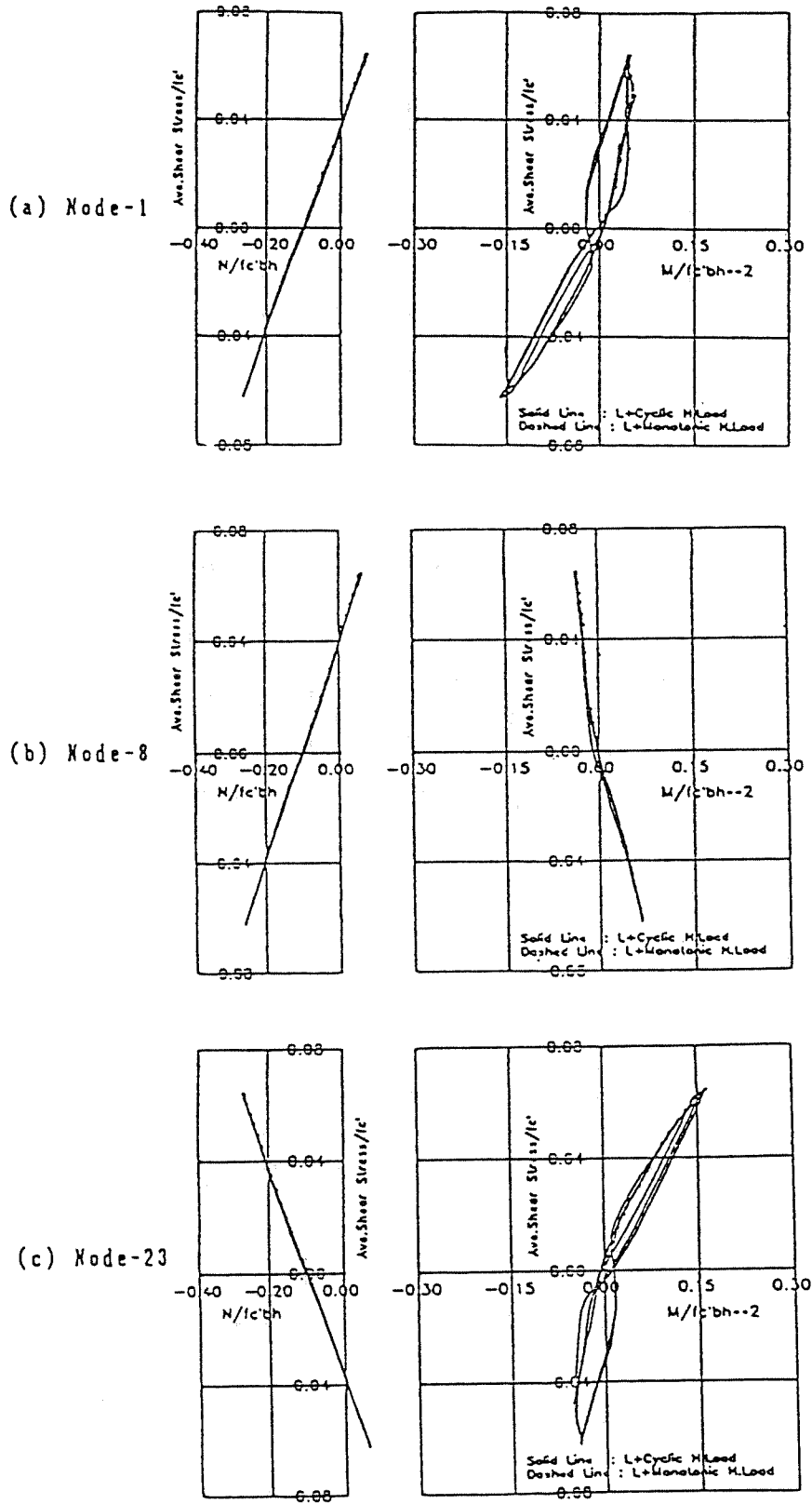
Fig.7-24   Load-Axial Force and Load-Flexural Moment
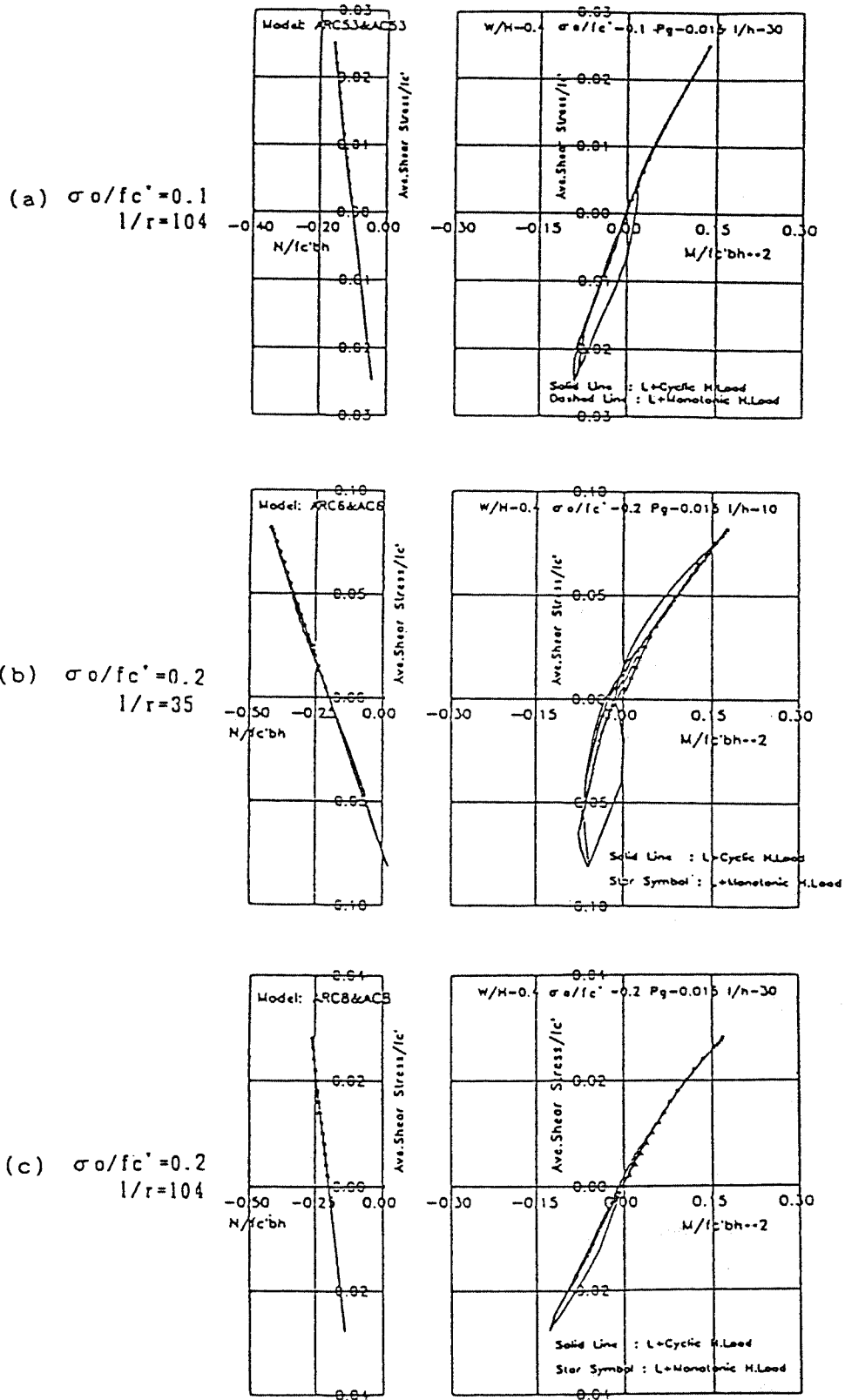(W/H=0.4   σo/fc'=0.1   Pg=0.015   1/r=35)

Fig.7-25    Load-Axial Force and Load-Flexural Moment
(W/H=0.4    Pg=0.015)

under cyclic load, it tends towards the maximum point previously reached and no significant difference in ultimate stress is observed compared to the monotonic loading result.

## (3) Variation of External Moment

The objective of this section is to investigate the contribution of secondary moment on a total internal moment.

An external moment can be written as follows accounting for the component due to geometic change.

$$M_{out} = M_H + \Delta M_D \qquad \cdots\cdots\cdots\cdots(7.5)$$

The right side of above equation consists of $M_H$ based on initial geometry and an additional moment, $\Delta M_D$ based on geometric variation which includes gravity load contribution in the present model.

Meanwhile, the internal overturning moment at the base is written as

$$M_{int} = M_a + M_b + M_n + M_q \qquad \cdots\cdots\cdots\cdots(7.6)$$

where $M_a$ and $M_b$ are flexural moments, $M_n$ is due to internal axial forces and $M_q$ internal transverse forces.
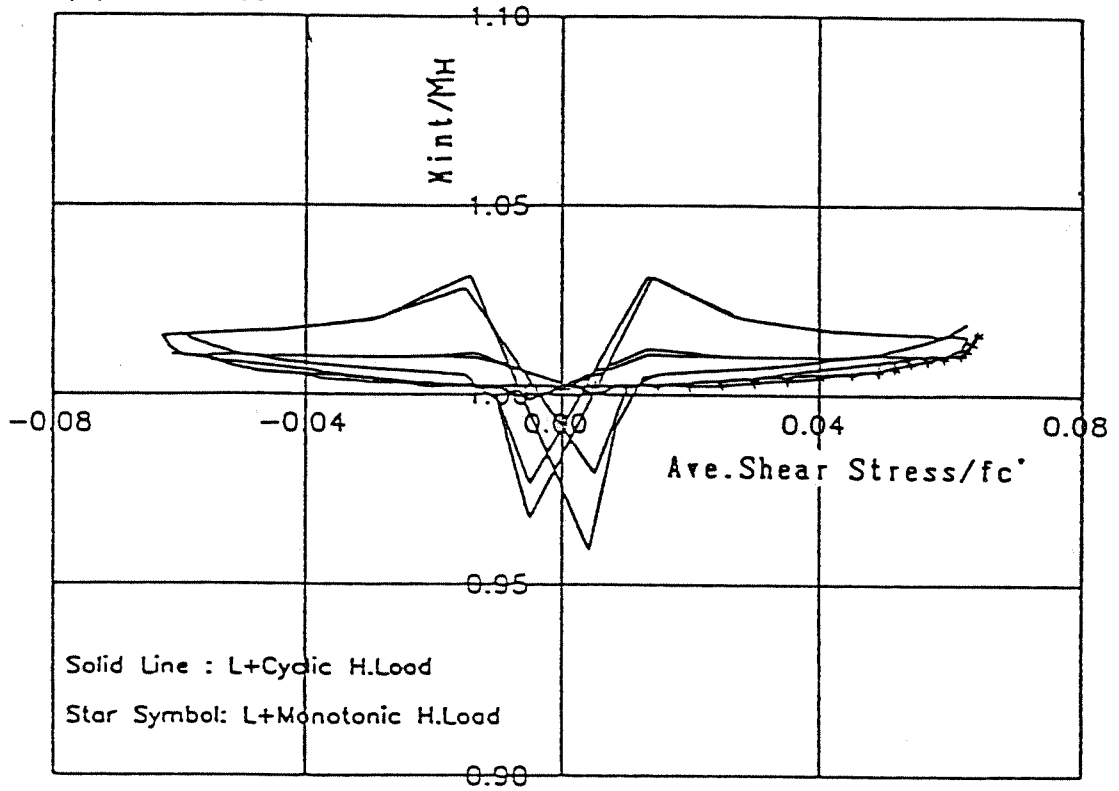
Divide equations (7.5) and (7.6) by an external moment, $M_H$ for initial geometry.

$$\frac{M_{out}}{M_H} = 1 + \frac{\Delta M_D}{M_H} \qquad \cdots\cdots\cdots\cdots(7.7)$$

$$\frac{M_{int}}{M_H} = \frac{M_a + M_b + M_n + M_q}{M_H} \qquad \cdots\cdots\cdots\cdots(7.8)$$

Fig. 7-26 provides the internal moment variation in non-dimensional form shown in eq.(7.8) against horizontal load. If assuming $M_{out} = M_{int}$,
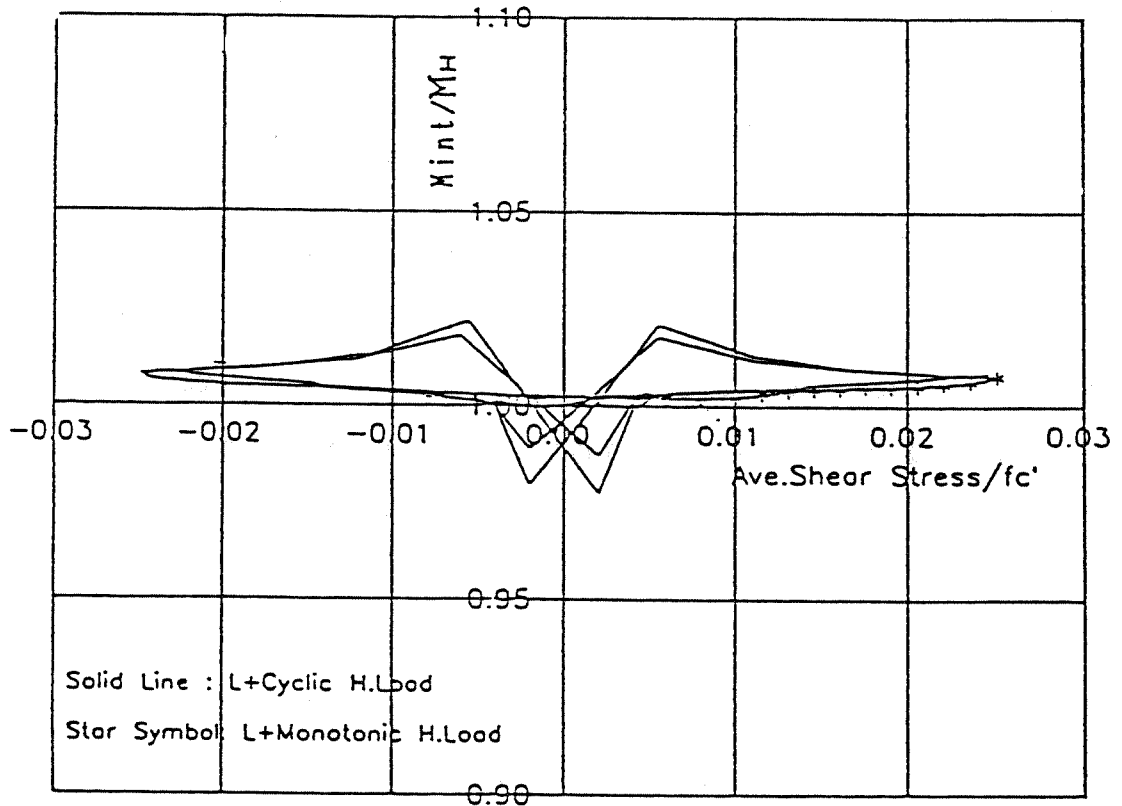
(a) l/h = 35



(b) l/h = 104



Fig.7-26   Moment Reaction-Load Relationship

(W/H=0.4   $\sigma o/fc'$=0.1   Pg=0.015)

$$\mu = \frac{M_a + M_b + M_n + M_q}{M_H} = 1 + \frac{\Delta M_D}{M_H} \qquad \cdots\cdots\cdots\cdots(7.9)$$
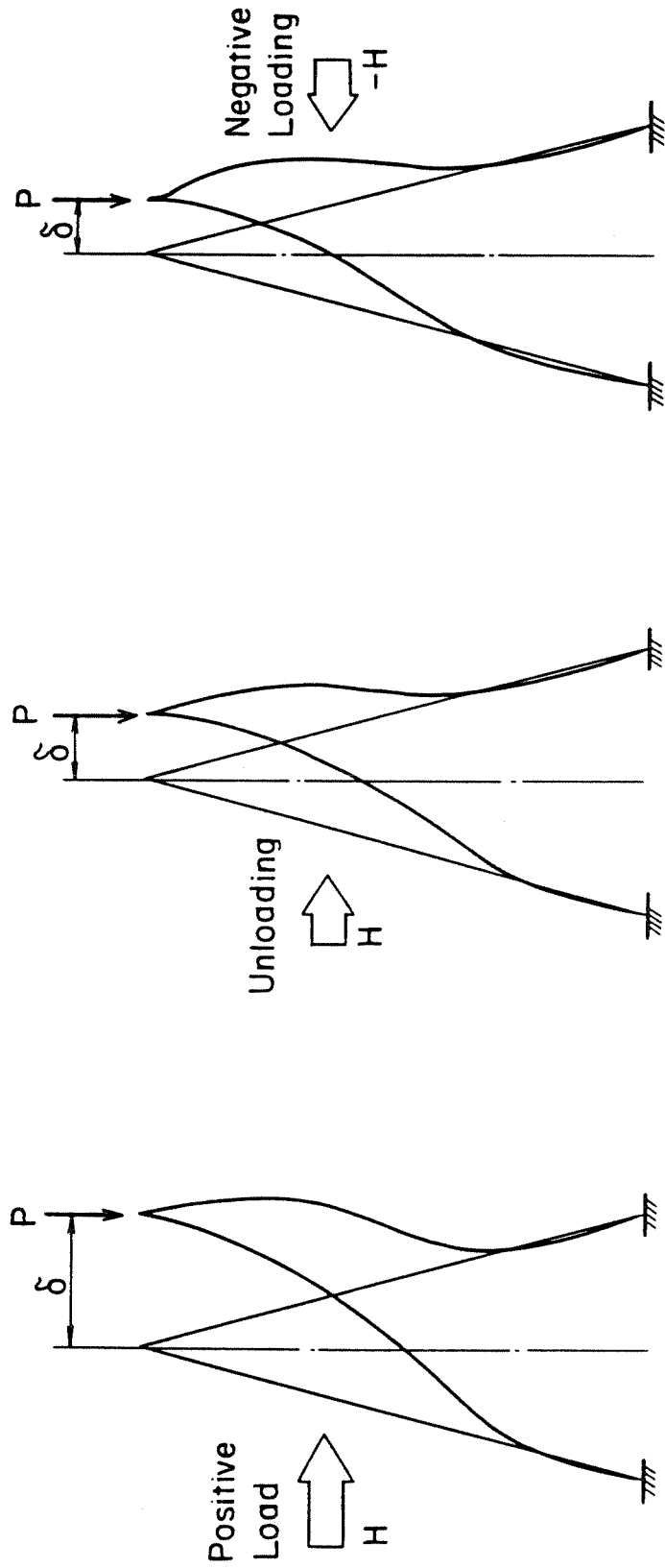
The deviation from unit value of $M_{int}/M_H$, i.e. $\mu = 1$ can be thought of as corresponding to an external moment variation based on geometric change. As far as a convergent solution is obtained, equation (7.9) should be consistent.

As the deformation becomes larger with increases of load, an additional moment expressed by the second term in the eq.(7.9) also increases. The reason why this value becomes larger under cyclic load than under monotoric lood is based on the hysteretic characteristic in which deformations become larger during cyclic load as shown in the following :

During unloading, the value moves on the different path from that during loading since the additional moment, $\Delta M_D$ based on geometric change including gravity load contribution can be relatively larger in comparison with $M_H$ because of the existence of residual deformation when an external lateral load is decreasing as shown in Fig.7-27b. On the other hand, directly after loaded in the negative region beyond origin, an additional moment, $\Delta M_D$ remains positive due to positive residual displacement and its sign differs from first moment $M_H$ (Fig.7-27c). Accordingly, the value of $\mu$ becoms less than one in that region. With an increase of lateral load, the value is recovered to be larger than one on the normal path. This value , however, is between one to two of perecentage deviation at maximum load of cycle and is at most two to three of percentage deviation even in the transient region around zero load.

(4) Moment Magnification Factor

The Fig.7-28~7-29 shows the moment magnification factor obtained by cyclic lateral load analyses (L + C.H) in addition to the results by monotonic lateral load analyses (L + H) with and without considering creep effect due to gravity load (S + H).

Fig 7-27  Participation of Secondary External Moment
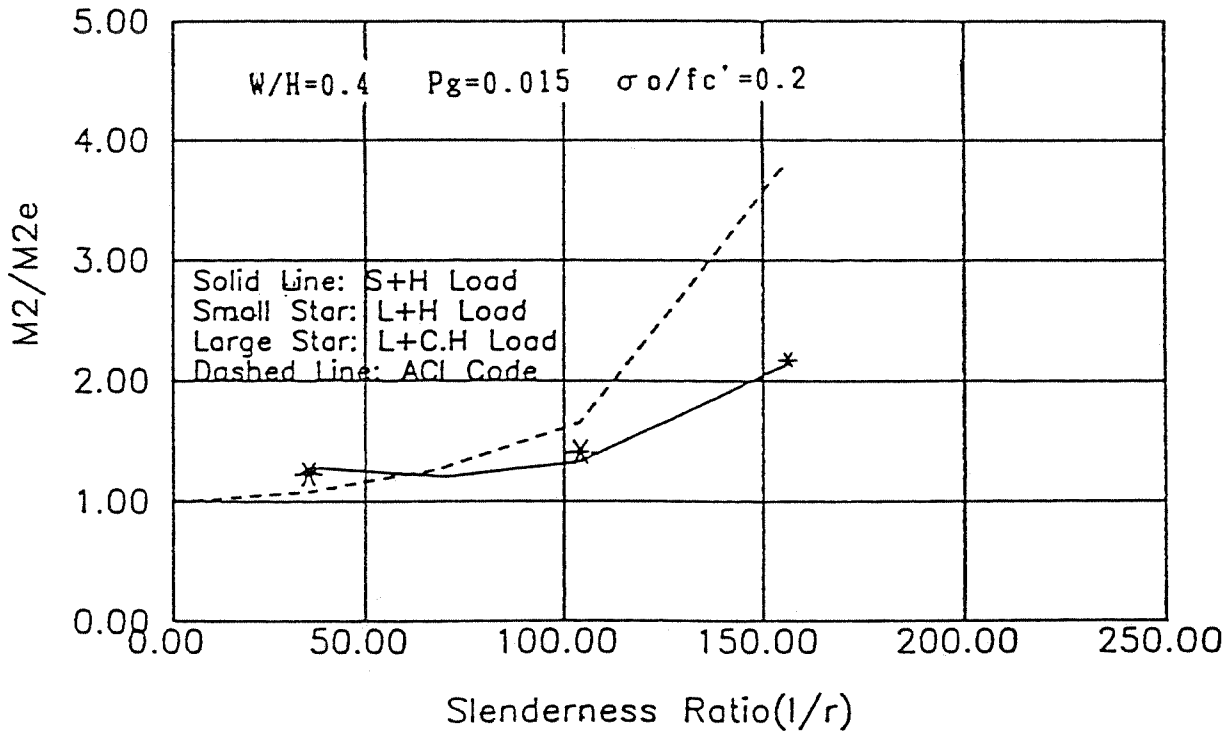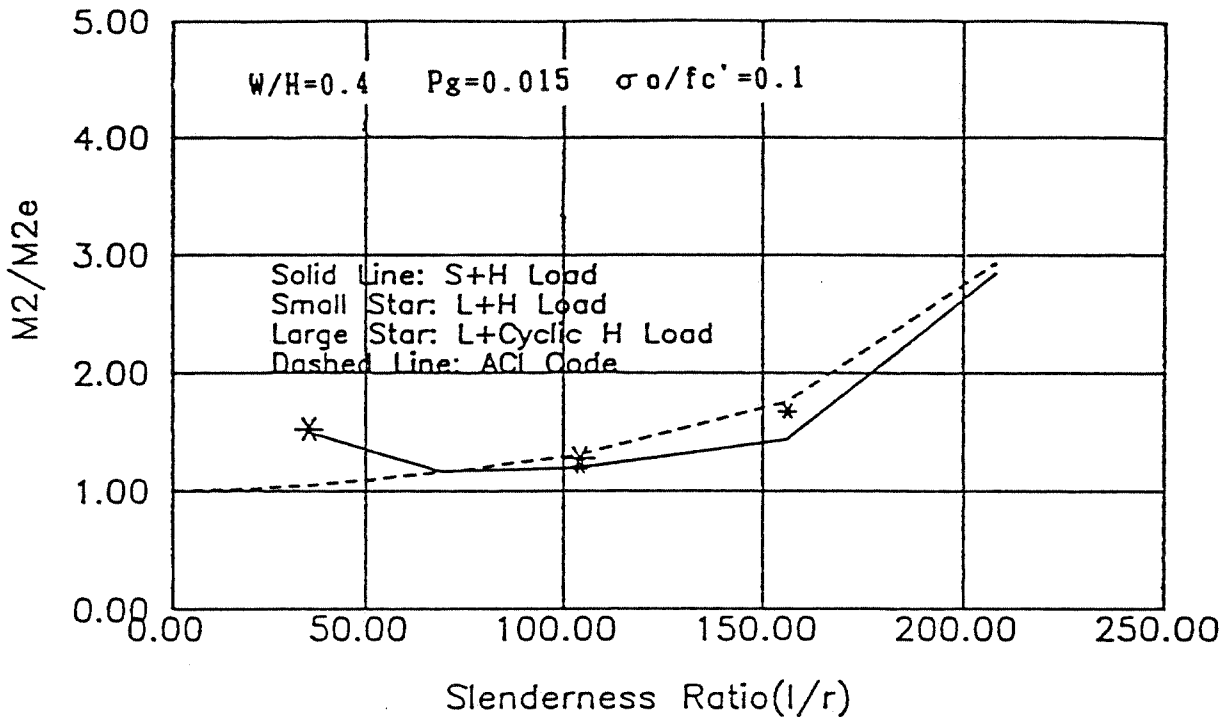
Fig. 7-28
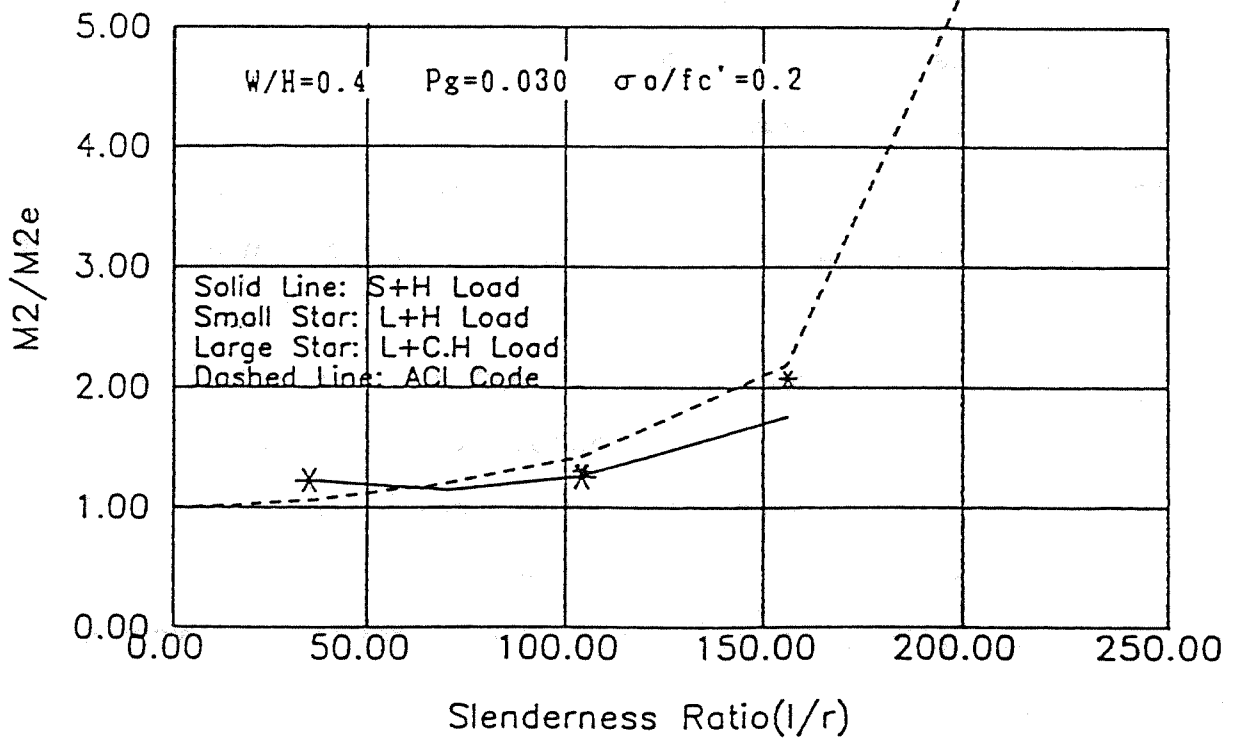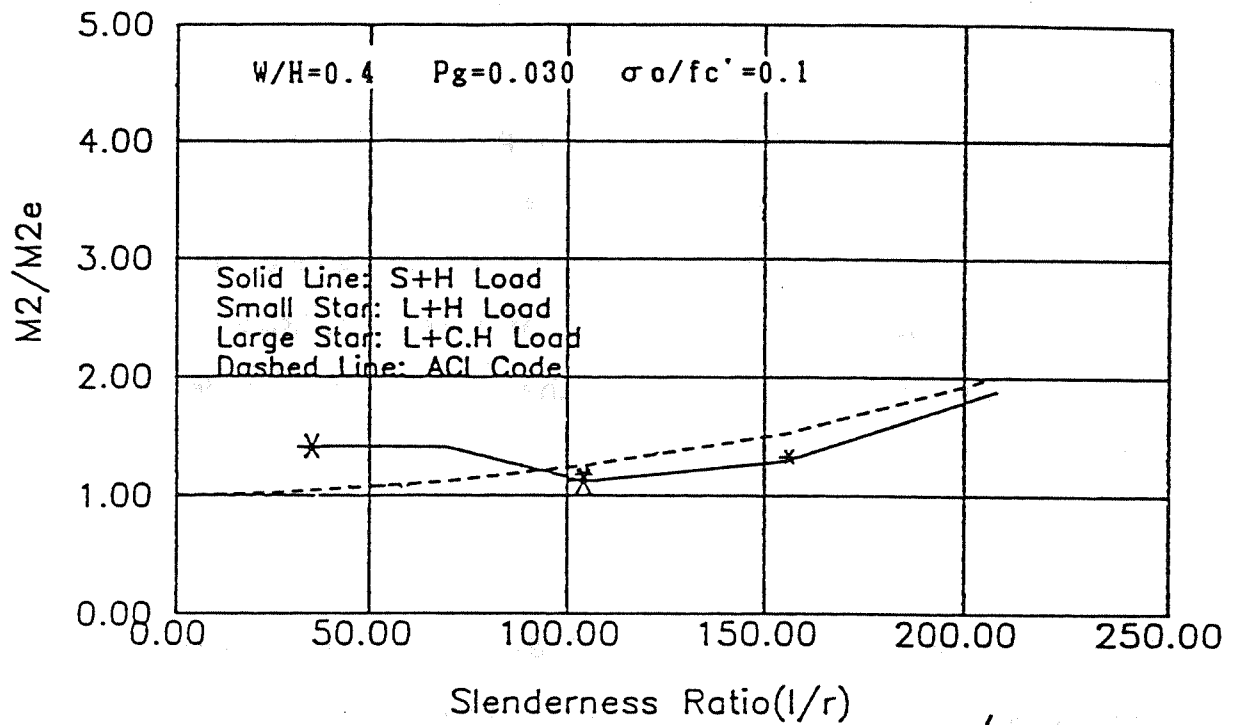Moment Magnification Factor—Slenderness Ratio(Pg=0.015)

Fig. 7−29
Moment Magnification Factor−Slenderness Ratio(Pg=0.030)

The results of cyclic load analyses are not so different from those of monotonic load analyses for the extent of $\sigma_0/f'_c = 0.1\sim0.2$ and $l/r = 35\sim104$, which is understandable from the moment behavior explained previously.    In case of $l/r = 35$, analytical values are somewhat above design values because of the predominance of frame action while in case of $l/r = 104$, all are below them.

Based on these studies, it can be said that moment redistribution due to axial force variation should be considered in the region of low slenderness ratio and that the current design method provides a conservative value in the region of larger slenderness ratio.

## 7.5  Ultimate Strength, Ductility and Failure Mode, and Cyclic Load Effect

The ultimate strength obtained by cyclic load analyses are provided in Fig.7-30~7-31.    As shown in Table7-1 of the section 7.1 , the reducation is within at most 5% against the monotonic loading result and therefore, no particular influence by cyclic load is observed.

The ductility factor also shown in the table suggests a slightly larger value provided than monotonic loading case for $p_g = 1.5\%$ case and at most 3% less value for $p_g = 3\%$ case.

Failure patterns show rank 1 mode for $\sigma_0/f'_c = 0.1$ and rank 2 mode for $\sigma_0/f'_c = 0.2$, which are similar modes to the monotonic loading cases respectively.

Accordingly cyclic load, even if creep effect is included, does not provide any siginificant influence on ultimate strength, ductility and failure mode as long as in the regon of low axial load of $\sigma_0/f'_c$ less than 0.2 and in the region of slenderness ratio, $l/r$ less than 100.
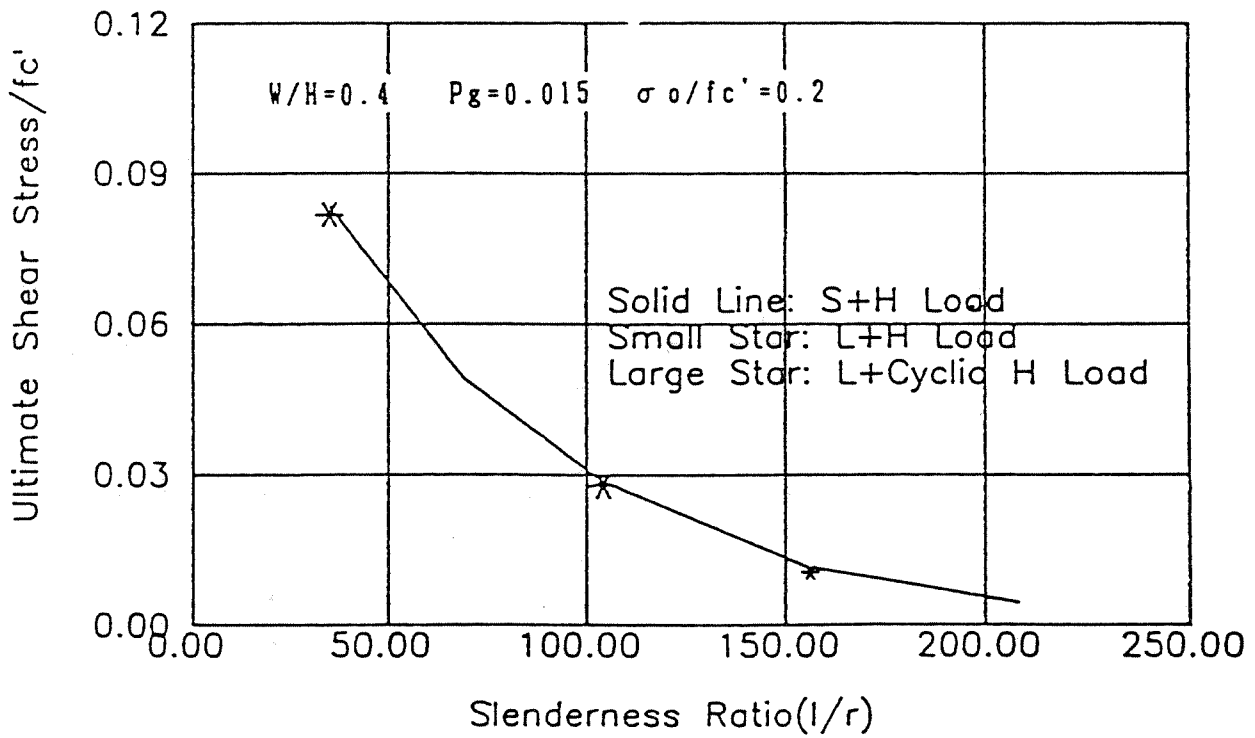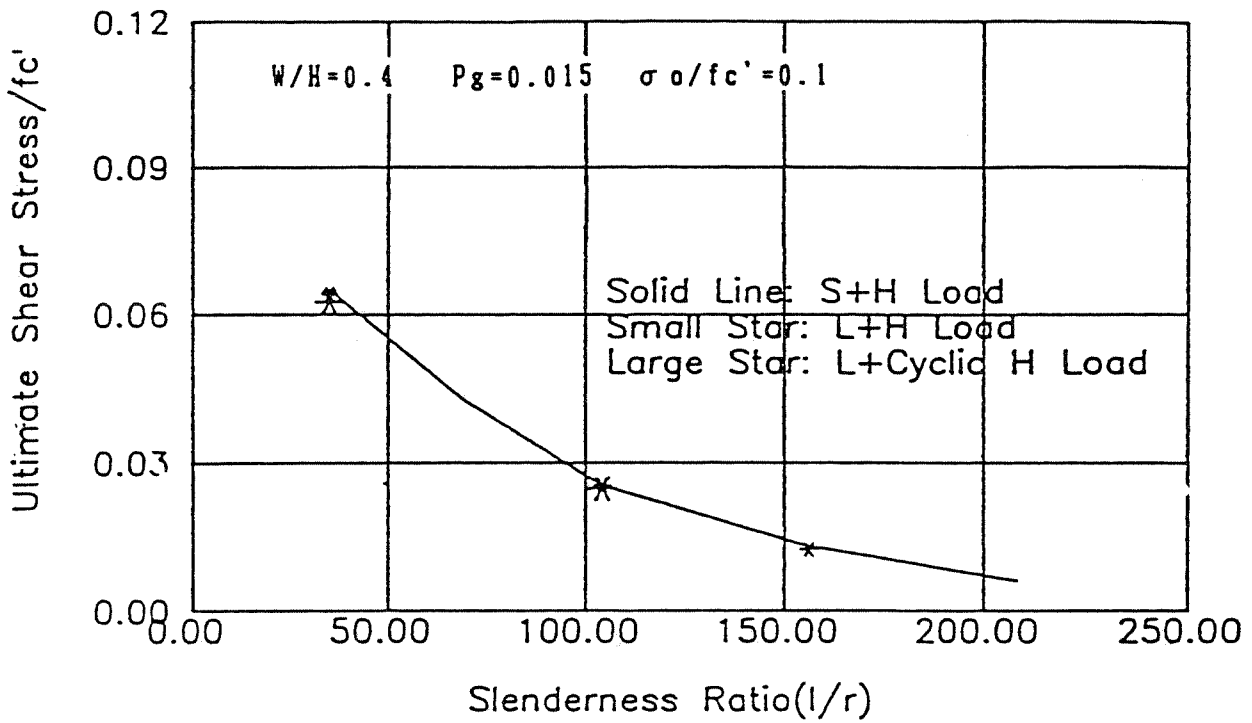
Fig. 7-30
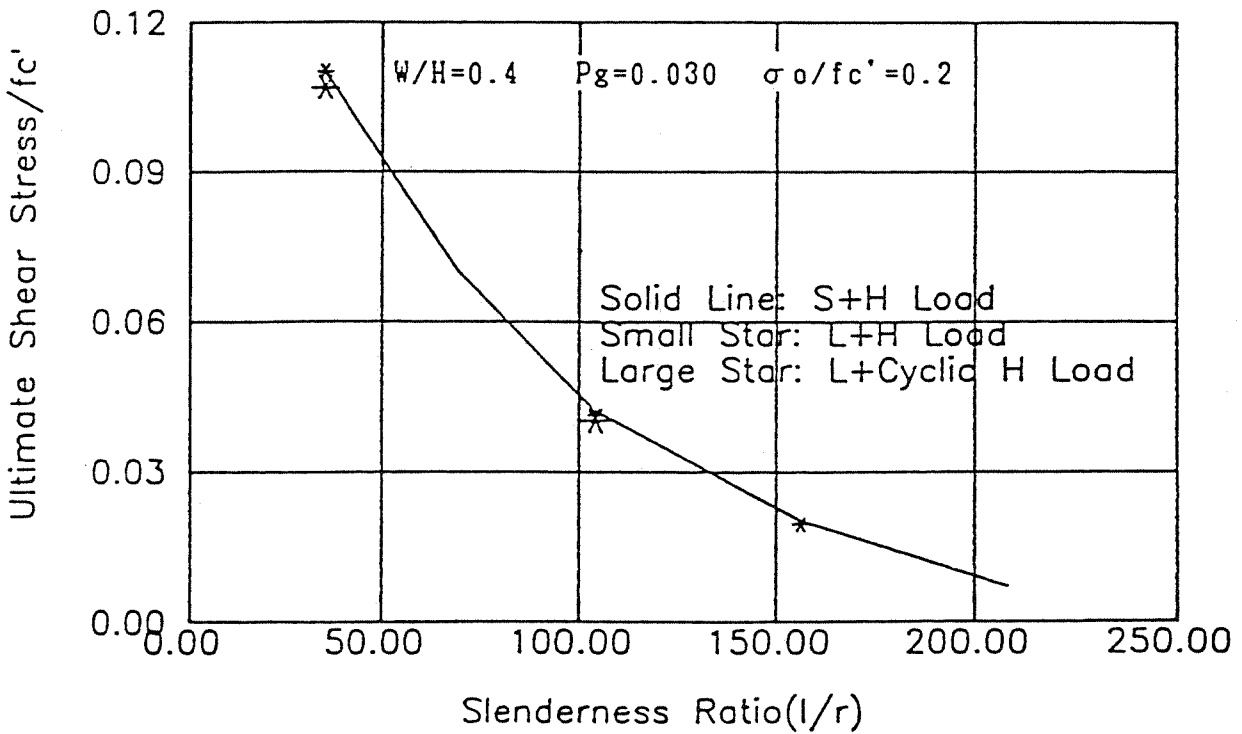Ultimate Strength—Slenderness Ratio Relationship(Pg=0.015)

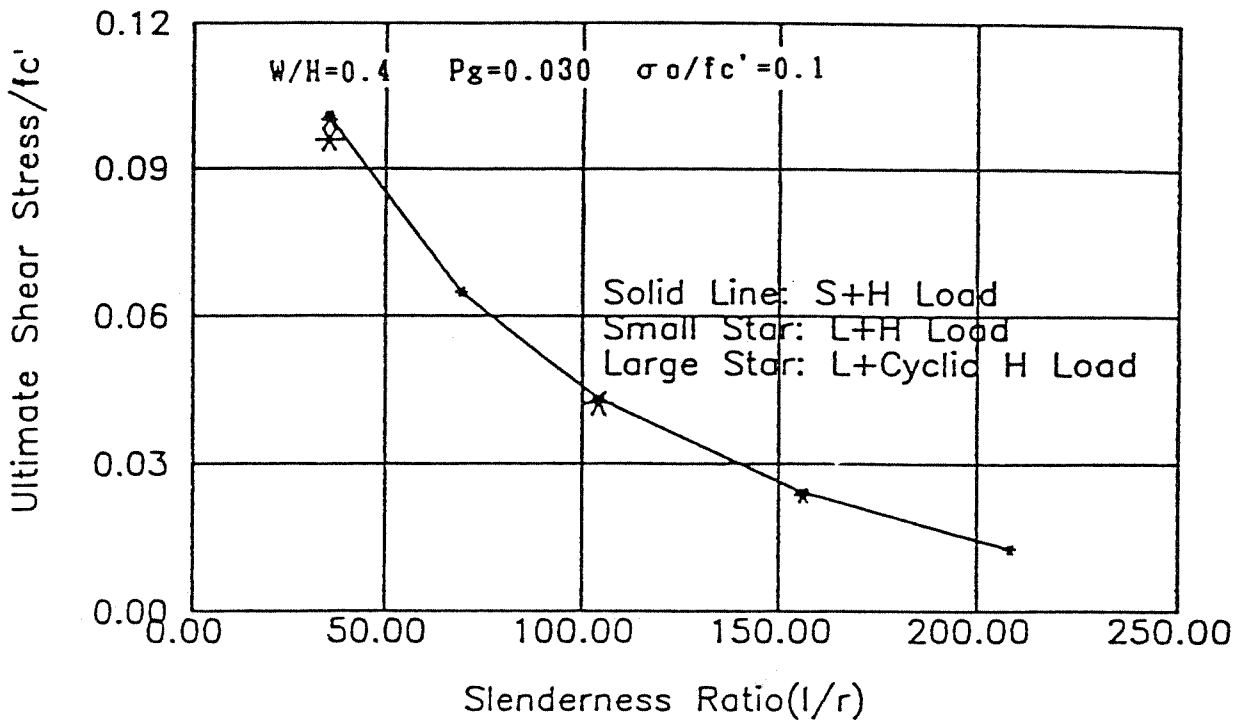Fig. 7−31
Ultimate Strength−Slenderness Ratio Relationship(Pg=0.03)

## 8. Conclusion

Based on the study presented in this report, the following conclusions can be stated:

(1) Ultimate Strength and Failure Mode

The ultimate strength becomes larger with an increase of the configuration factor of W/H, because of the predominance of frame action. That action, is especially effective when a slenderness ratio of column, l/r is less than around 100, but not when it is larger than that value. With an increase of axial load up to $\sigma_0/f'_c = 0.4$, the ultimate strength also becomes larger. Meanwhile, as an axial load increases and as a slenderness ratio, l/r becomes larger, a drastic failure tends to be introduced, especially buckling failure even under low axial load of $\sigma_0/f'_c = 0.1$ for $l/r \geq 150$. Particularly for the $\sigma_0/f'_c \geq 0.4$ and $l/r = 208$ cases, the unexpected result is that larger ultimate strength is obtained than the smaller slenderness-ratio case ($\sigma_0/f'_c \geq 0.4$ and $l/r = 156$) because of the gravity load moment action remaining during early stage of lateral load so that the overturning moment by lateral load is cancelled. As the rebar ratio increases, ultimate strength naturally becomes larger and more stable against buckling failure, but critical in concrete failure. Generally speaking, however, the rebar ratio is less sensitive in failure mode.

(2) Ductility and Absorbed Energy

For a lower axial load less than $\sigma_0/f'_c = 0.2$, ductility can be expectedly reached to some extent with plastic hinges created by tensile rebar yielding (for $\sigma_0/f'_c = 0.1$, $\mu = 1.8 \sim 4.3$ and for $\sigma_0/f'_c = 0.2$, $\mu = 1.3 \sim 2.2$ both with $l/r \leq 100$). For $\sigma_0/f'_c$ larger than 0.4, less ductility is obtained with rebar or concrete critical in compression. With regard to absorbed energy in case of lower axial load case ($\sigma_0/f'_c = 0.1$), more is obtained for smaller configuration of W/H and for smaller

slenderness ratio. With an increase of axial load and of rebar ratio, absorbed energy seems to decline and failures occur with smaller displacements due to concrete critical in compression. A sufficient value is likely to be obtained for a slenderness ratio less than 100, but less for that larger than 100.

## (3) Creep Effect on Lateral Load Behavior

Concrete is unloaded in compression during sustained gravity load, while the rebar is loaded to compensate for it. As a result, a higher initial stiffness is recovered followed by the earlier stiffness reduction due to crack occurence and then failure with somewhat lower loading capacity under lateral load when comparing the case with no creep effect involved. However, in the case of $\sigma_0/f'_c \leq 0.2$, no considerable difference in loading capacity is obtained, at most only a two percent reduction especially for $l/r \leq 100$. Ductility, on the other hand, tends to be reduced and a maximum 20% reduction is obtained in comparison with the case of no creep effect.

Based on above studies, the following restrictions for practical design usage can be suggested.

- Axial load $\sigma_0/f'_c$ at least less than 0.2
- Slenderness ratio, $l/r$ less than 100

## (4) Cyclic Lateral Load Analysis

Based on the above proposal, a series of static analyses under cyclic horizontal load have been conducted with $\sigma_0/f'_c = 0.1$ and 0.2, $l/r = 35$ and 104, and $P_g = 1.5$ and 3% as parameters.

The cyclic load analyses considering the creep effect of concrete provide at most a 5 percent reduction in loading capacity and slightly larger in ductility. This makes it possible to conclude that there are no significant influences of cyclic load and creep on loading capacity and ductility as far as design usage of axial load and

slenderness ratio is restricted in the above region.

Load-displacement characteristics provide somewhat pinching shapes for $\sigma_0/f'_c = 0.1$ case, but a thin-shape for $\sigma_0/f'_c = 0.2$ case. In addition, ductility factors are obtained of 2.2~4.2 for $\sigma_0/f'_c = 0.1$ and of 1.3~2.1 for $\sigma_0/f'_c = 0.2$. Therefore, when considering characteristics of absorbed energy under cyclic lateral loads, limitation of axial load, $\sigma_0/f'_c$ less than 0.1 and usage of confined concrete are suggested for better ductility performance.

(5) Moment Magnification Factor

In comparing current design values with the present analytical results in regions of $\sigma_0/f'_c$ less than 0.6 and of l/r less than 200, the cases with small slenderness ratio of l/r = 35 and with small axial load of $\sigma_0/f'c$ less than 0.2 present larger analytical values than design. The main reason is that moment redistribution takes place between both legs due to axial force variation. And this phenomenon is more significant as a gravity load decreases and as a slenderness ratio becomes small. The current design method, meanwhile generally provides a conservative value except in the above region. There are no significant influences of cyclic load and of creep on this factor for the axial load, $\sigma_0/f'_c$ less than 0.2 and for the slenderness ratio, l/r less than 100 region where the present structure provides stable failure.

# References

1) T. Y. Lin : State of the Art in Cable-Stayed Bridges with Concrete Deck Structure, Annals of the New York Academy of Sciences, vol.352, pp.103-121,1980

2) F. Leonhardt and W. Zeller : Long span bridges, O. H. Ammann centennial conference, The N. Y. Academy of Sciences

3) AISC :Commentary and Specifications for the Design, Fabrication, and Erection of Structural Steel for Buildings, American Institute of Steel Construction, N.Y., 1969

4) ACI Committee 318 :Building code requirement for reinforced concrete, ACI 318-83,3rd Printing, Dec., 1985

5) J. G. Macgregor, J. E. Breen and E. O. Phrang : Design of slender concrete columns, ACI Journal / Jan. 1970, pp6~28

6) J. E. Breen, J. E. Macgregor : Determination of effective length factors for slender concrete columns, ACI Journal / Nov. 1972, pp669~672

7) Y. J. Kang : Nonlinear geometric, material and time dependent analysis of reinforced and prestressed concrete frames, UCB / SESM77-1, Jan / 1977

8) Park and Pauley : Reinforced Concrete Structures, Wiley-Interscience, 1975

9) Fung, Y. C. : Foundations of Solid Mechanics, Prentice-Hall Inc., New Jersey, 1965

10) J. Hellesland, D. Choudhury and A. C. Scordelis : Nonlinear analysis and design of RC bridge columns subjected to imposed deformations, UCB / SESM-85/03, Apr. 1985

11) ACI Committee 209 :Prediction of creep, shrinkage and temperature effects in concrete structures, ACI special Publication SP-76, 1982, pp193~300

12) Rita Robinson : Cable stays catch on, Civil Eng., Jun. 1986, pp58~61

13) P. R. Taylor and alt., Annacis cable-stayed bridge-design for earthquake, Can. Journal of Civil Engineering, vol, 12, 1985, pp 472~482

14) Hybrid girder in cable-stay debut, ENR, Nov. 15, 1984

15) Arvid Grant : The Pasco-Kennwick Intercity Bridge, PCI Journal, May-June 1979 pp90~124

16) The task committee on cable-suspended structures : Comentary on the tentative recommendations for cable stayed bridge structures, ASCE ST5, May 1977, pp941~959

17) R. W. Poston, M. Diaz and J. E. Breen : Design trend for concrete bridge piers, ACI Journal, Jan-Feb. 1986, pp14~20

18) R. W. Poston, T. E. Gilliam, Y. Yamamoto and J. E. Breen : Hollow concrete bridge pier behavior, ACI Journal, Nov.-Dec. 1985, pp779~787

19) D. Ristic, Y. Yamada and H. Iemura : Stress-strain based modelling of Hysteretic structures under eathquake induced bending and varying axial loads, Research Report No. 86-ST-01, Kyoto Univ., March 1986

20) ACI Committee 318 :Commentary on Building Code Requirement for Reinforced Concrete (ACI 318-83) ,3rd Printing, Oct., 1985